REFERENCE ONLY

UNIVERSITY OF LONDON THESIS

Degree PhD Year 2005 Name of Author DENHAM, A C

Design and Evaluation of a Coherent Multistatic Radar System

by

Thomas Edward Derham

A thesis submitted for the degree of Doctor of Philosophy of the University of London

Faculty of Engineering
Department of Electronic & Electrical Engineering
University College London

The United Kingdom

April 2005

ProQuest LLC
789 East Eisenhower Parkway
P.O. Box 1346
Ann Arbor, MI 48106-1346

Abstract

Modern radar systems are required to perform a multitude of functions including highly accurate detection, parameter measurement, classification and tracking of targets over long distances. These targets may have low effective visibility and exist in a hostile environment of noise and interferences. Significant improvements in traditional monostatic radar require brute-force approaches such as larger antennas and power amplifiers, which are impractical and expensive. Multistatic radar, comprising a system of multiple, spatially separated transmitters and receivers, is one promising solution to this problem.

This thesis concerns the design, development and construction of such a radar at low cost, in particular where each dispersed component of the system is mutually coherent and networked to allow cooperative operation and the joint processing of all received signals.

The statistical theory of multistatic detection is analysed and processing algorithms are developed for implementation in the system. Models for the predicted coverage of the radar are developed, and illustrations of the system instrument function are presented based on the derivation of the ambiguity function for a range of topologies and modes of operation.

The requirements for obtaining spatial coherency across the system are considered, and methods of fulfilling these requirements at low cost are devised. A complete design strategy for the radar is developed, based on the use of commercial components and open architecture interfaces. The development of each major subsystem is explained, and the construction of the multistatic radar completed. Finally, the system is tested and calibrated, and some initial experiments are performed in order to determine its performance and demonstrate the advantages of this type of radar.

Acknowledgments

In any work of this nature, the support and guidance of one's supervisors is fundamental to its success. I would therefore like to sincerely thank Dr Karl Woodbridge and Professor Chris Baker for their unwavering support, advice (and cajolement!) over the entire period of my studies, as well as their assistance with the preparation and proofing of this document. I am deeply grateful to them both, and have learned a great deal from their tutorage.

I would also like to acknowledge the other members of the Microwaves, Radar and Optics Group at UCL led by Professor Hugh Griffiths. In particular, I thank Dr Richard Bullock and Aric Whitewood for providing excellent sounding boards for ideas. Aric shall be glad to have one less person 'borrowing' his hard-to-find SMA adaptors, cables and scarce stable oscillators! I am indebted to many other friends for their support and encouragement, in particular Richard James, who also deserves credit for improving my programming skills.

Shaun Doughty has the dubious pleasure of inheriting the legacy of my hardware development, for which I wish him well, and also thank him for his assistance with system calibration and practical experiments. Further, I am grateful to Professor Mike Inggs from the University of Cape Town for his advice and have benefitted greatly from his 'hands-on' experience.

To my partner Tomoko Kasai, I am sincerely grateful for her love, indefatigable support, and for giving me both the time and encouragement to complete this work.

As a recipient of the AHW Beck Memorial Scholarship, I am grateful to the Beck family for founding the award and their enthusiasm and interest in my studies.

Finally, I would like to thank my family, particularly my father, whose long-standing support for my education has made it possible for me to complete this work.

Copyright

Code

Pseudocode is used in-line for brevity in descriptions of digital signal processing algorithms in Chapter 5.

Electronic versions of all code, including the FPGA core (VHDL/Verilog), DSP code (C), source code for the custom-designed NetRad control software (Visual C++ .NET), Agilent ADS simulations, and Matlab code relating to the ambiguity function simulations in Chapter 3 and the detection algorithms used with the prototype system in Chapter 5, together with experimental data, hardware documentation and test procedures are archived at the Department of Electronic & Electrical Engineering, University College London.

Typesetting

This document was typeset using LaTeX[1] in Times font. Figures were created using Adobe Illustrator CS in Myriad font. Graphs were generated with Matlab and NetRad.

[1] http://www.latex-project.org

Table of Contents

List of Tables

List of Figures

List of Principal Symbols

a_{si}	rms amplitude of signal at the ith receiver
$\chi(\omega)$	Fourier transform of received signal
dBc	power in decibels relative to the carrier
dBFS	power in decibels relative to 'full scale'
dBm	power in decibels relative to 1 mW
dBpp	power in decibels relative to the maximum value of the peak power
i	receiver index
k	transmitter index
m	number of receivers
n	number of transmitters
φ_{si}	initial phase of the signal at the ith receiver
$\Psi(\omega)$	Fourier transform of wanted (reference) signal
s_{0k}	complex envelope of signal used by kth transmitter
$S_i(t)$	wanted signal at the ith receiver
τ	time of arrival / lag
t_{si}	propagation delay of signal at the ith receiver
$\boldsymbol{\Theta}$	vector of signal parameters
$X_i(t)$	total signal at the ith receiver
ω_0	carrier frequency
Ω	doppler frequency

Abbreviations

ADC	Analogue to Digital Converter
CAD	Computer Aided Design
CAN	Controller Area Network
CMOS	Complementary Metal Oxide Semiconductor (logic)
COTS	Commercial Off-The-Shelf
CW	Continuous Wave
DAC	Digital to Analogue Converter
DDS	Direct Digital Synthesis / Synthesiser
DFT	Discrete Fourier Transform
DLL	Delay Locked Loop
DSP	Digital Signal Processing / Processor
DTFT	Discrete-Time Fourier Transform
ECL	Emitter Coupled Logic
ECM	Electronic CounterMeasures
EIRP	Effective Isotropic Radiated Power
EMIF	External Memory InterFace (Texas Instruments C6000 bus)
FFT	Fast Fourier Transform
FPGA	Field Programmable Gate Array
GPS	Global Positioning System
IC	Integrated Circuit
IP	Intellectual Property
IQ	In-phase - Quadrature
ISM	Industrial, Scientific and Medical (band)
JTAG	Joint Test Action Group (standard)

LVPECL	Low Voltage Positive Emitter Coupled Logic
MLVDS	Multipoint Low Voltage Differential Signalling
MIL-STD	Military Standard
MAC	Medium Access Control
ML	Maximum Likelihood
MRC	Maximal-Ratio Combiner
MSPS	Mega-Samples Per Second
MSRS	MultiSite Radar System
MTI	Moving Target Indicator
NCO	Numerically Controlled Oscillator
OEM	Original Equipment Manufacturer
OFDM	Orthogonal Frequency Division Multiplexing
PCB	Printed Circuit Board
PLL	Phase Locked Loop
PRF	Pulse Repetition Frequency
PRI	Pulse Repetition Interval
RCS	Radar Cross Section
SNR	Signal to Noise Ratio
SoC	System-on-a-Chip
SSB	Single Side-Band
TDOA	Time Difference Of Arrival
TOA	Time Of Arrival
TTL	Transistor Transistor Logic
UWB	Ultra-WideBand
VHDL	Very high speed integrated circuit Hardware Description Language
VME	Versa Module Europa (bus)

Chapter 1

Introduction

1.1 Overview

This thesis is concerned with the design, development, construction and testing of a networked radar system. Radar research over the past fifty years has frequently focussed on obtaining greater target detection certainty and accuracy of parameter estimation. Simultaneously, there is a demand for radars with improved coverage that are capable of detecting complex targets with low effective visibility in the presence of considerable interference. It is desired that greater target information be obtained so that the radar can perform reliable classification in addition to simple detection.

Recent developments in radar *component* technology have allowed the production of cheaper, lighter and more versatile systems. Nevertheless, to dramatically increase the range and detection capability in a traditional monostatic system (with colocated transmitter and receiver) requires a *brute-force* approach, i.e. larger amplifiers and antennas, which are heavy, large, immobile, power-hungry and expensive.

Over the last few years a new topology has received attention, which comprises several radar *nodes* or *stations* that are spatially separated. Such *multistatic* systems have been common in the literature for decades, but recent approaches take advantage of modern technologies such as digital data networks and time transfer methods in order to more tightly couple the nodes comprising the system. These technologies may enable a system of diversely located, networked transmitter and receiver modules to be considered as a single, distributed radar, incorporating spatial coherency and seamless integration of received signals at a low level. Such architectures have been variously described in the literature as *netted radar*, *multiradar* or *multisite radar* without strict definition. 'Netted' radar often refers to a network of monostatic radars that can operate cooperatively, whereas 'multistatic' emphasises the spatial distribution as an abstraction of bistatic radar, with 'multisite' being the more generic term.

A multistatic system can use its spatial diversity for energy and information gains by receiving the radiated electromagnetic field from a target in several directions. Modern *stealth* aircraft such as the B-2 Spirit Bomber present considerable detection problems for monostatic radar by using radar absorbent material (RAM), body shaping and active cancellation to reduce backscatter reflectivity(1). In general, stealth aircraft are designed to minimise their frontal backscatter, so a multistatic system may be able to use spatially separated receivers

to detect the larger reflected signal in other scattered directions, particularly from the side and above(2). In addition, if each node is capable of transmission and reception, it may be possible to provide greater coverage through diversity of look-angle, greater combined receiver sensitivity and more linear distribution of power density, compared to a monostatic system with the same total transmitted power(3). Range and doppler resolution may also be improved where the additional *redundant* information obtained by using several nodes observing the same target from different aspects can be used to increase accuracy(4). It has been proposed there may be further advantages to multistatic systems in terms of clutter rejection(5), tolerance to electronic countermeasures(6) and survivability(7).

Multistatic radar is a topic of current interest to the radar research community, and major radar conferences frequently have sessions devoted to the subject. There is not, however, a large volume of dedicated texts, nor has an integrated approach to the design of such systems been published in the literature. This thesis documents the development and evaluation of a prototype low-cost coherent multistatic system, together with analysis of the associated theory and design issues, in order to understand the nature of the instrument function and attainable performance when using such architectures.

1.2 Thesis Outline

This chapter provides a brief introduction to the fundamentals of radar, its applications, and an overview of the topologies for monostatic, bistatic and multistatic systems including definitions of terminology used later in this thesis. A critique of the potential benefits of multistatic radar is presented, as well as the disadvantages and challenges involved in the implementation of such systems. This is followed by an outline of the history of radar development with an emphasis on bistatic and multistatic configurations, and a literature review focussing on the current research in this field and its context to this work.

In Chapter 2, consideration is given to methods of target detection and parameter estimation in multistatic radar. In monostatic systems, detection is usually performed by applying a threshold to the received signal processed by a 'matched filter'. However, the equivalent detection process in a coherent multistatic system should take account of the optimal method of combining the signals at *all* receivers. Appropriate forms of this detector are presented based on statistical detection theory. These algorithms are used in

subsequent chapters to determine coverage, the ambiguity and instrument functions, and as a basis for the signal processing system implemented in the prototype multistatic radar. Then, methods of optimal estimation of the target parameters are considered, which can take advantage of the extra information afforded by the multistatic spatial diversity.

Chapter 3 considers some important theoretical aspects relating to the characterisation and performance prediction of this type of multistatic radar. It begins with an analysis of range and sensitivity in multistatic systems. The well-known 'radar equation' is extended to account for the total multistatic system sensitivity using the results derived from the previous chapter, and may be used to determine the specification for the prototype system. Then, a multistatic form of the 'ambiguity function' is derived based on the detection algorithms in Chapter 2, and is used to analyse the response of the complete system with a given topology to the presence of an arbitrary target. This model allows theoretical determination of the 'instrument function' for the system, and a series of simulated results are presented that may be used as a benchmark for experiments with the prototype radar.

Chapter 4 sets the framework for the design of the prototype system. In the first section, a review is undertaken of potential technologies to fulfil the design requirements for a coherent multistatic system. The design methodology chosen maximises the use of commercial components and generic open architectures, and these concepts are examined in the context of low-cost radar design. In addition, a survey of modern digital components for data capture, signal processing and networking is carried out with reference to the requirements for a real-time system. It is expected that the quality and synchronisation of oscillators and waveform generators in such a radar will be a major influence on performance, so an analysis of oscillator stability is presented that is used to determine the system requirements. This is followed by the development of a time-domain computer simulation for a generic coherent radar system. The distributed nature of the system makes analytic evaluation of the effect of non-idealities on the full instrument function complicated, so this simulation can be used to aid this analysis and guide the hardware design process. In particular, the effects of oscillator noise and clock jitter are analysed as drivers for models of critical subsystems in the design.

Chapter 5 describes the development and construction of the prototype multistatic system. The design of each hardware module and the engineering techniques utilised in order to meet the system specification at a low cost are described, and a budgetary analysis for

the component hardware is carried out. The networking and synchronisation architectures are explained, together with an account of the design of the system control software. The design of the signal processing system is described, based on the algorithms in Chapter 2.

Chapter 6 describes the calibration and experimental testing of the prototype system. A summary of the Acceptance Test Procedure for the system is presented, and is followed by the results of a series of initial experiments designed to calibrate the system, focussing on determination of the system instrument function and coherency. The results are analysed with comparison to the developed theory and baseline monostatic performance.

Chapter 7 concludes with a summary of the work described in this thesis, and the consideration of potential avenues for further research in this area.

1.3 Radar Fundamentals

1.3.1 The Basics

The design of a multistatic radar system must take into account its possible topologies, which are inherently more complicated than those for monostatic and bistatic systems. Therefore it is appropriate here to introduce the subject in general terms and summarise the distinguishing attributes of these three types of radar.

'Radar' is formally an acronym standing for *RAdio Detection And Ranging*, although it is now commonly spelt in lower case. It concerns the use of radio waves to detect objects and measure their position. Radar is used in a multitude of applications including military detection, tracking and guidance, air and sea traffic control, collision avoidance, weather forecasting and industrial measurement. Modern radar has developed many additional capabilities such as target identification and high resolution imaging. An *active* radar 'set' comprises a transmitter and receiver, whereas a *passive* system has a receiver only, making use of external transmitting sources such as other radars, radiating targets (such as ships and aeroplanes) and the so-called *illuminators of opportunity* such as television and radio broadcast signals - most notably the Lockheed Martin Silent Sentry system(8).

In an active system, which is the main focus of this work, the transmitter sends out a radio signal, which will scatter off any objects that it encounters. In a *continuous wave (CW) radar* the transmitted signal is broadcast continuously over the period of operation, whereas a *pulse radar* transmits short intermittent bursts of radio energy. The receiver detects some

(usually very small) part of that reflected signal, and processes it to calculate the required parameters. Much radar research concerns methods of maximising the information that can be extracted from this received signal.

In a *monostatic* system such as that in Figure 1-1 where the transmitter and receiver are colocated (and may share the same antenna), a pulse radar can calculate the range R (the distance from the radar to a target) from the delay τ between transmitting the pulse and receiving its echo:

$$R = \tfrac{1}{2}c\tau \tag{1.1}$$

where c is the propagation speed of the pulse.

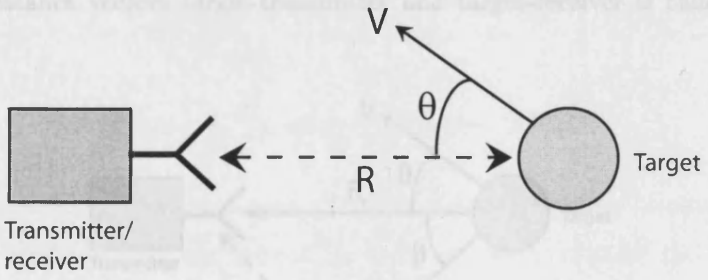

Figure 1-1: Topology of a monostatic radar

If a target is moving with velocity vector V such that the component of its velocity in the radial direction (to or from the radar) $V\cos(\theta)$ is constant, a doppler frequency shift f_D will occur:

$$f_D = f_R - f_T \tag{1.2}$$

where f_T is the (fixed) transmitted frequency. $V\cos(\theta)$ is equal to the negative of the *range rate* $\dot{R}$ (a decreasing path length creates a positive doppler shift). If the received frequency f_R can be measured by the radar, the velocity component can be calculated by:

$$V\cos(\theta) = -\dot{R} = -\frac{dR}{dt} = \tfrac{1}{2}f_D\lambda \tag{1.3}$$

where λ is the wavelength of the transmitted signal.

1.3.2 Bistatic Radar

Bistatic radar also comprises a single transmitter and receiver, but in this case they are non-colocated. This separation means that separate antennas are required, although as a result a 'duplexer' is not necessary. In addition, the sensitive receiver does not require special protection from the transmitted pulse. Bistatic systems have a further advantage (chiefly in a military situation) that the receiver station is passive and hence its location is undetectable. In certain configurations, less transmitted power is required to detect targets using this topology compared to a monostatic system. The distance between the two components is called the *bistatic baselength* L as shown in Figure 1-2. The angle β between the distance vectors target-transmitter and target-receiver is called the *bistatic angle*.

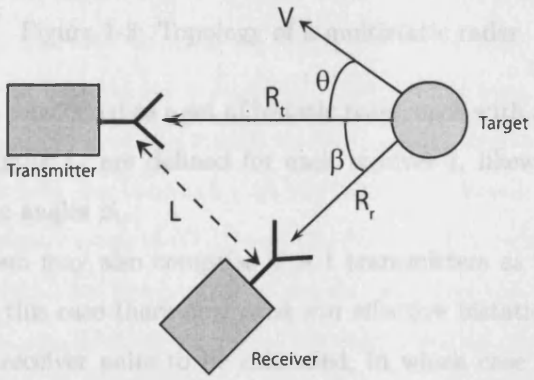

Figure 1-2: Topology of a bistatic radar

In a bistatic radar, the delay τ gives a measure of the total range $R_t + R_r$:

$$R \equiv R_t + R_r = c\tau \tag{1.4}$$

The apparent doppler frequency is proportional to the total range rate $\dot{R}_t + \dot{R}_r$. Assuming that the transmitter and receiver are stationary, this can be expressed in terms of the component of the target velocity in the direction of the bistatic bisector (given by $V cos(\theta + \beta/2)$ for the topology shown in Figure 1-2) such that:

$$V cos(\theta + \beta/2) = -\frac{1}{2}\frac{d(R_t + R_r)}{dt} = \tfrac{1}{2} f_D \lambda \tag{1.5}$$

1.3.3 Multistatic Radar and Terminologies

Bistatic systems can be considered the simplest case of multistatic radar as they comprise components at two distinct locations. However the usual definition is of a system comprising a single transmitter and multiple spatially separated receivers $1..m$, as shown in Figure 1-3.

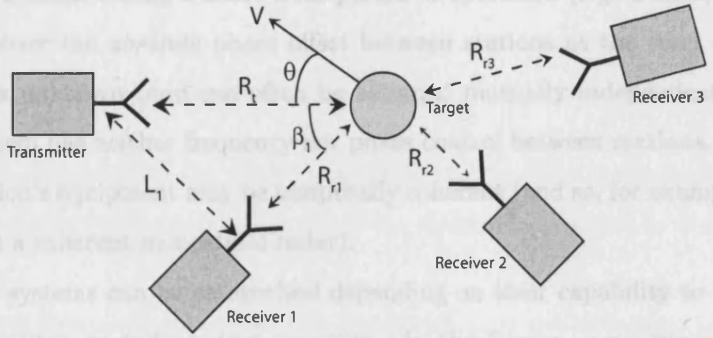

Figure 1-3: Topology of a multistatic radar

The system can be considered as a set of bistatic pairs, each with a common transmitter. Therefore the baselengths L_i are defined for each receiver i, likewise the target-receiver ranges R_{ri} and bistatic angles β_i.

A multistatic system may also comprise $n > 1$ transmitters as well as (or instead of) multiple receivers. In this case there now exist mn effective bistatic pairs. It is allowable for some transmitter/receiver pairs to be colocated, in which case the system contains a combination of bistatic and monostatic components.

The abbreviation $MSRS$ (MultiSite Radar Systems) has been coined by Chernyak(9) to define *a radar system including several spatially separated transmitting, receiving and (or) transmitting-receiving facilities where information pertaining to each target from all sensors is fused and jointly processed*[1]. This definition therefore includes the wider sense of multistatic radar described above, but excludes single bistatic systems, and emphasises the spatial separation of stations (or *nodes*) and the centralised processing of combined data.

Such systems can be categorised in a number of ways, the most important of which will be considered here. Firstly the *degree of spatial coherence* is defined. A fully spatially coherent system is capable of maintaining dependence between the phase of RF signals in each station. This implies that each contains a *coherent reference oscillator*, and frequency

[1] slightly paraphrased from the original text for clarity

and phase control exists between all such oscillators so that the phase difference (or 'offset') between them is deterministic[2].

A system with *short-term spatial coherence* contains reference oscillators that have the same nominal frequency, and are stable enough that the *change* in relative phase offset between them is small during a short-term period of operation (e.g. a scan, or integration interval). However the *absolute* phase offset between stations at the start of each operational period is unknown (and can often be assumed mutually independent). A *spatially incoherent* system has neither frequency nor phase control between stations, although each individual station's equipment may be temporally coherent (and so, for example, be capable of operating as a coherent monostatic radar).

Multistatic systems can be categorised depending on their capability to perform either *cooperative reception* or *independent reception.* In the former, more versatile case, each receiver has knowledge of every transmitted signal (its exact time, frequency, phase and waveform characteristics), so that the scattered signals derived from each can be processed in every receiver. In the latter case, the system essentially consists of a network of monostatic systems where each receiver has knowledge of only its local transmitted signal.

In addition to the maintenance of RF phase relationships, the reference oscillator usually provides a timing reference for the control of 'events' (such as the start of receiver signal capture). Hence, gross synchronisation errors between stations often preclude the use of the cooperative reception method. Therefore in practice, the degree of coherency dictates the type of processing (data fusion) that can be performed, and in doing so affects the requirements for the data network between stations. In general, it is proposed that a system using cooperative reception can improve performance by the central integration of complex raw data from all receivers, which implies a high bandwidth network, whereas for systems using independent reception, higher level fusion methods (e.g. plots or tracks) are more appropriate.

A multistatic system is by definition *dispersed*, i.e. its constituent nodes are located in different positions. The term *distributed* has a similar meaning, but may also imply that the control or signal processing systems are comprised of multiple non-colocated networked modules (compare with, for example, distributed computer architectures).

Finally, a distinction can be made between systems with *small* and *large baselengths* (the

[2]Usually this means that these phase differences must be constant.

length of the constituent bistatic baselines), ostensibly to indicate the degree of correlation of scattered signals from a given target at each receiver, assuming some model for the signal fluctuation characteristics. However, this is a somewhat simplistic definition as other dependent factors (operation mode, topology, target type and dimensions, etc) limit the validity of the delineation, and a more appropriate model will be discussed later.

1.4 A Critique of Multistatic Radar

Here the main motivations for the use of multistatic radar systems are summarised, together with a brief review of their disadvantages and the challenges involved in their development and deployment.

It is expected that augmentation of the number of receivers in a radar system will lead to an increase in system *sensitivity*, as the combined signal power received is increased (although it may be at least partially offset by an increase in total noise power). The addition of multiple transmitters into a system capable of cooperative reception allows each receiver to exploit the power from all transmitters, leading to further gains. The spatial distribution of transmitters, and therefore linearisation of power density, may allow the replacement of large transmitters with smaller ones, with a corresponding decrease in cost. The issue of multistatic coverage is discussed in more detail in Chapter 3.

In the usual case, a monostatic system has considerably better range resolution in the radial direction compared to the cross-range direction. A multistatic radar consisting of several such spatially distributed systems can *improve position estimation accuracy* by integrating these uncertainty regions (for example, by finding the intersection volume). Equally, the blindness to doppler frequency shifts in the cross-range direction in a monostatic radar, and in the direction orthogonal to the bistatic bisector in a bistatic radar, can be mitigated by the diversity of look-angle in a multistatic system. It may also be possible to accurately measure position derivatives such as velocity and acceleration vectors in three dimensions.

The measurement of a target's scattering characteristics from several angles implies an increase in the total *target information*,which may improve identification and allow estimation of higher order parameters (e.g. size, structure and relative movement)(10). Systems with very high resolution may be capable of three-dimensional target imaging.

Multistatic radar may have some *tolerance to electronic countermeasures* (ECM) such as

directional jamming, particularly in the case where the jamming signal is coherently detected by multiple receivers and so can be adaptively cancelled(11). Multistatic systems provide the same immunity to enemy detection as bistatic radar if receivers are spatially distributed (and not colocated with transmitters), in which case they are passive and undetectable.

Further, the multiplicity of nodes may lead to an increase in survivability - for example if one station is destroyed or fails, the system could be designed to continue operation (albeit probably with reduced performance). However, any overall reliability improvements may be compensated by additional modes of failure (e.g. of the data communications network or control centre).

The major disadvantages and design challenges include the necessity for a reliable, and possibly reconfigurable, data communications network, timing synchronisation and the significant complexity and computational power required in the system control and signal processing systems that perform the data fusion and decision-making processes. In general, highly accurate location information must be available for every station (although spatial self-calibration may be possible to some degree(12)). Finally, in spatially coherent systems, a highly accurate method of distributed oscillator frequency and phase control is also necessary. These requirements can be summarised as *a distributed common awareness of time and space.*

The design of the multistatic system described in Chapter 5 requires, even at a prototype level, consideration of these issues. In particular, an analysis of the requirements for temporal synchronisation and coherency using computer simulation is presented in Chapter 4. In general, a system suitable for deployment will have yet more strenuous requirements and present greater design challenges - for example, covert operation and the minimisation of weight and power consumption.

1.5 The Context of this Work

1.5.1 Introduction

In this section, previous and current research on multistatic radar is described in order to place the work of this thesis in context. The section begins with a summary of the history of radar, concentrating on developments concerning bistatic and multistatic systems. Then, a literature review is carried out, focussing particularly on design aspects of multistatic radar,

but also encompassing relevant signal processing, data fusion, detection theory, and known prototype and commercial multistatic systems. Finally, the scope and novel aspects of this thesis are defined in the context of the work previously described.

1.5.2 The History of Bistatic and Multistatic Radar

Radar was invented by Christian Hulsmeyer, documented by a patent in 1904 for a collision prevention device for ships. However, the first major development of radar systems came as a result of research that occurred almost simultaneously in the few years prior to the 2nd World War in a number of countries, including the UK, US and Germany, into the feasibility of using radio waves to detect targets. Robert Watson-Watt of the Radio Research Station in Slough, UK made radar measurements in 1935 performing tests to detect a bomber aircraft(13). This radar was what is now known as *passive continuous wave (CW) bistatic*, using the short-range BBC broadcast from Daventry as the transmitter and a non-colocated receiver set to detect the beat frequency of the direct signal and the doppler shifted reflection as the aircraft crossed the bistatic baseline. The 'Chain Home' system used by the UK during the 2nd World War was an active pulsed system, with the transmitting and receiving stations positioned along the British coast. The Germans also (parasitically) used these transmitters for their own bistatic system 'Klein Heidelberg'(14). However, pulsed monostatic systems became popular after the invention of the duplexer by the US Naval Research Laboratory in 1936 as a common antenna could be used for transmission and reception, and bistatic systems did not become popular again until the 1950s.

In 1957 a very early implementation of netted radar was used to track the first 'Sputnik' satellite in the USSR(9), comprising several pulse monostatic radars linked by telephone wires to a central fusion centre. Considerable further development on multistatic systems took place in both Russia and the USA. In 1977 the US Army and the Defense Advanced Research Project Agency (DARPA) launched the 'Netted Radar Program', which in 1981 developed a prototype consisting of five heterogeneous radars linked by a narrowband data channels over which tracks from each radar were communicated to a 'Target Integration Centre'(15).

In 1980 the 'Multistatic Measurement System' developed at Massachusetts Institute of Technology (MIT) was deployed at the Kwajalein Missile Test Range in the Marshall Islands. Two unmanned receivers process echoes from re-entry targets, which are transmitted in

coherent form (amplitude and phase) by radio link to a fusion centre. The system can measure dual-frequency target signatures, three-dimensional target position and velocity with high accuracy using time-difference-of-arrival measurements between the two receivers, which are synchronised by the processing of signals from quasars(16).

More modern installations include the Jindalee Over-the-horizon Operational Radar Network, which is designed to detect aircraft and marine traffic off Australia's north coast, comprising two cooperative but spatially incoherent bistatic radars with centralised control, which are capable of measuring range, azimuth and velocity of targets(17).

There has also been some multistatic radar development for civilian applications, including research into networks of high resolution *miniradars* for airport surveillance(18), and closely spaced sensor networks for automotive cruise control and collision avoidance(19).

1.5.3 Literature Review

A review of the literature pertaining to multistatic radar has revealed four distinct areas of research, which are described in order below. Firstly there are reports of several current large-scale, long-term initiatives, primarily by national defence organisations, which are based on the integration of multiple sensors, data processing units, weapon control systems and so on into an integrated network. Evidently some portion of this research relates to radar sensors in multistatic configurations. Secondly, there is research considering data fusion methodologies for multistatic radar, most of which is concerned with non-coherent integration of plots and tracks. Thirdly, there is literature regarding detection and theoretical performance analysis for multistatic systems, and lastly there is a body of work analysing issues related to particular aspects of multistatic radar design, although many of these are not radar specific. This final category is reviewed separately in the discourse on technologies for multistatic radar in Chapter 4. The latter two categories are considered in more detail due to their greater application to the design of a coherent prototype multistatic radar.

The Cooperative Engagement Capability (CEC) is a wide-reaching project by the US Navy that has been under development since 1995 in order to integrate a diverse range of sensors on the battlefield to enable information sharing and integrated coordination. The CEC program is designed to take advantage of the spatial and capability diversity of each sensor, and operate the totality as a single distributed defence system. The emphasis is

particularly on the ability for the system to be integrated into existing legacy equipment. Features include distributed track acquisition cueing, threat analysis, and coordinated co-operative engagements(20). Composite tracking is performed by centralised data fusion of information from several sensors, although given the heterogeneity of the system, such data is primarily shared at the plot level (range, bearing, elevation, doppler, etc). The processing and data transfer elements include a 'cooperative engagement processor' and a high bandwidth data distribution system using phased array based point-to-point microwave links. Accurate temporal synchronisation is achieved using stable oscillators and network updates to microsecond accuracy, although the system is *spatially incoherent* using the definitions of Section 1.3.3.

The UK Ministry of Defence Network Enabled Capability (NEC)(21) is an initiative with similar aims to the CEC. It encompasses a range of projects to research and promote the integration of sensors, decision makers, weapon systems and support in order to enhance the overall strategic capability. Further similar projects include the Royal Australian Air Force UC^2 (Ubiquitous Command and Control)(22), which emphasises devolved decision making, automation and diversity. In particular, it is proposed that correct management of this diversity using 'biological' or fuzzy processes could engender survivability and system robustness.

In December 2004 the US Air Force Research Laboratory (AFRL) launched the first of a planned cluster of micro-satellites(23) under the 'TechSat 21' program. The system is not yet operational as a multistatic sensor, but will be capable of performing experiments for precise geolocation, sparse aperture and interferometric SAR imaging using sensors on each satellite that are synchronised using GPS receivers. A number of research papers have resulted from the development of this system. Waveform coding schemes have been developed in order to reduce transmission grating lobes and range/doppler ambiguities(24). A processor using Kalman filters has been devised to estimate and correct position biases resulting from carrier-phase differential GPS location measurements of each satellite sensor. Real-time position accuracy to within 2-5 cm has been documented(25). Differential GPS is also used to provide relative timing synchronisation to within ± 20 ns, and ultra-stable reference oscillators on each satellite are used to maintain local time precision of ± 5 ps over the five second maximum integration period. There has recently been increased interest in the field of multistatic synthetic aperture radar (SAR), such as the concept of using a

cluster of coherent airborne receivers to form an 'interferometric cartwheel' (similar to the TechSat 21 system) in order to create improved resolution in range and doppler in the final combined images(26).

A project that is still in the initial stages of development, called the 'Square Kilometre Array'(27), shares many of the same design challenges found in coherent multistatic radar. This project aims to build a highly distributed radio-astronomy system for next-generation telescopy, comprising a sparse aperture synthesis array with individual antennas or clusters of antennas positioned over the one million square metre two-dimensional aperture. In particular, requirements for aperture coherency, data transfer, signal processing, and a necessarily low cost per station design due to the large number of antennas mean that many design principles are common to the system described in this thesis.

There are several papers dating back over three decades, discussing high-level processing in multistatic radar. These are largely based on the generic sensor data fusion theory found in texts such as Waltz(28). At this level, the fusion process is concerned with transformation of sensor data to a common coordinate system, compensation for misalignment errors, *co-registration* (the process of examining 'reports' of plots or tracks to determine if they refer to the same target), and filtering algorithms to generate the optimal fused target parameter information. Performance of the co-registration process where there are large sensor alignment errors is analysed by Bath(29). Fusion techniques based on multi-hypothesis tracking of small and stealthy targets by a netted radar are examined by Weiyan et al(30). The design of fusion algorithms from a constant false-alarm rate (CFAR) perspective is described by Thomopoulis(31), whilst an architecture is proposed by López et al(32) for the management of task negotiation and allocation in a decentralised fusion processor. The advantage of the high-level approach is that the amount of data that must be transferred between stations is very low, and it is relatively straightforward to apply to legacy systems. However, the fusion algorithms are dependent on the detection and plot/track estimation performance of each station individually. It is intuitive that the decentralised decision-making process causes loss of information (and hence, poorer performance) compared to the fusion of 'raw' signals(33).

The detection theory for multistatic radar, including that for spatially coherent systems, is developed and analysed in some detail in Chernyak(34). Similar analysis for the incoherent case only can be found in Baumgarten(35). In Fishler et al(36), the case is made for

eschewing spatial coherency in favour of highly dispersed topologies where the diversity of signal fluctuations is maximised. It is suggested that this approach may be optimal in situations where deep fades would limit detection performance in a coherent system. Methods of multistatic detection as they relate to the processing algorithms and performance of the prototype system are discussed in Section 2.4.

There are few recent accounts of multistatic experimental results or performance analysis in the literature, still less for spatially coherent systems. It is expected that TechSat 21 will be able to perform multistatic detection and imaging, although determination of coherent multistatic performance *per-se* is not a major focus of the proposed experimental campaign. A current project by the Norwegian Defence Research Establishment has developed a prototype multistatic system comprising multiple transmitters and a single receiver, which are synchronised using GPS. Some initial experiments detecting a helicopter using a bistatic configuration have been published(37) and further results are expected. Finally, a team at MIT Lincoln Laboratory have recently released details of a coherent multistatic system they have developed for experimental purposes(38). This comprises two transmit/receive and two further receive antennas at fixed locations approximately ten metres apart. The system has been used to observe test targets over a range of seven miles, both in coherent and non-coherent modes, although these results and the exact details of the design have not been published.

1.5.4 Scope and Principle Contributions of the Thesis

There are no known accounts in the open literature of experimental results using a spatially coherent multistatic radar with multiple transmitters and receivers. In addition there is only limited analysis of the theoretical, design and implementation issues relating to such systems. Nevertheless it is clear that a coherent system enables the use of signal processing and data fusion methods that are impossible using incoherent systems, and that these may offer considerable performance benefits.

Therefore, the objective of this study is the design and build of such a system. Here, the principle contributions of this work are outlined. In Chapter 2, having described the background theory to the detection process in multistatic systems, an analysis is presented of the relative performance of the resulting coherent and incoherent detection algorithms in the presence of target fluctuations and multipath. In Chapter 3, an original derivation

of the ambiguity function for multistatic systems is described, and results are expressed in order to demonstrate the resolution and measurement accuracy possible in such radars and the factors on which this performance is dependent. In Chapter 4, a comprehensive analysis is presented of the mutual relationship of noise pertaining to each oscillator in a multistatic radar, and its effects on performance. A computer simulation is devised to incorporate this analysis into a model to determine system coherency requirements. In Chapter 5, the development of a novel design for a low-cost multistatic prototype radar is presented, together with the original application of discrete-time signal processing methods for the implementation of the detection algorithms analysed in Chapter 2. In Chapter 6, initial experiments with the newly-developed system allow the practical determination of the viability of the design and its application to future research. The overall contribution is derived from the development of the prototype system itself, analysis of the design, its underlying theory, and determination of the characteristics of the system from simulation and experiments. The result is an increase in our understanding of the limitations and performance achievable from spatially coherent multistatic radar systems.

Chapter 2

Detection and Parameter Estimation Theory for Multistatic Radar

2.1 Introduction

The design of a coherent multistatic radar necessitates the development of a signal processing methodology to optimise its performance taking into account the unique features of the system, particularly spatial diversity and coherency. In essence, this involves integration of the signals at each receiver at the 'raw data' level[1], as by definition all other methods (for example, integration of plots or tracks) result in loss of information prior to detection. Subsequently, decisions can be made as to the presence of targets and their parameters based on the combined processed signal.

In this chapter, the theoretical basis for the process leading to detection in a multistatic radar is described. A series of suitable detection algorithms is presented and their relative performance analysed. These algorithms are later used in Chapter 3 as a basis for determining radar coverage and prediction of the system instrument function, and again in the system simulation in Chapter 4 and the implementation of the signal processing system of the prototype radar in Chapter 5.

Radar signal processing is chiefly concerned with the detection of wanted received signals (normally 'echoes' resulting from the scattering of transmitted electromagnetic energy by a target) in the presence of noise and interference. In the monostatic case, it is well-known that the optimal receiver for slowly-fluctuating signals in a background of white Gaussian noise is the *matched filter*. The output of this filter may then be thresholded at a level based on specified performance criteria in order to make a decision as to the presence of a target (see Figure 2-1). In the multistatic case where there are multiple transmitters and/or receivers, the nature of this optimal 'filter' is somewhat more complex. An analysis is presented here, based first on a general consideration of the nature of noise in radar signal paths, then by development of the *likelihood ratio test* to the multistatic case, from which specific detectors are defined based on a series of assumptions about the radar and its environment.

The observation of received signals can also be used to extract target information contained within the signal. It is expected that the multiple simultaneous observations possible with a multistatic radar can be used to improve the accuracy of estimation of these tar-

[1] 'Raw data' will typically be the digitised signal obtained directly following coherent demodulation and analogue-to-digital conversion at a receiver antenna.

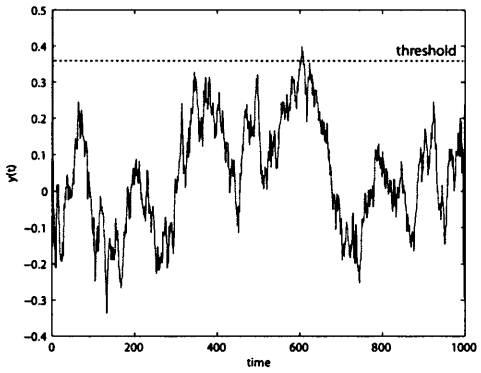

Figure 2-1: A voltage trace from the output of a matched filter used to make detection decisions based on a pre-determined threshold

get parameters. Optimal methods of signal processing for this purpose are considered, concentrating on the determination of target location co-ordinates. The conclusions from this chapter provide a theoretical basis for the design and implementation of the prototype system.

2.2 Noise Analysis in Radar Signals

2.2.1 Introduction

The processes of target detection and parameter estimation in a radar receiver are concerned with the extraction of wanted signals from a background of noise and interferences (in this section, these are collectively described as 'noise'). In a multistatic radar, there may be several receiving antennas and signal paths; therefore analysis of the total noise in the system is more complex. An understanding of the derivation and nature of these noise sources is required in order to develop optimal signal processing algorithms, which can then be applied to the prototype multistatic system.

When targets are (effectively) small or distant from the radar, the wanted signal can be dominated by noise from the environment or that generated internally by the radar receiver. In this situation, it is typical that noise will limit the detection capability of a radar. In this section the following categories of noise are considered:

1) Noise in radar signal paths that is generated by the receiver itself;

2) Noise in radar signal paths that is derived from the external environment and captured by the antenna.

These categories are considered in turn below. In addition, there may exist noise in the receiver signal path that has been derived from some other part of the radar system. These sources fall into two further categories:

a) *Breakthrough* noise from the transmitter, digital electronics, oscillators, etc, which has coupled into the receiver chain;

b) *Phase noise* pertaining to the signal itself, which may be derived from the internal downconversion and reference oscillators, or other non-linear processes.

The noise in category (a) may consist of wideband and narrowband noise, and may be highly time dependent. However it is essentially an engineering problem, can be minimised by careful low-noise design and layout, and is not considered here further.

Phase noise in category (b) has manifest and multiple effects on the performance of a radar system. However, whilst it may considerably degrade target detectability *in the presence of other targets* (particularly for a moving target amongst strong clutter), its inherent relationship with the wanted signal means it is not relevant to the structure of the detection algorithm itself (that concerned with discrimination between the signal and a background of noise), and is considered further in Chapter 4.

2.2.2 Receiver Self-Noise

This section analyses the receiver self-noise that is described by category (1) above. Noise is unwanted electrical or electromagnetic energy, which can be defined as an error that is superimposed on top of a wanted signal. A voltage $v(t)$ measured at a point in the receiver signal path will invariably comprise noise plus (possibly) some wanted signal. Here, the three major sources of electrical self-noise are described.

Thermal or Johnson 'voltage noise' tends to be the dominant self-noise contributor within an electrical circuit, and exists even in the absence of a current, caused by the chaotic fluctuation of electrons in a resistor. Since a very large number of independent identical events contribute to this noise, the Central Limit Theorem applies and the noise is a Gaussian random process. Nyquist(39) demonstrated analytically that thermal noise

has a flat power spectral density and even phase distribution over a very wide bandwidth. The total rms noise power in a bandwidth $B = f_2 - f_1$ is given by:

$$P_t = \int_{f_1}^{f_2} kTdf = kTB \tag{2.1}$$

where k is Boltzmann's constant and T the temperature in Kelvin. Within the frequency range of radar, the bandlimited noise power is independent of centre frequency and depends only on the receiver bandwidth, which acts as a bandpass filter of the noise.

Shot noise is created because electrons have a finite charge and do not pass through a system in a perfectly uniform way, generating random fluctuations in the instantaneous current. It is generally most evident where current flows across a potential barrier such as a transistor junction. The rms shot noise current over bandwidth B is given by:

$$i_{\text{sn}} = \sqrt{2qIB} \tag{2.2}$$

where I is the forward current and q is the charge on an electron. Each single electron 'shot event' is impulse-like in the time domain, so has a flat power density, resulting in the bandlimited shot noise power also being independent of centre frequency.

Flicker noise is caused by various complex surface effects in resistors and transistors(40), and has an approximate rms noise current over bandwidth B given by:

$$i_{\text{fn}} = \sqrt{m\frac{I^a}{f}B} \tag{2.3}$$

where a and m are constants dependent on the device characteristics. The ac noise current has a $f^{-1/2}$ dependency on frequency, so flicker noise is often known as '*1/f* noise' due to the inverse power spectral density relationship - hence it is usually significant only at low frequencies (i.e. < 1 kHz). The receiver bandwidth of a radar is typically large compared to the maximum frequency where flicker noise is significant, so it can be disregarded as a contributor in the signal path. However, its effect is important in radar components with low frequency analogue control circuits such as phase locked loops and oscillators.

It is concluded that the self-noise in a radar receiver signal path can normally be approximated to the thermal noise contribution. This can be modelled by considering the noise 'generator' to be an arbitrary resistor at the input to the receiver (the model is usu-

ally appropriate as it is this noise that experiences gain from all amplifiers in the receiver chain, thus dominating noise generated further on). The noise process $n(t)$ at this point is stationary, zero-mean, white and Gaussian, and can be modelled with a power spectral density S_n such that:

$$S_n(f) = N_0/2 = kT \quad -\infty < f < \infty \tag{2.4}$$

where N_0 is the one-sided noise density. Using the well-known relationship between the power spectrum and autocorrelation function $R_n(\tau)$ for stationary random processes:

$$R_n(\tau) = \mathrm{E}[n(t)n(t-\tau)] = \int_{-\infty}^{\infty} S_n(f)\exp(j\omega\tau)df \tag{2.5}$$

we can write:

$$\mathrm{E}[|n(t)|^2] = R_n(0) = \int_{-\infty}^{\infty}\left(\frac{N_0}{2}\right)df = \infty \tag{2.6}$$

where E[] denotes the *expected value.* Clearly this model is an idealisation at it implies the expected (mean) square value of the noise process is infinity[2]. Nevertheless it allows analysis of the effect of the receiver itself on the noise. Assuming that the receiver consists of linear processes only with total frequency response function $H(\omega)$, we can apply the identity:

$$S_y(f) = |H(j\omega)|^2 S_n(f) = kT|H(j\omega)|^2 \tag{2.7}$$

where $S_y(f)$ is the output power spectrum. Therefore the noise at the output of the receiver due to self-noise is completely defined by the receiver frequency response function.

2.2.3 External Noises

This section analyses the environmental noises that are described by category (2) above. They are generated outside the radar equipment and are picked up by the receiver antenna. These noises are predominantly derived from three sources, which are described below.

Sky noise is the combined noise from background radiation and astronomical sources such as stars and galaxies. It is effectively white Gaussian noise, and clearly will be most evident where receiver antennas are directional and elevated.

Thermal radiation noise is also white, zero-mean and Gaussian, and is derived from all

[2]The conundrum is resolved because the thermal noise is in fact Planck Black Body noise, which only appears white at frequencies in the 'long wavelength' (Rayleigh-Jeans) region.

objects in the receiver antenna field of view due to their non-zero temperature. Sources that produce white noise can be conveniently described by their *noise temperature* T in Kelvin, which is equivalent to a spectral power density of kT. There will be some atmospheric contribution to the total thermal radiation, which can be calculated by modelling the atmosphere as a 'grey body' homogenous layer with given depth, emissivity and effective noise temperature. It can be shown that the atmospheric noise power present at ground level is related to the atmospheric attenuation coefficient[3], so is also dependent on meteorological conditions (for example, the noise level is higher when it is raining). In addition, there is likely to be a significant contribution resulting from the thermal radiation of all objects on the ground (such as buildings) as well as the earth itself. Each of these noise sources is independent and Gaussian, so the noise temperature components from each can be summed. In summary, the total sky and thermal radiation noise evident to a radar receiver is dependent on atmospheric conditions as well as the direction and pattern of the antenna. In general however, particularly on a dry clear night, the sky can be considered 'cool' (low noise power) compared to the 'warm' earth.

The final category of external noise is *man-made* noise, sometimes known as *interferences*. These may include wideband but non-stationary local noise from sources such as light bulbs and electric drills, as well as narrowband broadcast transmissions such as TV and radio signals. Some interferences are out-of-band for radar and can be eliminated by a bandpass filter at the receiver input, although certain radars may operate in frequency bands shared with other electronic devices (for example, wireless network transceivers using the IEEE 802.11 protocol in the ISM band). In a military environment, a further important class of man-made noise is *jamming* - a deliberate attempt to prevent operation of the radar by transmitting a high power directional signal towards the receiver antenna, often consisting of fairly narrowband pseudorandom noise.

2.2.4 Mutual Correlation of Noises in a Multi-Receiver System

Having considered the nature of the noise components likely to be present in a given receiver signal path, it is now pertinent to analyse the expected relationship between these noises in a multistatic radar system comprising m receivers.

[3]Therefore the spectral density is actually frequency dependent, but can usually be considered flat over a typical receiver bandwidth with power density determined by the operating frequency.

It has been shown that the self-noise at each receiver is a white Gaussian process, and given that each is generated internally, they are mutually uncorrelated and independent. In the usual case where antenna patterns for the m receivers overlap, or when directional (as opposed to 'local') interferences are present, the externally generated noise received in each case may be completely or partially mutually correlated due to commonality of the signal entering each receiver.

The total system self-noises and interferences (which we define to include all other noises) can be described by vector $\mathbf{N}$, written in complex form[4] such that:

$$\mathbf{N}^*(t) = [N_1^*(t), ..., N_m^*(t)] \tag{2.8}$$

where each $N_i(t)$ describes the noise and interferences received at the ith receiver. Assuming all N_i are Gaussian processes, the mutual correlation between receivers can be quantified using the covariance matrix (which is identical to the correlation matrix if all sums of noise and interference have zero mean). An arbitrary element of the covariance matrix $\mathbf{B}$ is defined as[5]:

$$B_{ik} = 0.5\overline{N_i(t_1)N_k^*(t_2)} \quad i,k = 1..m \tag{2.9}$$

In the case that there are no external interferences at all, $\mathbf{N}$ consists only of white, stationary, mutually uncorrelated Gaussian processes, so by definition:

$$\begin{aligned} B_{ik} = 0.5\sigma^2 = 0.5\overline{|N_i(t)|^2} = \overline{[\text{Re } N_i(t)]^2} \quad i = k \\ B_{ik} = 0 \quad i \neq k \end{aligned} \tag{2.10}$$

In general, large spatial diversity of receiver antennas will result in low mutual correlation of atmospheric noise at each receiver, although in the case of the narrowband interferences (particularly jamming sources), there is the potential for strong mutual correlation, with a resulting non-trivial covariance matrix.

[4]The symbol * for vectors and matrices represents the 'Hermitian transpose' - i.e. the transpose and complex conjugate.

[5]The factor 0.5 is used so that the variance $B_{ii}(0)$ is equal to the power in the real part of the signal.

2.2.5 Summary

In a multistatic radar, man-made and jamming interferences may result in some degree of mutual correlation between the total noise at each receiver. Therefore, the analysis is similar to that of a conventional array antenna, where it is assumed that receiver self-noise is independent between sensors (and therefore their noise powers sum), and interferences are described using the space-time covariance matrix(41). However, it is expected that the greater spatial separation of receivers in the multistatic case will, in general, result in weaker mutual correlation of the total noise **N**.

Practically, the total noise in a monostatic radar is often approximated to the thermal noise kTB for the purposes of detector design and coverage calculations(42). If, in the first instance, the same assumption is made for each of m identical receivers in a multistatic radar, it follows that the optimal multistatic receiver performs the maximum possible filtration of this total noise power $N = mkTB$, whilst maximising the total signal power at its output.

2.3 The Background to Detection Theory

2.3.1 Introduction

The two basic operations performed by a radar are the detection of the presence of reflecting targets, and extraction of information from the received signal(s) relating to that target. In this section, optimal methods of performing the detection operation are considered. The detection problem can be divided into two parts - the specification of the optimum receiver characteristic for the detection of weak signals in noise, and the development of some criteria for making a decision about the presence or absence of a signal(43).

The performance of the detection operation is usually described statistically, as random noises such as those described in Section 2.2 make it impossible for the detector to *always* make the correct decision. Then, the *optimal* detection method is one that, in a given situation, best meets some pre-defined statistical criteria for its performance. In a monostatic radar, these optimal methods are well understood. The optimal receiver characteristic takes the form of a 'matched filter', and the detector itself is a thresholding device, its value based on statistical hypothesis testing criteria. This detection system, comprising the 'filter' and the 'thresholder', is shown in Figure 2-2.

It is well-known that the matched filter maximises the signal-to-noise ratio at its output

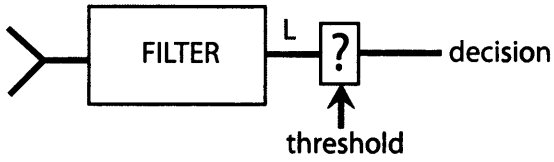

Figure 2-2: The monostatic detection process comprising a (matched) filter receiver and thresholding detector

when the input noise component is white and Gaussian. The output variable L from this filter is compared directly against a threshold, and the resulting binary output designates a target detection decision. The receiver can 'probe' the existence of a target at a particular range by observing the thresholder output at time τ (the time of arrival), referenced to the pulse transmission time. In a monostatic radar, τ is linearly related to range R as shown in Equation 1.1. Assuming no further information is available, the target location is now defined as being at some point on a spherical surface at range R from the radar. For narrowband signals, the receiver may also probe the existence of a target with a certain velocity by tuning the filter to the expected doppler frequency. Bistatic radars, as well as multistatic radars that perform data fusion at plot or track level, can use an identical detection method. In the bistatic case, the time at which to observe the thresholder output should be determined from the geometry as described in Equation 1.4.

Now let us consider conceptually a simple multistatic system comprising a single transmitter and two spatially separated receiver antennas, where it is desired to perform combined detection at the 'raw data' level. Hence, the detection process is not performed at each receiver[6] individually, but instead the received signals are transferred from the antenna directly to a central processor as shown in Figure 2-3. The 'filter' component now has two inputs which correspond to the two receiver antennas, and should have a single output upon which the thresholder can make detection decisions. The term 'filter' will continue to be used for the purpose of extending the analogy, although it is clear that its implementation is more complex than the mono-dimensional 'matched filter' in the monostatic case.

Intuitively, one expects that the optimal 'filter' for this system will attempt to sum the wanted signal components at both inputs, whilst rejecting as much of the total noise as possible. Given that the antennas are spatially separated, in general the time-of-arrival of

[6]A 'receiver' in this context is simply a point at which a signal is received from an antenna (and may be amplified). It does not imply that any signal processing occurs at this point.

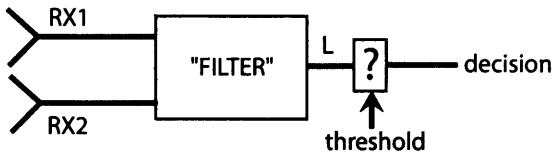

Figure 2-3: The multistatic detection process

the wanted signal at each receiver will be different. Therefore, we further expect that the 'filter' must delay (or 'time shift') one input so that the wanted signal components can be summed constructively. If we now extend the system to comprise m receivers, it is clear that the 'filter' must have m inputs, and perform time shifts on each input according to the expected relative time-of-arrival in each case. Hence, instead of probing the existence of a target at a given range (the origin of which is arbitrary in the multistatic case), we can consider the probing of a particular locus in two or three-dimensional space, from which the expected time-of-arrival at each receiver can be determined by the multistatic geometry.

The detection process in a multistatic radar is in many ways analogous to that employed with a conventional array antenna(78). Here, the signal at each sensor (or 'element') of the array is applied to an individual matched filter receiver, time shifted according to the spacing of the elements and the expected direction of the signal (jointly described by the *array manifold vector*) and then summed. In the situation where the product of the bandwidth of the received signal B_s and the maximum difference in signal propagation time between elements $\Delta T_{\max}$ is much less than one, the 'narrowband approximation' holds, and the time shifts can be replaced by phase shifts. This is typically true when array elements are closely spaced, and is known as a *phased array.*

We can then define the 'filter' (as shown in Figure 2-3) as the system performing this entire operation, which now has m inputs corresponding to each element of the array. Therefore the monostatic matched filter receiver is replaced by a *system* of matched filters, time or phase shifters, and a summer in the case of an array antenna. This total receiver is known as the delay-and-sum (or 'conventional') beamformer[7]. It is well-known that this process results in an *array gain*, defined by the improvement in signal-to-noise ratio at the output of the receiver compared to that at one of the input elements. This gain results from adding wanted signals coherently, and noise incoherently. Assuming that, following

[7]The resulting beam pattern and its equivalence in multistatic radar are not relevant to the simple detection process, although are considered in terms of the instrument function in Section 3.3.

time shifting, the wanted signals sum perfectly, and the noise at each element is white and uncorrelated, it is known that the standard uniformly-weighted array provides the optimum array gain, which is equal to the number of elements.

In a multistatic system, many of the assumptions used in the conventional array processor do not hold in the general case:

- When receivers are widely spaced, there may be significant differences in signal-to-noise ratio at each antenna, caused by differing signal propagation losses over each target-receiver range. Therefore, the maximum possible SNR (and hence maximum detection performance) at the 'filter' output is not universally achieved by simple unweighted summation of each time-shifted signal;

- It is assumed for the conventional array that the target is in the far field of the array aperture, so that the received signal can be approximated by a plane wave, and the array manifold vector is dependent only on the array geometry and the expected angle of arrival. In the multistatic case, this assumption is not generally true due to the sparse distribution of receivers. Hence, the time shifts must be calculated at each receiver based on the expected *location* of the target as well as the geometry;

- The directional pattern of each element of this distributed array and its topology (i.e. the location of elements) will have a large impact on the effective radiation pattern of the system in the near-field, and so are important factors in determining the resolution and measurement capability of the radar;

- This sparsity also implies that signal fluctuations may not be completely mutually correlated between receivers, in which case coherent summation may not be optimal. Further, coherent processing clearly requires the radar equipment itself to be spatially coherent, which is not necessarily true in multistatic systems due to the practical difficulties of maintaining coherency over large distances. In the ideal case, a multistatic system should be capable of operating in several processing modes, and be able to adapt based on the observed nature of the received signals and its environment;

- Finally, such a system is not limited to acting as a distributed abstraction of an array antenna - it is also possible for each transmitter and receiver pair to behave like a set of bistatic radars, provided the signals from each transmitter can be discriminated.

The signals from each bistatic pair may still be jointly processed at the 'raw data' level provided each station is operating cooperatively.

In order to determine the optimal detection method(s) for a multistatic system in the general case, it is necessary to revisit the statistical theory from which the monostatic matched filter receiver and threshold detector was shown to be optimal(45). The aim is to determine the structure of the 'filter' component of Figure 2-3, and the nature of its output variable L, which can then be used to set the threshold and predict detection performance. In this section, the relevant theory is explained, culminating in a general analytic equation for the desired optimal detection method. The analysis begins with consideration of the *likelihood ratio test* - a rigorous statistical approach to defining the detection process. It is shown how this relates to the matched filter, and how it can be extended to account for multistatic systems. Much of this theory as it applies to monostatic systems is documented elsewhere(46)(47), however a clear understanding of its basis and assumptions is necessary in order to apply it to this new case. The formulation of such algorithms is necessary for the purpose of designing the signal processing system in the prototype multistatic radar, as well as for prediction of the resulting instrument function.

2.3.2 The Generalised Likelihood Ratio

It is known that the monostatic matched filter maximises signal-to-noise ratio given a background of white Gaussian noise, and intuitively one expects that in general minimising the corrupting noise power must lead to optimal detection. However, the strict criterion for optimality is not signal-to-noise ratio, but the statistical performance of the detector compared to some chosen criterion. It is analysis of this statistical test which allows the detection theory to be extended to the multistatic case.

Firstly, we consider a generic monostatic detection receiver such as that in Figure 2-2. The receiver is used to probe the existence of a target at a given range by observing the detector output at the corresponding time-of-arrival. There are two possible hypotheses - H_1 that a target exists at that range, and H_0 that the target is absent. These hypotheses can be written in terms of the total expected received signal $x(t)$ at the input to the receiver

at that time:

$$\begin{aligned} H_1 &: x(t) = s(t) + n(t) \\ H_0 &: x(t) = n(t) \end{aligned} \tag{2.11}$$

where $s(t)$ is the wanted signal, and $n(t)$ is the sum of (unwanted) noise and interferences. The *likelihood ratio test* forms a statement for the optimal detector in terms of the probability density functions p_1 and p_0 of the received signal $x(t)$ for the two hypotheses H_1 and H_0 respectively:

$$\mathrm{L} = \lambda(y) = \frac{p_1(y)}{p_0(y)} > \lambda_0 \tag{2.12}$$

The test shows that the output variable L is given by the ratio of these two probability density functions, and that the decision that a target exists should be made when this variable is above a given threshold λ_0. It can be said therefore that the optimal detector performs the following test:

> *For a given value y of the received signal x, make the decision that a target is present if that value is λ_0 times more likely to have occurred because hypothesis H_1 is true than because H_0 is true.*

The detection receiver structure can be clearly seen from this equation - the 'filter' component must have an output equal to the ratio $p_1(y)/p_0(y)$, and the threshold component is set to the value λ_0. It can be shown that the output of the 'matched filter' is equivalent to this ratio when the input is a combination of wanted signal and additive zero-mean Gaussian noise(48). Therefore, in this case the matched filter is also the optimal detection receiver by the likelihood ratio test. The decision threshold is usually set by the requirement for a fixed probability of false-alarm[8], which can be determined by the Neyman-Pearson criterion. The background theory to the likelihood ratio test and the matched filter is presented in Appendix A.

It is clear that the optimal detection receiver for a multistatic radar can be found by application of the likelihood ratio test to this specific model. In particular, it is noted from Section 2.2 that the nature of the vector of noise and interferences (with elements for each receiver) may be non-trivial and mutually correlated, and this must be taken into account.

[8] A false alarm occurs if the decision that a target is present is made, when in fact the target is absent.

Of course, there also exists a vector of wanted signals at each receiver, and the aim is to find the form of the likelihood ratio test for this total *combination* of raw data signals.

We start by generalising the likelihood ratio test for an arbitrary receiver. From there, development to the multistatic case is straightforward. The problem is defined over a finite time period $-T/2 \leq t \leq T/2$, which corresponds to the observation time of the radar receiver. The variable $s_1(t)$ is the wanted signal component at a given receiver if a target is present (hypothesis H_1), and $s_0(t) = 0$ corresponds to the null hypothesis H_0 if a target is absent. The noise and interference component $n(t)$ is assumed to be zero-mean and Gaussian. In this most general case, the noise is not white (i.e. coloured), and not necessarily stationary, meaning the statistics of the total signal $x(t)$ are time-variant with correlation function:

$$E[x(t_1)x^*(t_2)] = R(t_1, t_2) \tag{2.13}$$

It is known that, in the case of the matched filter, optimality from a signal-to-noise ratio perspective is maintained in the presence of coloured noise if the matched filter is combined with a whitening filter with frequency response function $W(j\omega)$ given by:

$$|W(j\omega)|^2 = 1/S_n(f) \tag{2.14}$$

where $S_n(f)$ is the Fourier transform of the covariance function $R_n(\tau)$ of the coloured noise $n(t)$. The resulting *total* filter $H_{nw}(j\omega)$ is non-causal and has an infinite impulse response. If the constraint of finite time processing is included in the optimisation, then the resulting optimal filter can be found from the Wiener-Hopf equation(49):

$$\int_a^b h(T, v)R_n(v, u)dv = s(u) \quad a \leq u \leq b \tag{2.15}$$

where $h(T, v)$ is the impulse response of the optimal filter, $R_n(v, u)$ is the correlation function of the noise process, and $s(u)$ is the wanted signal.

In order to determine the likelihood ratio given coloured noise and a finite observation period, the strategy is to make the transition from the process $x(t)$ of signal and coloured noise to a new process computed from $x(t)$ defined in such a way that the corresponding noise is white. As long as the procedure is reversible, the detection problem can be worked equally well using this new process. This procedure amounts to solving the Wiener-Hopf

equation above using the Karhunen-Loève expansion, a derivation for which is given in Appendix A. The result is an expression for the likelihood ratio that can be written as:

$$\lambda = \frac{p_1[x(t)]}{p_0[x(t)]} = \exp\left\{\mathrm{Re}\int_{-T/2}^{T/2}\int_{-T/2}^{T/2} s_1^*(t_1)R^{-1}(t_1,t_2)x(t_2)dt_1dt_2 - \frac{1}{2}\int_{-T/2}^{T/2}\int_{-T/2}^{T/2} s_1^*(t_1)R^{-1}(t_1,t_2)s_1(t_2)dt_1dt_2\right\} \tag{2.16}$$

This equation is valid for complex envelopes, although the derivation shows the real case for simplicity. It describes the optimal detector for the received signal $x(t)$ at an arbitrary receiver over a finite observation time where the noise and interference is Gaussian but not necessarily stationary or white. From this, it is simple to define the likelihood ratio for a multistatic radar consisting of m receivers by replacing $x(t)$ with the vector[9] $\mathbf{X}^*(t) = [X_1^*(t), ..., X_m^*(t)]$ where $X_i(t)$ is the signal at receiver i. $\mathbf{X}(t)$ can then be written as:

$$\mathbf{X}(t) = \mathbf{S}(t) + \mathbf{N}(t) \tag{2.17}$$

where $\mathbf{S}(t)$ is the vector of wanted signals at each receiver, and $\mathbf{N}(t)$ is the vector of noise and interference defined similarly.

The resulting likelihood ratio suitable for multistatic systems is given by:

$$\Lambda = \exp\left\{\mathrm{Re}\int_{-T/2}^{T/2}\int_{-T/2}^{T/2} \mathbf{S}^*(t_1,\boldsymbol{\Theta})\mathbf{R}(t_1,t_2)\mathbf{X}(t_2)dt_1dt_2 - \frac{1}{2}\int_{-T/2}^{T/2}\int_{-T/2}^{T/2} \mathbf{S}^*(t_1,\boldsymbol{\Theta})\mathbf{R}(t_1,t_2)\mathbf{S}(t_2,\boldsymbol{\Theta})dt_1dt_2\right\} \tag{2.18}$$

where $\boldsymbol{\Theta}$ is the vector of signal parameters. The total noise and interference vector $\mathbf{N}(t)$ is assumed Gaussian but in this general case is non-stationary and with non-trivial covariance. Therefore the possible mutual correlation[10] of noise between receivers described in Section 2.2 is accounted for. Then, the matrix $\mathbf{R}(t_1,t_2)$ is the solution of the equation:

$$\int_{-T/2}^{T/2} \mathbf{B}(t_1,\tau)\mathbf{R}(\tau,t_2)d\tau = \mathbf{I}\delta(t_1-t_2) \quad -T/2 \le t_1,t_2 \le T/2 \tag{2.19}$$

[9]The symbol * for vectors and matrices represents the 'Hermitian transpose' - i.e. the transpose and complex conjugate.

[10]Covariance and correlation coincide where the sum of noise and interferences is assumed to be zero-mean.

where the kernel $\mathbf{B}(t_1, t_2)$ is the $m \times m$ space-time covariance matrix of $\mathbf{N}(t)$[11].

Equation 2.18 forms the basis for the development of optimal signal processing algorithms for multistatic radar where m 'raw data' signals can be jointly processed. We can compare this algorithm to the monostatic detector in Figure 2-2. The receiver characteristic (the 'filter') is now defined by the system of integrals in Equation 2.18, which has the vector of received signals as its input, and is dependent on the expected signals and the space-time covariance matrix of the noise and interferences vector. The variable Λ is equivalent to L, and provides the input to a single thresholding detector that makes binary decisions as to the presence of a target. The performance of this combined detector (e.g. the probability of detection *of the system* for a given probability of false-alarm) is completely determined by the statistical nature of Λ.

2.3.3 Frequency Domain Implementation of the Likelihood Ratio

The general likelihood ratio equation given in Equation 2.18 consists of a system of integral equations that are complicated to resolve for use in signal processing algorithms. It can be shown that it is convenient instead to express the likelihood function in the frequency domain(50).

In order to perform the transform, the noise/interference vector $\mathbf{N}(t)$ is assumed to be wide-sense (weakly) stationary, such that the covariance matrix $\mathbf{B}(t_1, t_2) = \mathbf{B}(t_1 - t_2)$ is dependent only on $t_1 - t_2 = \tau$, not the actual values of t_1 and t_2. This is often a reasonable assumption over a short observation interval $-T/2, T/2$, as non-stationarity of interferences has not sufficient time to manifest itself.

The Fourier transform of this covariance matrix $\mathbf{B}(t_1 - t_2)$ is given by $\mathbf{\Phi}(\omega)$, and that of $\mathbf{R}(t_1 - t_2)$ is given by $\mathbf{f}(\omega)$. Assuming that T is much longer than the correlation interval of the noise and all wanted signals occur within this observation period, the integral limits can be replaced by infinity so that:

$$\mathbf{\Phi}(\omega)\mathbf{f}(\omega) = \mathbf{I} \tag{2.20}$$

Then, by further assigning the Fourier transform of the wanted signal vector $\mathbf{S}(t)$ to be $\mathbf{\Psi}(\omega)$, and that of the received signal vector $\mathbf{X}(t)$ to be $\chi(\omega)$, the corresponding likelihood

[11]Note the redefinition of R in Equation 2.18 compared to Equation 2.16

ratio in the frequency domain can be given by:

$$\Lambda = \exp\left\{\mathrm{Re}\frac{1}{2\pi}\int_{-\infty}^{\infty}\mathbf{\Psi}^{*}(\omega,\mathbf{\Theta})\mathbf{f}(\omega)\boldsymbol{\chi}(\omega)d\omega - \frac{1}{4\pi}\int_{-\infty}^{\infty}\mathbf{\Psi}^{*}(\omega,\mathbf{\Theta})\mathbf{f}(\omega)\mathbf{\Psi}(\omega,\mathbf{\Theta})d\omega)\right\} \quad (2.21)$$

It can be seen by comparison with Equation 2.18 that the set of integral equations in the time domain has been reduced to a much simpler set of functional equations in terms of spectral functions.

2.3.4 Summary

This section has described the optimal form of the detection process based on the likelihood ratio test, for a multistatic radar where signals at each receiver can be combined at the 'raw data' level. Equation 2.21 describes the 'filter' component (that which replaces the monostatic matched filter) in the frequency domain. The output variable Λ forms the input to the thresholding detector. Implementation of the receiver can be performed by applying Equation 2.21 to particular models for the expected noise covariance matrix and vector of signals.

The ideal instrument function for monostatic radar is given by the point-spread function which results from the correlation (matched) filter. Therefore the instrument function for a multistatic radar may ultimately be determined from analysis of Equation 2.21. In the next section this result is used to form useful processing algorithms that can be implemented in the prototype system. In addition, it will be shown how these algorithms compare to the monostatic and conventional array detectors described in Section 2.3.1.

2.4 Detection Algorithms for Multistatic Radar

2.4.1 Introduction

In this section, a series of detection algorithms are described, based on the likelihood ratio test derived in Section 2.3.3. The derivation of these algorithms broadly follows the lines of the work by Chernyak(34), and the same notation is used to avoid ambiguity in future work. However, an effort has been made to present the algorithms in such a way that they can be directly compared and implemented in a practical system. The derivations are described in some detail, as some aspects of the theory are not widespread in the literature, and it

is necessary to highlight the assumptions made in order to determine the appropriateness of the algorithms for practical situations. Further, a thorough understanding is required in order to translate the detectors into a format suitable for the signal processing system in the prototype radar.

The optimal detection method described by Equation 2.18 is based on the processing of the vector of received signals and noise $\mathbf{X}(t)$. Therefore it might be expected that its implementation depends on the mutual relationship between elements of this vector. In particular, where certain parameters of the received signals are random, such is the case when signals are fluctuating, the mutual (spatial) correlation of each received signal is important, and changes the structure of the optimal 'filter' itself. For example, a detector that performs coherent summation of each complex fluctuating signal is clearly sub-optimal if those fluctuations are mutually independent. This is quite different from a single-element monostatic radar, where only temporal fluctuations need be considered, which do not change the optimality of the matched filter, but simply change the nature of its output with corresponding effect on detection performance[12].

Firstly the case for completely deterministic received signals is considered, in a background of receiver self-noises only. Then, the case of fluctuating signals is analysed, where the fluctuations may be either mutually correlated or uncorrelated at each receiver. The extended form for multiple transmitters (as well as multiple receivers) is considered, also taking into account the nature of each transmitted signal. In each case, expressions for the algorithms define the output variable L of the derived 'filter'. The statistical nature of L is then defined so that, in the following section, their relative performance can be compared.

2.4.2 Deterministic Signals

Here a detection algorithm is defined for the case that the signal received at each receiver consists of completely deterministic wanted signals in a background of mutually independent self-noises (no external interferences are received). This is clearly the simplest and most ideal case, but it provides an analysis from which more realistic detectors can be developed.

A multistatic system is considered comprising a single transmitter, and m receivers[13].

[12]The nature of any fluctuations does, however, influence the optimal method of temporal integration of signals corresponding to multiple pulses.

[13]Again, a 'receiver' in this context is simply a point at which a signal is received from an antenna.

The wanted signal received by the ith receiver is given by:

$$S_i(t) = a_{si} \exp(-j\varphi_{si}) s_0(t - t_{si}) \exp[j(\omega_0 + \Omega_{si})(t - t_{si})] \tag{2.22}$$

where a_{si} is the rms amplitude, φ_{si} is the initial phase, t_{si} is the signal propagation delay, Ω_{si} is the doppler shift, and ω_0 the carrier frequency. The function $s_0(t)$ is the normalised complex waveform, which is defined such that the received signal energy E_i is given by:

$$E_i = \frac{1}{2} \int_{-\infty}^{\infty} |S_i(t)|^2 dt = \frac{a_{si}^2}{2} \int_{-\infty}^{\infty} |s_0(t - t_{si})|^2 dt = a_{si}^2 T_s \tag{2.23}$$

for signal duration T_s. The spectrum $\Psi_i(\omega)$ of the received signal is found by taking the Fourier transform of Equation 2.22 to give:

$$\Psi_i(\omega) = a_{si} \exp(-j\varphi_{si}) \Psi_0(\omega - \omega_0 - \Omega_{si}) \exp(-j\omega t_{si}) \tag{2.24}$$

where $\Psi_0(\omega)$ is the Fourier transform of $s_0(t)$, expressed with Parseval's theorem as:

$$\frac{1}{2\pi} \int_{-\infty}^{\infty} |\Psi_0(\omega)|^2 d\omega = \int_{-\infty}^{\infty} |s_0(t)|^2 dt = 2T_s \tag{2.25}$$

In this fully deterministic case, each of the signal parameters of $S_i(t)$ (which are jointly defined as the vector $\boldsymbol{\Theta}$ in Equation 2.21) are known for all i. In addition, the total noise at each receiver is mutually uncorrelated, white Gaussian self-noise with power spectral density N_i. Therefore $\mathbf{f}(\omega)$ (also defined in Equation 2.21) becomes[14]:

$$\mathbf{f}(\omega) = \text{diag}(N_1^{-1}, ..., N_m^{-1}) = ||\delta_{ik} N_i^{-1}|| \tag{2.26}$$

The first integral in Equation 2.21 is the *sufficient statistic* for the deterministic case as it alone involves the observations $\chi(\omega)$, and $\boldsymbol{\Theta}$ and $\mathbf{f}(\omega)$ are both known. Therefore the second integral has no effect on the signal processing and can be discarded. Inserting Equations 2.22 and 2.26 into Equation 2.21 with this simplification gives the log likelihood

[14] δ_{ik} is the Kronecker delta.

ratio (named L_1) for deterministic Θ in a background of white interferences:

$$L_1 = \ln(\Lambda) = \mathrm{Re}\sum_{i=1}^{m} \frac{a_{si}\exp(j\varphi_{si})}{2\pi N_i} \int_{-\infty}^{\infty} \chi_i(\omega)\Psi_0^*(\omega - \omega_0 - \Omega_{si})\exp(j\omega t_{si})d\omega \qquad (2.27)$$

It is perhaps easier to visualise the components of this processing algorithm by transforming Equation 2.27 back into the time domain by substitution of the previously defined Fourier pairs $\chi_i \Leftrightarrow X_i$ and $\Psi_0 \Leftrightarrow s_0$, yielding:

$$L_1 = \mathrm{Re}\sum_{i=1}^{m} \frac{a_{si}\exp(j\varphi_{si})}{N_i} \int_{-T/2}^{T/2} X_i(t)s_0^*(t - t_{si})\exp[-j(\omega_0 + \Omega_{si})(t - t_{si})]dt \qquad (2.28)$$

We can then compare this algorithm with the general time-domain form of a correlation (matched) filter:

$$y(\tau) = \int_{-\infty}^{\infty} x(u)h^*(u - \tau)du \qquad (2.29)$$

The fundamental procedure in algorithm L_1 is the cross correlation of each received signal $X_i(t)$ with the wanted signal $s_0(t)$ over the period $-T/2, T/2$, including equalisation for the known phase offset φ_{si} of the reference oscillator at each receiver and the expected doppler frequency Ω_{si}. The outputs of the correlations at $\tau = t_{si}$ are taken, weighted by the ratio a_{si}/N_i, and then coherently summed. The time-of-arrival t_{si} will in general be different for all i, so in practice time-shifting of each signal is required to allow the summation.

It is clear that this algorithm is fundamentally the same as the conventional array detector described in Section 2.3.1, comprising a bank of matched filters for each received signal, time-shifting and coherent summation. This is perhaps not surprising, as when all signal parameters are deterministic, there is little difference between the vector of expected signals in both cases. However, the signal-to-noise ratios at each receiver of the multistatic system will in general be different, and hence an amplitude weighting given by a_{si}/N_i is applied to each received signal. This ratio of the rms signal amplitude to noise power is in fact identical to that defined by the *maximal-ratio combiner* (MRC) commonly used in wireless communications(51), which it is known results in the maximum possible signal-to-noise ratio of a coherent sum of signals in white noise.

In this completely (artificial) deterministic case, all absolute phase shifts are known, so L_1 is found simply by taking the real part of the summation, and a decision is made as to the existence of a target by comparison of L_1 against some threshold. The structure of this

algorithm is shown in Figure 2-4.

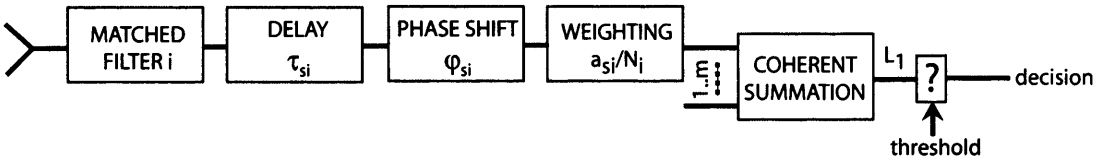

Figure 2-4: Structure of the detection algorithm for deterministic signals

The nature of the output variable L_1 can be determined for the two hypotheses H_0 and H_1 of Equation 2.11. For H_0 where there is no signal present, the inputs to the receiver consist of zero-mean Gaussian self-noises only. For H_1 where a signal is present, the inputs consist of a combination of Gaussian self-noise and deterministic signal. It is clear from Equation 2.27 that the receiver consists of linear processes only, so the well-known result can be used that the output of a linear receiver with a Gaussian noise input is also Gaussian. Therefore L_1 is fully determined by its mean and variance only. For any linear system $\mathbb{L}\{\}$, the fundamental theorem exists that(52):

$$\mathrm{E}[\mathbb{L}\{x(t)\}] = \mathbb{L}\{\mathrm{E}[x(t)]\} \tag{2.30}$$

so the mean $\eta_y(t)$ of the output of the filter equals the response of the system to the mean $\eta_x(t)$ only of the input, i.e. $\eta_y(t) = \mathbb{L}\{\eta_x(t)\}$. Hence the mean value of L_1 is found by replacing the received input signal $X_i(t)$ in Equation 2.28 with its mean $\overline{X_i(t)}$. In the case of hypothesis H_0, $\overline{X_i(t)}$ is zero by definition. Therefore the integral in Equation 2.28, and hence the mean of L_1, resolve to zero.

In the case of hypothesis H_1, $\overline{X_i(t)} = \overline{S_i(t)}$ (see Equation 2.22), so substituting into Equation 2.28 and using Equation 2.23 gives:

$$\overline{L_1} = \sum_{i=1}^{m} 2a_{si}^2 T_s/N_i = \sum_{i=1}^{m} 2E_i/N_i \quad \text{for } H_1 \tag{2.31}$$

As the wanted signal (if it exists) is deterministic, the variance σ^2 of L_1 is the same for both hypotheses (i.e. it depends on the noise component only). Therefore for simplicity hypothesis H_0 is considered where $\mathrm{E}[L_1] = 0$ and $X_i(t) = n_i(t)$ is some realisation of the

Gaussian self-noise process, such that:

$$\sigma^2(\mathrm{L_1}) = \mathrm{E}[{\mathrm{L_1}}^2] = \overline{\left[\mathrm{Re}\sum_{i=1}^{m}\frac{a_{si}\exp(j\varphi_{si})}{N_i}\int_{-T/2}^{T/2} n_i(t)s_0^*(t-t_{si})\exp[-j(\omega_0+\Omega_{si})(t-t_{si})]dt\right]^2} \tag{2.32}$$

For narrowband signals (such that ω_0 is much greater than the signal bandwidth), it can be shown that the approximation $(\mathrm{Re}\ y)^2 = 0.5\mathrm{Re}\ yy^*$ holds(34), so $\sigma^2(\mathrm{L_1})$ can be calculated by multiplying the expression under the bar with the complex conjugate of itself and finding the real part. By definition the noise process variance is given by:

$$0.5\overline{n_i(t_1)n_i^*(t_2)} = \sqrt{N_i N_i}\delta(t_1 - t_2) \tag{2.33}$$

where $\delta(t)$ is the Dirac delta function (for which $\int_{-\infty}^{\infty}\delta(t)dt = 1$). Substituting into Equation 2.32 and using Equation 2.23 gives:

$$\sigma^2(\mathrm{L_1}) = \sum_{i=1}^{m} 2a_{si}^2 T_s/N_i = \sum_{i=1}^{m} 2E_i/N_i \tag{2.34}$$

The output signal-to-noise ratio of the detector algorithm is defined by the ratio of the squared modulus of $\mathrm{L_1}$ for a signal only (no noise) to the variance of $\mathrm{L_1}$ for noise input only. From Equations 2.31 and 2.34 it is given by:

$$\mathrm{SNR_{out}} = q_{\mathrm{out}}^2 = \frac{|\mathrm{L_{1sig}}|^2}{\sigma^2(\mathrm{L_{1noise}})} = \sum_{i=1}^{m} 2E_i/N_i \tag{2.35}$$

Therefore the mean of the Gaussian variable $\mathrm{L_1}$ (for hypothesis H_1), its variance and its signal-to-noise ratio are all given by the sum of $2E_i/N_i$ over all $i = 1, m$, where $2E_i/N_i$ is the signal-to-noise ratio[15] of the signal *at each receiver* (which may be called the *partial* SNR). This improvement in signal-to-noise ratio is equivalent to the 'array gain' described in Section 2.3.1 for the conventional array antenna. Indeed, if all partial signal-to-noise ratios in Equation 2.35 are equal (as was assumed the case for the conventional array), $\mathrm{SNR_{out}} = m \times \mathrm{SNR_{partial}}$, so the same result is obtained.

The probability density functions of $\mathrm{L_1}$ for the two hypotheses can now be easily ex-

[15]Note this is the signal *energy* to noise *power* ratio

pressed using the standard Gaussian probability density function equation as:

$$\begin{aligned} p_{H_0}(x) &= \frac{1}{\sqrt{2\pi q_{\text{out}}^2}} \exp(\frac{-x^2}{2q_{\text{out}}^2}) \\ p_{H_1}(x) &= \frac{1}{\sqrt{2\pi q_{\text{out}}^2}} \exp(\frac{-(x-q_{\text{out}}^2)^2}{2q_{\text{out}}^2}) \end{aligned} \tag{2.36}$$

The false alarm rate for the detector is then given by:

$$P_{\text{fa}} = \int_{u_t}^{\infty} p_{H_0}(x)dx \tag{2.37}$$

for threshold u_t, which simplifies using the well-known equations (see, for example, (53)) to:

$$P_{\text{fa}} = 0.5[1 - \text{erf}(u_0/\sqrt{2})] \tag{2.38}$$

where $\text{erf}(x)$ is the error function:

$$\text{erf}(x) = \frac{2}{\sqrt{\pi}} \int_0^x \exp(-t^2)dt \tag{2.39}$$

and $u_0 = u_t/\sigma(\text{L}_1)$ is the normalised threshold level. The probability of detection is given similarly by

$$P_{\text{d}} = 0.5[1 - \text{erf}([u_0 - q_{\text{out}}]/\sqrt{2})] \tag{2.40}$$

These equations are the same as for the monostatic case, but now the signal-to-noise ratio q_{out}^2 of L_1 is determined by the sum of partial signal-to-noise ratios in Equation 2.35.

In summary, the 'filter' component of the optimal detection process for deterministic signals consists of a matched filter for every received signal, the outputs of which are individually time and phase equalised, weighted according to the ratio of signal amplitude to mean noise power, and then coherently summed. The output of this 'filter' (which we have now seen is in fact the processed sum of a bank of matched filters) equals the likelihood ratio for the hypothesis of a target at a given location, determined by the time-of-arrival equalisation calculated from the multistatic geometry. The design of the thresholder itself is equivalent to the monostatic case, other than the redetermination of the threshold level in order to obtain improved performance due to the higher signal-to-noise ratio of input variable L_1.

2.4.3 Fluctuating and Fading Signals

In practice, completely deterministic received signals can almost never occur, if only because of the unknown phase shift applied to the signal by the target and propagation medium. As a result, the initial phase φ_{si} of the received signal in Equation 2.22 comprises this 'propagation component' as well as the 'engineering component' caused by known (for a spatially coherent radar) phase offsets between reference oscillators in each receiver. Therefore in order to find a detection algorithm suitable for implementation in the prototype multistatic system, it is necessary to loosen the constraints of the detector presented above. Here, the detection problem is considered for the case when the received signals are *fluctuating*, i.e. the wanted signals have random complex amplitudes. It will also be shown that one of the same detectors is optimal when there are no fluctuations, but the absolute phase of the received signal is unknown. Fluctuations can be caused by small variations in the propagating medium, by destructive interference caused by multipath, or by small relative movements of a complex target consisting of multiple scattering points. The possible nature of fluctuations caused by particular classes of *targets* is considered in more detail in Appendix B.

For the purposes of determining optimal detection algorithms, the interest is in the *mutual spatial correlation of these fluctuations between receivers*, rather than their time-dependent characteristics. However, it is useful to firstly consider the well-known models for the nature of temporal fluctuations, which are known as the Swerling cases(54). Four situations are described for the nature of the fluctuations over time. In particular, 'case 2' models fluctuations resulting from a complex target containing many similar reflecting points (or 'flare spots'). It is stated that the fluctuations are independent from pulse to pulse, and that the PDF of the signal-to-noise ratio at the receiver has an exponential distribution (which is equivalent to Rayleigh distributed amplitude fluctuations). 'Case 4' models fluctuations relating to a target comprised of one dominant flare spot as well as many smaller ones. Here the PDF of the signal-to-noise ratio has a chi-square distribution with four degrees of freedom. Cases 1 and 3 correspond to identical probability distributions, but apply to the situation where fluctuations are much slower, and are only independent from one scan period to the next. The appropriateness of these models depends on the scan and pulse repetition rates, as well as the nature of the target (for example, objects

where small changes in orientation result in large changes in the reflected signal power are likely to result in rapidly changing fluctuations). However, the application of these models to multistatic systems is limited as they state nothing about the spatial correlation of fluctuations when a target is observed from multiple angles. Nevertheless, one could surmise that if small rotational changes of a target are adequate to cause independent fluctuations between pulses, simultaneous observations separated by large angles would also be independent.

The effects on detection performance resulting from these models in a monostatic radar have been calculated by Swerling. In certain cases, much greater performance degradation results from fading due to multipath effects. Here, scattered signals from the target in directions other than the direct path reflect off clutter, and cause destructive interference with the main echo. Particularly wild fluctuations in signal amplitude at the receiver are predicted at low elevation angles, where multipath signals reflect on the ground and undergo a π phase shift, such that small differences in the path lengths result in elevation-dependent null patterns(55). In the real world surfaces are more complex, although these patterns are observed in many applications(53). In cases where fluctuations are caused by specular reflection (such as in maritime radar), multipath can result in repeated missed detections when the 'revisit' times for a particular coverage region coincide with deep fade conditions(56). There has been considerable recent research into the spatial correlation of multipath fading for wireless multi-antenna communications applications, e.g. Shiu(57). Low fading correlation has been observed with antenna spacings of only 6 cm on mobile devices operating at 2.4 GHz in an environment surrounded by scatterers, however evidently the effect in a multistatic radar system will be highly dependent on the geometry and environment.

At this point, we are interested not in detection performance degradation caused by fluctuations or multipath, but instead in determining optimal detection algorithms *taking into account these factors.* Given the complex set of potential contributors to the fluctuations of the wanted signal described above, let us consider the two extreme situations - firstly that there is complete mutual correlation of fluctuations between receivers, and secondly the case that the fluctuations are mutually independent. It then remains a separate problem to fit a given situation to the most appropriate model, or develop additional detectors for optimality in the case of partial correlation.

The problem of determining algorithms for combining multiple spatially fluctuating

signals does have some similarities with the design of optimal integrators for a train of fluctuating pulses, which has been well studied in the context of monostatic radar(46). However the multistatic detector must also take account of differences in signal and noise power and time-of-arrival between receivers, which are normally consistent for each pulse in the monostatic case. The multistatic algorithms described here refer to the detection of a single pulse only, however evidently the appropriate temporal integrators can also be used on the signal at each receiver prior to the multistatic detection process. It should be noted however that incoherent (e.g. 'square law') integration at a single receiver clearly precludes the subsequent use of a coherent multistatic detection algorithm.

The derivation of the optimal detector for the fluctuating case begins with the assumption that the complex amplitude is in all cases constant during the period of a single pulse (as is also assumed in all Swerling cases). It can be seen from Equation 2.22 for the wanted signal that the two random parameters are the initial phase φ_{si} and rms amplitude a_{si}. Therefore the vector of wanted signals $\mathbf{\Psi}(\omega, \mathbf{\Theta})$ in Equation 2.21 (where $\mathbf{\Theta}$ is the vector of parameters) can be expressed as:

$$\mathbf{\Psi}(\omega, \varphi_s, \mathbf{a}_s) = \tilde{\mathbf{\Psi}}(\omega)\tilde{\mathbf{E}}(\varphi_s)\mathbf{a}_s \tag{2.41}$$

where $\tilde{\mathbf{\Psi}}$ is the diagonal matrix containing only deterministic parameters:

$$\tilde{\mathbf{\Psi}} = ||\delta_{ik}\Psi_0(\omega - \omega_0 - \Omega_{si})\exp(-j\omega t_{si})|| \tag{2.42}$$

and the random parameters can be expressed as[16]:

$$\begin{aligned} \tilde{\mathbf{E}}(\varphi_s) &= \mathrm{diag}[\exp(-j\varphi_{s1}, ..., \exp(-j\varphi_{sm}))] \\ \mathbf{a}_s^{\mathrm{t}} &= (a_{s1}, ..., a_{sm}) \end{aligned} \tag{2.43}$$

It is assumed that the fluctuations in complex amplitude are Gaussian, therefore by definition $\mathbf{a}_s$ will take the Rayleigh pdf $w(\mathbf{a}_s)$, whilst φ_s will have a flat pdf $w(\varphi_s)$, the two of which are mutually independent such that $w(\mathbf{\Theta}) = w(\varphi_s)w(\mathbf{a}_s)$.

The likelihood ratio test of Equation 2.21 is now conditional at fixed $\mathbf{\Theta}$. The unconditional form can be generated by integrating over $\mathbf{\Theta}$ and substituting the expressions in

[16]Superscript $^{\mathrm{t}}$ denotes the transposed matrix

Equations 2.41 and 2.43 into Equation 2.21 to give:

$$\tilde{\Lambda} = \int_{\boldsymbol{\Theta}} w(\boldsymbol{\Theta})\Lambda(\boldsymbol{\Theta})d\boldsymbol{\Theta} = \int_{\mathbf{a}_s}\int_{\varphi_s} w(\mathbf{a}_s)w(\varphi_s)\exp\left\{\mathbf{a}_s^{\mathrm{t}}\,\mathrm{Re}\left[\tilde{\mathbf{E}}^*(\varphi_s)\frac{1}{2\pi}\int_{-\infty}^{\infty}\tilde{\boldsymbol{\Psi}}^*(\omega)\mathbf{f}(\omega)\chi(\omega)d\omega\right]\right.$$
$$\left. -\frac{1}{2}\mathbf{a}_s^{\mathrm{t}}\tilde{\mathbf{E}}^*(\varphi_{\mathbf{s}})\left[\frac{1}{2\pi}\int_{-\infty}^{\infty}\tilde{\boldsymbol{\Psi}}^*(\omega)\mathbf{f}(\omega)\tilde{\boldsymbol{\Psi}}(\omega)d\omega\right]\tilde{\mathbf{E}}(\varphi_s)\mathbf{a}_s\right\}d\varphi_s d\mathbf{a}_s \tag{2.44}$$

To simplify this equation, the vector $\mathbf{G}$ and matrix $\mathbf{C}$ are defined as:

$$\begin{aligned}\mathbf{G} &= \frac{1}{2\pi}\int_{-\infty}^{\infty}\tilde{\boldsymbol{\Psi}}^*(\omega)\mathbf{f}(\omega)\chi(\omega)d\omega \\ \mathbf{C} &= \frac{1}{2\pi}\int_{-\infty}^{\infty}\tilde{\boldsymbol{\Psi}}^*(\omega)\mathbf{f}(\omega)\tilde{\boldsymbol{\Psi}}(\omega)d\omega\end{aligned} \tag{2.45}$$

Firstly it is assumed that the noise background consists of receiver self-noises only, so $\mathbf{f}(\omega)$ is given by Equation 2.26. Then elements of $\mathbf{G}$ and $\mathbf{C}$ can be written as:

$$\begin{aligned}G_i &= \frac{1}{2\pi N_i}\int_{-\infty}^{\infty}\chi_i(\omega)\Psi_0^*(\omega-\omega_0-\Omega_{si})\exp(j\omega t_{si})d\omega \\ C_{ii} &= \frac{1}{2\pi N_i}\int_{-\infty}^{\infty}|\Psi_0(\omega-\omega_0-\Omega_{si})|^2 d\omega = 2T_s/N_i\end{aligned} \tag{2.46}$$

The elements G_i can be rewritten in the time domain as:

$$G_i = \frac{1}{2\pi N_i}\int_{-T/2}^{T/2} X_i(t)s_0^*(t-t_{si})\exp[-j(\omega_0+\Omega_{si})(t-t_{si})]dt \tag{2.47}$$

which, as was demonstrated previously, describes the time-shifted matched filtering of the ith received signal, normalised by its own noise power N_i. Equation 2.44 becomes:

$$\tilde{\Lambda} = \int_{\mathbf{a_s}}\int_{\varphi_{\mathbf{s}}} w(\mathbf{a_s})w(\varphi_{\mathbf{s}})\exp\left[\mathbf{a}_{\mathbf{s}}^{\mathbf{t}}\mathrm{Re}[\tilde{\mathbf{E}}^*(\varphi_{\mathbf{s}})\mathbf{G}] - T_s\mathbf{a}_{\mathbf{s}}^{\mathbf{t}}\mathbf{N}^{-\mathbf{1}}\mathbf{a_s}\right]d\varphi_{\mathbf{s}}d\mathbf{a_s} \tag{2.48}$$

The case can also be considered where the noise at each receiver is coloured (although also mutually uncorrelated). This may occur in a multistatic system where there are directional interference sources local to particular receivers, and these receivers are fairly widely separated. This situation may be modelled by considering the noise at a receiver as comprising a combination of white noise and some non-white interference that has a complex envelope with normalised power spectral density given by $F_i(\omega)$. As the total noises are

spatially uncorrelated, $\mathbf{f}(\omega)$ is also diagonal, with entries given by:

$$f_{ii}(\omega) = \frac{1}{N_i[1 + q_{Ii}^2 F_i(\omega - \omega_0)]} \tag{2.49}$$

where q_{Ii}^2 is the power interference-to-noise ratio. Then the detectors for fluctuating signals can be used by replacing elements of $\mathbf{G}$ and $\mathbf{C}$ (Equation 2.46) with:

$$\begin{aligned} G_i &= \frac{1}{2\pi N_i} \int_{-\infty}^{\infty} \frac{\chi_i(\omega)\Psi_0^*(\omega - \omega_0 - \Omega_{si}) \exp(j\omega t_{si})}{1 + q_{Ii}^2 F_i(\omega - \omega_0)} d\omega \\ C_{ii} &= \frac{1}{2\pi N_i} \int_{-\infty}^{\infty} \frac{|\Psi_0(\omega - \omega_0 - \Omega_{si})|^2}{1 + q_{Ii}^2 F_i(\omega - \omega_0)} d\omega = 2K_i T_s / N_i \end{aligned} \tag{2.50}$$

where K_i is a proportionality factor, equal to unity when q_{Ii}^2 is zero. These substitutions result in optimal detectors for spatially uncorrelated 'coloured' noises.

Equation 2.48 can now be used to derive optimal detectors given the two previously described models for the mutual correlation of signal fluctuations between receivers.

2.4.4 Mutually Correlated Fluctuations

In the first case, it is assumed that the amplitudes and phases are fully mutually correlated, hence they are functionally connected:

$$\begin{aligned} \varphi_{si} &= \varphi_{s1} - \Delta\varphi_{si1} \\ a_{si} &= A_{i1} a_{s1} \end{aligned} \tag{2.51}$$

where φ_{s1} and a_{s1} are the random phase and amplitude values of the signal at some 'reference' receiver, the values at other receivers φ_{si} and a_{si} being determinable from these by some known phase offset $\Delta\varphi_{si1}$ and amplitude scaling factor A_{i1}. This model may be applicable when, for example, the receiver antennas are positioned relatively close together or observed targets are simple. Clearly it also requires the radar equipment itself to be spatially coherent. The probability density functions of φ_{s1} and a_{s1} are given by:

$$\begin{aligned} w(\varphi_{s1}) &= 1/2\pi \quad \varphi_{s1} \in (-\pi, \pi) \\ w(a_{s1}) &= (2a_{s1}/\sigma_1^2) \exp(-a_{s1}^2/\sigma_1^2) \quad a_{s1} \in (0, \infty) \end{aligned} \tag{2.52}$$

Substituting these into Equation 2.48, integrating[17] and omitting terms that are independent of **G** (the processing component involving the observations), produces the optimal receiver for mutually coherent fluctuations named L_2:

$$L_2 = \left| \sum_{i=1}^{m} A_{i1} \exp(-j\Delta\varphi_{si1}) G_i \right| \tag{2.53}$$

Comparison with L_1 in Equation 2.27 shows a common general structure in the form of the bank of matched filter kernels **G**, which now include the noise normalisation weighting factor $1/N_i$. However, the phase equalisation term $\exp(-j\Delta\varphi_{si1})$ is now a differential phase with respect to the random phase at the 'reference' receiver $i = 1$. This differential phase should comprise only the 'engineering component' due to known offsets between reference oscillators. Likewise the signal weighting term $A_{i1} = \sqrt{a_{si}^2/a_{s1}^2}$ is the square root of the ratio of the signal power and that of the reference receiver. Finally the output variable is calculated by linear *envelope detection* of the coherent sum of contributions from each receiver, as the absolute phase of this summation is random. The algorithm structure is shown in Figure 2-5.

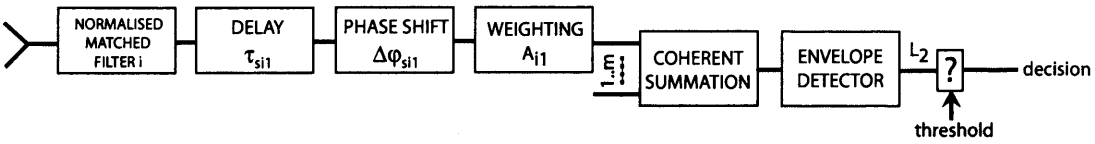

Figure 2-5: Structure of the detection algorithm for mutually correlated fluctuating signals

Performance of the detector can be analysed by determination of the nature of the output signal L_2. It is convenient to consider the variable ι where $L_2 = |\iota|$ (i.e. before the envelope detection). For hypothesis H_0 the input is zero-mean mutually independent Gaussian noise only, so ι_{H_0} is also zero-mean Gaussian. The variance $0.5\overline{\iota_{H_0}\iota_{H_0}^*}$ is found from Equation 2.53 using Equation 2.33:

$$\sigma^2(\iota_{H_0}) = \frac{1}{2}\sum_{i=1}^{m}\sum_{k=1}^{m} A_{i1}A_{k1}\exp[-j(\Delta\varphi_{si1} - \Delta\varphi_{sk1})]\overline{G_{ni}G_{nk}^*} = \sum_{i=1}^{m} 2A_{i1}^2 T_s/N_i \tag{2.54}$$

For hypothesis H_1, we assume the 'optimal' case where the input is a combination of Gaussian noise plus mutually correlated signals with zero-mean Gaussian complex ampli-

[17] using the identity $\frac{1}{2\pi}\int_{-\pi}^{\pi} \exp\{a_{s1}\mathrm{Re}[\exp(j\varphi_{s1})\mathbf{A}^t\mathbf{E}^*\mathbf{G}]\}d\varphi_{s1} = I_0(a_{s1}|\mathbf{A}^t\mathbf{E}^*\mathbf{G}|)$

tude. Then, ι_{H_1} will again be a zero-mean Gaussian variable. The variance of this sum of two Gaussian variables is equal to the sum of the individual variances. The value of ι_{H_1} *for signal only* is considered first at some fixed values of a_{s1} and φ_{s1}, which are equal to the mean output when the input consists of signal and noise. Hence $\overline{\chi_i(\omega)} = \overline{\Psi_i(\omega)}$ can be substituted from Equation 2.24 into Equation 2.53 to give:

$$\iota = a_{s1} \exp(-j\varphi_{s1}) \sum_{i=1}^{m} 2A_{i1}^2 T_s/N_i \tag{2.55}$$

Then the variance of the signal only is given by:

$$\sigma^2(\iota) = 0.5\overline{\iota\iota^*} = 0.5\sigma_1^2 \left(\sum_{i=1}^{m} 2A_{i1}^2 T_s/N_i \right)^2 \tag{2.56}$$

since $\overline{a_{s1}^2} = \sigma_1^2$. Therefore the total variance of H_1 is:

$$\sigma^2(\iota_{H_1}) = \sum_{i=1}^{m} \frac{2A_{i1}^2 T_s}{N_i} \left(1 + \sigma_1^2 \sum_{k=1}^{m} \frac{A_{k1}^2 T_s}{N_k} \right) = \sum_{i=1}^{m} \frac{2A_{i1}^2 T_s}{N_i} \left(1 + \sum_{k=1}^{m} \frac{\overline{E_k}}{N_k} \right) \tag{2.57}$$

where $\sigma_1^2 A_{i1}^2 T_s = \sigma_i^2 T_s = \overline{E_i}$ is the average energy in the fluctuating wanted signal at receiver i.

The signal-to-noise ratio at the output of the detector is identical to that of ι, defined by the ratio of the variance of ι for signal only to the variance of ι for noise input only. Using Equations 2.56 and 2.54 this is given by:

$$\mathrm{SNR_{out}} = \tilde{q}_{\mathrm{out}}^2 = \frac{\sigma^2(\iota_{\mathrm{sig}})}{\sigma^2(\iota_{\mathrm{noise}})} = 0.5\sigma_1^2 \sum_{i=1}^{m} \frac{2A_{i1}^2 T_s}{N_i} = \sum_{i=1}^{m} \overline{E}_i/N_i \tag{2.58}$$

The detector output ι before envelope detection is Gaussian for both hypotheses, so $\mathrm{L}_2 = |\iota|$ always has a Rayleigh distribution. The false alarm probability is then given by the well-known equation e.g. see (53):

$$P_{\mathrm{fa}} = \exp(-u_0^2/2) \tag{2.59}$$

where $u_0 = u_t/\sigma(\iota_{H_0})$ is the normalised threshold. Then the probability of detection can be calculated indirectly using:

$$P_{\mathrm{d}} = P_{\mathrm{fa}}^{1/(1+\tilde{q}_{\mathrm{out}}^2)} \tag{2.60}$$

Therefore the performance characteristics for this detector are again similar to the mono-static case. However, as was the case for detector L_1, the signal-to-noise ratio of the output should be calculated by the summation of the average partial SNR E_i/N_i of the signal at each receiver.

2.4.5 Mutually Independent Fluctuations

Now the case is considered where the fluctuations are completely mutually uncorrelated between receivers. This model may be appropriate where, for example, the receiver antennas are spaced considerable distances apart and the target is a complex scatterer, or in the case that rich multipath is present. The initial phases φ_{si} and rms amplitudes a_{si} are mutually independent for all i. It is assumed that the complex fluctuations are zero-mean Gaussian, so the probability density functions of Equation 2.52 now apply to the phase and amplitude for *all* i (i.e. the values are no longer functionally related). Substituting into the general Equation 2.48 and proceeding similarly to the previous case, the optimal detector becomes:

$$L_3 = \sum_{i=1}^{m} \frac{A_{i1}^2 |G_i|^2}{1 + \overline{E}_i/N_i} \tag{2.61}$$

where $\overline{E}_i = \sigma_i^2 T_s$ is the average energy in the fluctuating wanted signal at receiver i. The output of the noise-normalised, doppler and time-delay equalised vector of matched filters $\mathbf{G}$ is first square-law detected before being weighted by a value proportional to the relative signal power and partial signal-to-noise ratio. The summation of the outputs from the bank of matched filters is incoherent. The algorithm structure is shown in Figure 2-6.

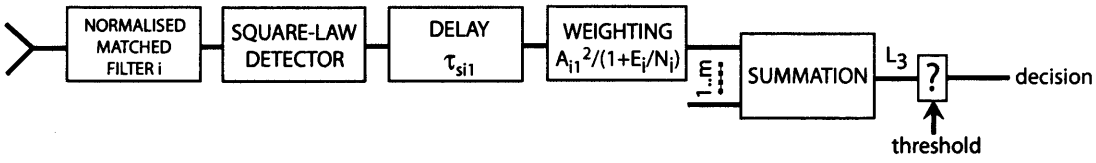

Figure 2-6: Structure of the detection algorithm for mutually independent fluctuating signals

Determination of the characteristics of L_3 is complicated by the square-law envelope detection of the matched filter component G_i and the likely variable signal-to-noise ratios at each receiver. For hypothesis H_0 (noise only), L_3 can described by a chi-square probability

distribution with $2m$ degrees of freedom *if* the partial SNR at each receiver is equal[18]. Then the false alarm probability is given by:

$$P_{\text{fa}} = \exp(-u_0/2) \sum_{k=0}^{m-1} \frac{(u_0/2)^k}{k!} \tag{2.62}$$

If however the partial SNR at each receiver is different, it is necessary to use a generalised chi-square probability distribution, such that(34):

$$P_{\text{fa}} = \sum_{i=1}^{m} \alpha_i \exp(-u_t/2Q_i^2) \tag{2.63}$$

where

$$\alpha_i = -(-1)^{i+1} Q_i^{2(m-1)} \left[\prod_{k=1}^{i-1} (Q_k^2 - Q_i^2) \prod_{l=i+1}^{m} (Q_i^2 - Q_l^2) \right]^{-1} \tag{2.64}$$

where the weights $Q_i = A_{i1}^2/(1 + \overline{E}_i/N_i)$ from Equation 2.61 are arranged in decreasing order ($Q_1^2 > ... > Q_m^2$).

The probability of detection takes a similar form to the probability of false alarm in Equation 2.62 as, provided there really is no correlation of complex amplitudes between receivers and the partial SNR at each receiver is equal (i.e. $\tilde{q}_{\text{out}i}^2 = \tilde{q}_{\text{out\_p}}^2$), L_3 is formed from the sum of random Gaussian contributions from both noise and signal alike, so the signal variance is added to give:

$$P_d = \exp\left[-\frac{u_0/2}{1 + \tilde{q}_{\text{out\_p}}^2} \right] \sum_{k=0}^{m-1} \frac{(u_0/2^k)}{k!(1 + \tilde{q}_{\text{out\_p}}^2)^k} \tag{2.65}$$

If the partial signal-to-noise ratios at each receiver are different, it is necessary to estimate the probability of detection by computer simulation.

2.4.6 Unknown Parameters

Here the situation is considered where the vector $\boldsymbol{\Theta}$ from Equation 2.21 contains parameters that, whilst not random, are unknown. It was stated in the previous section that this will almost always be the case for practical radars, as phase offsets caused by the target and

[18]Note this distribution is the same as that resulting from the temporal integration of m pulses where each signal is an independent squared Gaussian variate.

propagation path are generally not a-priori available. Alternatively the parameters may be random but with unknown probability distribution. In these cases, an adaptive approach can be used by replacing $\boldsymbol{\Theta}$ with its *maximum likelihood estimate* $\hat{\boldsymbol{\Theta}}$, in which case the detector for deterministic signals is optimal(58):

$$\mathrm{L_{ml}} = \mathrm{Re}\frac{1}{2\pi}\int_{-\infty}^{\infty} \boldsymbol{\Psi}^*(\omega, \hat{\boldsymbol{\Theta}})\mathbf{f}(\omega)\boldsymbol{\chi}(\omega)d\omega \tag{2.66}$$

This form is sometimes known as the 'generalised likelihood ratio'(59). The situation can be described by taking the model of randomly fluctuating, mutually correlated signals, but applying the algorithm for fixed values of amplitude and phase. The log likelihood ratio from Equation 2.48 can be used with Equation 2.51 to give:

$$\ln\Lambda = a_{s1}\mathrm{Re}[\exp(j\varphi_{s1})\mathbf{A}^t\mathbf{E}^*\mathbf{G}] - a_{s1}^2 T_s \mathbf{A}^t\mathbf{N}^{-1}\mathbf{A} \tag{2.67}$$

The maximum likelihood method assumes that the received signal depends on the unknown parameter(s), and chooses the value for each parameter that most likely caused the observed data to occur(52). This is done by finding the parameter value for which the partial derivative of the log likelihood function with respect to the parameter equals zero. In this case we can find the expression for the maximum likelihood of the unknown phase φ_{s1} by writing:

$$\frac{\partial[\ln\Lambda]}{\partial\varphi_{s1}} = a_{s1}\mathrm{Re}[j\exp(j\varphi_{s1})\mathbf{A}^t\mathbf{E}^*\mathbf{G}] = 0 \tag{2.68}$$

Therefore the maximum likelihood estimate of φ_{s1} is found where the term inside the Re[] is imaginary, i.e. $\hat{\varphi}_{s1} = -\mathrm{arg}\mathbf{A}^t\mathbf{E}^*\mathbf{G}$. Then:

$$\ln\Lambda = a_{s1}|\mathbf{A}^t\mathbf{E}^*\mathbf{G}| - a_{s1}^2 T_s \mathbf{A}^t\mathbf{N}^{-1}\mathbf{A} \tag{2.69}$$

Similarly the maximum likelihood estimate for the rms amplitude at the reference station is found by taking the partial derivative with respect to $\hat{a}_{s1}$, giving:

$$\hat{a}_{s1} = |\mathbf{A}^t\mathbf{E}^*\mathbf{G}|/2T_s\mathbf{A}^t\mathbf{N}^{-1}\mathbf{A} \tag{2.70}$$

which can be substituted into Equation 2.69 and, having discarding factors independent of $\mathbf{G}$, it is found that the same algorithm $\mathrm{L_2}$ is derived again. Therefore the optimal algorithm

for an unknown complex amplitude that is functionally related between receivers is the same as the algorithm obtained for Gaussian spatially correlated fluctuations.

Now, the situation is considered where the amplitude and phase of signals received at *all* stations is constant but unknown. Hence, no functional relationship of these values is assumed between receivers. This may be the case, for example, when different aspects of the same non-fluctuating target are observed. Returning to Equation 2.48, but this time for fixed values of φ_{si} and a_{si} for all i, the log likelihood ratio becomes:

$$\ln\Lambda = \sum_{i=1}^{m} a_{si}\mathrm{Re}[\exp(j\varphi_{si})G_i] - T_s\sum_{i=1}^{m} a_{si}^2/N_i \tag{2.71}$$

Then taking partial derivatives with respect to the unknown parameters gives $\hat{\varphi}_{si} = -\arg G_i$ and $\hat{a}_{si} = |G_i|/2T_s$. Inserting these back into the log likelihood ratio produces:

$$\mathrm{L}_4 = \sum_{i=1}^{m} |G_i|^2 N_i \tag{2.72}$$

which, save for the weighting, is identical in form to L_3.

In summary, the detection algorithms L_2 and L_3, which were designed for optimality when the received signals have Gaussian complex fluctuations (mutually correlated and uncorrelated respectively), are also optimal when either: (a) there are no fluctuations, but the absolute values of amplitude and phase are unknown, or (b) there are fluctuations, but their probability distributions are unknown. Of course, if the probability distributions *are* known (and are not Gaussian), then it may be possible to derive a superior algorithm taking account of this knowledge. Nevertheless, this result is convenient for the usual case where there is limited a priori information regarding the nature of signal fluctuations. It is however necessary to know the mutual relationship of fluctuations between receivers in order to choose between detectors L_2 and L_3.

2.4.7 Systems with Multiple Transmitters

Until now, the developed algorithms have been designed for single transmitter multistatic radars. Here consideration is given to the effect of adding additional transmitters to the system. Two models are considered - firstly where the system of transmitters attempts to create a single 'phased' signal at a target, and secondly where each signal is transmitted

such that they can be discriminated at the receiver.

Firstly a system is considered comprising n transmitters in addition to m receivers, where each transmitter is synchronised such that the identical signals from each will arrive at a target in perfect phase. Then, the signal at each receiving station will appear to consist of a single echo only, however the rms amplitude will equal the sum of the contributions from each transmitter. The optimal detection algorithms are identical to those already derived, with a_{si} replaced by the total sum of contributions. For the coherent detectors where performance is completely determined by the sum of partial signal-to-noise ratios, the received signal energy E_i from Equation 2.23 is given by:

$$E_i = a_{si}^2 T_s = \left(\sum_{k=1}^{n} a_{sik} \right)^2 T_s \tag{2.73}$$

where a_{sik} corresponds to the contribution of each of k transmitters. Taking the simplest case where all N_i and a_{sik} are identical, the total signal-to-noise ratio at the output of the detector becomes:

$$q_{\text{out}}^2 = mn^2 q_{\text{out }0}^2 \tag{2.74}$$

where $q_{\text{out }0}^2$ is the output SNR of a monostatic radar (single transmitter, single receiver) with the same parameters.

An alternative system is now considered where the signals from each transmitter are designed to be resolved at each receiver. In the simplest case signal discrimination can be achieved by synchronising transmitters such that, for all receivers, the echoes corresponding to each transmitter arrive at a different point in time. Then, the signal at each receiver consists of n separate echoes. Each element of the vectors and matrices in the processing algorithms, specifically $\mathbf{G}$, $\tilde{\mathbf{E}}(\varphi_s)$, $\mathbf{a}_s$ and $\mathbf{N}^{-1}$ in Equation 2.48, become $n \times 1$ vectors or $n \times n$ matrices themselves. Given that the total noise at each receiver is uncorrelated, white and Gaussian, the noise process accompanying each of the mn echoes is independent.

Firstly this multiple transmitter model is applied to the case of fully correlated fluctuations between stations. In the single transmitter case, the optimum detector was found to be L_2. If we assume that the complex amplitude of *all* echoes is functionally related to a

single 'reference' echo, then L_2 can be written as:

$$L_{2m} = \left| \sum_{k=1}^{n} \sum_{i=1}^{m} A_{ik1} \exp(-j\Delta\varphi_{ik1}) G_{ik} \right| \tag{2.75}$$

where A_{ik1} is the square root of the ratio of the signal energy at receiver i pertaining to transmitter k compared to a 'reference' signal (e.g. that at receiver 1 which is derived from transmitter 1). If the signal from each transmitter is different, G_{ik} should be modified from Equation 2.46 by application of the appropriate matched filter frequency response function Ψ_{0k}. Detection performance parameters remain unchanged from L_2, except now the total signal-to-noise ratio of Equation 2.58 is calculated by summation of partial signal-to-noise ratios corresponding to all mn echoes. Hence, in the simplest case where all N_i and a_{sik}[19] are identical, the total signal-to-noise ratio at the output of the detector is given by:

$$q_{\text{out}}^2 = mnq_{\text{out }0}^2 \tag{2.76}$$

Now the multiple transmitter model is applied to the case where all mn signals have mutually independent complex amplitudes. This problem is identical to that for which detector L_3 was found to be optimal, except now the algorithm operates over all signals:

$$L_{3m} = \sum_{k=1}^{n} \sum_{i=1}^{m} \frac{\tilde{A}_{k1}^2 A_{i1}^2 |G_{ik}|^2}{1 + \overline{E}_{ik}/N_i} \tag{2.77}$$

where $\tilde{A}_{k1}^2$ is the ratio of averaged powers of signals derived from the kth transmitter compared to the nominal reference. Detection probabilities must be calculated in the same way as for L_3.

In practice, temporal resolution may be difficult to achieve where the total bistatic ranges between transmitter-receiver pairs are very different and only limited operation time T is permissible, as the separation of echoes from all transmitters is required in all receivers. Instead, it may be preferred to allow discrimination using frequency or waveform diversity. An analysis of these possibilities is presented in Appendix C. In this case, it is assumed that the echoes corresponding to each transmitter arrive at a given receiver during the same time period. A bank of matched filters corresponding to each transmitted signal

[19] the rms value corresponding to the kth transmitter's echo at the ith receiver

is required at every receiver. Consider an arbitrary receiver containing a bank of linear matched filters with frequency response functions $H_k(\omega)$ corresponding to the signal from the kth transmitter ($k = 1..n$). Then we define $S_{xx}(\omega)$ as the power spectral density of the common input signal, and $S_{kk}(\omega)$ as that of the output of the kth filter. We then state the identities(52):

$$\begin{aligned} S_{xk}(\omega) &= S_{xx}(\omega)H_k^*(\omega) \\ S_{kk}(\omega) = S_{xk}(\omega)H_k(\omega) &= S_{xx}(\omega)|H_k(\omega)|^2 \end{aligned} \tag{2.78}$$

where S_{xk} is the *cross power spectrum*, equal to the Fourier transform of the cross correlation of the input and output of the filter. Using this to apply to two chosen filters H_1 and H_2 from the bank we obtain:

$$S_{12}(\omega) = S_{x1}(\omega)H_2(\omega) = S_{xx}(\omega)H_1^*(\omega)H_2(\omega) \tag{2.79}$$

and

$$R_{12}(\tau) = \frac{1}{2\pi}\int_{-\infty}^{\infty} S_{xx}(\omega)H_1^*(\omega)H_2(\omega)\exp(j\omega\tau)d\omega \tag{2.80}$$

where R_{12} is the cross correlation of the output signals from the two filters. Assume firstly that the input to the filters consists only of white (wide-sense stationary) Gaussian noise, then $S_{xx}(\omega) = N$, and:

$$R_{12}(\tau) = \frac{N}{2\pi}\int_{-\infty}^{\infty} H_1^*(\omega)H_2(\omega)\exp(j\omega\tau)d\omega \tag{2.81}$$

Similar results can be obtained for all outputs from the filter bank. If the bank comprises matched filters with *non-overlapping frequency response functions*, then the integral becomes zero and the noise outputs will be mutually uncorrelated. In that case, the detection problem is one of processing mn separate signals, each in a background of mutually uncorrelated Gaussian noise, and the previously derived algorithms for multiple transmitters can be used.

If instead the bank comprises filters with overlapping frequency response functions, and the mutual covariance of the noise evaluated from Equation 2.81 is non-zero, then the detection problem is one of processing mn signals in a background of noises that are partially mutually correlated. Derivation of the optimal detection algorithm for this case

is therefore a more complex problem, based on deriving the likelihood ratio test given the expected correlation matrix, and is not considered here further.

2.5 Detection Performance and Analysis

2.5.1 Introduction

In this section, an original analysis of the relative performance of the detection algorithms described above is presented, and consideration is given to their implementation for simple multistatic designs.

The procedures described so far can be delineated into two categories (excluding the unrealistic deterministic detector L_1):

a) coherent gain summation detectors, e.g. L_2;

b) incoherent 'averaging' detectors, e.g. L_3.

Detectors of type (a) are comparable to the coherent summation of the signals at each element of a conventional array antenna, albeit taking into account factors related to the wide spatial distribution of receivers. They have been shown to be optimal in cases where there is no fluctuation, or the fluctuations are mutually correlated between receivers.

Detectors of type (b) are incoherent, and therefore do not require spatial coherency of the radar equipment itself. However, system coherency may still be beneficial in cases where, for example, it is desired to perform adaptive cancellation of correlated interferences prior to the detection of uncorrelated wanted signals. These detectors have been shown to be optimal where fluctuations are independent between receivers. If in addition each transmitter uses signals that can be discriminated at each receiver, the resulting system effectively comprises mn virtual bistatic radars with independent fluctuating characteristics. Such a radar cannot exploit the coherent gain available using coherent detectors where fluctuations are mutually correlated, but may provide increased detection performance due to the fluctuation 'smoothing' that will result in a more consistent total signal-to-noise ratio.

2.5.2 Performance Comparison

Here the relative performance of these detectors is considered based on the expressions for false-alarm and detection probabilities described above. In each case, these expressions re-

fer to the performance of the entire multistatic system, so are related to the characteristics of the output variable L_x for the derived 'filters', which is then thresholded to make the detection decision. We are concerned particularly with the effects on performance of adding additional transmitters or receivers to the system, as well as the comparative performance given particular models for fluctuations. The results may be applied to the prototype multistatic system in order to inform the choice of detection algorithm for a given experiment, and to guide the system topology (e.g. location of transmit and receive stations) to maximise detection performance.

Firstly the coherent detector L_2 is considered for the case of zero fluctuations (i.e. the complex amplitudes at each receiver are functionally related and fixed at some constant value). For hypothesis H_0 (noise only), the output is Rayleigh (the modulus of Gaussian variable ι) so the probability of false alarm is given by Equation 2.59 as before. For hypothesis H_1 at fixed values of a_{s1} and φ_{s1}, ι has a non-zero mean given by Equation 2.55. Therefore L_2 becomes a Rician variable such that the probability of detection can be written using Equation 2.58 as (e.g. (60)):

$$P_d = \int_{u_0}^{\infty} x \exp[-(x^2 + q_{\text{out}}^2)/2] I_0(x q_{\text{out}}) dx \tag{2.82}$$

where $u_0 = u_t/\sigma(\iota_{\text{noise}})$ is the normalised threshold level[20]. The fixed signal-to-noise ratio q_{out}^2 is given by:

$$q_{\text{out}}^2 = \frac{|\iota_{\text{sig}}|^2}{\sigma^2(\iota_{\text{noise}})} = \sum_{i=1}^{m} 2E_i/N_i = \sum_{i=1}^{m} q_{\text{out\_}i}^2 \tag{2.83}$$

In the case that the mutually correlated complex amplitude is indeed fluctuating, Equations 2.59 and 2.60 should be used. For a fixed false alarm rate, probabilities of detection are determined completely by the mean output signal-to-noise ratio $\tilde{q}_{\text{out}}^2$.

Figure 2-7 shows probability of detection as a function of signal-to-noise ratio for detector L_2 in both the fluctuating and non-fluctuating cases with fixed false alarm probabilities. It should be noted from Equations 2.58 and 2.83 that the total SNR for the fluctuating case is the mean value, whereas that for the non-fluctuating case is fixed.

The form of the graphs in Figure 2-7 is the same as for an equivalent monostatic detector, where the total signal-to-noise ratio $\tilde{q}_{\text{out}}^2$ or q_{out}^2 is given by Equation 2.76 as the sum of the

[20] $I_0()$ in Equation 2.82 is the modified Bessel function of the first kind with zero order.

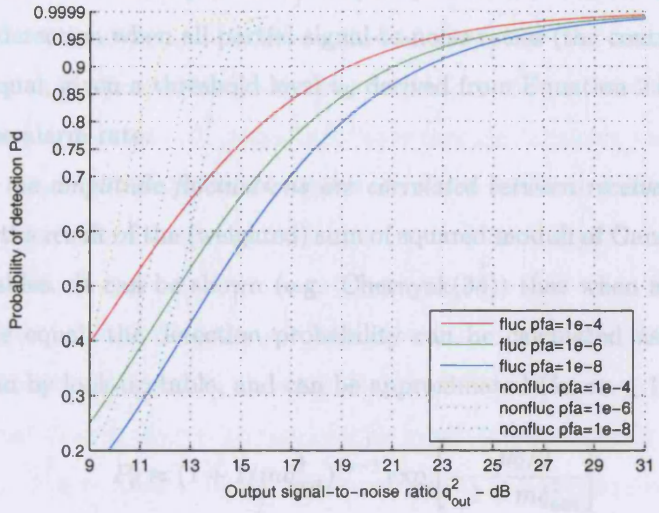

Figure 2-7: Probability of detection for algorithm L2

ratios from each receiver (or the double sum if the case of multiple transmitters). Hence, if the partial SNR at each receiver is the same, the effect of adding one further receiver to a m receiver multistatic system is to increase q^2_{out} by $10\log[(m+1)/m]$ dB, with the resultant improvement in probability of detection shown in Figure 2-7. It is clear therefore that the benefit of expanding the system is greatest when m (or n) is small. At very low signal-to-noise ratios, it can be seen that fluctuating signals actually improve the probability of detection compared to the fixed signals. This is because occasionally the instantaneous signal-to-noise ratio caused by the fluctuations is large compared to the mean, and in those cases the target is detected, whereas in the fixed case the SNR is constantly low. However, where high detection probabilities are required, fluctuating signals result in considerable loss of performance as the spatially correlated fluctuations cause low instantaneous signal-to-noise ratios at each receiver *simultaneously* with non-negligible probability, resulting in deep fading of the SNR of the algorithm output variable L_2.

We now consider detector L_3, which is optimal for the case of completely uncorrelated Gaussian complex fluctuations between receivers, and also (with small weighting adjustment) for the case where all complex amplitudes are unknown or have probability density functions that cannot be determined. *If the signal amplitude fluctuations are indeed uncorrelated* (phase is irrelevant due to the non-coherent summing), the output of the detector is the result of the (weighted) sum of squared moduli of mutually independent Gaussian

variables, as **G** involves linear procedures only. Equation 2.65 can be used to calculate the probability of detection when all partial signal-to-noise ratios (the contributions from each receiver) are equal, given a threshold level u_0 derived from Equation 2.63 by look-up table for a given false alarm rate.

If however the amplitude fluctuations are correlated between receivers[21], the output of the detector is the result of the (weighted) sum of squared moduli of Gaussian *but not jointly Gaussian* variables. It can be shown (e.g. Chernyak(34)) that when all partial signal-to-noise ratios are equal, the detection probability can be calculated using the incomplete gamma function by look-up table, and can be approximated (for $m \leq 10$) by:

$$P_d \approx (1 + 1/m\tilde{q}_{\text{out}}^2)^{m-1} \exp\left[-\frac{u_0/2}{1 + m\tilde{q}_{\text{out}}^2}\right] \tag{2.84}$$

where m is the number of receivers.

Figure 2-8[22] shows probability of detection as a function of the partial signal-to-noise ratio for detector L_3, for $m = 1$ and $m = 10$ receivers, in the cases of both correlated and uncorrelated amplitude fluctuations given a fixed probability of false alarm of 10^{-6}.

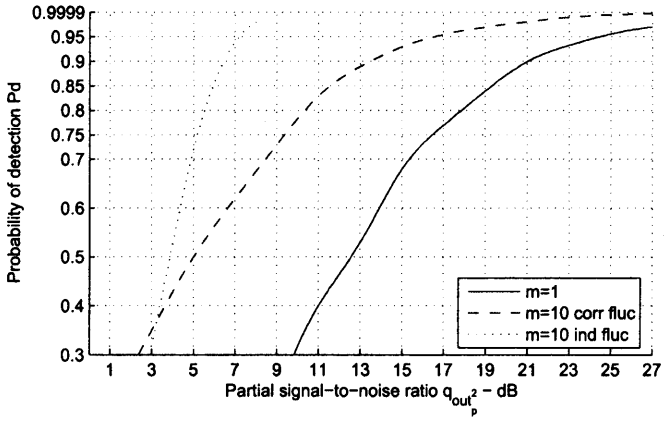

Figure 2-8: Probability of detection for algorithm L3 at $p_{fa} = 10^{-6}$

It is evident that, where fluctuations are in fact correlated between receivers, the *power gain* (defined as the allowable reduction in partial signal-to-noise ratio when adding additional receivers in order to maintain the same detection probability) is largely independent

[21] This is a situation for which this detector is not optimal, but it is informative to compare its performance in this way.

[22] After Chernyak(34)

of the probability of detection[23]. This is similar to detector L_2 where the power gain is calculated simply from the sum of partial signal-to-noise ratios (and so is also independent of probability of detection), although the power gain for the incoherent detector is not so strong. However, in the case of mutually independent fluctuations, the power gain is far greater at high detection probabilities. In all cases except for very low probability of detection, independent fluctuations result in improved detection performance compared to correlated fluctuations.

In order to compare detectors L_2 and L_3, let us choose typical radar parameters consistent with the models derived. Let $P_d = 0.9$, $P_{fa} = 10^{-6}$ (as above) and the signal-to-noise ratio of the signal at each of $m = 10$ receivers be equal. Then, from Figures 2-7 and 2-8, it can be seen that it is necessary for the output of the coherent algorithm L_2 to have a *total* SNR of 13 dB (a well-known monostatic result) when signal parameters are fixed, and a total mean value of 21 dB when signals are fluctuating (with complete mutual correlation). Given Equation 2.76 and a system comprising ten receivers, this equates to the necessity for *partial* signal-to-noise ratios of 3 dB and 11 dB respectively at each receiver. In the case of the incoherent detector L_3, it is necessary for the *partial* SNR at each receiver to be 13 dB where signals are fluctuating with complete mutual correlation, and 6.5 dB where fluctuations are independent. These figures for *the partial SNR required at each receiver in order to meet the stated detection criteria* are used here as *a measure of relative performance.* In essence, the lower the signal-to-noise ratio necessary, the higher the effective sensitivity of the system.

Firstly, it can be noted that in the situation common to both detectors (that of spatially correlated random fluctuations), the coherent detector L_2 outperforms L_3 by 2 dB. This improvement is consistent and often greater where alternative radar parameters (P_d, P_{fa}, m, etc) are chosen. Therefore, for any situation where fluctuations are mutually correlated, it is preferable to use coherent detection.

In the case of mutually independent fluctuations, the performance of detector L_3 by this criterion is 6.5 dB better compared to the case of correlated fluctuations. The power gain from a system of ten receivers compared to the monostatic case is some 14.5 dB where fluctuations are independent, which is 4.5 dB greater than that for the coherent detector

[23]In other words, the $m = 1$ and $m = 10$ 'corr fluc' lines are approximately the same distance apart in terms of SNR for $P_d < 0.95$.

with correlated fluctuations. Therefore, it is shown that for the situation where fluctuations are present and the required probability of detection is high, it is preferable (if possible) to arrange the system such that fluctuations are mutually independent and use the incoherent detector. This does not relate to the choice of detection algorithm, but instead to the choice of topology. In order to achieve independent fluctuations, it may be necessary to separate receivers by large distances, or use frequency diversity or other techniques. In cases where the available mean signal-to-noise ratio is low, arrangement of the radar such that fluctuations are mutually correlated provides the best performance. For example, at $P_d = 0.3$, a partial signal-to-noise ratio of 3 dB is required for independent fluctuations using detector L_3, but only 0 dB is required for correlated fluctuations using detector L_2.

The apparent performance improvement caused by detecting independently fluctuating signals when high detection probability is required is caused by 'smoothing' of instantaneous signal-to-noise ratio deviations. It is evident in this case that the spatial diversity 'gain' of L_3 outweighs the coherent processing gain of detector L_2. This is not to suggest that detector L_3 is always optimal - on the contrary, when fluctuations are indeed correlated at each receiver (due to closely spaced receivers, simple targets, lack of multipath or other reasons), the detector L_2 is clearly optimal due to its coherent processing gains. In addition when signal-to-noise ratios are low, the non-negligible probability of correlated instantaneous peaks in SNR in the coherent detector means it performs better than the smoothed but consistently low SNR in the incoherent detector.

2.5.3 Implementation

Here, consideration is given to how the multistatic detection algorithms described above can be implemented in a practical system. The two main classes of detector, which are known in the most general (multiple transmitter) case as L_{2m} and L_{3m}, both share a common signal processing core (G_{ik} in Equation 2.75 and 2.77). The 'filter' systems in each case consist of matched filter kernels that are specific to the signal at a particular receiver (or a bank of matched filters for each possible signal where multiple transmitters are used). Therefore it is possible to decentralise the total signal processing burden, and perform this stage of the processing at each local receiver. Then the coherent output data should be transferred to a centralised fusion processor, which performs the necessary time and phase shifting, weighting and summation for each 'hypothesised' target location (based on calculation of

the expected times-of-arrival t_{sik} in Equation 2.46 from the multistatic geometry), and finally the threshold detection of the combined signal L_x. It is also necessary for the radar to estimate the received signal energy and its own noise power. For experimental purposes it is likely that the nature of fluctuations will not be known a-priori (although they may be predicted), however it will clearly be possible to implement both algorithms concurrently, and compare their performance directly.

2.5.4 Summary

In this section, the derivations of some optimal detectors for coherent multistatic radar have been presented in a form suitable for implementation into the prototype system, and their performance analysed. It was shown how the typical combination of a matched filter and thresholder in the monostatic case could be developed to combine multistatic signals at the 'raw data' level and how, in certain circumstances, the optimal detector is analogous to the beamforming receiver of a conventional array antenna. The structure of the detection algorithms was realised by application of the generalised likelihood ratio test to specific models for the system. The general form of these 'filter' systems is based on a matched filter kernel for the signal at each receiver, the output of which is processed by phase and time equalisation, weighting, and summation. When multistatic systems comprise multiple transmitters, each matched filter in the detector is replaced by a bank of similar filters matched to the expected signal from each transmitter. The main differences between detectors are the calculation of weighting functions, and the position and type of envelope detection.

It was shown that, for fluctuating signals where the signal-to-noise ratio is high (and so the expected probability of detection is high), greater performance can be achieved by arranging the radar system so that these fluctuations are mutually independent at each receiver. In this case, particularly where the number of receivers is high, the average total energy will never exhibit deep fading. This is consistent with the conclusions drawn from (36), which uses a slightly different approach to determine the comparative performance of such a radar compared to a conventional phased array. The fluctuations may be caused by target scintillations, the propagation medium or multipath fading. It should be noted that these calculations assume Gaussian distributions for the complex amplitude fluctuations. In other cases, for example the spatial equivalent of Swerling case 4 (which is used to model

a fluctuating target with a dominant scattering point), it is known that the power gain resulting from non-coherent multistatic detection is considerably reduced. On the other hand, power gain from coherent integration is always constant.

Systems with multiple ($n > 1$) transmitters that operate under this assumption of independent fluctuations have recently been referred to in some preliminary literature as *MIMO radars*(36), due to certain similarities with Multiple-In Multiple-Out (MIMO) wireless communications. However, unlike the radar systems proposed so far, MIMO wireless communications does not usually require 'designed-in' discrimination of transmitted waveforms (e.g. from the use of orthogonal codes), as each transmitter-receiver path can be resolved by estimation of the channel matrix.

The conclusions drawn from this analysis are consistent with the results obtained from the MIT Lincoln Laboratory experiments(38) (see Section 1.5.3). There, it was demonstrated that coherent detection consistently outperformed incoherent processing, even when 'complex' targets were observed. However, the test set-up involves antennas spaced approximately ten metres apart observing targets some seven miles away, so the effective bistatic angle is very small, and strong correlation of fluctuations between receivers should be expected. It is proposed from the results in this section that, were the antennas to be more widely dispersed, incoherent detection would be expected to be optimal when fluctuating targets are observed.

The losses associated with *incoherent* data fusion, where all partial signal-to-noise ratios are identical, are the same as those related to incoherent temporal integration of multiple pulses, and are commonly cited in the literature (e.g. Blake(60)). Similarly, losses associated with higher-level data fusion techniques (e.g. 'plot-level' fusion) are equivalent to those for binomial temporal integration. However, in general the partial SNRs will be diverse in a multistatic radar, in which case it is expected the losses associated with post-detection fusion (i.e. not at the 'raw data' or 'signal' level) will be much greater. For example, in a simple binomial integrator, a plot from a receiver with very high signal-to-noise ratio is equally weighted with that from a very low SNR receiver, so the good statistical performance of the former receiver cannot be utilised.

In almost all cases, the addition of extra transmitters and/or receivers to the radar system results in *an increase in effective sensitivity compared to the monostatic case*, which is quantified in terms of improved signal-to-noise ratio when coherent processing is used, and

statistical performance improvement due to 'smoothing gain' when incoherent processing is used. The only exception is the addition of an extra receiver to a system performing incoherent detection that has a very low signal-to-noise ratio at its input[24]. Therefore, the use of multistatic topologies may provide considerable improvement in the detection performance of the radar.

2.6 Parameter Estimation

2.6.1 Introduction

In this section, consideration is given to extraction of useful information about a target from the received signals in a multistatic system. Estimation of target parameters is performed by estimating the parameters of the received signal(s), which in general amounts to measurement of arrival times, direction of arrival (DOA), doppler frequency and signal amplitude(46).

Here, we will focus on the determination of target location. Several methods are commonly used in monostatic and bistatic radar, including measurement of time-of-arrival (TOA), time-difference-of-arrival (TDOA) between two antenna elements, and a number of high resolution techniques using traditional array and sparse array antennas.

In the first instance, the process of detection described in Section 2.4 reveals the existence of a target as a function of time-of-arrivals t_{si}. Indeed, in a low signal-to-noise ratio situation, the detector is normally the optimal estimator of time-of-arrival(53). In the case of medium or high signal-to-noise ratio however, simple observation of the output of the detector can be replaced by direct measurement of signal parameters with increased accuracy. For example, the accuracy with which range in a monostatic radar can be measured from a 'peak' in the matched filter output corresponding to a target is dependent on the shape of the peak itself. Evidently a better estimate can be obtained if the peak is sharp than if it only just traverses the detection threshold, however measurement based on the detector binary output would have the same error in both cases. The 'radar uncertainty relation' for monostatic radar

[24]Coherent processing *always* yields performance improvement when extra nodes are added, even if the additional partial SNR is very low, provided all received signal powers can be accurately estimated and so the correct amplitude weighting applied. However, the addition of a low SNR receiver when using incoherent processing may degrade performance due to the minimal 'smoothing' effect being inadequate to offset the extra noise added to the system.

states that the accuracy with which time-of-arrival and doppler frequency may be measured simultaneously is proportional to the signal-to-noise ratio(46).

In monostatic systems, time-of-arrival measurements lead to the definition of target location at some point on a spherical iso-range surface. Resolution of this surface to a locus requires angle information. In the simplest case a single-element directional antenna is mechanically rotated during transmission and reception, and the output power of the matched filter observed. Then, the DOA accuracy is related to the antenna beamwidth. If instead a conventional array antenna is used, beamforming may be employed as described in Section 2.3.1 on transmit and/or receive. The resulting beam can be steered electronically by applying time delays or phase shifts to each element according to the array manifold vector. If the signal at each element is digitised individually, many angles can be simultaneously scanned by applying multiple steering vectors using digital signal processing - this is the well-known process of *digital beamforming.* The DOA accuracy is again related to the width of the resulting beam pattern, which in turn is related to the number of elements. In addition, several so-called *super-resolution* techniques have been invented for resolving the direction-of-arrival to greater accuracy within the beamwidth of such arrays, including maximum likelihood methods(61) and subspace algorithms such as MUSIC (MUltiple SIgnal Classification)(62). These are particularly effective at distinguishing multiple closely-spaced targets based on the DOA of their reflected signals.

In a conventional multistatic system comprising several non-cooperative monostatic radars where data fusion is performed at the plot level, target location can also be estimated in three-dimensions directly from multiple independent time-of-arrival measurements. This is known as the 'triangulation' or 'elliptic' method. The accuracy of this method is related to the time-of-arrival measurement error for each monostatic component and the multistatic geometry.

Evidently in a coherent multistatic system, each of these techniques is possible. First we consider the situation where a system of spatially coherent multistatic receivers acts as a very *sparse* or *distributed array.* In a conventional array antenna with uniformly spaced elements, grating lobes of the same height as the main lobe are formed if the distance between array elements is greater than $\lambda/2$ due to spatial aliasing, which cause ambiguities in the estimation of direction of arrival(63). These grating lobes can be reduced by the use of non-uniformly spaced elements(64), and are generally not evident at all in widely distributed,

randomly spaced arrays. However, sparse arrays suffer from high sidelobe levels compared to dense arrays and a wider main beamwidth(65), although it has been shown that ultra-wideband sparse arrays may be constructed without these problems(66). Nevertheless, in the case where array elements are *very* widely spaced (as may generally be the case for a multistatic system), it was shown in Section 2.3.1 that the plane wave approximation does not hold as the origin of received signals may often be in the near field of the aperture of the *whole* array. Therefore the 'beamforming' process does not produce a directional beam in the traditional sense, but instead results in the focussing of the distributed array system at some 'probed' point in space. This concept has been termed 'nearfield spot-beamforming' by Flaig(67). In this case the effective antenna pattern over the region of interest will be complex and highly dependent on topology and the number and directivity of the elements(68). It was shown in Section 2.4.2 that in fact the previously derived algorithms L_1 and L_2 perform this coherent focussing of the receiver system during the detection process. In general, sparse arrays can allow improved direction-of-arrival estimation with fewer sensors. It has been shown that the super-resolution methods such as MUSIC have superior performance with such antennas(69), and some studies have considered their adaptation for the near-field case(70), although there are no known studies on their suitability for widely distributed arrays with irregular topology, and further consideration of such techniques is beyond the scope of this thesis.

Both the 'beamforming' and super-resolution techniques rely on spatial correlation of the received signals, as well as coherency of the radar system itself. Simulations of the ability of the coherent detector to perform native target location estimation are presented in Section 3.3. It is apparent that the optimal method of estimation may be dependent on the topology of the multistatic system. In the next section, a method is considered that can be used in systems of arbitrary spatial coherency, and for which the accuracy of estimation can be simply defined.

2.6.2 Time-of-Arrival Location Estimator

Here, a method of target location estimation is presented that is based only on measurements of signal time-of-arrival. Several works have considered the use of this 'elliptic' method for non-cooperative multistatic systems. It was shown by Chengyou et al(71) that the estimation accuracy, expressed in terms of the *Geometric Dilution of Precision* (GDOP -

the ratio of the rms target location error in three dimensions to the rms ranging error) is dependent on the topology and the target location. In the case where more than three times-of-arrival are available, the equation system for determining the target location is overdetermined. If these equations are expressed in matrix form, one method of reconciling the estimates is to find the matrix pseudo-inverse, which calculates the least squares estimate based on all of the available data(72).

In the method presented here, which is derived from Chernyak(73), estimation is performed not from discrete time of arrival measurements (with associated errors), but instead from the combined processing of the 'raw data' signals from *all* bistatic pairs in the system in order to improve the estimation accuracy. For simplicity the problem is considered in two dimensions (i.e. estimation of target location co-ordinates on a 2d plane), although can easily be extended to the three-dimensional case.

Let us consider a multistatic system comprising a single transmitter and m receivers. Two arbitrary, independent and error-free measurements of time-of-arrival t_{si} define the target location[25] perfectly; thus the remaining $m-2$ values are functionally related to these two measurements, provided the geometry of the system is known. Therefore, the optimal location estimator on this basis calculates the optimal estimates for these two time-of-arrival values. Signals from the 'redundant' receivers are used to improve the accuracy of measurement of these two values. Conversion of these estimates to a location co-ordinate is simply performed by appealing to the geometry.

The likelihood ratio test defined in Equation 2.21 can be used in order to determine this optimal estimate. The target location is defined completely by the times of arrival, which are one of the signal parameters in vector $\mathbf{\Theta}$. The likelihood ratio test is formed from the ratio of the probability density functions for the received signal vector given the two possible hypotheses (Equation 2.12). Then, the probability density function for hypothesis H_1 given by $p_1(\mathbf{X}, \mathbf{\Theta})$, considered as a function of $\mathbf{\Theta}$, is the likelihood function for $\mathbf{X}$(52). This likelihood function quantifies the probability that a hypothesis for $\mathbf{\Theta}$ is correct given the data $\mathbf{X}$. Therefore, finding the maximum value of the likelihood ratio amounts to finding the maximum likelihood (ML) estimate for $\mathbf{\Theta}$. It can be shown that, given conditions that often

[25]Strictly an additional measurement is required to resolve the ambiguity between two intersecting points, formed from two-dimensional cuts through the iso-range spherical (receiver colocated with transmitter, i.e. monostatic) or prolate spheroid (bistatic) surfaces corresponding to each receiver. However often one point can be discarded due to its location or by using directional antennas.

arise in practice, the ML estimator is unbiased and as the sample size increases, it approaches the theoretical minimum variance estimate. Therefore the maximum likelihood estimate is an efficient estimator, and is used widely in radar parameter estimation theory(74).

Here, the vector $\mathbf{\Theta}$ contains m useful parameters (the times of arrival $t_{s1}, .., t_{sm}$) and $2m$ non-useful parameters $a_{s1}, ..., a_{sm}$ and $\varphi_{s1}, ..., \varphi_{sm}$ (doppler frequencies are ignored). Using Equation 2.43 for the non-useful parameters, and Equation 2.46, the likelihood ratio can be written in terms of the two times-of-arrivals to be estimated as follows:

$$\tilde{\Lambda} = \mathbf{a}_s^t \mathrm{Re}[\tilde{\mathbf{E}}^*(\varphi_s)\mathbf{G}(t_{s1}, t_{s2}, h_i(t_{s1}, t_{s2}))] - T_s \mathbf{a}_s^t \mathbf{N}^{-1} \mathbf{a}_s] \tag{2.85}$$

where $h_i(t_{s1}, t_{s2})$ is the geometric function calculating the remaining time-of-arrival parameters t_{si} $(3 \leq i \leq m)$ from the chosen two values t_{s1} and t_{s2}, and it is assumed the noise and interferences in the received signal vector are mutually uncorrelated.

Then, values of unknown non-useful parameters in $\mathbf{\Theta}$ should be replaced with their maximum likelihood estimates. When complex fluctuations are mutually correlated, calculation and substitution of maximum likelihood estimates for φ_{s1} and a_{s1} yields:

$$\tilde{\Lambda} = \left|\mathbf{A}^{\mathrm{t}} \mathbf{E}^* \mathbf{G}(t_{s1}, t_{s2}, h_i(t_{s1}, t_{s2}))\right| \rightarrow \max(t_{s1}, t_{s2}) \tag{2.86}$$

which can be written in scalar form as:

$$\tilde{\Lambda} = \left| \sum_{i=1}^{2} A_{i1} \exp(-j\Delta\varphi_{si1}) G_i(t_{si}) + \sum_{i=3}^{m} A_{i1} \exp(-j\Delta\varphi_{si1}) G_i[h_i(t_{s1}, t_{s2})] \right| \tag{2.87}$$

If instead complex fluctuations are mutually independent, maximum likelihood estimates for all φ_{si} and a_{si} produce (in scalar form):

$$\tilde{\Lambda} = \sum_{i=1}^{2} N_i |G_i(t_{si})|^2 + \sum_{i=3}^{m} N_i |G_i[h_i(t_{s1}, t_{s2})]|^2 \tag{2.88}$$

It can be seen that these expressions for location estimators have an identical structure to the detection algorithms L_2 and L_4 in Equations 2.53 and 2.72 respectively. This is not surprising as these detectors were also derived from ML estimates for the case where the probability density functions of the 'fluctuating' parameters was unknown.

The scalar equations are split into two parts, such that the first sum is dependent on

the two times-of-arrival to be estimated, and the second sum is dependent on the remaining values calculated from the geometry by $h_i(t_{s1}, t_{s2})$. The optimal estimates for t_{s1} and t_{s2}, which together define the target location unambiguously, can be found by finding their values at which $\tilde{\Lambda}$ is maximum. If several targets are present, there will be several such maxima. Implementation of the algorithm is simplified by the small number of parameters to be estimated, so a 'grid search' could be used in the first instance to find approximate locations of the peaks, followed by gradient searching around those regions. Alternatively, approximations for two arbitrary times of arrival may be made by finding pairs of peaks in the one-dimensional 'partial' outputs of the matched filter components for individual bistatic pairs, which can then be used as initial estimates and searching performed in the same way. In each case, the remaining time-of-arrival values are calculated from the hypothesised estimates using $h_i(t_{s1}, t_{s2})$. Having found the values at which $\tilde{\Lambda}$ is maximum, these estimates are converted to the maximum likelihood target location from the geometry.

In essence, these derivations show that optimal location estimate based on time-of-arrival measurements only, given a background of white uncorrelated noise and interference, can be found by the evaluation of expressions almost identical to the optimal detectors. However, whereas the detector compares the algorithm output value against some threshold, the location estimator searches for the point(s) at which the output is maximum. The location estimator is expressed as a function of only the two fundamental time-of-arrival parameters, so that 'redundant' information from receivers $3 \leq i \leq m$ is used to improve the estimation of the *true* values of t_{s1} and t_{s2} that define the target location. It can be seen that, if $m \leq 2$, only the first sum remains in Equations 2.86 and 2.88, in which case the estimator resolves to a one-dimensional algorithm for each i:

$$\tilde{\Lambda} = |G_i(t_{si})| \rightarrow \max(t_{si}) \tag{2.89}$$

which is identical to the monostatic and non-cooperative multistatic estimators discussed earlier.

Having determined an expression for the maximum likelihood estimator for target location based on time-of-arrival, an analytic expression for the accuracy of the resulting estimate is required so that the improvement due to the use of a multistatic system can be quantified. It can be shown that in a monostatic radar, the accuracy of radar range mea-

surement (which is equivalent to time-of-arrival measurement) is a function of the signal-to-noise ratio and the waveform of the signal used, specifically its mean-square (or 'effective') bandwidth(46).

Given an unbiased estimator such as the ML estimate for a set of unknown parameters $\boldsymbol{\Theta}$, the Cramér-Rao bound gives the lowest theoretical bounds for the variances of the output of the estimator. The general form for an estimator vector $\mathbf{T}(\mathbf{x})$ using random process $\mathbf{x}$ with joint probability density $f(\mathbf{x};\boldsymbol{\Theta})$ to estimate parameters $\boldsymbol{\Theta}$ is given by(52):

$$\mathrm{Cov}\{\mathbf{T}(\mathbf{x})\} \geq J^{-1}(\boldsymbol{\Theta}) \tag{2.90}$$

where $\mathbf{J}(\boldsymbol{\Theta})$ is the Fisher information matrix, describing information contained in the data set about parameter vector $\boldsymbol{\Theta}$. Elements of the matrix are given by:

$$J_{np} = \mathrm{E}\left[\frac{\partial \log f(\mathbf{x};\boldsymbol{\Theta})}{\partial \Theta_n}\frac{\partial \log f(\mathbf{x};\boldsymbol{\Theta})}{\partial \Theta_p}\right] \tag{2.91}$$

This technique is normally used where all unknown parameters related to a likelihood function are to be estimated. For a multistatic radar, the total number of parameters may be very large, and inversion of the matrix in Equation 2.90 may be difficult. A technique is described in (73), and presented in Appendix A, for deriving a Fisher information matrix that takes into account all parameters (including non-useful 'stray' parameters) of vector $\boldsymbol{\Theta}$, but its dimension is determined by the number of useful parameters only. The resulting equation for the Fisher information matrix can be written:

$$\tilde{J}_{np}^{(t_s)} = 2E_i\delta_{np}\overline{\Delta\omega_n^2}/N_i + \sum_{i=3}^{m}\frac{2E_i\overline{\Delta\omega_n^2}}{N_i}\frac{\partial h_i(t_{s1},t_{s2})}{\partial t_{sn}}\frac{\partial h_i(t_{s1},t_{s2})}{\partial t_{sp}} \tag{2.92}$$

where $\overline{\Delta\omega_n^2}$ is the mean-square (effective) bandwidth of the general spectrum.

Equation 2.92 shows that, if the number of receivers $m \leq 2$, $\mathbf{J}^{(t_s)}$ is diagonal, and its inversion realises the Cramér-Rao lower-bound variance as:

$$\sigma^2(\hat{t}_{sn}) = \frac{N_i}{2E_i\overline{\Delta\omega_n^2}} \tag{2.93}$$

Hence the errors in estimating the times of arrival are identical to the individual monostatic or bistatic cases, being inversely proportional to the signal-to-noise ratios and mean-square

bandwidth.

However, if $m > 2$, measurements from the additional receivers increase the Fisher information and hence reduce the measurement error of the time-of-arrivals t_{s1} and t_{s2}. The resulting lower-bounds can be determined from the Fisher information matrix, elements of which are dependent on the partial derivatives of the geometric equations $h_i(t_{s1}, t_{s2})$, and hence the geometry, with respect to particular t_{si}. The resulting Cramér-Rao bound for location error can then be determined from the errors for t_{s1} and t_{s2} and the bistatic geometry from which they were measured. It is clear that in the extreme (singular) case where a third TOA measurement is taken from an identical topology to one of the fundamental values (e.g. $h_3(t_{s1}, t_{s2}) = t_{s1}$), $\mathbf{J}^{(t_s)}$ remains diagonal, and the additional receiver acts only to increase the effective signal-to-noise ratio described in Equation 2.93. Evidently the Cramér-Rao bound for the two fundamental TOAs can be more efficiently reduced if measurements are taken using a diverse topology where all partial derivatives in Equation 2.92 are non-zero, as might be expected intuitively.

2.7 Conclusions

In this chapter, the theoretical basis of target detection and parameter estimation has been considered in order to inform the design, signal processing and experimental campaign for the prototype radar. An analysis of the derivation of noise sources in a multistatic system allowed the conditional use of assumptions in development of optimal algorithms. The general likelihood ratio was derived, and detection algorithms were presented for deterministic and fluctuating signals with particular spatial mutual correlation. A discussion of the nature of fluctuating and fading signals coupled with analysis of the algorithms showed that in some circumstances it is beneficial to ensure mutually independent fluctuations and use incoherent detection. The relationship between the matched filter and the optimal detector kernels was described with a view to implementation in the prototype system. Finally, a method of optimal location vector estimation was presented using joint estimation of time-of-arrival parameters for multilateration, together with a theoretical analysis of its error bounds. It was shown that, in general, such a multistatic system can provide substantial increases in sensitivity and measurement accuracy, although the achievable performance is dependent on the topology, environment and choice of detection algorithms.

Chapter 3

Aspects of Multistatic Radar Characterisation and Performance

3.1 Introduction

This chapter considers some fundamental aspects of the characterisation and performance of a multistatic radar system. The results presented from this analysis mainly take the form of graphical models from numerical computer simulations. In Chapter 2, it was shown that the addition of transmitters and receivers to a system, combined with the use of the coherent multistatic detection algorithms described, results in an increase in sensitivity compared to the monostatic case. For fixed detection criteria, this corresponds to an increase in radar coverage capability. Therefore this section begins with an analysis of range and sensitivity in multistatic systems. The well-known 'radar equation' is extended to account for the total multistatic system sensitivity based on these detection algorithms, and coverage maps are presented for different topologies compared to the monostatic case. Then, an original multistatic form of the 'ambiguity function' is derived, again based on the optimal detection algorithms, which is used to analyse the response of the complete system to an arbitrary target with given location and velocity. This model allows theoretical determination of the 'instrument function' for the system, from which the resolution capability and measurement accuracy can be determined. A series of simulated results are presented that can be used as a benchmark for experiments with the prototype system.

3.2 Range and Coverage

3.2.1 Introduction

In this section the aim is to derive estimates for the coverage of a multistatic radar, which can be used to determine the specification of the prototype system and guide its topology. One of the defining characteristics of a monostatic radar system is its maximum range - that is, the maximum distance away from the radar set at which a given target can be detected. The definition of 'detection' normally becomes a statistical one, and here will be the requirement for a minimum probability of detection for a known target for a given false alarm rate (the Neyman-Pearson test). Other criteria are possible, for example based on the error variance of target parameter estimation.

In bistatic and multistatic radar, the distributed topology means that the coverage volume, which in the monostatic case is always spherical with radius given by the maximum

range (assuming isotropic antennas), has a shape that is dependent on the geometry. Here, the standard equations used for estimating range and coverage in monostatic and bistatic radar are reviewed, and typical plots produced by computer simulation of the resulting coverage. Then, with reference to the optimal detection algorithms for the prototype system developed in Chapter 2, a similar model is developed for the multistatic case.

3.2.2 Monostatic and Bistatic Range Equation

The widely-quoted monostatic *radar range equation* gives an indication of the performance of a specified radar system in terms of its fundamental parameters. It is derived as follows:

If a radar transmits a signal with output power at its terminals P_t using an ideal isotropic antenna, the power spreads with spherical symmetry, so the power flux at a range R from the antenna is given by:

$$\text{Power flux } = \frac{P_t}{4\pi R^2} \tag{3.1}$$

If instead the antenna has a directional gain G_t and is pointing towards a target, the power density at the target area (again at range R from the antenna) is:

$$\text{Power density } = \frac{P_t G_t}{4\pi R^2} \tag{3.2}$$

The energy may be intercepted by a target, in which case the proportion of incident power reflected back towards the radar is given by the radar cross section σ. Then the reflected power flux incident at the radar receiver antenna (colocated with the transmitter) is given by:

$$\text{Power flux at receiver antenna } = \frac{P_t G_t \sigma}{(4\pi R^2)^2} \tag{3.3}$$

The amount of power received by the antenna is determined by its *effective area* A_e, which is defined as(53):

$$A_e = \frac{G_r \lambda^2}{4\pi} \tag{3.4}$$

where G_r is the gain of the receiving antenna and λ is the wavelength of the received signal. Combining these equations and including a factor L to represent general system losses ($L \geq 1$) we obtain the received signal power P_r:

$$P_r = \frac{P_t G_t G_r \sigma \lambda^2}{(4\pi)^3 R^4 L} \tag{3.5}$$

It is convenient now to redefine the equation in terms of the signal-to-noise ratio *at the output of the matched filter*, which (it is shown in Appendix A) is given by the ratio E/N_0, where E is the signal *energy* and N_0 is the noise power spectral density. It was also shown that the probability of detection under the Neyman-Pearson criterion for non-fluctuating signals is determined completely by this signal-to-noise ratio (and can be proven via the likelihood ratio test by, for example, resolving detector L_1 in Equation 2.27 to the single receiver case where $m = 1$).

We assume for convenience that the filter is matched to a single uncompressed pulse of length μ, such that the received energy from that pulse is given by $E = P_r\mu$, and the nominal bandwidth of the matched filter is $B = 1/\mu$. Then, we assume that the noise at the input to the receiver is white Gaussian (thermal) noise with spectral density $N_0 = kT$, so we can write SNR $= E/N_0 = P_r/kTB$. Now the radar equation can be expressed in its traditional form(46) in terms of the maximum range R_{max} at which a specified SNR at the output of the matched filter will occur:

$$R_{max} = \left(\frac{P_t G_t G_r \sigma \lambda^2}{(4\pi)^3 kTB(\text{SNR})L} \right)^{1/4} \tag{3.6}$$

In the bistatic case, the transmitter and receiver are non-colocated as shown in Figure 1-2. The length of the distance vectors target-transmitter and target-receiver, are R_t and R_r respectively, and the equivalent bistatic radar equation, expressed in terms of signal-to-noise ratio, is given by:

$$\text{SNR} = \frac{P_t G_t G_r \sigma_{\text{bistatic}} \lambda^2}{(4\pi)^3 R_t^2 R_r^2 kTBL} \tag{3.7}$$

It is shown in Appendix B that for most real targets, the RCS σ is a function of many factors including look-angle, and the bistatic RCS σ_{bistatic} is not equal to the monostatic value. We can now define the bistatic radar coverage as being the region of space for which a target can be positioned (with a given $\sigma_{bistatic}$) so that the SNR at the output of the receiver will be at least a given threshold, calculated from the required detection probabilities.

Figure 3-1 shows intensity plots, generated using Matlab, of the signal-to-noise ratio calculated using Equations 3.6 and 3.7 for monostatic and bistatic radar respectively, given an isotropically reflecting target (with unity RCS). Calculations are limited to the two-dimensional *bistatic plane* (the surface passing through the locations of the transmitter, receiver and target) for simplicity. The radar parameters used are summarised in Table 3.1,

and are indicative of the specification for the prototype design described in Chapter 5.

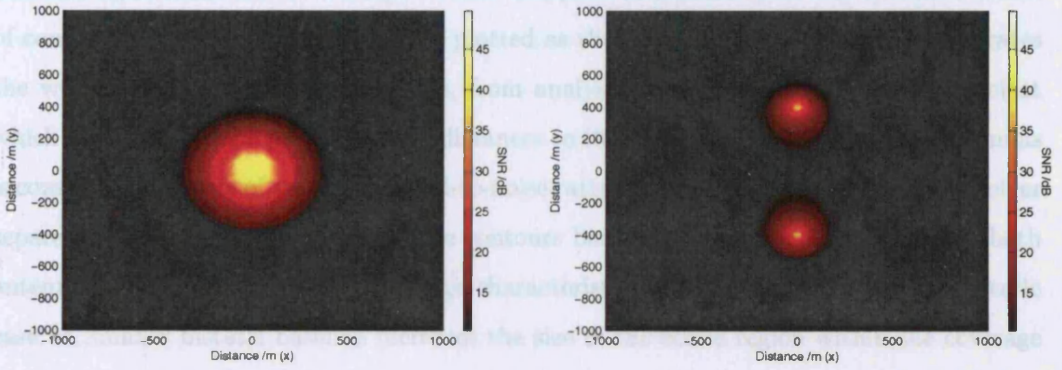

Figure 3-1: Coverage for monostatic and bistatic radar

The detection threshold has been set at 13 dB, which it is known provides the detection probability $P_d \approx 0.9$ for a false-alarm probability of 10^{-6} given a non-fluctuating signal. Regions coloured in black correspond to positions where the location of the target would result in a signal-to-noise ratio at the receiver below this threshold, and so are outside the coverage region. The coverage map in the monostatic case is circular (or spherical in three-dimensions), and geometrically is dependent only on the target range[1].

In the bistatic case, the transmitter and receiver in Figure 3-1 are positioned 800 m apart. This baselength is arbitrary, but is chosen to be approximately the maximum length that maintains contiguous coverage along the baseline for these parameters. It is clear that the shape of the coverage region has become elongated. In this case the coverage area in the bistatic plane (bounded by the region shown in the figures) is almost identical to the monostatic figure, although as the coverage volume approximates two adjacent spheres

[1]Strictly, the directional antenna gain $G > 1$ implies it is necessary to perform multiple observations over the entire 4π steradians using an electronically or mechanically steered antenna in order to achieve the coverage indicated.

Parameter	Value
Transmitter power (peak)	200 mW
Antenna gain	250 (24 dBi)
Wavelength	0.125 m (2.4 GHz carrier)
Temperature	290 K
Receiver bandwidth	50 MHz
Losses	1.2

Table 3.1: Radar parameters for models of radar coverage

with smaller radius compared to the monostatic case, coverage in the third dimension is reduced. This reduction in coverage volume is typical of bistatic systems(75). Iso-contours of constant signal-to-noise ratio can be plotted as shown in Figure 3-2. This demonstrates the well-known *ovals of Cassini* which, from analysis of Equation 3.7, define the loci at which the square of the product of the distances to the transmitting and receiving antennas is constant. Contours of very high signal-to-noise ratio surround the transmitter and receiver separately, however for lower values the contours become more circular, surrounding both antennas. In this *cosite* region, coverage characteristics become similar to the monostatic case. A smaller bistatic baseline increases the size of the cosite region within the coverage area.

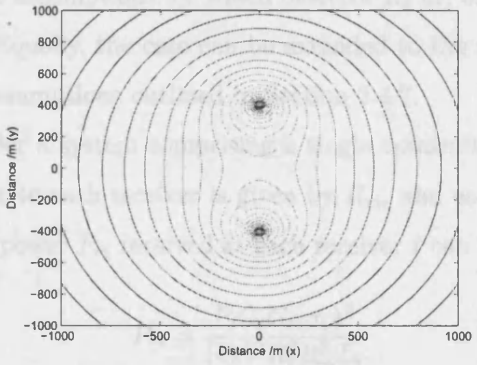

Figure 3-2: Iso-contours of signal-to-noise ratio for a bistatic radar

3.2.3 Multistatic Coverage

Here, a series of new expressions are derived for multistatic coverage based on the detection algorithms developed in Chapter 2. The coverage of a multistatic system is defined similarly to the bistatic case, except that now detection probabilities are considered for the entire system, which implies dependence on the chosen data fusion technique and detection criteria. It was shown in Section 2.5 that in the case of the coherent detection algorithm L_2, which is optimal where the complex signal amplitudes (whether fixed but unknown or fluctuating) are mutually correlated between receivers, the probability of detection is dependent only on the total signal-to-noise ratio at the output of the detector, which in turn is determined completely by the 'partial' signal-to-noise ratios at each receiver (Equation 2.58). Therefore, there is an unambiguous relationship between total SNR and the detection probabilities.

However, in the case of the incoherent algorithm L_3 that is optimal for independent mutual fluctuations in a multistatic radar of arbitrary spatial coherence, the performance increase is due only to 'smoothing' of the noise and fluctuating signals, so this simple relationship does not hold. Of course, other fusion methods are possible, such as decentralised algorithms based on plots from each receiver and various high-level logic-based fusion methodologies. In these cases coverage must be calculated directly from individual probabilities of detection and the chosen fusion criteria.

For the spatially coherent systems that are the focus of this work, it is reasonable to calculate coverage regions in a single transmitter, m receiver multistatic radar on the basis of the sum of partial signal-to-noise ratios, on the understanding that the exact form is strictly applicable only with the assumptions for which detector L_2 or, of course, the deterministic detector L_1, are valid. Equally, the case can be extended to the multiple transmitter case, taking account of the assumptions outlined in Section 2.4.7.

Firstly, let us consider a system comprising a single transmitter and m receivers. The distance from the target to each receiver is given by R_{ri}, and each receiver antenna has a gain of G_{ri}. The signal power P_{ri} received at each receiver i can then be written as:

$$P_{ri} = \frac{P_t G_t G_{ri} \sigma_i \lambda^2}{(4\pi)^3 R_t^2 R_{ri}^2 L_i} \tag{3.8}$$

where σ_i is the apparent RCS of the target at receiver i, and L_i represents the loss at that receiver. Equation 2.58 shows that the total signal-to-noise ratio at the output of L_2 is given by the sum of the partial SNRs for all i. These partial SNRs can be expressed at the output of each matched filter kernel (i.e. G_i in Equation 2.53) as:

$$\mathrm{SNR}_i = \frac{E_i}{N_0} = \frac{E_i}{\overline{kT}} = \frac{P_{ri}}{kTB} \tag{3.9}$$

where it is assumed the noise at the input of receiver i is thermal, and hence white, mutually uncorrelated and Gaussian. Then, the total SNR can be written as:

$$\mathrm{SNR}_{\mathrm{tot}} = \sum_{i=1}^{m} \mathrm{SNR}_i = \sum_{i=1}^{m} \frac{P_t G_t G_{ri} \sigma_i \lambda^2}{(4\pi)^3 R_t^2 R_{ri}^2 kTBL_i} \tag{3.10}$$

Now, let us consider a system comprising n transmitters and m receivers, where all transmitters operate coherently in order to 'phase' their signals at the hypothesised target

position. The distance from the target to the kth transmitter is R_{tk}, which produces an output power P_{tk} into an antenna with gain G_{tk}. The phasing of transmitted signals results in the total *field strength* (the square root of the power density) at the target location being equal to the sum of contributions from each transmitter, so we can write the total power density as:

$$\text{Power} = \left[\sum_{k=1}^{n} \sqrt{\frac{P_{tk}G_{tk}}{4\pi R_{tk}^2}}\right]^2 \tag{3.11}$$

Then, the received power P_{ri} at receiver i is given by:

$$P_{ri} = \left[\sum_{k=1}^{n} \sqrt{\frac{P_{tk}G_{tk}}{4\pi R_{tk}^2}}\right]^2 \frac{G_{ri}\sigma_i\lambda^2}{(4\pi)^2 R_{ri}^2 L_i} \tag{3.12}$$

and the resulting total SNR at the output of L_2 can be written as[2]:

$$\text{SNR}_{\text{tot}} = \sum_{i=1}^{m}\left[\sum_{k=1}^{n} \sqrt{\frac{P_{tk}G_{tk}}{4\pi R_{tk}^2}}\right]^2 \frac{G_{ri}\sigma_i\lambda^2}{(4\pi)^2 R_{ri}^2 N_0 B L_i} \tag{3.13}$$

If we now take the simplest case where $P_{tk} = P_t$, $G_{tk} = G_t$ and $R_{tk} = r_t$ for all k, then the SNR equation becomes:

$$\text{SNR} = \sum_{i=1}^{m} \frac{n^2 P_t G_t G_{ri}\sigma_i\lambda^2}{(4\pi)^3 R_t^2 R_{ri}^2 N_0 B L_i} \tag{3.14}$$

A comparison with Equation 3.10 shows that in this case the SNR is increased by n^2 compared to an equivalent multistatic system with a single transmitter and m receivers.

Lastly, we consider again a system comprising n transmitters and m receivers, but now where the transmitted signals are not phased, and instead can be discriminated at each receiver. Then, the received power P_{rik} at receiver i *as a result of echo signal received that originated from transmitter* k is given by:

$$P_{rik} = \frac{P_{tk}G_{ri}G_{tk}\sigma_{ik}\lambda_k^2}{(4\pi)^3 R_{tk}^2 R_{ri}^2 L_{ik}} \tag{3.15}$$

where σ_{ik} is the apparent RCS pertaining to the bistatic pair geometry involving transmitter k and receiver i. L_{ik} represents the total losses associated with that part of the multistatic

[2]The substitution $N_0 = kT$ has been made to avoid confusion between the transmitter index k and the Boltzmann constant.

system. Then, Equation 2.58 shows that the total signal-to-noise ratio at the output of L_2 is given by the sum of SNR_{ik} over all i and k:

$$SNR_{tot} = \sum_{k=1}^{n} \sum_{i=1}^{m} \frac{P_{tk} G_{tk} G_{ri} \sigma_{ik} \lambda_k^2}{(4\pi)^3 R_{tk}^2 R_{ri}^2 N_0 B_k L_{ik}} \tag{3.16}$$

where B_k is the bandwidth of the matched filter for the kth transmitted waveform. This equation is similar to that presented by Hume and Baker(76) for an idealised coherent netted radar. If we take the simple case where all transmitters and receivers are identical apart for the waveforms transmitted in each case, which have identical carrier frequencies but for which the set of matched filters is orthogonal, then Equation 3.16 simplifies to:

$$SNR_{tot} = \frac{P_t G^2 \sigma \lambda^2}{(4\pi)^3 N_0 B L} \sum_{i=1}^{n} \sum_{k=1}^{m} \frac{1}{R_{tk}^2 R_{ri}^2} \tag{3.17}$$

The three results in Equations 3.10, 3.13 and 3.16 can be used to realise the coverage characteristics of a multistatic radar in a given topology for each mode of operation. It is evident that the 'phasing' method may provide by far the greatest signal-to-noise ratio, although it is noted that it can only be realised at the point(s) in space where the signals from all transmitters sum constructively. Clearly the power density in other regions is highly dependent on the transmitter topology, and is not considered further in this discussion.

Figures 3-3 and 3-4 demonstrates the effect on coverage of adding two additional spatially separated receivers to the bistatic system based on Equation 3.10. Identical detection criteria are used as for the monostatic and bistatic cases. In Figure 3-3, the extreme case is presented where the transmitter and all receivers are colocated, resulting in 19.1% coverage of the two-dimensional plane shown (compared to 11.1% in Figure 3-1 for the monostatic case). In Figure 3-4, the single transmitter is positioned in the centre of the image, and the three receivers placed with baselengths of (a) 600 m and (b) 750 m. The 600 m separation results in increased coverage of 26%, but at 750 m this falls to 19% as the region over which there is substantial 'cooperation' between receivers is reduced. It is apparent that in all cases, the addition of receivers increases the total sensitivity of the system (and hence the coverage).

Now the effect of multiple transmitters is considered, based on Equation 3.16 where there is discrimination of each transmitted signal (e.g. by time, frequency or waveform diversity).

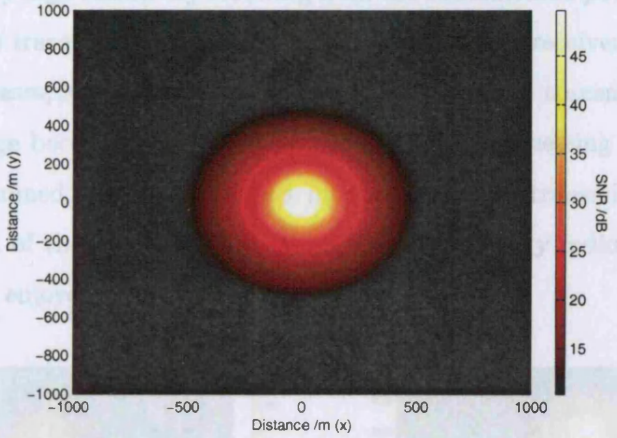

Figure 3-3: Coverage for a multistatic system comprising a single transmitter and three receivers that are all colocated

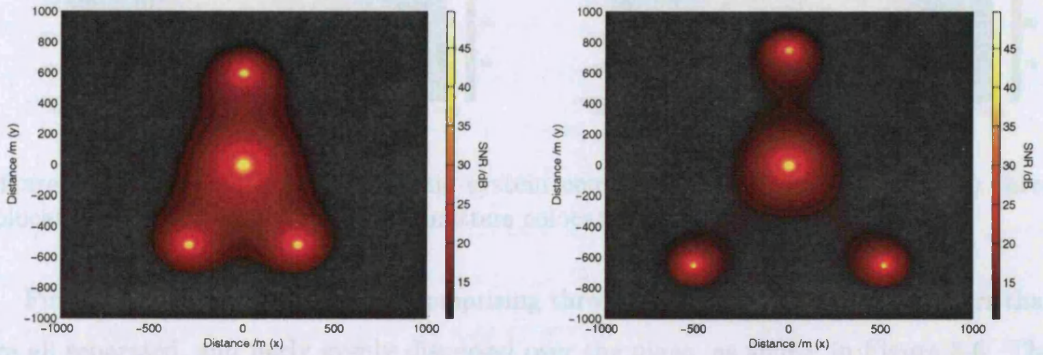

Figure 3-4: Coverage for a multistatic system comprising a (central) single transmitter and three spatially separated receivers with baselengths of (a) 600 m, (b) 750 m

Firstly we wish to determine the effect of 'linearising' the total transmitted power density by replacing a single transmitter with several of proportionally lower power. Small transmitters are generally cheaper and more lightweight, which may be a considerable advantage where mobility is required. Figure 3-5 shows the coverage region for such a system where the receivers are in the same locations as shown in Figure 3-4(a) (i.e. 600 m from the centre point). On the left hand side, all three transmitters (each with the same transmit power as previously) are placed centrally, in order to imitate a single transmitter that has three-times greater transmit power[3], resulting in 42.3% coverage in the plane shown. There is a

[3]A simple *power* summation of the contribution from each transmitter is performed, so it is assumed a method of discrimination such as frequency or code multiplexing is used.

central region of very high sensitivity resulting from the concentrated power density. On the right hand side, the transmitters are colocated with each of the receivers, resulting in 47% coverage. In both cases, it can be seen that the addition of extra transmitters affords large increases in coverage because the sensitivity acquired from processing every bistatic pair in the system is summed. There is a further increase when the transmitters are separated due to linearisation of the power density. However, the topology indicates that the same benefits will not be enjoyed in the third dimension.

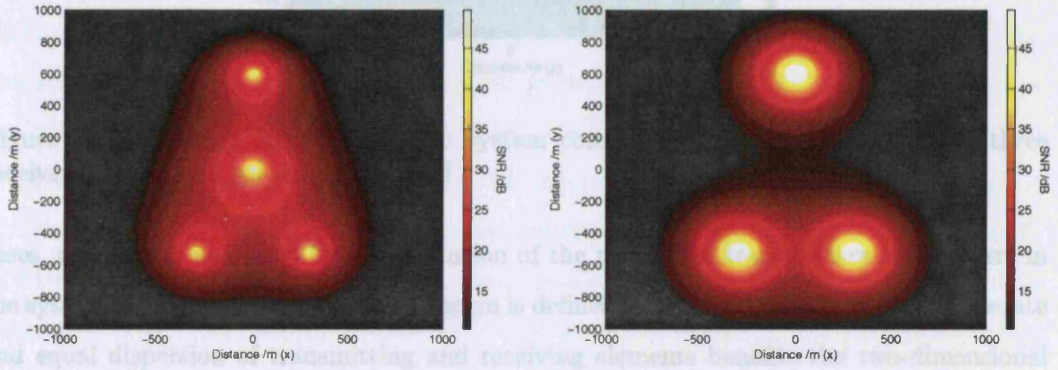

Figure 3-5: Coverage for a multistatic system comprising three receivers and (a) three colocated transmitters (b) three transmitters colocated with each receiver

Finally, a topology is considered comprising three transmitters and three receivers that are all separated, and fairly evenly dispersed over the plane, as shown in Figure 3-6. The resulting coverage is 52.6%, suggesting that complete dispersion provides the best coverage performance. There is of course a limit to gains from spatial separation - for example, very large distances between colocated transmitter-receiver pairs prevent each receiver from acquiring sensitivity resulting from co-operative signal reception, so the system would resolve to that of three independent monostatic radars.

3.2.4 Summary

In this section the radar range equation has been extrapolated as a model for predicting coverage in the prototype multistatic system. The definition of coverage is based on a threshold determined by the system probability of target detection for a given probability of false alarm. The multistatic radar equation developed in Equation 3.16 applies directly to the detection algorithm L_2 subject to the assumptions that define its optimality. In all

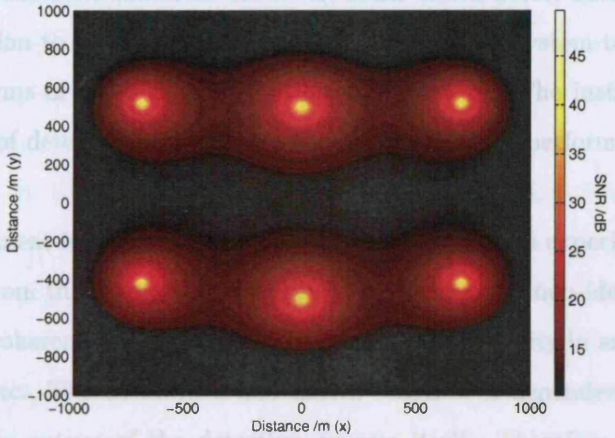

Figure 3-6: Coverage for a multistatic system comprising three transmitters and three receivers that are all spatially separated

cases, coverage is increased by augmentation of the number of transmitters *or* receivers in the system. The shape of the coverage region is defined by the topology; in general moderate and equal dispersion of transmitting and receiving elements benefits the two-dimensional coverage area. The coverage region in this plane also increases when a fixed transmission power is 'shared' between multiple transmitters, due to greater linearisation of the power density. This means it may be possible to make the system more transportable or mobile by using several smaller (and lighter) transmitters rather than one large one.

It is difficult to provide analytic solutions for the optimisation of topology in terms of coverage due to the many dependent factors including all radar parameters, geometry and detection criteria. In any case, frequently the aim is to ensure coverage of a particular region of space (which may not be contiguous), for which it is sufficient to use this model to ascertain detection range within the chosen bounds.

3.3 The Multistatic Ambiguity Function

3.3.1 Introduction

A primary aim for this thesis is the determination of the 'instrument function' for the prototype multistatic radar that is described in Chapter 5. This is formally defined as the response of an arbitrary system to a delta function input. This definition may be taken literally, in which case it refers to the output of the receiver only when the input is a

(suitably constrained) delta function. However, in an active device such as radar, we may expand the definition to refer to the response of the complete system to the presence of a *point target*, in terms of the output of its detection receiver. The instrument function is used as a method of determining the characteristics, and hence performance of the system for any stimulus.

The real instrument function of a radar must be obtained from experimental calibration, and may deviate from the theory due to noise, interferences and non-idealities in the radar hardware such as coherency or synchronisation errors, non-linearity in amplifiers and waveform generators, etc. The theoretical instrument function is dependent on certain radar parameters and the nature of the detection process itself. Therefore in the case of the prototype multistatic system, the response is a result of the joint processing of all received signals. In this section, the theoretical instrument function for the prototype system is developed based on the expressions for the detection algorithms developed in Chapter 2. This results in the derivation of a multistatic form of the *ambiguity function*, which it will be shown is an equivalent expression of the system response, and can be used as a method of determining the target resolution ability and range/doppler measurement accuracy.

Resolution is the ability of the radar to distinguish between multiple targets that are in close proximity in terms of location and/or velocity. In general, the further separated in range or radial velocity two targets are, the easier it will be to distinguish between them. *Measurement accuracy* is simply the ability of the radar to determine the true location and velocity parameters of a given target. It was shown in Section 2.6 that the optimal location estimator using time-of-arrival measurements is essentially the process of finding maximal values of the output of the detection algorithms. Therefore the ambiguity function can be used to describe the relative performance of this estimation method.

For a monostatic radar, it was shown in Section 2.3 that the optimal detection method by the Neyman-Pearson criterion for a wanted signal in a background of white Gaussian noise is a thresholded matched (or 'correlation') filter. If considered in real-time, its effect is to concentrate the entire energy of the received signal into an output peak at a time delay equal to the time-of-arrival t_p. The filter performs the cross-correlation of the expected (or 'reference') waveform with the received signal, which for a point target in the ideal case is simply its (scaled) time-shifted replica. This is equal to the autocorrelation or 'point-spread' function that has been shifted in time by t_p. Alternatively, using off-line

signal processing, the filter can be 'matched' to all possible times of arrival by time-shifting the reference waveform by the expected amount. Then, if the received signal arrives at this expected time, the output of the filter (at $t = 0$, or 'zero lag') will equal the centre peak of the autocorrelation function. If the received signal arrives at some other time, the filter response is given by the autocorrelation value at the corresponding offset. Therefore, ignoring doppler, the autocorrelation function of the transmitted signal, plotted against time (or equivalently, range), is the theoretical instrument function for a monostatic system.

The optimum normalised instrument function in range is a delta function, as this provides error-free measurement of the time-of-arrival (and hence range), as well as perfect resolution of multiple targets that may be arbitrarily close together. However, such an autocorrelation function corresponds to a signal with flat spectral density for all frequencies such as (infinite length) white noise, which is not practical as a radar signal. Therefore the matched filter will always exhibit some response away from the main peak. If the main peak is broad, this implies uncertainty of time-of-arrival measurement accuracy. Further, it limits resolution ability - for example, when the radar attempts to detect a 'weak' target positioned close to a stronger one, the presence of a broad peak from the strong target may mask the response from the weaker one.

The detection receiver output is usually plotted against radial velocity as well as range, so that targets that are close in range but separated in velocity can be easily distinguished. This measurement can be performed in real-time using a 'doppler bank' of filters, each of which is matched to one of a broad range of doppler frequencies. Then, the simultaneous output of each filter is plotted against the corresponding velocity. This is of course equivalent to finding the Fourier transform of the received signal. Alternatively, using off-line signal processing, the filter can be 'matched' to all possible values of velocity by frequency shifting the reference signal by the corresponding amount. Then, if the filter is perfectly matched to the doppler frequency of the received signal, the maximum response will be obtained. Clearly the optimum instrument function in terms of velocity is also a delta function.

The response of the detection receiver away from the ideal delta function (or 'thumbtack response') in both delay and doppler is known as ambiguity, and can be quantified by the 'ambiguity function', which we can now see is equivalent to the theoretical instrument function. This function is typically plotted in three-dimensions on the delay-doppler (or range-velocity) plane, which is known as the 'ambiguity diagram'.

The ambiguity function can be considered in two ways, which are completely equivalent. Firstly, we can define the centre point to correspond to the fixed parameters of a point target that result in a particular received signal. Then, the output of the filter consists of a matrix of values corresponding to each point on the range-velocity plane of the ambiguity diagram. These may be found in off-line signal processing by applying the filter to the received signal, matched to each point in turn. In that case, the ambiguity function shows the 'spread' of the filter response away from the main peak, which defines the measurement accuracy of the system for this target. In the monostatic case, the shape of the plot is independent of the 'matched' values at its centre, so the measurement accuracy is the same for a target with any parameters.

Alternatively, the centre point can be defined to be some fixed values at which the filter is matched, and we consider the output of the filter for just this single value. The range-velocity plane then corresponds to all possible target positions from which the input signal may be received. Ideally this filter, which is matched to the centre point, should only respond to an input signal corresponding to those matched values, in which case it is a perfect 'discriminator' for that {range,velocity} position. The ambiguity diagram shows the actual response of the matched filter to a received signal of equal amplitude with parameters that are offset by some amount from the matched point. As the shape of the function is independent of the matched values, it indicates the ability of the system to resolve any two targets that are offset by certain amounts in range and velocity.

For monostatic systems, the ambiguity function is dependent only on the waveform of the transmitted signal, and is usually plotted in terms of time delay and doppler shift. Hence, its analysis allows appropriate waveforms to be chosen dependent on the maximum ambiguity allowable in regions of the delay-doppler plane of interest. In fact, as we have seen, the useful parameters for measurement are not delay and doppler, but the range and speed of the target. In a monostatic system, these parameters are linearly related such that conversion is simply a change of variables (where the speed measured is the radial velocity). In bistatic and multistatic systems however, the relationship is not linear due to the geometry. In addition, the ambiguity function in the multistatic case is dependent on the detection algorithm used, which in general is no longer a simple matched filter.

Here the ambiguity function for a multistatic radar is derived, based on the optimal detection algorithms in Section 2.4. Having analysed the background to the monostatic

function, the problem is considered for a system with a single receiver and m receivers, where the signals from each are combined at the 'raw data' level. Then, the model is developed for the n transmitter case, where each may be transmitting a different waveform. It will be shown that in the bistatic and multistatic cases, the ambiguity function is dependent on the topology. Hence, simulations of the derived function are presented to demonstrate the theoretical instrument response of the system for a range of possible topologies, which can be used as a basis for future experiments with the prototype multistatic system.

3.3.2 Background to the Ambiguity Function

We consider a transmitted signal given by:

$$S_T(t) = \sqrt{2}\mathrm{Re}\left\{\sqrt{E}s_0(t)\exp(j\omega_0 t)\right\} \tag{3.18}$$

where E is the transmitted signal energy and, in common with Equations 2.22 and 2.23, $s_0(t)$ is the normalised complex waveform. The signal at the receiver reflected from a moving point target (ignoring propagation losses) is given by:

$$S_R(t) = \sqrt{2}\mathrm{Re}\left\{\sqrt{E}s_0(t - t_p(t))\exp[j\omega_0(t - t_p(t))]\right\} \tag{3.19}$$

where $t_p(t)$ is the propagation delay (which is a function of time due to the target movement). If however the target has constant velocity (non-manoeuvring) and the signal is narrowband, the approximations:

$$\begin{aligned} s_0(t - t_p(t)) &\approx s_0(t - t_a) \\ \exp[j\omega_0(t - t_p(t))] &\approx \exp[j(\omega_0 + \Omega_a)t] \end{aligned} \tag{3.20}$$

can be made where t_a is the value of $t_p(t)$ at the time the signal is received, and Ω_a is the resultant doppler shift. Then the total received signal takes the form:

$$X(t) = \sqrt{2}\mathrm{Re}\left\{\sqrt{E}s_0(t - t_a)\exp[j(\omega_0 + \Omega_a)t] + n(t)\right\} \tag{3.21}$$

where $n(t)$ is a complex white Gaussian process representing the noise background. The complex envelope of $X(t)$ can be found by demodulating the carrier to give:

$$\tilde{x}_a(t) = \sqrt{E} s_0(t - t_a) \exp[j\Omega_a t] + n(t) \tag{3.22}$$

It was shown in Equation 2.28 (for $m = 1$) that the optimal receiver under the Neyman-Pearson test is given by:

$$\Lambda = \int_{t_s}^{t_s+T} \tilde{x}(t) s_0^*(t - t_s) \exp(-j\Omega_s t) dt \tag{3.23}$$

This is the correlation filter that has been matched to time-delay t_s and doppler shift Ω_s. We can now determine the ambiguity function by finding the output of this filter for received signals with all possible values of time-of-arrival t_a and doppler shift Ω_a. This can be expressed (discarding noise terms) by:

$$\Lambda = \sqrt{E} \int_{t_s}^{t_s+T} s_0(t - t_a) s_0^*(t - t_s) \exp(-j(\Omega_s - \Omega_a)t) dt \tag{3.24}$$

Then, the ambiguity function can be defined as the magnitude of the response of the filter matched to a signal with normalised complex waveform $s_0(t)$, time-delay t_s and doppler shift Ω_s when the received signal has time-delay t_a and doppler shift Ω_a:

$$|\chi(t_a, \Omega_a)| = \left| \int_{-\infty}^{\infty} s_0(t - t_a) s_0^*(t - t_s) \exp[-j(\Omega_s - \Omega_a)t] dt \right| \tag{3.25}$$

We have expressed this function for a filter with fixed matched values in terms of its response to received signals with all possible delay offsets $t_s - t_a$ and doppler offsets $\Omega_s - \Omega_a$, which can be thought of as the resolution capability. It was stated that the relative response of the filter for delay and doppler offsets $\tau = t_s - t_a$ and $\Omega_d = \Omega_s - \Omega_a$ is independent of t_a and Ω_a, so the function may be expressed in the 'normalised' form:

$$|\chi(\tau, \Omega_d)| = \left| \int_{-\infty}^{\infty} s_0(t) s_0^*(t - \tau) \exp[-j\Omega_d t] dt \right| \tag{3.26}$$

The integral limits in both equations have been extended to infinity as $s_0(t)$ is zero outside the range $0..T$. In some literature, the modulus is replaced by the squared modulus.

It is clear from Equation 3.26 that at the matched delay-doppler point ($\tau = 0$, $\Omega_d = 0$),

the value of the ambiguity function is unity, given by the energy in the (normalised) complex waveform. At all other points, the output is given by the cross correlation of the waveform with its time and doppler shifted replica. In addition, it can be shown that:

$$\int_{-\infty}^{\infty}\int_{-\infty}^{\infty} |\chi(\tau,\Omega_d)|^2 d\tau d\Omega_d = 1 \tag{3.27}$$

Hence, the total volume under the ambiguity function 'surface' is fixed, and the ideal 'thumb-tack response' at $\tau = 0$, $\Omega_d = 0$ is unrealisable. Therefore it is necessary to design waveforms for particular purposes, where the ambiguity energy exists only in delay-doppler regions that are not of interest.

We also recall that the shape of the function applies equally to its measurement accuracy for a given fixed received signal. It can be shown that the second partial derivative of the ambiguity function with respect to delay is proportional to the rms bandwidth of the signal, and that with respect to doppler is proportional to the rms signal duration. These two quantities define the Cramér-Rao bounds for estimation performance when the two variables are unknown, as was also discussed in Section 2.6.

In the monostatic case, delay t_s and doppler frequency Ω are linearly related to the useful parameters range R and radial velocity v by the expressions:

$$\begin{aligned} R &= \tfrac{1}{2}ct_s \\ v &= -\dot{R} = \tfrac{1}{2}\Omega\lambda \end{aligned} \tag{3.28}$$

where λ is the carrier wavelength, and $\dot{R} = dR/dt$ is the *range rate.*

In the bistatic case, the topology (see Figure 1-2) shows that the delay t_s is proportional to the total range $R = R_t + R_r$, and the doppler frequency Ω is proportional to the *total* range rate $\dot{R}$, which itself is proportional to the target velocity component in the direction of the bistatic bisector. Therefore the traditional ambiguity function plots against delay and doppler are not conducive to obtaining insight into the real ambiguity in measurements of the wanted parameters range and velocity. An alternative 'bistatic ambiguity function' has been derived by Tsao et al(77), using the target-receiver range R_r and velocity component along the bistatic bisector V as independent variables in lieu of t_s and Ω. This non-linear correspondence between R_r and t_s, and similarly in doppler, means that the function is dependent on the actual range and velocity values to which the filter is matched, so an

equivalent 'normalised' form such as that of Equation 3.26 cannot be used in terms of these parameters. Therefore, the bistatic ambiguity function for a given waveform must be plotted for constant values of these matched parameters, transmitter and receiver locations, and the direction from some fixed point at which R_r is measured.

It is clear that in the multistatic case the number of dependent factors will increase considerably - encompassing the relative location of all the transmitting and receiving stations comprising the system, as well as method of overall detection. Nevertheless, it is expected that such a function will afford knowledge of the general nature of the ambiguity properties for particular situations, and therefore the instrument function of the prototype radar.

3.3.3 The Derivation of an Ambiguity Function for Multistatic Radar

Here, an original expression for the ambiguity function of a multistatic radar is derived. The bistatic ambiguity equation derived by Tsao et al expresses the geometric components trigonometrically in terms of the bistatic baseline distance L, target-receiver distance R_r and the direction of the target θ_R with reference to the 'North' axis with origin at the receiver and aligned perpendicularly to the baseline. For a multistatic system, such trigonometric manipulation becomes quite unwieldy, so instead a vectorial approach is adopted. Given such a function is dependent on the entire multistatic geometry, its expression in terms of an arbitrary co-ordinate system does little to harm the generality.

Consider the bistatic element of a multistatic system in Figure 3-7. The transmitter has location vector $\mathbf{T_1}$, the receiver $\mathbf{R_1}$ and the target $\mathbf{A}$ on Cartesian axes. Then lengths R_r and R_t are given by the magnitude of the distance vectors $|\mathbf{R_r}| = |\mathbf{A} - \mathbf{R_1}|$ and $|\mathbf{R_t}| = |\mathbf{A} - \mathbf{T_1}|$ respectively. The velocity of the target is given by vector $\mathbf{V}$.

Similar assumptions regarding the narrow-band signal and constant target velocity are made as in the monostatic case. Then, the propagation delay t_s from $\mathbf{T_1}$ to $\mathbf{R_1}$ is given by:

$$t_s = (|\mathbf{R_r}| + |\mathbf{R_t}|)/c \tag{3.29}$$

The range-rate of R_t due to $\mathbf{V}$ is given by:

$$\dot{R}_t = \frac{\mathbf{R_t} \bullet \mathbf{V}}{|\mathbf{R_t}|} \tag{3.30}$$

where $\bullet$ is the vector dot-product, and with $\dot{R}_r$ similarly defined, the doppler frequency

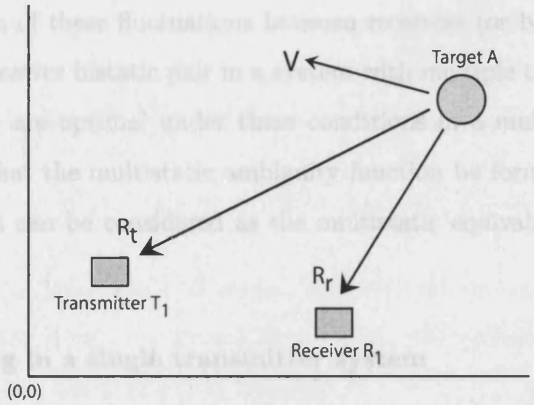

Figure 3-7: Vectorial representation of a bistatic element in a multistatic system

apparent at the receiver at $\mathbf{R_1}$ is given by:

$$\Omega = -\left(\frac{\mathbf{R_t}\bullet\mathbf{V}}{|\mathbf{R_t}|} + \frac{\mathbf{R_r}\bullet\mathbf{V}}{|\mathbf{R_r}|}\right)/\lambda \tag{3.31}$$

Therefore it is possible to calculate values of delay and doppler apparent at a receiver for any hypothesised situation. These can then be inserted into an equivalent form of Equation 3.25 (taking into account the multistatic detection algorithm used) in order to find the ambiguity function.

We shall plot the target-receiver range R_{r1} for the nominal 'reference' receiver at $\mathbf{R_1}$ in place of the 'delay' axis used for the monostatic function, defined along some angle-vector with origin at the receiver, as this is the most illustrative parameter and analogous to the well-known monostatic function. On the 'doppler' axis, we shall plot target speed v in a direction defined by an angle-vector with origin at the target *for a given value of* R_r. An alternative used by Tsao(77) is to plot against target speed in the direction of the bistatic bisector, as this is proportional to total range-rate. However, in a multistatic system with multiple receivers, the choice of bistatic angle is arbitrary and so meaningless, and secondly it has the unfortunate effect of making the velocity component direction dependent on the hypothesised target-receiver range.

Next, we come to the issue of formulating the ambiguity function for a multistatic radar. The spirit of the monostatic ambiguity function is that it should demonstrate the response of the optimal detection receiver given a deterministic or slowly fluctuating Gaussian signal in a background of white Gaussian noise. It is noted from Section 2.4.3 that, depending on

the mutual correlation of these fluctuations between receivers (or between signals relating to each transmitter-receiver bistatic pair in a system with multiple transmitters), detection algorithms L_2 and L_3 are optimal under these conditions in a multistatic radar. Therefore it is reasonable that the multistatic ambiguity function be formulated based on these two algorithms, which can be considered as the multistatic equivalents to the monostatic matched filter.

Coherent processing in a single transmitter system

We begin with algorithm L_2 for the case of a multistatic system with a single transmitter and m receivers, and from Equation 2.53 we see that the output of the algorithm is the result of the coherent summation of matched filter kernels G_i in each receiver. It is this processing system that takes the place of the matched filter in Equation 3.23. Transforming G_i in Equation 2.46 to the time domain, and 'matching' it to time-delay t_{sia} and doppler frequency Ω_{sia}[4], we can write:

$$G_i = \frac{1}{2\pi N_i} \int_{-\infty}^{\infty} X_i(t) s_0^*(t - t_{sia}) \exp[-j(\omega_0 + \Omega_{sia})(t - t_{sia})] dt \tag{3.32}$$

We now restate for convenience the expression for the wanted signal $S_i(t)$ in Equation 2.22, which has a time-delay t_{sih}, doppler frequency ω_{sih}, amplitude a_{si} and initial phase φ_{si}:

$$S_i(t) = a_{si} \exp(-j\varphi_{si}) s_0(t - t_{sih}) \exp[j(\omega_0 + \Omega_{sih})(t - t_{sih})] \tag{3.33}$$

Then, discarding noise components, the received signal $X_i(t)$ is equal to $S_i(t)$, so we can substitute into Equation 3.32 to give:

$$\begin{aligned} G_i = \frac{a_{si}}{2\pi N_i} \exp(-j\varphi_{si}) \exp[j\{\omega_0(t_{sia} - t_{sih}) + \Omega_{sia} t_{sia} - \Omega_{sih} t_{sih}\}] \\ \times \int_{-\infty}^{\infty} s_0(t - t_{sih}) s_0^*(t - t_{sia}) \exp[-j(\Omega_{sia} - \Omega_{sih})t] dt \end{aligned} \tag{3.34}$$

It can be seen that the integral in Equation 3.34 is identical to the monostatic matched filter of Equation 3.25 prior to envelope detection. The whole expression can be substituted

[4]Note that these values must be calculated for every $i = 1, m$ using the multistatic geometry

into Equation 2.53 for detector L_2, taking into account Equation 2.51 to give:

$$|\chi_{L_2}| = \Big|\frac{1}{2\pi a_{s1}} \exp(-j\varphi_{s1}) \sum_{i=1}^{m} \frac{a_{si}^2}{N_i} \exp[j\{\omega_0(t_{sia} - t_{sih}) + \Omega_{sia}t_{sia} - \Omega_{sih}t_{sih}\}] \times \int_{-\infty}^{\infty} s_0(t - t_{sih}) s_0^*(t - t_{sia}) \exp[-j(\Omega_{sia} - \Omega_{sih})t] dt\Big| \tag{3.35}$$

The 'matched' values t_{sia} and Ω_{sia} and actual 'received' values t_{sih} and Ω_{sih} in Equation 3.35 should be calculated from Equations 3.29 and 3.31, which describe the dependency of the ambiguity function on the multistatic topology.

In this equation, each integral involving the normalised complex envelope of the signal is phase shifted and then weighted by the signal-to-noise ratio at the corresponding receiver. The assumption for the ambiguity function is of a background of mutually uncorrelated white Gaussian noise, so it is reasonable to assume thermal self-noise is dominant, and therefore in the usual case all noise powers will be equal. If this is not the case, then expected values can be substituted if a specific model is required. Therefore, the weighting of each term in the summation is proportional to the mean-square amplitude of the received signal only.

We note however that the ambiguity function in the monostatic case is normalised, and its shape is independent of the amplitude of the received signal. However, it is clear from Equation 3.35 that the shape of the filter output is dependent on the relative amplitudes of signals at each receiver, and disregarding these factors in the multistatic case is unacceptable. Therefore, we decide to make some reasonable assumptions in order to simplify the analysis. It was shown in the derived 'multistatic radar equation' (Equation 3.16) that, for a real radar, the received signal amplitude is dependent on the target radar cross-section, carrier wavelength, transmitter and receiver antenna gains (i.e. beam patterns in the direction of the target) and the target-transmitter and target-receiver ranges, which collectively determine the propagation loss. Firstly it is assumed that the target RCS is constant for all bistatic angles and aspects. Secondly, all transmit and receive antennas have constant gain in the direction of the target, i.e. they are either isotropic, or are steered mechanically or electronically to the required direction. In that case, the signal amplitude is dependent only on the ranges between the target and the antennas. Therefore, if the received signals are deterministic, the amplitude weighting in Equation 3.35, which we shall call Q_i, is given

by:

$$Q_i \propto \frac{1}{|\mathbf{R_t}|^2|\mathbf{R_{ri}}|^2} \tag{3.36}$$

where $\mathbf{R_t}$ and $\mathbf{R_{ri}}$ are the distance vectors from the matched target location to the transmitter and the ith receiver respectively. In order to not bias the ambiguity function output, the values of Q_i for all receivers corresponding to the matched range must be normalised to a sum of unity. In that case, the weighting has an effect only on the *relative* contribution of each bistatic pair to the response. In the case that the received signals are fluctuating, we note that the fundamental assumption for the optimality of this detection algorithm is that the fluctuations are mutually correlated between receivers, so the relative values of a_{si} and hence Q_i remain constant. The fluctuating 'reference' amplitude a_{s1} in Equation 3.35 (together with the reference phase φ_{s1}) can be removed from the ambiguity function as they do not affect its normalised shape.

Coherent processing in a multiple transmitter system

Now we analyse the nature of the ambiguity function for a multistatic system comprising multiple transmitters. Firstly, the case is considered where each transmitter outputs the same signal, time synchronised such that they 'phase' perfectly at the target location. In the general case where the elements are widely distributed, this may take the form of transmission nearfield 'spot-beamforming', as described in Section 2.6.1. The transmitter beam pattern is not relevant to the ambiguity function as it simply results in the target being illuminated more strongly, and it was shown in Section 2.4.7 that the optimal receiver in this case is the same as that for a single transmitter system

Next, we consider the case where each transmitted signal can be resolved at each receiver through the use of methods such as time or frequency separation. If frequency diversity is used, the narrowband assumption in Equation 3.20 must apply to the totality of all signals. Otherwise, the ambiguity function must be calculated on the basis of separate carrier frequencies for each transmitter. There will be no interference between the transmitted signals subject to the assumptions outlined in Section 2.4.7, so the system can be considered as a set of $m \times n$ bistatic pairs. In this case, the multiple transmitter form of the detection algorithm should be used, and the weights Q_{ik} must be calculated for each of these bistatic pairs.

If the target is moving, it is necessary to take into account two further factors. It is expected that the signals from each transmitter reach the target at the same time, or if not (for example if time multiplexing is used), extrapolation of the measured parameters is required to account for the movement of the target between each transmitted signal. Secondly, it should be noted that the propagation delay time t_s, measured at some time t, is actually proportional to the total range $R_t + R_r$ at time $t - t_r$, where t_r is the target-receiver propagation time. The ambiguity function assumes that these issues have been taken into account, but they must be considered in the processing of a real multistatic system.

Equation 3.16 shows that the amplitudes of received signals are also dependent on the transmitted power, so for convenience we make the assumption that the power of all transmitters in the system is equal. Then, we can use the form of detector $\mathrm{L_{2m}}$ in Equation 2.75 to give the multistatic ambiguity function for signals that are non-fluctuating or where fluctuations are mutually correlated at each receiver, in a background of receiver self-noises:

$$\chi_{\mathrm{L_{2m}}} = \Big| \frac{1}{Q_{\mathrm{sum}}} \sum_{k=1}^{n} \sum_{i=1}^{m} Q_{ik} \exp[j\{\omega_0(t_{sika} - t_{sikh}) + \Omega_{sika} t_{sika} - \Omega_{sikh} t_{sikh}\}] \times \int_{-\infty}^{\infty} s_{0k}(t - t_{sikh}) s_{0k}^{*}(t - t_{sika}) \exp[-j(\Omega_{sika} - \Omega_{sikh})t] dt \Big| \tag{3.37}$$

where $Q_{\mathrm{sum}} = \sum_{k=1}^{n} \sum_{i=1}^{m} Q_{ik}$ and $Q_{ik} = 1/|\mathbf{R_{tk}}|^2 |\mathbf{R_{ri}}|^2$, where $\mathbf{R_{ri}}$ and $\mathbf{R_{tk}}$ relate to the matched location (i.e. corresponding to t_{sika}). The complex envelope s_{0k} refers to the waveform transmitted by the kth transmitter. Again, the values of t_{si} and Ω_{si} in Equation 3.37 should be calculated from Equations 3.29 and 3.31. This equation resolves to the single transmitter case simply by setting $n = 1$.

Incoherent processing

In the case of the incoherent detector, it is convenient to choose to use algorithm L_4 in Equation 2.72, which is optimal when complex fluctuations are mutually independent and the amplitudes are unknown. This detector is almost identical to L_3, but its modelling does not require knowledge of the absolute noise power. Then the detector can be expressed for

an n transmitter, m receiver system as:

$$\mathrm{L_{4m}} = \sum_{k=1}^{n}\sum_{i=1}^{m} N_{ik}|G_{ik}|^2 \tag{3.38}$$

Then, from Equation 3.34, the squared modulus of G_{ik} is given by:

$$|G_{ik}|^2 = \frac{a_{sik}^2}{4\pi^2 N_{ik}^2}\left|\int_{-\infty}^{\infty} s_{0k}(t - t_{sikh}) s_{0k}^*(t - t_{sika}) \exp[-j(\Omega_{sika} - \Omega_{sikh})t]dt\right|^2 \tag{3.39}$$

It is assumed for this detector that all a_{sik} are independently fluctuating. If we assume these fluctuations are Gaussian, then a_{sik}^2 should be replaced by their second moment (or variance). If we then further assume that the variances corresponding to each bistatic pair are dependent only on propagation losses, then we can substitute the weighting factor:

$$Q_{ik} \propto \frac{1}{|\mathbf{R_{tk}}|^2|\mathbf{R_{ri}}|^2} \tag{3.40}$$

Then, assuming all noise powers are constant as before, the multistatic ambiguity function for signals where fluctuations corresponding to each bistatic pair in the system as independently fluctuating, in a background of receiver self-noises is given by substituting into Equation 3.38 to give:

$$\chi_{\mathrm{L4m}} = \frac{1}{Q_{\mathrm{sum}}}\sum_{k=1}^{n}\sum_{i=1}^{m} Q_{ik}\left|\int_{-\infty}^{\infty} s_{0k}(t - t_{sikh}) s_{0k}^*(t - t_{sika}) \exp[-j(\Omega_{sika} - \Omega_{sikh})t]dt\right|^2 \tag{3.41}$$

where Q_{sum} is defined as per Equation 3.37.

The ambiguity functions derived in Equations 3.37 and 3.41 both have the matched filter integral as their kernel. It is dependent on both the matched and 'hypothesised' values of time delay and doppler, which due to the non-linear relationship with range and velocity must be individually calculated for every point in the ambiguity function. In Equation 3.37, these values are phase shifted, weighted and then coherently summed. In Equation 3.41, their moduli are first squared, then weighted and (non-coherently) summed.

Typically, monostatic ambiguity functions are generated by calculating discrete cross-correlations of the complex waveform with a series of doppler-shifted replicas, over the time lags of interest (or equivalently in the frequency domain for a series of time lags). However,

due to the non-linear relationship between delay/doppler and the plotted independent variables in the bistatic and multistatic cases, the required values will not generally occur at sample points, so this method requires resorting to some form of interpolation or fractional delay shifters. Fortunately, closed-form analytic expressions for Equation 3.25 are available for many well-known complex signals[5].

3.3.4 Ambiguity Diagram Simulation Results

Here, some illustrative examples of the plots of the ambiguity function derived above are given, in order to determine the effect of multistatic topologies and the detection algorithm on the resolution and parameter measurement capabilities of the system.

Verification of Simulation Model

We begin by confirming that $\chi_{L_{2m}}$ gives identical results to the ambiguity function derived by Tsao when reduced to the monostatic and bistatic cases ($n = m = 1$). A waveform comprising a train of three coherent rectangular pulses is considered, with pulse length 40 ns, and PRF 10 kHz. For comparative purposes the monostatic ambiguity function is calculated first by co-locating a single transmitter and receiver ($\mathbf{R_1} = \mathbf{T_1}$). Velocity vector V is chosen to point towards the target, so the speed plotted equals the radial velocity. The 'matched' values of range and speed are $R_{r1a} = 60$ km and $v_a = |V| = 600$ m/s, and the plotted values are $2 \times 10^4 \leq R_{r1h} \leq 10 \times 10^4$ m for range and $-4 \times 10^4 \leq v_h \leq 4 \times 10^4$ m/s for speed. The carrier frequency is chosen to be $3 \times 10^8/2\pi$ Hz. In fact, as was shown in Equation 3.26, the monostatic ambiguity function is dependent only on the difference between 'matched' and actual range and radial velocity, not their absolute values. However the matched values are defined now for consistency with the multistatic case, and in order to match the parameters used in the examples in Tsao(77) for the bistatic function. The resulting contour and surface plots of the *square*[6] of the ambiguity function are shown in Figure 3-8.

The main peak corresponding to the fully matched case (unity response) is clearly visible

[5]It should be noted however that in several texts these equations are expressed as real functions or where the modulus has been taken. Care should be taken when calculating ambiguity based on detector L_{2m} that it is the *complex* responses of each matched filter component response that are coherently summed.

[6]The square of the ambiguity function, which indicates the normalised power at the output of the detection filter, is plotted here as this is the most common form in the literature.

on these well-known plots. Ambiguities arise in any situation where measurements are made in a discontinuous manner(43), such as this case where the waveform consists of three discrete pulses. Therefore a series of ambiguity sub-peaks are present that are related to the PRF - the inter-pulse period 1×10^{-4} corresponds to monostatic 'second-time-around' echoes separated by 15 km and 'blind speeds' at intervals of $\approx 3.1 \times 10^4$ m/s.

It is worthwhile at this stage reiterating the interpretation of the ambiguity diagram such as that in Figure 3-8. When considered in terms of resolution, the graph shows the response of a filter with fixed matched parameters (range 60 km, velocity 600 m/s) to a gamut of possible received signals with equal amplitude from a target at each position on the {range, velocity} plane. In this case, the fixed filter, which should respond only to a received signal corresponding to its matched parameters, also responds strongly to targets placed at each of the eight large ambiguity sub-peaks shown, for example at {$\approx$ 75 km range, $\approx$ 0 m/s velocity}. Due to the independence of the function shape on the centre point in the monostatic case, if the filter were matched to this value instead, it would exhibit equal ambiguity at the original matched position. Therefore the matched filter is a poor discriminator of targets at those two locations, and they can only be resolved in very high signal-to-noise ratio conditions.

When considered in terms of measurement accuracy, the graph shows the response of the matched filter to a fixed received signal from a target positioned at a range of 60 km with radial velocity of 600 m/s. This response can be found by matching or 'tuning' the filter to each point on the {range, velocity} plane. The graph is in fact inverted in both range and velocity in this case[7], but the shape is identical due to its symmetry. In addition, the independence of the function shape on the centre point means that the response is the same for equal offsets from any matched position. Of greatest import in this context is the breadth of the main lobe (or specifically its second derivative), as this gives a measure of the range and radial velocity estimation accuracy.

Now, the equation is re-evaluated for a bistatic topology ($\mathbf{R_1} \neq \mathbf{T_1}$) with baselength of 100 km. The target direction plotted from the receiver is close to the baseline, and the velocity vector V is perpendicular to the baseline as shown in Figure 3-9. It is well-known that a bistatic system has poor effective resolution for these parameters. The contour and

[7]In other words, the response of the filter at positive range and velocity compared to the matched value is shown by the corresponding negative offsets on the graph.

surface plots for the square of the ambiguity function are shown in Figure 3-10.

It is clear that the response of this receiver (which is still matched to parameters of {60 km, 600 m/s}) is very broad, particularly at near range. As the range increases such that it approaches the transmitter, the ambiguity begins to decrease because small changes in range start to have a larger effect on the total range $R_t + R_r$ and hence the time of arrival. Essentially, this graph is equivalent to that in Figure 3-8 after being 'warped' by the bistatic geometry. The non-linear delay-range and doppler-velocity relationships mean that the 'unity volume' law given in Equation 3.27 does not apply *when the function is plotted on range-velocity axes.*

The result shown is perhaps somewhat unfair on the bistatic system. After all, it would be quite possible to plot a (rather unconventional) monostatic ambiguity function for a velocity vector with very small radial component with much the same effect, and the monostatic system is of course completely blind to *location* on iso-range contours. However, these facts are well understood for monostatic systems, and are not evident from the traditional delay-doppler plots. It is the topology of bistatic and multistatic systems that forces the ambiguity function to become dependent on position and velocity vectors. The graphs shown here agree fully with those derived in Tsao(77) for the bistatic function using the same parameters.

We now demonstrate the effect of changing the centre point on the bistatic function. The ambiguity diagram for the same topology as above, but for a 'matched' range of 100 km, is shown in Figure 3-11. The matched velocity is identical to the previous case, and the limits of the range axis are changed so to maintain the matched position in the centre of the plot.

The main peak is now much sharper, because the matched target position is close to the edge of the bistatic baseline. The sub-peak corresponding to a second-time-around ambiguity is also visible. Together, these graphs demonstrate that the resolution capability of the receiver at each matched point is not fixed. For example, the filter matched to {60 km, 600 m/s} has a very similar response to a target at a range of 100 km as it does to a target at its matched position. However, the filter matched to {100 km, 600 m/s} has a very small response to a target at 60 km. Hence, on the basis of these two filters only, the presence of a target at 60 km would produce a large system response corresponding to that range only. However, the presence of a target at 100 km would produce large system responses corresponding to ranges of both 60 km and 100 km (and in fact all values between the two).

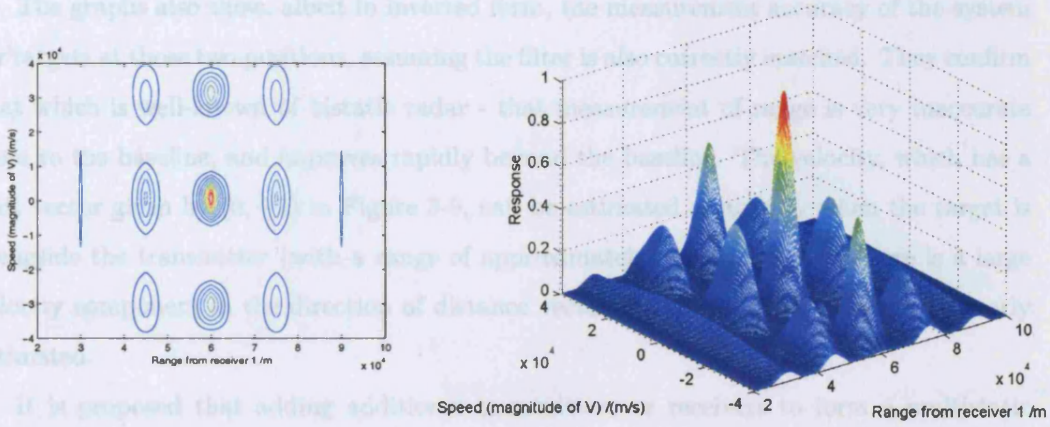

Figure 3-8: Contour and surface plots of the monostatic ambiguity diagram for three rectangular pulses

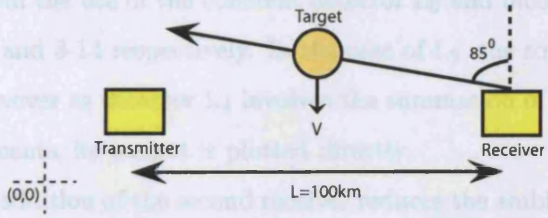

Figure 3-9: Bistatic topology used in Figures 3-10 and 3-11

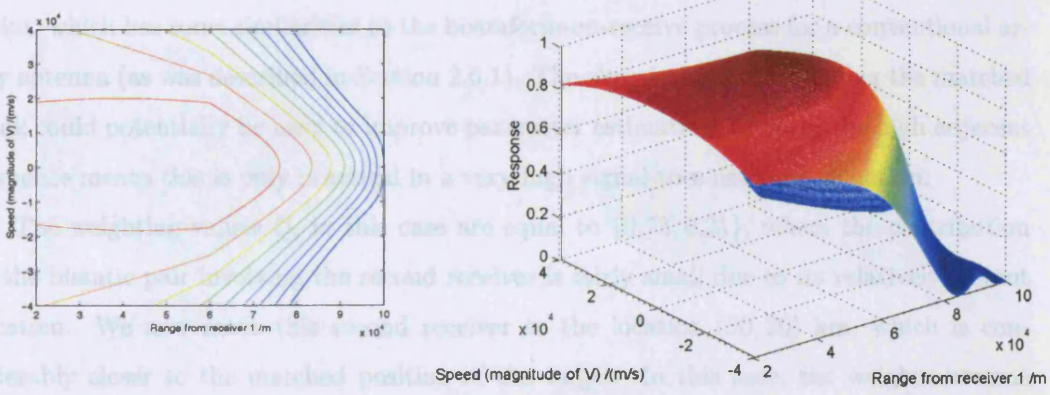

Figure 3-10: Contour and surface plots of bistatic ambiguity function, receiver matched to {60 km, 600 m/s}

Hence, the resolution capability of a bistatic radar is biased according to its topology.

The graphs also show, albeit in inverted form, the measurement accuracy of the system for targets at those two positions, assuming the filter is also correctly matched. They confirm that which is well-known of bistatic radar - that measurement of range is very inaccurate close to the baseline, and improves rapidly beyond the baseline. The velocity, which has a unit vector given by $(0, -1)$ in Figure 3-9, can be estimated accurately when the target is alongside the transmitter (with a range of approximately 100 km) as here there is a large velocity component in the direction of distance vector $\mathbf{R_t}$, although elsewhere it is poorly estimated.

It is proposed that adding additional transmitters or receivers to form a multistatic system could reduce the overall ambiguity if they are spatially separated. We now return to the original model based on a matched range of 60 km (as per Figure 3-10), but add a second receiver as shown in Figure 3-12. Contour and surface plots of the ambiguity diagrams resulting from the use of the coherent detector L_2 and incoherent detector L_4 are given in Figures 3-13 and 3-14 respectively. In the case of L_2, the square of the function is plotted as before. However as detector L_4 involves the summation of squared moduli of the matched filter components, its output is plotted directly.

In both cases, the addition of the second receiver reduces the ambiguity in the vicinity of the target compared to the bistatic equivalent in Figure 3-10, as a clear (although still rather broad[8]) peak can now be seen. The appearance of the function for the coherent detector is a great deal more complex than that of the incoherent detector, due to the presence of an interference pattern relating to coherent 'focussing' of the received signals at the matched point, which has some similarities to the beamform-on-receive process for a conventional array antenna (as was described in Section 2.6.1). The close-in nulls surrounding the matched peak could potentially be used to improve parameter estimation, however the high adjacent response means this is only practical in a very high signal-to-noise ratio situation.

The weighting values Q_i in this case are equal to $\{0.73, 0.21\}$, where the contribution of the bistatic pair involving the second receiver is fairly small due to its relatively distant location. We now move this second receiver to the location $(50, 20)$ km, which is considerably closer to the matched position of the target. In this case, the weights become $\{0.29, 0.71\}$, and the resulting ambiguity diagram is shown in Figure 3-15. Evidently any

[8]It is noted that the target location is also quite close to the baseline of the second bistatic pair.

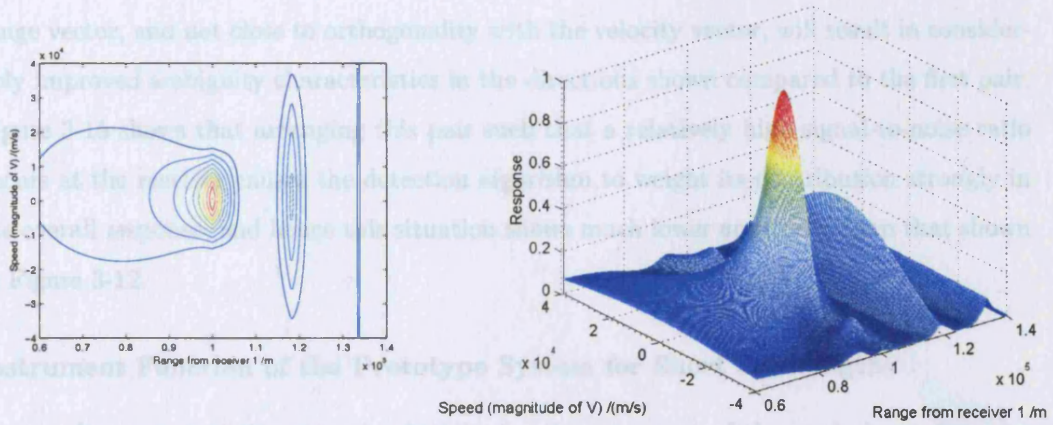

Figure 3-11: Contour and surface plots of bistatic ambiguity function, receiver matched to {100 km, 600 m/s}

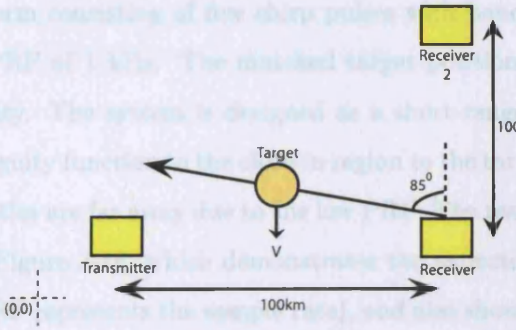

Figure 3-12: Multistatic topology used in Figures 3-13 and 3-14

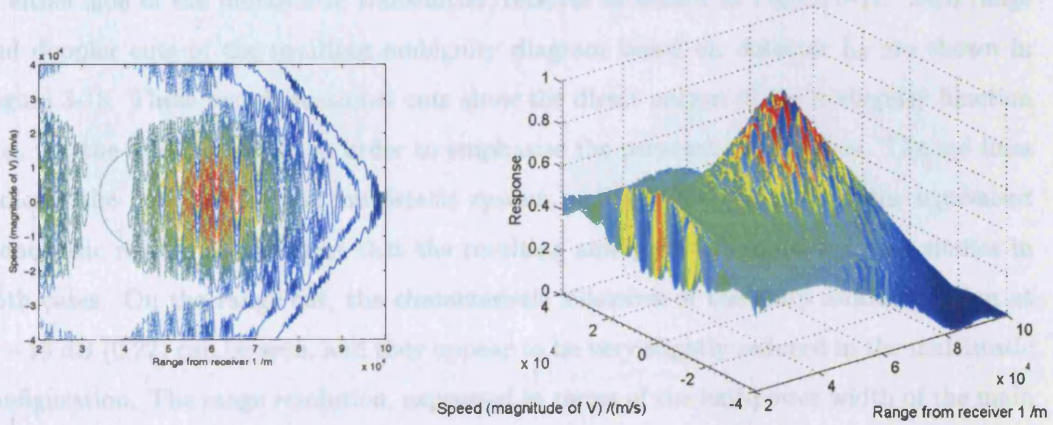

Figure 3-13: Contour and surface plots of multistatic ambiguity diagram using coherent detector L_2 with a single transmitter and two receivers

additional bistatic pair arranged such that its baseline is not closely aligned with the target range vector, and not close to orthogonality with the velocity vector, will result in considerably improved ambiguity characteristics in the directions shown compared to the first pair. Figure 3-15 shows that arranging this pair such that a relatively high signal-to-noise ratio occurs at the receiver causes the detection algorithm to weight its contribution strongly in the overall response, and hence this situation shows much lower ambiguity than that shown in Figure 3-12.

Instrument Function of the Prototype System for Short Baselengths

Having demonstrated the general principle, for the next part of the analysis we focus on radar parameters that are compatible with the prototype system described in Chapter 5. Firstly we consider a monostatic element of the system, with carrier frequency of 2.4 GHz, transmitting a waveform consisting of five chirp pulses with bandwidth of 50 MHz, pulse length of 1 μs, and PRF of 1 kHz. The matched target position is at a range of 500 m, and zero radial velocity. The system is designed as a short-range sensor, so we limit the range axis of the ambiguity function to the close-in region to the target, as the multiple-time-around range ambiguities are far away due to the low PRF. The resulting squared ambiguity diagram is shown in Figure 3-16, which demonstrates the expected blind velocities due to aliasing (where the PRF represents the sample rate), and also shows that there is zero range ambiguity outside the main peak (within the region of interest).

We now consider the effect of adding two additional receivers to this system, placed 50 m either side of the monostatic transmitter/receiver as shown in Figure 3-17. Zero range and doppler cuts of the resulting ambiguity diagram based on detector L_2 are shown in Figure 3-18. These two-dimensional cuts show the direct output of the ambiguity function (i.e. not the squared value), in order to emphasise the presence of sidelobes. The red lines indicate the response for the multistatic system, and the blue lines show the equivalent monostatic result. It is evident that the resulting ambiguity diagrams are very similar in both cases. On the range cut, the characteristic sidelobes of the chirp autocorrelation at ≈ -13 dB (0.22) can be seen, and they appear to be very slightly reduced in the multistatic configuration. The range resolution, expressed in terms of the half-power width of the main peak, is approximately 3 m, as expected for a 50 MHz bandwidth. It is evident that whilst such a 'short baselength' multistatic configuration may provide sensitivity gain, it does not

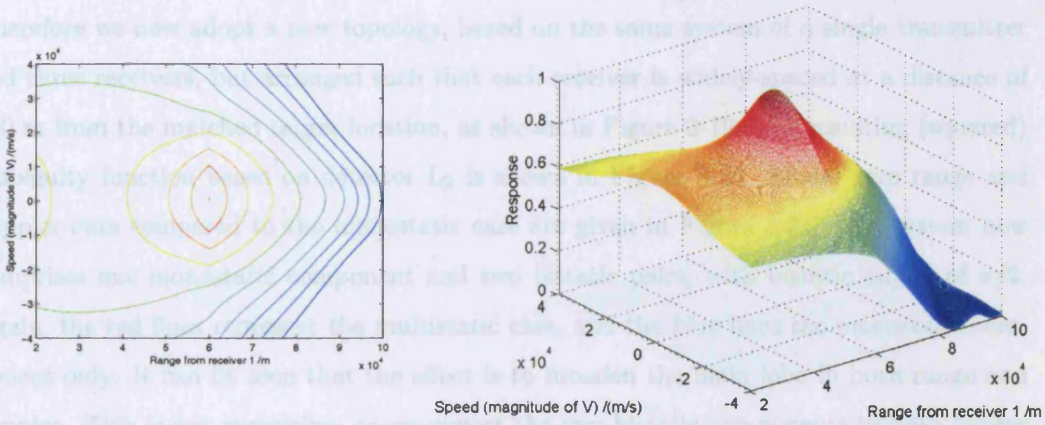

Figure 3-14: Contour and surface plots of multistatic ambiguity diagram using incoherent detector L_4 with a single transmitter and two receivers

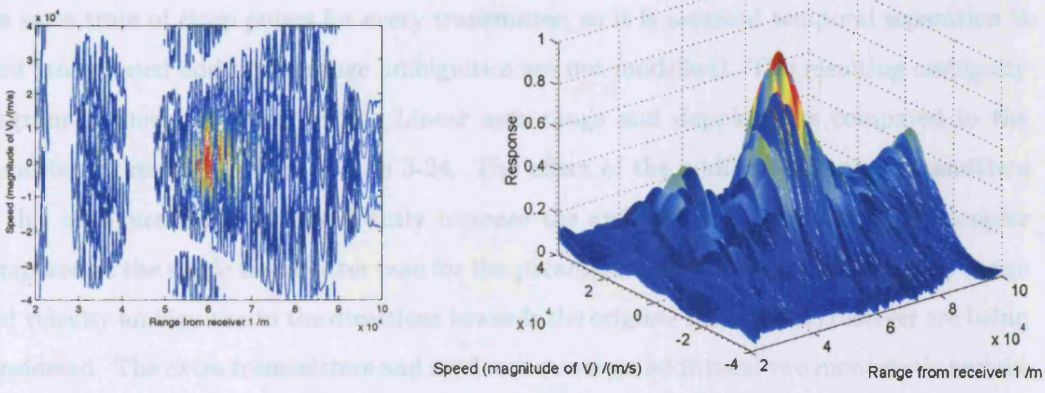

Figure 3-15: Contour and surface plots for the same case as Figure 3-13 where the second receiver is located at $(50, 20)$ km

significantly affect the ambiguity (or instrument function) *for these parameters.*

Instrument Function of the Prototype System for Large Baselengths

Therefore we now adopt a new topology, based on the same system of a single transmitter and three receivers, but arranged such that each receiver is widely-spaced at a distance of 500 m from the matched target location, as shown in Figure 3-19. The resulting (squared) ambiguity function based on detector L_2 is shown in Figure 3-20. Linear zero range and doppler cuts compared to the monostatic case are given in Figure 3-21. The system now comprises one monostatic component and two bistatic pairs, with bistatic angles of $\pi/2$. Again, the red lines represent the multistatic case, and the blue lines the monostatic component only. It can be seen that the effect is to broaden the main lobe in both range and doppler. This is not surprising, as we expect the two bistatic components to have poorer range and doppler resolution than the monostatic component in the directions indicated. The close-in interference pattern resulting from the coherent summation of received signals is evident in the range cut. In addition, the blind-doppler ambiguities for the bistatic components correspond to different velocities to the monostatic component, so the effect is to spread out these ambiguities over the velocity axis. Hence, the apparent ambiguities at ≈ 60 m/s are reduced compared to the monostatic case.

We now add to the system an additional two transmitters, which are colocated with the receivers as shown in Figure 3-22. For the sake of simplicity, the function is modelled here for the same train of chirp pulses for every transmitter, so it is assumed temporal separation is used (the related additional range ambiguities are not modelled). The resulting ambiguity diagram is shown in Figure 3-23. Linear zero range and doppler cuts compared to the monostatic case are given in Figure 3-24. The effect of the addition of extra transmitters in this configuration is to significantly increase the ambiguity in both range and doppler compared to the single transmitter case for the parameters shown. We recall that only range and velocity ambiguities in the directions towards the original transmitter/receiver are being considered. The extra transmitters and receivers create an additional two monostatic and six bistatic components, all of which by definition have inferior ambiguity properties compared to the original monostatic system. Therefore the close-in ambiguity when measured in this way will always be impaired compared to that of the first monostatic radar. However, it is clear that the ambiguity of measurement and resolution in *other* range and velocity

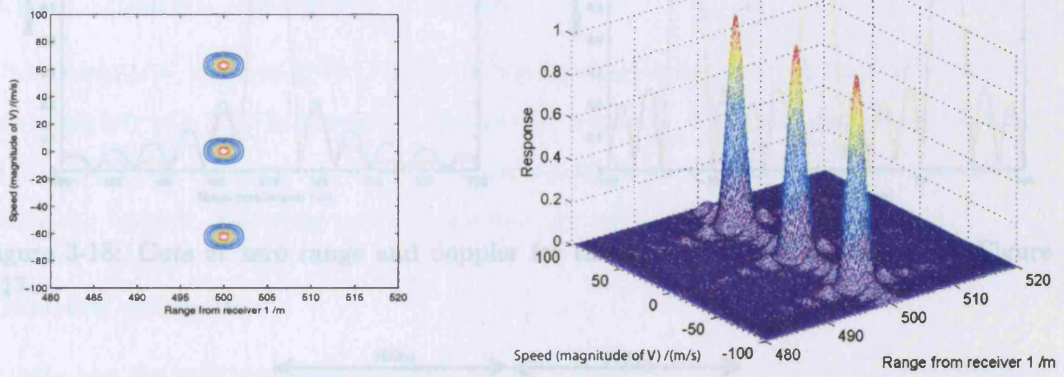

Figure 3-16: Contour and surface plots for a monostatic radar transmitting five chirp pulses

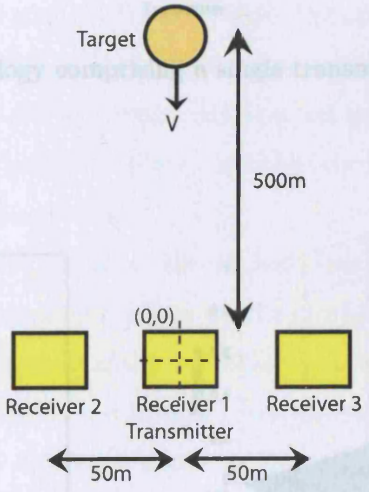

Figure 3-17: Multistatic topology comprising a single transmitter and three closely-spaced receivers

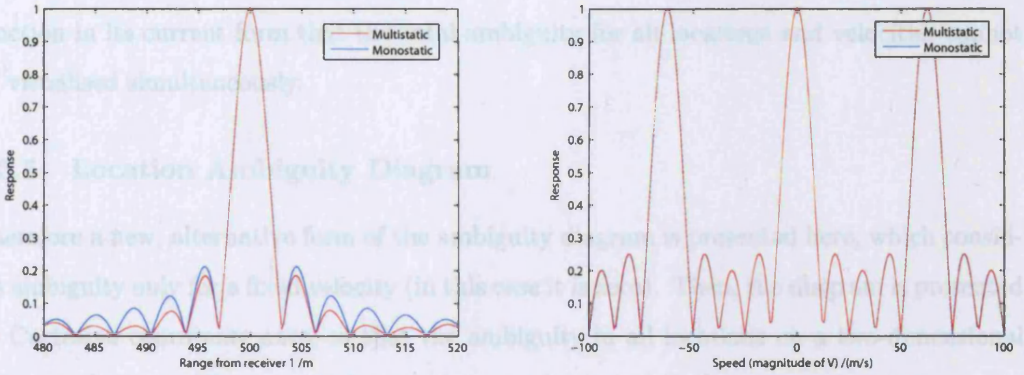

Figure 3-18: Cuts at zero range and doppler for the ambiguity function based on Figure 3-17

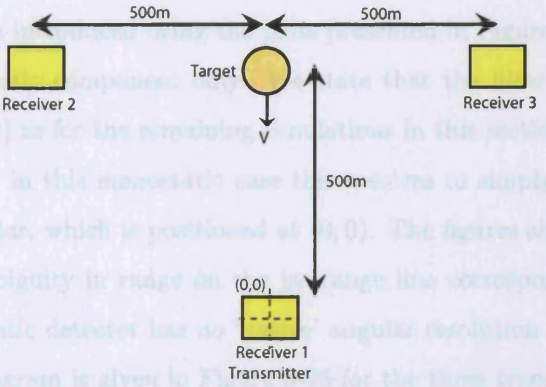

Figure 3-19: Multistatic topology comprising a single transmitter and three widely-spaced receivers

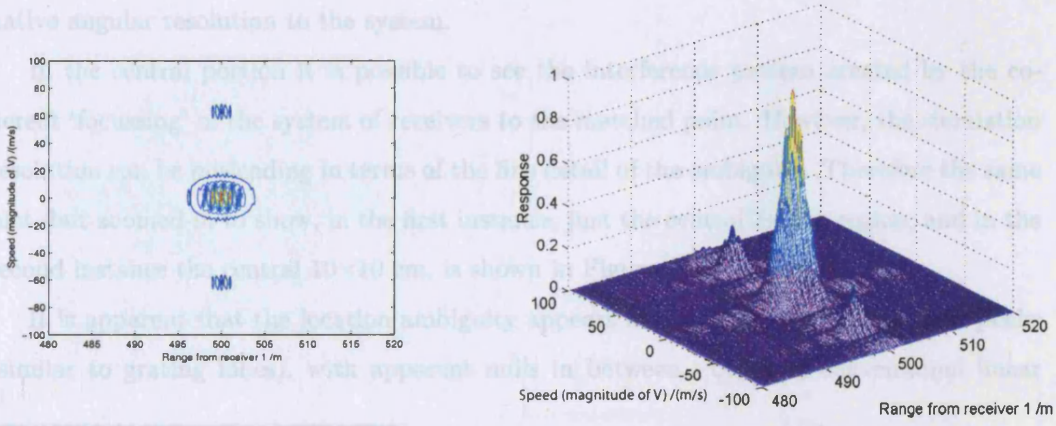

Figure 3-20: Contour and surface plots for the multistatic system shown in Figure 3-19

directions would be significantly improved. It is one of the limitations of the ambiguity function in its current form that the total ambiguity for all locations and velocities cannot be visualised simultaneously.

3.3.5 Location Ambiguity Diagram

Therefore a new, alternative form of the ambiguity diagram is presented here, which considers ambiguity only for a fixed velocity (in this case it is zero). Then, the diagram is presented on Cartesian coordinate axes, so that the ambiguity in all locations on a two-dimensional plane can be seen. The same radar parameters are used as in the previous section.

Coherent detection

Firstly, the diagram is introduced using the plots presented in Figure 3-25 on two different scales for the monostatic component only. We state that the filter is matched to target *co-ordinates* of $(0, 500)$ m for the remaining simulations in this section although, as can be seen from the graphs, in this monostatic case this resolves to simply matching to a *range* of 500 m from the radar, which is positioned at $(0, 0)$. The figures show that, as expected, there is complete ambiguity in range on the iso-range line corresponding to the matched position, as a monostatic detector has no 'native' angular resolution capability.

Now, the same diagram is given in Figure 3-26 for the three transmitter, three receiver multistatic system of Figure 3-22. A surface plot is also shown to highlight the shape of the ambiguity[9]. It is evident that the multistatic function has significantly reduced the *overall* range ambiguity in the two-dimensional plane - in other words, the spatial diversity affords native angular resolution to the system.

In the central portion it is possible to see the interference pattern created by the coherent 'focussing' of the system of receivers to the matched point. However, the simulation resolution can be misleading in terms of the fine detail of the ambiguity. Therefore the same plot, but zoomed-in to show, in the first instance, just the central 3×3 m region, and in the second instance the central 10×10 cm, is shown in Figure 3-27.

It is apparent that the location ambiguity appears as a pattern of closely spaced peaks (similar to grating lobes), with apparent nulls in between. Unlike a conventional linear

[9]Note that, despite its appearance, this is a location plot, not a traditional ambiguity diagram.

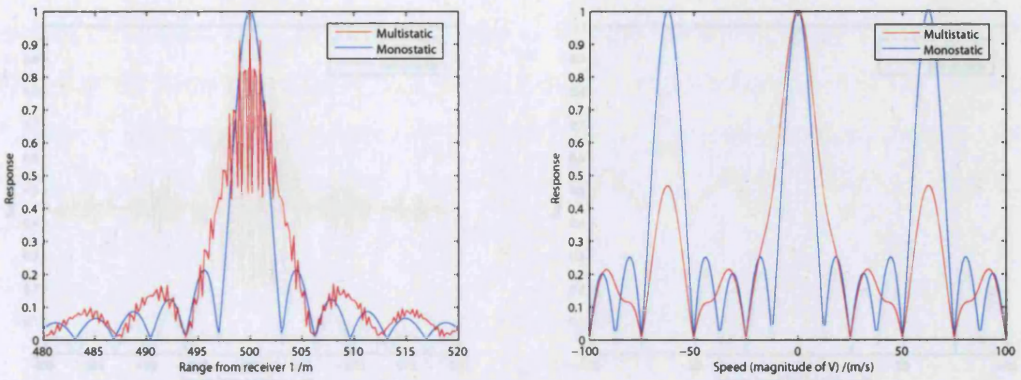

Figure 3-21: Cuts at zero range and doppler for the ambiguity function based on Figure 3-19

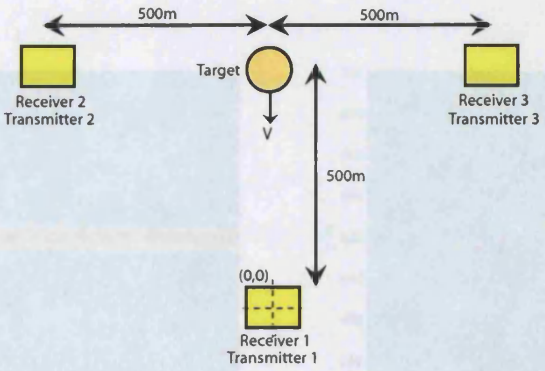

Figure 3-22: Multistatic topology comprising three colocated widely-spaced transmitters and receivers

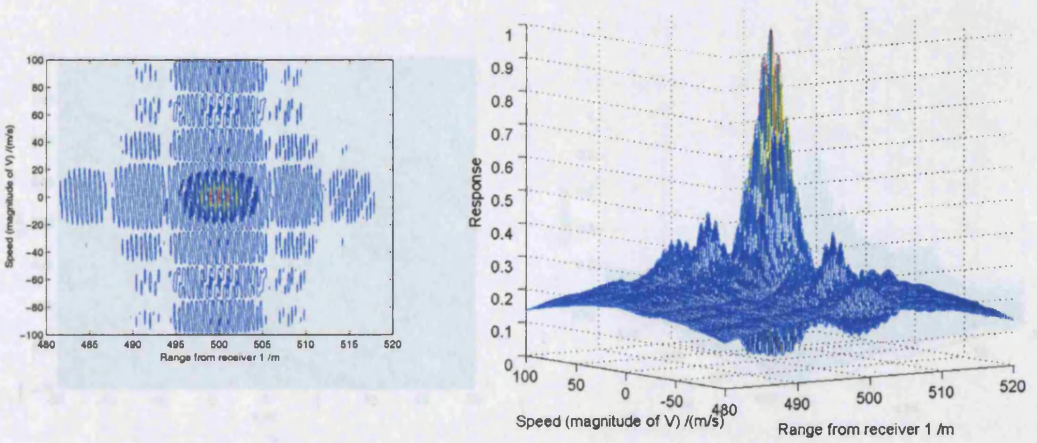

Figure 3-23: Contour and surface plots for the multistatic system shown in Figure 3-22

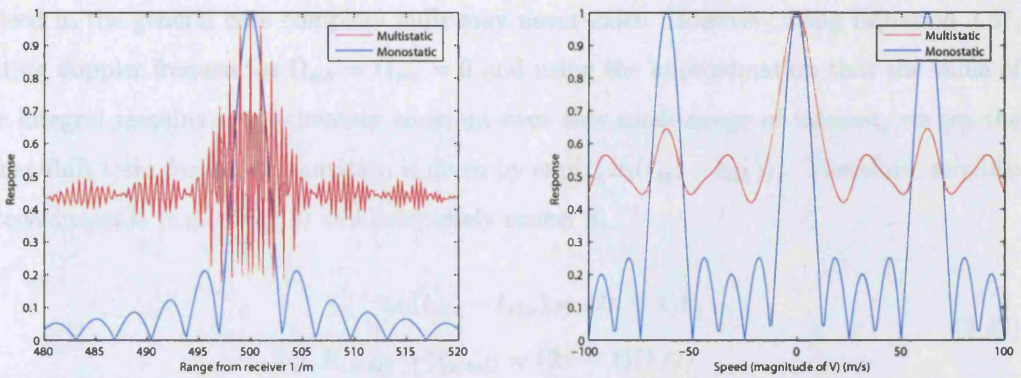

Figure 3-24: Cuts at zero range and doppler for the ambiguity function based on Figure 3-22

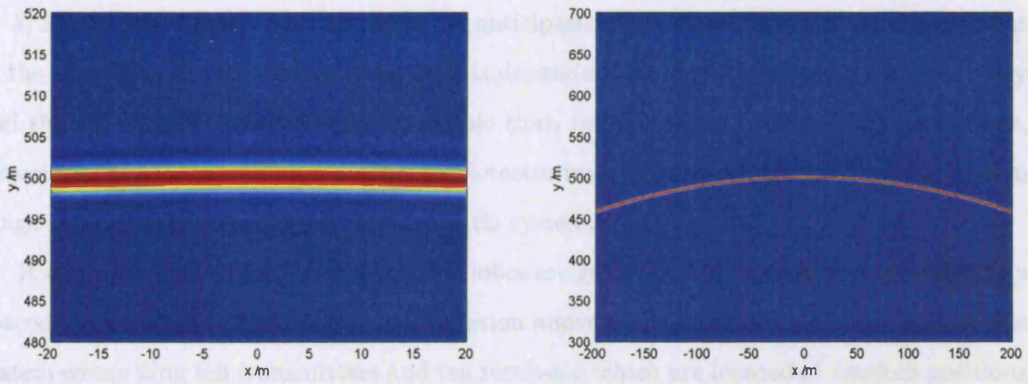

Figure 3-25: Location ambiguity diagram for a monostatic system

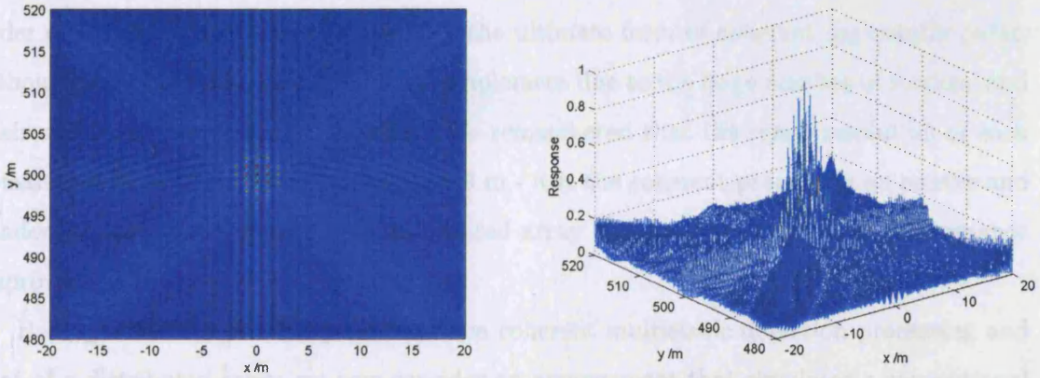

Figure 3-26: Location ambiguity diagram for the multistatic system of Figure 3-22

array, there are no simple expressions for determining the positions of these nulls, and indeed in the general case complete nulls may never exist. However, using Equation 3.37, setting doppler frequencies $\Omega_{sih} = \Omega_{sia} = 0$ and using the approximation that the value of the integral remains approximately constant over this small range of interest, we see the phase shift term for each summation is given by $\exp[j\{\omega_0(t_{sia} - t_{sih})\}]$. Therefore, any two received signals (e.g. $i = 1, 2$) will completely cancel if:

$$\begin{aligned} \omega_0(t_{s2a} - t_{s1a}) &= (2n+1)\pi \\ \therefore R_{\text{total2}} - R_{\text{total1}} &= (2n+1)(\lambda/2) \end{aligned} \tag{3.42}$$

for all integer n. In an arbitrary multistatic system, complete nulls will only occur if the summation of signals from all bistatic pairs cancel at a point. Nevertheless, in this regular topology we see partial nulls at $\lambda/4$ from the centre point, and peaks similar to grating lobes at $\lambda/2$ from the centre point, as might be anticipated from Equation 3.42. It is clear that in the general case, the ambiguity pattern is dependent on the topology, doppler frequency and the wavelength. Therefore it is possible that, in high signal-to-noise ratio conditions, measurement accuracy using the coherent detector may be considerably better than the 3 m range resolution of the equivalent monostatic system.

It was stated in Section 2.6 that grating lobes are generally not evident in large, randomly spaced sparse arrays. Therefore, the simulation above was repeated for a larger multistatic system comprising ten transmitters and ten receivers, which are located at random positions over a 1 km^2 plane with the target at the centre. The result is shown in Figure 3-28. It is clear that the ambiguous peaks similar to grating lobes have almost disappeared, and the result is a system response only at the target location with measurement accuracy in the order of ± 2 cm. This represents possibly the ultimate form of coherent multistatic radar, although in practice the most difficult to implement due to the large number of stations and their coherency requirements. It should be remembered that the range resolution of each constituent bistatic pair is no better than 3 m - it is the coherent processing on receive and random topology in the style of a distributed array that produces this large performance improvement.

Having noted the similarity between the coherent multistatic detection processing and that of a distributed array, we now consider an arrangement that simulates a conventional

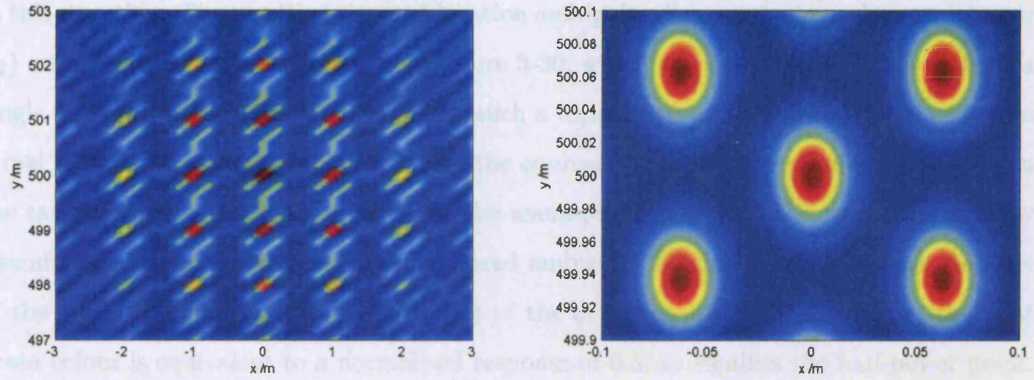

Figure 3-27: Centre portion of the location ambiguity diagram for the multistatic system of Figure 3-22

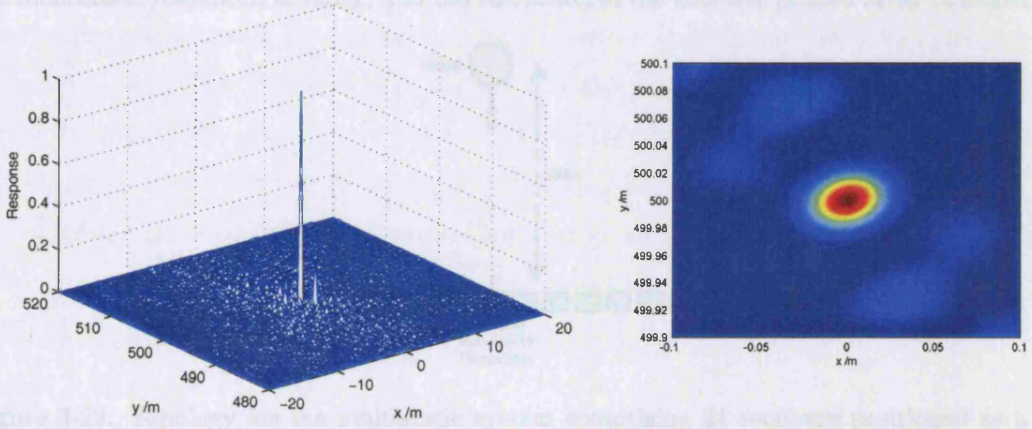

Figure 3-28: Location ambiguity diagram for a multistatic system with 10 transmitters and 10 receivers that are randomly located on a 1 km^2 plane

array antenna, comprising a single transmitter and 21 receivers, spaced at $\lambda/2$ apart (corresponding to 62.5 mm for a 2.4 GHz carrier) as shown in Figure 3-29. It was shown in Chapter 2 that the coherent algorithm effectively performs 'delay-and-sum' beamforming-on-receive in this situation. The resulting squared location ambiguity diagram (using coherent detector L_2) on two different scales is shown in Figure 3-30, which can be compared with that for a single element only in Figure 3-25. Whilst such a topology is unlikely to be implemented in a real multistatic system, it demonstrates the equivalence of the detection algorithm when the target is in the effective far-field and the assumptions on which the conventional array beamformer are based hold true. The squared ambiguity function gives a relative measure of the power in the response at the output of the detection filter. In this figure, the light green colour is equivalent to a normalised response of 0.5, so signifies the half-power point. For a linear array spaced by $\lambda/2$, the half-power beamwidth in degrees is given by(78):

$$\theta_{\text{HPBW}} \approx 102.1/N \tag{3.43}$$

where N is the number of elements. For a target at 500 m, this corresponds to a half-power cross-range resolution of approximately 42 m, which is consistent with the results in Figure 3-30. It should be noted that the ambiguity diagram is not the same as a beam pattern plot, but in this context it demonstrates the resolution capability is equivalent, and is defined by the monostatic resolution in range, and the resolution of the effective phased array in angle.

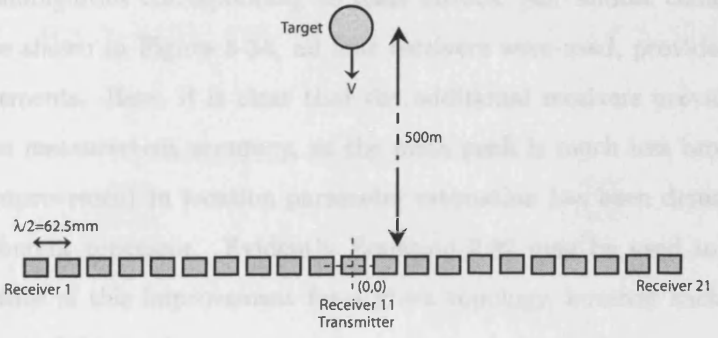

Figure 3-29: Topology for the multistatic system comprising 21 receivers positioned as a linear array

Incoherent detection

Where a coherent radar system is not available, or received signals are independently fluctuating, such processing is not possible. We now return to the topology of Figure 3-22 and consider the performance of the incoherent detector L_4. The resulting location ambiguity diagram (which is linearly plotted due to the square law summation within the detector) is given in Figure 3-31. It is clear that the incoherent processing results in a smooth main ambiguity lobe surrounding the centre matched position, which essentially comprises the power sum of the ambiguities of each bistatic and monostatic component. There are also strong ambiguity curves pertaining to iso-range lines for each of these components. The apparent ambiguity suppression caused by the interference patterns in Figure 3-26 resulting from use of the coherent detector is not present here.

Finally, it was shown in Section 2.6 that the addition of spatially separated transmitters or receivers into a system improves the theoretical estimation accuracy of location regardless of whether coherent or incoherent detection is used. The minimum number of independent time-of-arrival measurements to determine location on the plane is two. Therefore the simulation was run again for detector L_4, using the topology shown in Figure 3-32. In the first instance shown in Figure 3-33, only receivers 1 and 2 were used in a 'short baselength' topology, providing the minimum two time-of-arrival measurements. This figure shows large location measurement ambiguity , exacerbated by the short baselength, which means the iso-range ambiguities corresponding to each bistatic pair almost coincide. Then, in the second case shown in Figure 3-34, all four receivers were used, provided four time-of-arrival measurements. Here, it is clear that the additional receivers provide considerable improvement in measurement accuracy, as the main peak is much less broad. Therefore, a qualitative improvement in location parameter estimation has been demonstrated when using the incoherent processor. Evidently Equation 2.92 may be used to quantitatively predict the nature of this improvement for a given topology, however such an analysis is beyond the scope of this work.

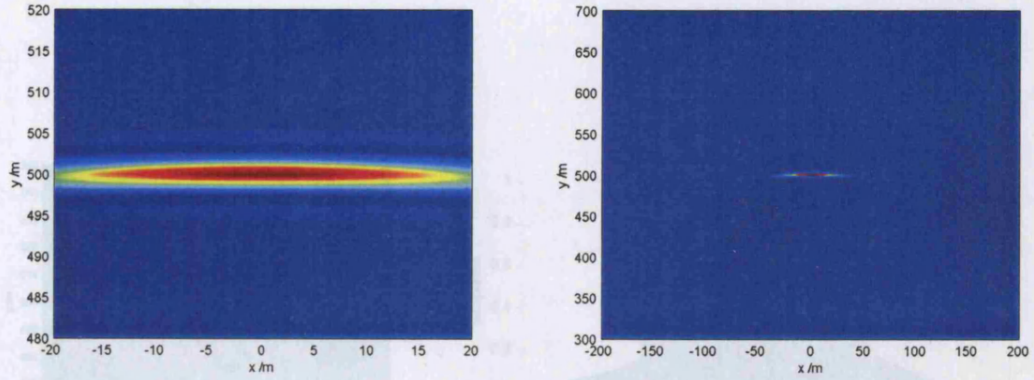

Figure 3-30: Location ambiguity diagram for the 'linear array' topology shown in Figure 3-29

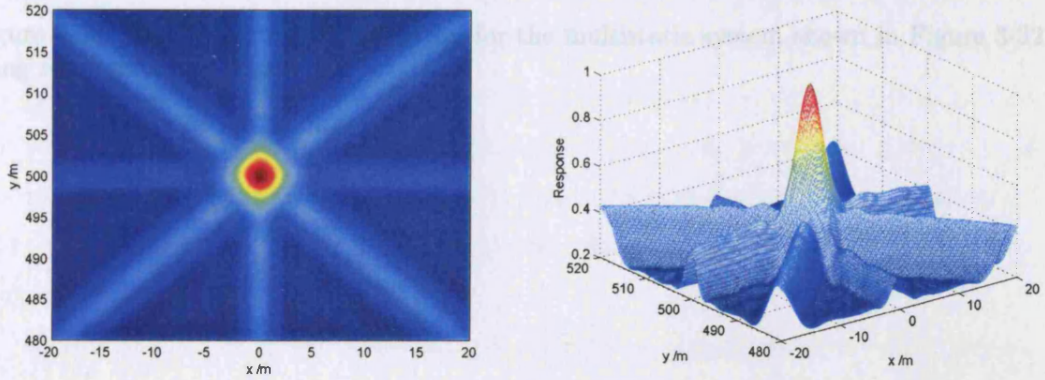

Figure 3-31: Location ambiguity diagram for the multistatic system using detection algorithm L_4

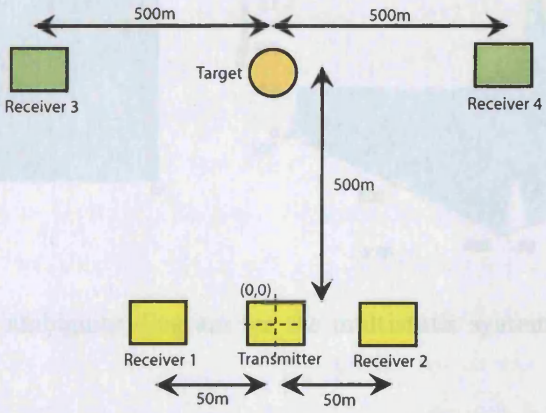

Figure 3-32: Multistatic topology for parameter estimation simulation

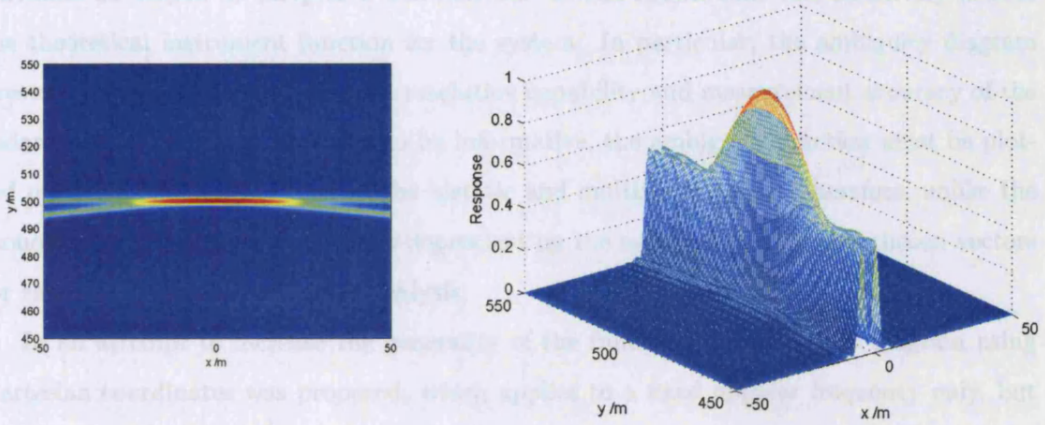

Figure 3-33: Location ambiguity diagram for the multistatic system shown in Figure 3-32 using receivers 1 and 2 only

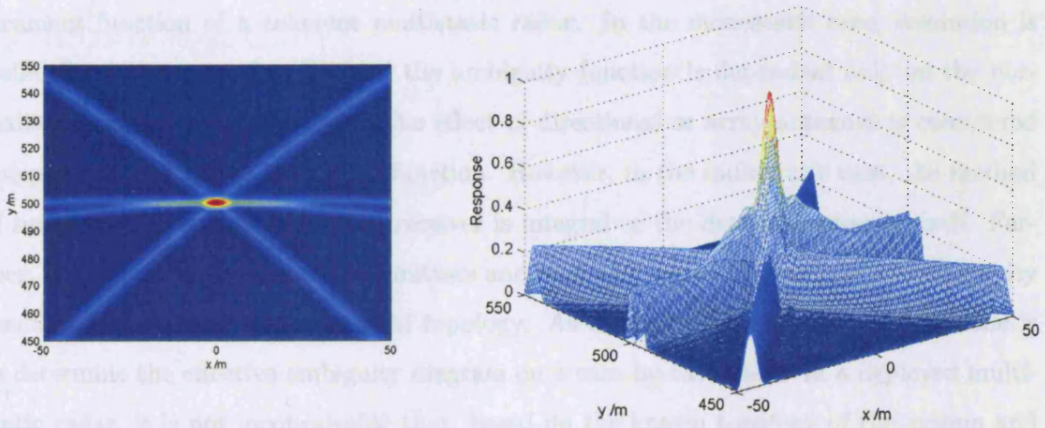

Figure 3-34: Location ambiguity diagram for the multistatic system shown in Figure 3-32 using all receivers

3.3.6 Summary

In this section, the ambiguity function for a multistatic radar based on the detection algorithms developed in Chapter 2 was derived. It was shown that this effectively defines the theoretical instrument function for the system. In particular, the ambiguity diagram presents a method of visualising the resolution capability and measurement accuracy of the radar. It was noted that, in order to be informative, the ambiguity function must be plotted on range and velocity axes in the bistatic and multistatic cases. Therefore, unlike the monostatic function, the function is dependent on the system topology and chosen vectors for range and velocity ambiguity analysis.

In an attempt to increase the generality of the function, an equivalent diagram using Cartesian coordinates was proposed, which applies to a fixed doppler frequency only, but allows analysis of all *location* ambiguities on a two-dimensional plane. It was shown that, in general, a multistatic system provides some suppression of ambiguities due to its spatial diversity. In particular, coherent detection creates interference patterns that may provide increased measurement accuracy under high signal-to-noise ratio conditions, and results in apparent suppression of ambiguity over a wider range. If a large coherent system of randomly positioned transmitters and receivers can be used, unambiguous location estimation with very high accuracy is possible.

This discussion has shown the additional complexity involved in determining the instrument function of a coherent multistatic radar. In the monostatic case, resolution is well-defined in terms of range, and the ambiguity function is dependent only on the normalised complex waveform used. The effect of directional or array antennas is considered independently from the ambiguity function. However, in the multistatic case, the method of summation of signals from each receiver is integral to the detection process itself. Further, the spatial separation of transmitters and receivers means the shape of the ambiguity function is no longer independent of topology. As a result, the best that can be done is to determine the effective ambiguity diagram on a case-by-case basis. In a deployed multistatic radar, it is not inconceivable that, based on the known topology of the system and coverage region of interest, the radar control system may determine in real-time its own ambiguity function. This could then be used to optimise the remaining degrees-of-freedom such as waveforms and even its own topology (if stations are mobile) in order to maximise

its resolution capability and parameter estimation accuracy.

3.4 Conclusions

In this chapter, the issues of radar coverage and determination of the ambiguity function have been examined. Simulations of coverage regions were based on extending the traditional 'radar equation' to the multistatic case, and the use of derived expressions for the signal-to-noise ratio achievable using the detection algorithms in Chapter 2. It was shown that coverage is topology dependent, but the addition of transmitters or receivers to the system is beneficial. The derivation of a multistatic 'ambiguity function' based on these same detection algorithms allowed the theoretical instrument function of such a system to be determined. Again, it was shown that ambiguity in such systems is highly dependent on the multistatic topology, the 'matched' target position, and the vectors on which ambiguity is calculated. A location-based ambiguity diagram was presented to show the entire ambiguity pattern on a two-dimensional surface, and it was shown that significant ambiguity suppression was achieve using multistatic systems. In particular, the coherent detector creates a 'focussed' narrow main peak at the matched position, which may be used to increase location measurement accuracy in high signal-to-noise ratio conditions. The results in this section can be used to determine suitable topologies for experiments with the prototype system and give a theoretical indication of the expected instrument function for a particular set of parameters.

Chapter 4

System Design and Simulation

4.1 Introduction

This chapter documents the development of a design for the prototype system based on an analysis of the requirements for its performance. The structure of a generic coherent radar is shown in Figure 4-1, where the transmitter and receiver systems have been logically divided. In a bistatic radar, these systems will be located separately, whereas in a multistatic system there will be multiple instantiations of the transmitter and/or receiver systems at arbitrary locations. Further, as was demonstrated in Chapter 2, the signal processing unit associated with each receiver in the figure may in fact be partially or completely centralised in multistatic radars.

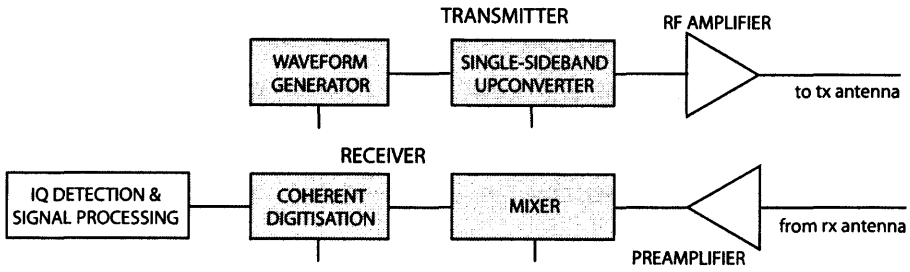

Figure 4-1: Generic structure of a coherent radar

The shaded components represent those for which coherency is necessary. Each is marked with a second input, to demonstrate that their coherency is derived from an external oscillator or clock. This model deviates slightly from the traditional 'STALO/COHO' (stable/coherent local oscillator) scheme (e.g. Skolnik(46)) as, in general, digital components are employed both in waveform generation and coherent reception so an explicit IF stage (e.g. using a 'sidestep' mixer) can be avoided.

The design of the prototype system is approached in a rather unconventional manner. In place of a 'performance-based specification', the focus is instead on obtaining the maximum performance possible within the available budget. However, clearly minimum requirements exist for critical components of the design in order for the system to be viable, and these are highlighted during this analysis. The headline design specification for the system is a three-transmitter, three-receiver, short-range coherent multistatic radar. Here, short-range implies a maximum detection range of the order of 1,000 m. The definition of coherency requirements is unspecified at the outset, although performance should be adequate to implement and test the detection algorithms described in Chapter 2, and provide doppler

measurement capability for future experiments. The total budget for the system hardware is approximately £6,000.

The first part of this chapter provides an overview of modern techniques and trends in radar system design, particularly concerning the use of commercial components from a low-cost perspective. A review is undertaken of the current state-of-the-art in technologies for the 'signal processing' and 'digitisation' elements shown in Figure 4-1, and an outline of the design for this section of the radar is described.

The second part of the chapter focusses on technologies related to the coherent components in Figure 4-1 and issues relating to their mutual coherency in a multistatic radar. The fundament of coherency is the deterministic nature of signal phases, which is related to the noise associated with the oscillators and clocks driving these components. Firstly, an analysis of these noise sources is presented, which leads to a statement of the requirements for these components in the prototype system. Then, an overview is presented of appropriate techniques and technologies for the generation and synthesis of these oscillators and clocks, followed by methods for maintaining their mutual coherency, and then implementation of the coherent components themselves. Finally, the development and results pertaining to a time-domain computer simulation of these aspects of the radar system are documented. This simulation is designed to model the effects of certain aspects of coherency errors, noise and non-synchronisation on the instrument function of the prototype radar, and in so doing confirm the specification for its design.

The design methodology for deployed radar systems has undergone a considerable transformation over the last fifteen years. In particular, systems that were traditionally built 'from the ground up', using custom-designed hardware components and proprietary software, are being replaced by designs based on largely commercial components, at a lower cost, with shorter design cycles and more flexible capabilities(79). This change has largely been driven by the military, as the nature of their threat has shifted from that of predictable threats from known opponents to dynamic and rapidly evolving threats from previously unknown opponents, which has mandated the use of more capable and versatile sensor systems(80).

The modern requirement is for radars that are flexible in their modes of operation and coverage regions. For example, radar transmitters may be capable of being instantly programmed to use a wide range of pulse lengths, PRFs, pulse bandwidths and signal wave-

forms. Back-end subsystems must be capable of controlling the system hardware with a high level of synchronisation, as well as providing versatile signal processing capabilities such as multi-mode doppler processing and an adaptive response to interference and noise, including cancellation, reselection of operating frequencies and so on. Antenna systems may be required to provide versatile electronically-steerable beam patterns, multiple simultaneously beams and modes, and concurrent operation in different modes in different azimuth and elevation sectors(79).

In general, analogue microwave components are expensive compared to digital processing systems, so recent designs have aimed to provide much of this capability in the digital domain. The so-called 'digital receiver' is one implementation of this strategy, where received signals are digitised as close to the antenna as possible, normally eliminating all IF stages so that the analogue signal chain consists of (at most) only amplification and a single-stage frequency converter[1]. In contrast, traditional 'analogue' receivers may contain several stages of downconversion and amplification, and possibly limiting or thresholding prior to analogue signal processing or narrowband digitisation. Such digital designs tend to be smaller, cheaper, more tolerant to thermal and aging effects, and have better unit-to-unit repeatability(81). Transmitter systems can be similarly designed to use wide bandwidth digital waveform generators followed by simple, single-stage analogue frequency modulators. It is possible to reprogram these predominantly digital systems without hardware changes, so subject to the availability of suitably specified digital components, these designs may lead to greater flexibility and radar capability. The same technologies that have enabled this design paradigm shift in high-end radars have also enabled the development of new classes of low-cost systems that were previously inconceivable due to prohibitive development costs, such as that described here.

4.2 Trends in Radar System Design

4.2.1 COTS

Here, a critique is presented of the issues relating to the use of modern commercial components in radar design, in terms of performance, verification and compatibility. The suitability of such components to form the basis for the prototype system design is then considered.

[1] In 'ultra-wideband' radar, no frequency translator is generally required at all.

Radar design has always pushed the underlying technology to its limits, particularly the signal processing requirements for multi-receiver and array antenna beamforming systems, where multiple high bandwidth channels must be simultaneously processed in real-time. Further, such systems must often operate in extreme temperatures and be subjected to physical shocks considerably in excess of those typical for light commercial and consumer electronic systems. Therefore traditionally these requirements were met using custom hardware and software systems, their development often being a significant portion of the total system cost(82). This development was assisted by the provision of *MIL-STD* components by commercial electronics manufacturers, which included both analogue devices and digital ICs that met specific criteria defined by the defence industry such as extended environmental tolerances, as well as offering formally verified reliability and performance specifications.

However, the *Perry Initiative*, launched by Dr William Perry in 1995 as part of the US Defense Acquisition Reform, mandated that suppliers of military systems and components (known as 'Original Equipment Manufacturers' or OEMs) should use commercial practices in order to improve value-for-money. In addition, responsibility for reliability and maintainability was to be shifted from the US Department of Defense (DoD) to the OEMs, qualified by performance-based specification. In order to ensure competitiveness, the OEM system suppliers adopted the use of 'Commercial Off-The-Shelf' (COTS) components, particularly integrated circuits such as digital signal processors, where development had been rapid and the large emerging commercial market for such products ensured high levels of competition.

COTS has provided performance in military systems that is vastly superior to the former custom-designed systems in terms of capabilities, and many new COTS-based systems(83) and legacy upgrades(84) are currently in production. Indeed, COTS is the primary *enabler* of modern multistatic radar, as it has provided very high performance digital processing, control and networking components at a low cost. Recent developments in the commercial sector, particularly mobile communications, have allowed considerable *technology transfer* into military hardware design - the digital processing and control platforms of modern radars are remarkably similar in terms of architecture and hardware to those for software radio and wireless basestations(85).

As demand for MIL-STD components has declined, manufacturers have reduced production to the point where OEMs are forced to *uprate* COTS devices via their own testing procedures. Still, lack of information about the fabrication process prevents full verification,

although some manufacturers have responded by manufacturing new lines with improved traceability and verification but without the cost of full MIL-STD testing(86). The lifespan of military systems is typically several decades compared to an average 'introduction rate' of two years for COTS microprocessors and only nine months for memory families(87). OEMs have attempted to mitigate this obsolescence, either by stockpiling components at design-time to cover maintenance for the entire expected lifespan (which may be difficult to manage and financially infeasible), or by substitution or partial redesign at regular periods during the deployment period. Similar problems exist in other sectors where systems must be serviceable for long periods of time, such as the commercial aerospace industry. Recent approaches have involved multiple OEMs cooperating in order to maintain common component specifications(88) and more systematic management of the selection and substitution of components based on quality assurance and traceability(89).

The total cost of obsolescence is often greatest in the case of software programmable devices such as microprocessors and digital signal processors due to the costs of porting existing code, which may involve considerable redevelopment and testing, even if the replacement component is part of a defined upgrade path and supports a common programming language(90). Recent initiatives have attempted to develop more *generic* programming methodologies that are largely independent of the design-time choice of component within a broad device family. The most high profile, such as that at the Defence Technology Centre for Electromagnetic Remote Sensing, have been based around the use of Field Programmable Gate Arrays (FPGAs), which are becoming more pervasive in the commercial sector. FPGAs differ fundamentally from microprocessors in so far as they contain no arithmetic/logic unit (ALU) as such, but instead comprise a very large number of *uncommitted* logic cells that may be jointly assigned to a wide range of numeric or logical functions. The upgrade path of these devices is largely based on increasing the number of cells and the speed of routing between them, whilst maintaining a generic structure onto which high-level languages can be compiled or 'building block' soft-cores can be mapped. This structure allows the decoupling of valuable application-specific intellectual property (IP), such as signal processing algorithms or timing and control systems, from the silicon itself.

In general, the same cost benefits resulting from COTS design are not found in RF analogue components, as they are still designed for a specialist low-volume market. However, the proliferation of wireless communications products has created a new market sector

for certain RF components with particular specifications - for example, frequency range, power handling capability and dynamic range. It is evident that the cost of the prototype system may be reduced significantly if such products can be used. In particular, the current popularity of the IEEE 802.11 wireless networking protocol, the most common variants of which operate at 2400 MHz in the unlicensed ISM (Industrial, Scientific and Medical) band, has resulted in the availability of a wide variety of low-cost power amplifiers, low-noise amplifiers, filters and directional antennas. This carrier frequency is in the radar S-band, the main disadvantages of which are relatively large antennas, poorer angular resolution and smaller (and so harder to detect) doppler shifts compared to higher frequencies. Further, the design of radar systems that use the same frequency spectrum as consumer devices has the potential to cause interference problems if used in built-up areas(91). Nevertheless, for the short range, low power requirements of the prototype system, it is expected that these constraints and the limited dynamic range of the low-cost components will not be prohibitive.

Apart from high-end, low volume radar systems, COTS has also enabled the development of true low-cost *systems*, designed for consumer or commercial applications where volumes are greater. There are many emerging applications for such systems, including automotive collision avoidance radar using multiple, highly integrated, multi-beam doppler sensors(92), commercial maritime and civilian security applications. There are several such prototype systems documented in the literature, including a low-cost adaptive multimode radar using a COTS architecture(93), and an ultra-wideband COTS-based digital waveform generator(94). A system in production developed by Plextek(95) uses exclusively low-cost commercial components - the microwave modules were originally designed for the satellite communications industry, and the transmission and receiver processing is performed in a single embedded digital system. The low-cost model becomes increasingly enticing for multistatic systems, particularly where the number of transmitters and receivers comprising the network is large, although there are no known published accounts of such designs.

4.2.2 Open Architectures

It is evident that the design of COTS based radar systems must take into account the likely obsolescence of components during the serviceable lifetime of the system. Then, it may be possible to substitute replacement components at low cost that allow significant per-

formance improvements as part of a planned mid-life upgrade path. This strategy is only feasible if it is possible to decompose the radar system into discrete functional subsystems, which can then be upgraded and developed individually, thus allowing for easier integration of new components as they become available. Such an architecture depends on the *interfaces* between each component and their subsystems. *Open Architectures* is a term used to describe components conforming to formal interface specifications, which are publicly available and fully defined by group consensus(96). Common examples include those of personal computer interfaces such as the IEEE1394 standard (Firewire) and the PCI bus. Designs based on an open architecture approach allow the substitution of functionally compatible equipment from different manufacturers based on performance and/or price, and replacement of components without consideration of the impact on the remainder of the system beyond the interface.

In radar design, open architectures provide a way of interfacing the major digital subsystems together, including data capture, signal processing, timing and control subsystems. Traditional examples such as the VME backplane bus have been common in radar development for many years, although modern replacements such as the PCI Mezzanine Card (PMC) are becoming popular due to their lower cost and lighter weight(97). These specifications define the physical interface only, so some radar-specific architectures have been proposed such as the US Army ROSA system(98), which incorporates a high level software protocol over a VME frame.

It is certainly not the case that COTS components are inherently open architectures compliant. The requirement for open interfaces can be specified for individual ICs, or alternatively at the 'board' or submodule level. The latter is more common, as it is typical for individual COTS components to have proprietary interfaces, and such an approach enables OEMs to design these components into a functional board-level subsystem, where the necessary control logic for translation to the open architectures interface is developed. However, this approach leads to an additional vendor-specific layer between the COTS components themselves and the interface. Further, the benefits of open architectures can only be achieved if the chosen interface is (and remains) popular enough to receive considerable commercial support. The likely obsolescence of a standard during the lifetime of the radar will remove the opportunity for modular upgrade. The interface must also be able to support the real-time requirements for intercommunication between modules, in terms

of bandwidth and latency. Lastly, support for a defined hardware interface standard does not ensure compatibility. For example, PMC-based submodules must also support a common software interface layer, often through the use of device drivers. In low-cost embedded systems, the overhead (both physical and in terms of processing power) may outweigh the advantages.

An alternative to the use of open architecture hardware interfaces is a design based around modular 'soft-cores' implemented in a configurable logic device such as a FPGA. The 'virtual' interfaces between the cores are now defined by an open architecture software standard, such as the Wishbone interface developed by Opencores(99). The resulting system is known as *System On a Chip* (SoC). The virtual interface between soft-cores may be considered to be equivalent to a backplane hardware interface, consisting of data and address busses plus control lines, all of which are synchronous to the FPGA reference clock. Therefore the interface has a *variable timing specification*, such that the speed (and therefore effective bandwidth) of the interface is not specified explicitly, but instead is determined by the design and routing performance of the underlying physical matrix on the FPGA. Therefore, the entire soft-system may be transferred to a more modern (faster) logic device with minimal development overhead, yet an increase in performance of both the modular cores and their interfaces may be realised. In the case that another virtual interface standard were to usurp the incumbent, the development of a software-based logic translator for existing IP cores is a relatively trivial task.

Of course, the SoC module must still be able to communicate with the 'outside world', which may include data converters, waveform generators and the user interface. These hardware COTS components may be connected directly to assignable pins on the logic device, so that no explicit hardware interface is required. OEMs may provide soft-cores (with appropriate licensing) that provide the logic functionality that was previously embedded into custom board level hardware. The disadvantage of such an approach is that, to make best use of SoC, the entire system must be able to fit onto a single logic device. It is possible to design a system where soft cores are shared amongst several FPGAs, although this necessitates a physical interface between each chip that adds somewhat to design complexity. Nevertheless, as increasingly powerful logic devices are being continually developed, this constraint is becoming less onerous.

4.2.3 Summary

In summary, it is clear that whilst COTS components have enabled the development of very high performance radars at relatively low cost, the issues of physical interfaces and obsolescence are limiting factors. The potential benefits are too great to ignore for the prototype multistatic system, so it is evident that the design must be based on commercial components if it is to meet budgetary constraints. A further concern is that it should provide a flexible test-bed for future development within the University, and so where possible modular and generic design approaches should be used in order to facilitate capability and performance upgrades. At the same time, a necessary balance must be found between design ideology, cost and development time. In the next section, a review of commercially available components for the digital radar back-end is undertaken such that a specific design strategy can be formulated.

4.3 Digital Subsystems

It was suggested in the previous section that greater system flexibility at low cost may be achieved if a 'digital receiver' design is used in the radar, which implies minimisation of the number of analogue components in the receiver chain. Similar flexibility may be achievable if the transmitter is also designed in this way. However, such an approach places greater emphasis on the capability of the digital components. In this section, a review is undertaken of the currently available commercial components for the major digital subsystems in a radar - analogue-to-digital conversion, system timing and control, and digital signal processing.

Analogue-to-digital converters (ADCs) provide the interface between the analogue and digital domains in the receiver. An 'integrated' ADC comprises a 'sample-and-hold' mechanism (which keeps the input signal steady whilst its digital value is determined), combined with the quantiser itself. ADCs are specified by two 'headline' parameters - the maximum sample rate and the resolution. The maximum sample rate states the maximum frequency that may be applied at the reference clock input, and therefore, by the Nyquist criterion, dictates the maximum bandwidth of an input signal that may be digitised without aliasing. The 'analogue input bandwidth' is sometimes stated separately, and relates to the linear frequency response range of the sample-and-hold amplifier at the input of the converter. If this value is well above the maximum sample rate, it is possible to 'subsample' a bandpass

signal at an IF within that range without prior conversion to baseband. Resolution is stated as the number of bits that comprise the digital output word, and is directly related to the quantisation noise and maximum theoretical dynamic range. However, non-linearities in the quantisation process(100) limit the converter's performance in terms of signal-to-noise ratio and spurious-free dynamic range (SFDR). They are often expressed in terms of a single value, known as the 'effective number of bits' (ENOB), which is an amalgam of the 'ideal' quantisation noise and the noise resulting from the various non-linearities. The ENOB is usually (weakly) dependent on the signal input frequency and sample rate.

Analogue-to-digital converters are commonly available in several different architectures, including 'successive approximation' and 'integrating' converters (which do not require a sample-and-hold) for low bandwidth applications, and 'delta-sigma' converters for moderate bandwidths, which provide very high resolution by oversampling the input signal and digitally decimating. The most common architecture in the range from a few MHz to over 100 MHz is the 'pipelined' ADC. Here, the input signal is kept stable by the sample-and-hold, and its output quantised at low resolution (e.g. 3 bits). This quantised signal is then converted back to an analogue voltage and compared to the stable input voltage. The resulting residue is passed to the next in a chain of several such quantisers and comparators, which jointly determine the total quantised value. Such designs provide good resolution at large bandwidths, but have relatively high latency due to the multiple pipelined stages. The final class of converter is a pure flash converter, which consists simply of a sample-and-hold followed by a parallel bank of comparators for each possible code value. Such designs provide the highest possible sampling rate and very low latency. However, the number of comparators required increases by a factor of two for every bit of resolution, so very high resolution converters are not feasible.

Where converters are required at still higher sample rates, multiple parallel ADCs may be used, each operating from separate phase-aligned reference clocks (e.g. two such clocks in antiphase). The phase relationship between these clocks is very important for satisfactory performance, and adds to design complexity(101). However, 'digital clock management' (DCM) features on some of the most modern FPGAs allow multiple phase-adjusted signals to be generated from a single reference clock, with granularity as low as 1/256 of the input clock period(102), which provide an ideal method of clocking parallel converters provided the jitter is adequately low. Some of the fastest converters are custom-designed and integrated

into high bandwidth digital oscilloscopes(103).

At the system design time, ADCs were available *commercially* from mainstream manufacturers with maximum sample rates of 1 GHz at 8 bit resolution (flash), and 105 MHz at 12 bit (pipelined). A resurvey at the time of writing reveals that only modest improvements in these parameters have occurred. There exists a compromise between maximum sample rate and resolution, and in addition, the higher power requirements of top specification converters may need to be taken into account.

In a digital radar receiver, the ENOB of the ADC determines the baseline dynamic range (or signal-to-noise ratio) of the receiver[2], which is approximately given by:

$$\text{Dynamic range (dB)} = 6.02 \times \text{ENOB} + 1.76 \tag{4.1}$$

In a monostatic system, the use of sweep-gain amplifiers in the analogue chain can be used to extend this dynamic range. However, the digital receiver philosophy is to minimise the number of analogue components in the signal path, and in addition, in a multistatic radar there is not usually a linear temporal relationship with expected signal power from which the amplifier gain can be controlled.

In order to approximate the dynamic range required for the system, we resolve to the monostatic case. The two major requirements in this context are related to the simultaneous detection of targets with very small and very large RCS (including clutter), and the maximum size of the coverage region(46). A typical 8-bit converter has an ENOB of 7 bits, which produces a maximum dynamic range of 44 dB, whereas a 12-bit converter with ENOB of 11 bits results in a dynamic range of 68 dB. Typical values of RCS range from 0.1 to 150 m^2(53), which is a difference of 32 dB. The received signal power for otherwise fixed parameters is proportional to $1/R^4$ where R is the monostatic range (Equation 3.5). Therefore the ratio of minimum range to maximum range for a given target is 12.6 for the 8-bit device, and 50 for the 12-bit device. For a nominal minimum range of interest of 20 m, this gives rise to maximum ranges of 250 m and 1,000 m respectively. It is therefore concluded from this simple analysis that a 12-bit converter is adequate to meet the requirements for short range detection for a typical range of targets.

[2]In certain situations it may be appropriate to utilise appropriately shaped noise (dither) to 'randomise' the quantisation noise and reveal coherent signals present below this noise 'floor'(104).

The sample rate of the converter determines the maximum signal bandwidth that can be captured, and hence is related to the range resolution of the radar. Whilst analogue techniques such as inter-pulse stepping of the local oscillator can be used to increase range resolution whilst maintaining a common digitisation bandwidth, this additional complexity is undesired for reasons of complexity, cost and use of the 'digital receiver' design paradigm. For the applications envisaged for the prototype system, a moderate monostatic-equivalent range resolution of 3 m is considered adequate, which to a first approximation ($R_{\text{res}} = c/2B$) equates to a signal bandwidth of 50 MHz. For design simplicity, it is desired to use a single-channel ADC only, so a sampling rate of 100 MHz is required. These specifications fall conveniently into the high-end of the low-cost commercially available pipelined ADCs. Based on a survey of these devices, the Analog Devices AD9432 monolithic pipeline ADC was chosen for the prototype design. This allows a maximum sampling rate of 105 MSPS at 12-bit 'headline' resolution, with a typical ENOB of 11 over the baseband Nyquist range.

Clearly, digitisation of signals with high bandwidths and dynamic ranges is only feasible if the necessary signal processing can be performed within the required temporal bounds. For example, a real-time system may have stringent requirements for the latency of plot or track determination. The performance of digital signal processors has increased rapidly in the past few years, aided by the proliferation of personal computers and wireless communications devices at the consumer level. It is possible to delineate the commercially available components into four separate categories. Firstly, there is a range of general purpose CPUs that can also perform signal processing fairly efficiently - the Motorola PowerPC Altivec is particularly popular in radar applications(105). Secondly, there are 'dedicated' digital signal processor ICs, which are often referred to as just 'DSPs'. These include Analog Devices SHARC and Texas Instruments C5000/C6000 series, and are usually discriminated from standard CPUs by having a single-cycle multiply-and-accumulate (MAC)[3] and on-chip peripherals such as multi-channel DMA controllers, communications ports, shared resources for multi-chip applications, and facilities to assist integration and debugging in embedded systems (e.g. JTAG interface). The use of such DSP chips combined with an ARM core, which is a commercially licensed IP model that can be incorporated on third party OEM

[3]In fact, the TI DSP series has separate multiply and accumulate facilities, but uses a VLIW architecture to achieve high signal processing performance.

chip designs, is becoming increasingly popular in the embedded DSP market (e.g. mobile phones). Thirdly, there exist highly dedicated ASICs designed to perform one particular DSP procedure (such as the Graychip Digital DownConverter (DDC)). Lastly, it is also possible to implement signal processing algorithms on programmable logic devices such as FPGAs. Such an architecture may be combined with a virtual emulated CPU soft-core in order to provide a 'one chip' solution where the general processing requirements are not too great.

FPGAs can provide great performance advantages in signal processing compared to conventional processors due to the potential for vast parallelism. Many modern radar designs are based on a combination of an FPGA and the Motorola PowerPC Altivec CPU(105). Here, the FPGA is used to perform the intensive signal processing, whilst the CPU performs general control and management tasks. DSP development on logic devices using existing tools requires specialist skills, is time consuming and relatively inflexible, although new software tools such as Gedae(106) and Handel-C(107) offer 'building block' design and translation of legacy code to VHDL. Still, at present the best performance is obtained from careful direct coding and optimisation with native tools(108).

Traditionally, the relative performance of digital signal processors has been expressed in terms of MIPS (millions of instructions per second) or MACS (multiply-accumulates per second), which can be misleading due to many other dependent factors such as instruction complexity and memory access speed(109). FPGA and dedicated ASIC solutions are excluded from such comparisons as they do not have a central processing unit in the traditional sense. An alternative metric is the time taken to perform a single task - typically a fixed-length Fast Fourier Transform due to its ubiquity in digital signal processing applications. It was shown that an FPGA implementation of a 1024 point complex FFT using a relatively elderly Xilinx Virtex XCV1000 FPGA for a radar signal processing application had a processing time of 20.5 μs, some seven times faster than the equivalent optimised code for a PowerPC 750 CPU, and three times faster than a TI C6201 DSP(110). Where multiple received channels can be simultaneously processed (such as following element digitisation of an array antenna), the effective increase in performance is still greater.

In many cases, it is not important that the signal processing is performed coherently with a reference clock (so that the processing latency is exactly deterministic), as long as the output is available within certain bounds. However, a coherent radar always requires the

timing and control (T&C) system to be synchronised. This subsystem may be responsible for controlling the exact times of signal transmissions, determining the period over which the ADC captures data, timing the pulse repetition interval and so on. In a multistatic system, the synchronisation of these events is even more important as they must be controlled across the entire distributed system. In general, the synchronisation resolution must be to within a small fraction of the period of the clocks driving the coherent components (i.e. waveform generator and ADC). Therefore, the use of interrupt-based CPU and DSP systems to provide timing control is inadequate by many orders of magnitude, and these systems are now normally designed into FPGAs. The T&C system is essentially a logic device, so is ideally suited to implementation using high level languages such as VHDL. The logic cells within such a device can be defined to run synchronously from a provided reference clock, and an internal clock management system can be used to provide very low skew between the clock edges at each cell. An additional advantage of such an approach is that, due to the inherent parallelism of the FPGA architecture, timing and control cores can operate alongside DSP cores in the same device with zero impact on their mutual performance.

There are several other functions that may be implemented in the digital subsystem, such as control for the user interface and test equipment, network interfaces, and possibly digital waveform synthesis (see Section 4.5.3). Several IP soft-cores are available both commercially and 'open source' that provide implementations of open architecture network controllers and waveform synthesisers for FPGAs. It is clear therefore that the optimal digital design strategy for the prototype system is based on the use of an FPGA. The chip may be used for synchronous timing and control, interfacing other COTS components (for example data converters such as the ADC), soft-core implementations (such as a network controller), and may even perform signal processing. However, a suitable method of user interfacing is required, as well as provision for primary and secondary data storage. Further, signal processing development on FPGAs is generally slower and harder to debug than on traditional DSPs.

Therefore, it is decided to base the prototype design on the combination of an FPGA with a traditional DSP. The Xilinx Spartan IIE FPGA and Texas Instruments C6711 floating point DSP were chosen as representing a good compromise between performance and cost[4]. In this case, the non-synchronous processes (signal processing, user interface control, etc)

[4]A bill of materials is presented in Chapter 5.

may be firstly developed on the traditional processor, and migrated to the FPGA as required when they are stable.

The multiplicity of transmitters and receivers at diverse locations implies that a digital subsystem is required at each node (or station). Therefore it is decided to reduce costs as much as possible by co-locating pairs of transmitters and receivers. Then, spatial diversity of elements is still possible, but only three digital subsystems are required. The system will then comprise three 'nodes', each of which has the capabilities of a monostatic radar, plus a network interface and the necessary synchronisation and coherency capability so that each can operate as part of a co-operative multistatic radar.

In summary, there is a proliferation of commercially available components that can be used to perform data conversion, digital signal processing and timing and control in radar systems. Issues of obsolescence and proprietary interfaces have serious implications for the feasibility of upgrades and servicing to radar systems, as well as impacting on development (and debugging) time cycles. The use of FPGAs provides one way of circumventing these problems, by allowing the reuse of IP cores in future devices without redevelopment. However, it is still necessary to consider the nature of the physical I/O interface on COTS components, especially given the drive toward lower FPGA core voltages is resulting in some digital I/O standards being unsupported. Nevertheless, such an approach provides the necessary versatility and ease of development, combined with low total cost, required for the prototype system. An outline specification for the system has been decided, comprising three 'nodes' capable of both transmission and reception, each with a 100 MHz, 12-bit analogue-to-digital converter in the receiver, and local digital capability provided by a combination of an FPGA and digital signal processor.

4.4 Coherent Component Design Issues

4.4.1 Introduction

The remainder of this chapter concerns the shaded components in Figure 4-1, and methods of implementing their mutual coherency across the prototype multistatic system. The generic radar system shown in this figure is coherent if the phases of the oscillators and clocks driving these shaded components are deterministic. In the case of the single sideband upconverter and frequency mixer, the driving source is a local oscillator. In the case of the waveform

synthesiser and analogue-to-digital converter, the driving source is a clock. In a monostatic radar, the same oscillating source may be used in both the transmitter and receiver, so this coherency need be considered only temporally (i.e. whether the change in phase of the oscillator from time t_1 to t_2 is deterministic). In a multistatic radar, the separation between each transmitting or receiving element is such that the nature of the oscillator signal driving each cannot be assumed identical, so consideration of *spatial coherency* is also required.

Therefore the analysis begins with a review of the sources of noise in radar oscillators that cause instability, and is followed by the formulation of a specification for the requirements of these oscillators in the prototype system. Then, techniques for the generation and synthesis of these signals are considered, including methods of 'time transfer' in order to propagate coherent signals across the system. Finally, technologies for the coherent components themselves are considered based on the outline specification.

4.4.2 Noise Analysis

Here, the derivation of noise that pertains to an oscillator, and models for its analysis are presented. These noise sources are quite different from those described in Section 2.2, which included sources such as thermal and atmospheric noise that exist irrespective of the presence of a signal. The term 'oscillator' is used here to describe a sinusoidally oscillating signal (or the circuit that generates it) that is involved in the analogue signal path, such as the local oscillator driving a frequency mixer. The term 'clock' refers to some periodic signal that drives a threshold detector used to control a 'sampling' or digital device. Typically the threshold will be set to the mid-way or zero-crossing points, and will respond to either rising or falling edges of the clock. The shape of the clock signal away from these points can be arbitrary, although it will tend to be either a pulse waveform with sharply defined transitions, or a sinusoidal waveform, in which case the clock and oscillator are physically identical. The same analysis can be applied to oscillators and clocks, however it is typical for oscillator noise to be expressed in the frequency domain, whilst clock noise is expressed in terms of the temporal error associated with its rising or falling edges.

In the frequency domain, an ideal oscillator is represented by a suitably constrained delta function at the nominal oscillator frequency, with zero power elsewhere. Its parameters are a constant peak amplitude A, frequency f_0 and zero phase at time $t = 0$. In reality, noise is present at frequencies offset from f, which by definition causes some instability in the

oscillator signal. A noisy oscillator $v(t)$ can be described in the time domain in terms of time-varying error functions affecting these three fundamental parameters:

$$v(t) = A[1 + a(t)] \sin\{2\pi[f_0 + \Delta f(t)]t + \phi(t)\} \tag{4.2}$$

The function $a(t)$ represents amplitude noise, $\Delta f(t)$ is frequency noise, and $\phi(t)$ is phase noise. In the general case, for a good quality oscillating device, it can be assumed that amplitude noise is negligible compared to phase noise (at least at frequencies close to the carrier) and can be disregarded(111).

An oscillator circuit can be modelled as the combination of an amplifier and feedback circuit, or alternatively using the 'negative resistance' concept. Both approaches are shown in Figure 4-2. In the feedback model, the general expression is:

$$\frac{v}{v_i} = \frac{A}{1 - \beta A} \tag{4.3}$$

for an amplifier with gain $A(j\omega)$ and a frequency dependent feedback loop with transfer function $H(j\omega) = \beta A$. The feedback loop feeds a portion of energy from the output back to the resonator to compensate for its losses and maintain the oscillation. The input signal v_i is simply some transient noise at start-up, so in order for the oscillations to perpetuate when $v_0 = 0$, βA must be equal to unity and the phase shift around the complete loop must be 2π. The circuit is designed so that this occurs at the nominal frequency f_0. Whilst this is a useful conceptual model, oscillators are usually analysed with the negative resistance model. The tuned circuit shown will oscillate indefinitely once excited provided there is no resistive element to dissipate the energy. The required negative resistance $-R$ can be created from a transistor in an appropriate feedback circuit (such as is found in the well-known Colpitts, Hartley and Clapp oscillators(112)), and the resulting resonant frequency is given by $f_0 = 1/2\pi\sqrt{LC}$.

It is clear from the gain equation that an oscillator is an inherently non-linear device, which will cause intermodulation of signal and noise components in the loop. For a fairly high quality device, the oscillator loop can be considered to consist of a large, relatively clean carrier accompanied by various electrical noises, such as those described in Section 2.2. If the non-linearity in the operating range is reasonably small, intermodulation of noise components will be negligible, but intermodulation of these components with the large

carrier may be significant. In particular, flicker noise follows a modified $1/f$ power law such that its power close to DC is relatively large, and will beat with the carrier to produce close-in noise of significant amplitude.

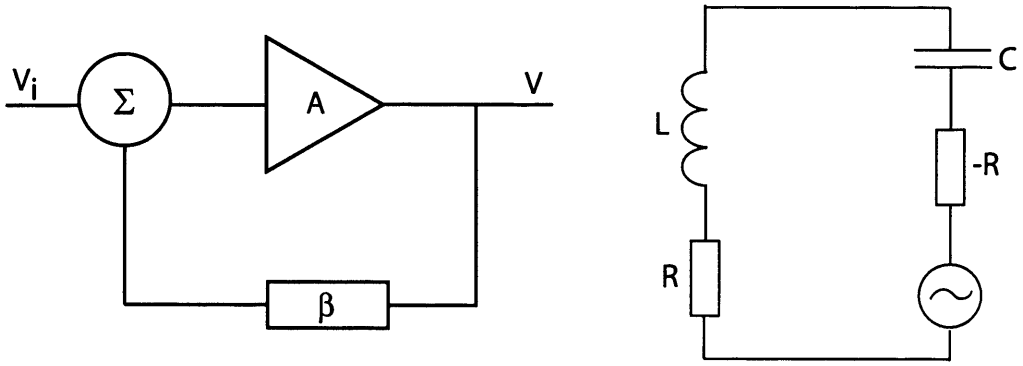

Figure 4-2: (a) Amplifier/feedback and (b) negative resistance oscillator models

For all other frequencies, a linear model can be used for analysis of the oscillator(113). A classic model developed by Leeson(114) consists of an ideal amplifier with noise figure F and a resonator. The noise at the output consists of loop noise amplified by the positive feedback and filtered by the effective Q of the resonator. The result can be expressed[5] for a carrier frequency f_0 and offset from the carrier f_m as:

$$\left(\frac{N_{op}}{P}\right)_{f_m} = \frac{FkT}{P}\frac{1}{8Q^2}\left(\frac{f_0}{f_m}\right)^2 \tag{4.4}$$

where N_{op}/P is the output noise density to carrier ratio, which is proportional to $1/f_m^2$. This expression suggests that the phase noise power density (in dBc/Hz) of an oscillator can be modelled by a $1/f^2$ power law (-20 dB per decade)[6], except close to the carrier where the $1/f$ Flicker noise contribution is amplified to create a $1/f^3$ region (-30 dB per decade). The transition point where the Flicker noise contribution dominates is known as the *flicker corner*. At larger offset frequencies the spectrum is flat due to white thermal noise. The transition point between these two regions is either where the $1/f^2$ contribution falls below the thermal noise floor, or at the edge of the oscillator resonator bandwidth (outside which, loop noise is not amplified). Therefore, for a very high Q oscillator where this bandwidth is less than the flicker corner frequency, the resulting power laws are $1/f^3$ amplified Flicker

[5]For clarity, this is expressed in slightly different notation from the original paper.

[6]Recent studies have shown that the phase noise power spectrum is in fact Lorentzian(115), and so the issue of noise power approaching infinity as the offset tends to zero is avoided.

noise as before, and $1/f$ unamplified Flicker noise. The resulting phase noise spectrum profiles for the two oscillator cases are shown in Figure 4-3.

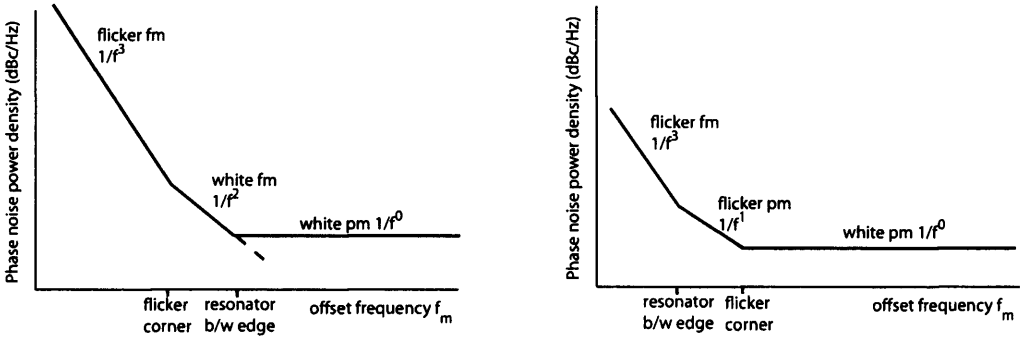

Figure 4-3: Phase noise spectrum for modelled oscillators with (a) low; (b) high Q

The four power law regions described are commonly known by the labels shown in Figure 4-3. These terms describe the apparent modulation of the carrier that is produced by the noise sidebands(116). A fifth power law called 'random walk FM' is sometimes significant, and has a $1/f^4$ relationship with frequency so is dominant very close to the carrier. It is thought that this noise is related to the oscillator's physical environment, such as mechanical shock and temperature changes. The phase noise power density to carrier ratio $\overline{\phi_0^2}(f)$ shown in Figure 4-3 is proportional to the power spectral density of the complete signal, except for the omission of the carrier. This noise power may also be expressed in terms of the frequency deviation density $(\delta f_0)^2_{f_m}$, given that frequency is the first derivative of phase(113):

$$(\delta f_0)^2_{f_m} = \overline{\phi_0^2}(f) f_m^2 \tag{4.5}$$

It has been shown by Allan (117) that the power law profiles can also be represented using a well-defined time domain stability measure $\sigma_y(\tau)$ known as the *Allan Variance*, defined as:

$$\sigma_y(\tau) = \left\langle \frac{1}{2} \left(\overline{y(t+\tau)} - \overline{y(t)} \right)^2 \right\rangle^{\frac{1}{2}} \tag{4.6}$$

where <> represents the expectation (infinite time average), and $\overline{y}$ is the average fractional frequency, given by the ratio of the frequency deviation (with density given by Equation 4.5) to the nominal frequency f_0. Therefore there is a relationship between the phase noise profile and the time domain *stability*. The Allan variance can be calculated directly using frequency measuring equipment by taking discrete fractional frequency averages over time

intervals τ, and finding the mean of the difference between adjacent values. Allan shows that each of the noise spectral density power laws in Figure 4-3 produce similarly characteristic slopes of $\sigma_y(\tau)$ for a given observation period τ, as shown in Figure 4-4.

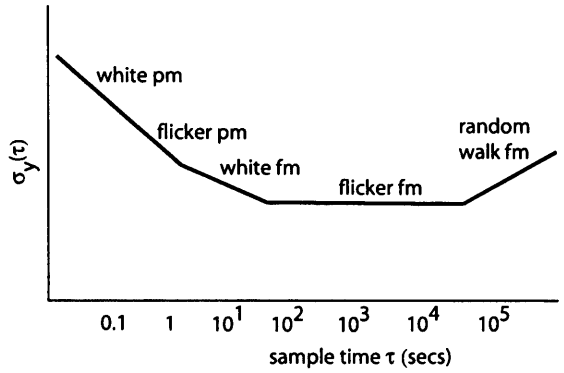

Figure 4-4: Time domain Allan Variance

This demonstrates an important result - that noise power at larger offsets from the carrier (i.e. white phase noise) results in frequency deviations measured over short time intervals, whereas noise power close to the carrier results in longer term frequency deviations. As expected, the Allan variance decreases for the most part with observation time, as longer averaging times cause cancellation of the random processes. However, beyond a certain point, the variance increases as *systemic* (non-random) effects dominate such as long-term aging and the environment related random walk noise.

Conceptually the equivalence can be further examined by analysing the modulation processes trigonometrically. Sinusoidal *phase* modulation of a carrier with a modulation frequency p and peak angular deviation θ is given by:

$$\begin{aligned} v(t)_{\text{pm}} &= \sqrt{2C}\sin[2\pi f_0 t + \theta\sin(2\pi pt)] \\ &= \sqrt{2C}[\sin(2\pi f_0 t)\cos(\theta\sin(2\pi pt)) + \cos(2\pi f_0 t)\sin(\theta\sin(2\pi pt))] \end{aligned} \tag{4.7}$$

which expands to a series of terms weighted by Bessel functions, which can be approximated for small values of θ as:

$$v(t)_{\text{pm}} = \sqrt{2C}\Big[\sin(2\pi f_0 t) + \frac{\theta}{2}\sin((2\pi(f_0+p))t) - \frac{\theta}{2}\sin((2\pi(f_0-p))t)\Big] \tag{4.8}$$

Sinusoidal *frequency* modulation of a carrier with a modulation index given by the ratio

of the peak frequency deviation to the modulating frequency $M = \Delta f/p$ is given by:

$$v(t)_{\text{fm}} = \sqrt{2C}\sin[2\pi f_0 t + M\sin(2\pi pt)] \tag{4.9}$$

which approximates to:

$$v(t)_{\text{fm}} = \sqrt{2C}\left[\sin(2\pi f_0 t) + \frac{M}{2}\sin((2\pi(f_0+p))t) - \frac{M}{2}\sin((2\pi(f_0-p))t)\right] \tag{4.10}$$

It can be seen that the effect in both cases is identical (where θ and M are interchanged), giving rise to sidebands at an offset of $\pm p$ Hz from the carrier. The equivalence can be expressed conceptually: spectral noise at moderate to large offsets from the carrier is considered 'phase noise' (small perturbations of phase on a fixed carrier), whereas noise at very small offsets can be considered as longer term frequency modulations of the carrier itself. The systematic processes, particularly temperature-dependent frequency drift and aging, are clearly long term processes (corresponding to observation times of several minutes or much longer), and their noise power exists extremely close to the carrier.

Finally, having considered the nature of noise on an oscillator in the frequency and time domains, we wish to determine its equivalent representation in the case that the oscillator is a *clock*. Here we are interested in the time deviation (or *jitter*) of the zero crossing points (or 'midway' points in the case of a DC bias), as this is nominally where a detection threshold is placed. This measurement is equivalent to determining the frequency stability of the oscillator. Firstly, the modulating effect of a superposed 1 Hz bandwidth noise sideband is considered at a frequency offset p Hz from a carrier with signal power C. A 1 Hz bandlimited noise signal is approximately sinusoidal for a period of one second, so the total signal $v(t)$ can be represented as:

$$\begin{aligned} v(t) &= \sqrt{2C}\sin(2\pi f_0 t) + \sqrt{2N_0}\sin[2\pi(f_0+p)t + \psi] \\ &= [\sqrt{2C} + \sqrt{2N_0}\cos(2\pi pt + \psi)]\sin(2\pi f_0 t) + [\sqrt{2N_0}\sin(2\pi pt + \psi)]\cos(2\pi f_0 t) \end{aligned} \tag{4.11}$$

where ψ is some initial phase, and N_0 the mean noise power. This is an equation in the form $A\sin(2\pi f_0 t) + B\cos(2\pi f_0 t)$ so the phase angle θ with respect to $\sin(2\pi f_0 t)$ is given by

$\tan(\theta) = B/A$. Given $C \gg N_0$ and $\tan(\theta) \approx \theta$ for $\theta \ll 1$, it is possible to write:

$$\theta(t) \approx \sqrt{\frac{N_0}{C}} \sin(2\pi pt + \psi) \tag{4.12}$$

The phase function $\theta(t)$ therefore varies sinusoidally, with an rms modulation index given by $\phi = \theta/\sqrt{2} = \sqrt{N_0/2C}$. Half of the power from this noise sideband is amplitude noise, and the other half phase noise, so the phase noise component can be denoted $N_{0p} = N_0/2$. Considering this sideband as a random process, the equivalent phase variance can be written as $\overline{\phi_0^2} = 2N_{0p}/C$. Assuming that modulation indices are small, the approximation of superposition can be used, and the phase jitter power density components over a given single-sided bandwidth b can be integrated to give the total phase jitter variance:

$$\overline{\phi^2} = \int_0^b \left(\frac{2N_{0p}}{C}\right)_f df \text{ rads}^2 \tag{4.13}$$

Then, the rms time jitter for a clock frequency f_0 is given by:

$$t_{jitter} = \frac{\overline{\phi}}{2\pi f_0} \tag{4.14}$$

The choice of upper and lower offset limits for the bandwidth b over which the jitter is calculated is dependent on the application. When the equipment is required to operate for a finite period T, frequency stability over time intervals much greater than T is irrelevant, so a lower limit of $1/2T$ is adequate(113). For the upper limit, it is noted that the phase noise density at large offsets is dominated by white noise, which corresponds to a *frequency* deviation density rising by 20 dB per decade. Hence, inappropriate specification of the upper limit may result in erroneous estimation of stability requirements. If the oscillator is used directly in the signal path, the upper limit may be set at the maximum RF or IF bandwidth of the system, as noise outside that range will be filtered. If the oscillator is used as a master oscillator (or reference clock), the limit should be determined by the effective bandwidth of the input to the system (such as frequency synthesiser or ADC) that is being driven. The consequences of this effect are considered in context in the following discussion.

In summary, a method for analysing the nature of noise in a radar oscillator has been presented based on well-known models. It was shown that the noise can be represented in the frequency domain by a series of power law models, and that the effect in the time

domain can be analysed using the Allan Variance. It is useful to consider very short term frequency deviations as modulation of instantaneous phase (wideband phase noise), and long term deviations as modulation of the carrier itself. It has also be shown how measurement of oscillator noise can be used to determine the equivalent jitter when the signal is used as a clock. These results form the basis on which the effects of oscillator noise on radar performance can be analysed, and a suitable design for the system of oscillators in the prototype multistatic system can be formulated.

4.4.3 Background to Coherency Requirements

The generic radar shown in Figure 4-1 generates and transmits an RF signal with known parameters, which any signal captured at the receiver can be compared to in order to discriminate the wanted signal from background noise. These parameters are the time of transmission, amplitude (although this is rarely used in radar measurements), the normalised baseband complex waveform, the carrier frequency and, in the case of a coherent transmitter, the phase. Therefore, the system should be synchronised so that there is a common reference on which the times of transmission are based. Further, in order for the complete system to be coherent, the unknown contribution to the phase of the digitised received signal should be related only to its propagation time - in other words, any phase shift imparted by the radar equipment should be deterministic.

The waveform generator is configured with the required (known) parameters to synthesise a baseband signal at time t_1, based on a reference oscillator or clock, which is then used to modulate a local oscillator in the single sideband upconverter, and the resulting RF signal transmitted. Upon reception at time t_2, the signal is downconverted by a further local oscillator, and then digitised using a reference clock. Non idealities in any of these processes will cause the received signal to non-deterministically deviate from the known parameters. There are two possible sources for these non-idealities - the components themselves, and the clocks/oscillators driving them. Here, we consider the latter case with the intention of defining the requirements for these oscillators in the prototype multistatic system based on the analysis of their related noise from Section 4.4.2.

Firstly, we consider the effect of gross synchronisation errors between the waveform generator and the digitiser. The waveform generator is defined to include the synthesiser itself, plus the timing logic for determining when signals are transmitted, both of which are

controlled by the same reference clock. The digitiser includes both the ADC and similar synchronisation logic for determining when data is collected. These logic counters perform frequency division of the reference, so there is inherent timing ambiguity equal to the period of the clock, and some external signal is required at start-up to simultaneously reset them to a known state. Inaccuracies in this synchronisation may result in large ranging errors. For example, a counter offset of 100 ns (10 cycles of the reference clock) results in a systematic monostatic range error of some 30 m. If instead the synchronisation is correct but there is a unknown phase offset between the reference clocks, the maximum error is bounded by the clock period, and equal to 1.5 m for a 100 MHz clock. In general, the requirement is for a ranging error that is much less than the native range resolution, so the synchroniser must have accuracy better than the reference clock period.

Ranging errors may also be derived from absolute reference clock frequency offsets due to a corresponding error in the ADC sampling rate. For the monostatic case, the error can be written as:

$$R_{\text{err}} = (\pm \Delta f / f) R \tag{4.15}$$

where R is the range being measured, and Δf is the reference clock frequency error away from its nominal value f. Again, we require a ranging error much less than the native range resolution (i.e. $R_{\text{err}} \leq 30$ cm) over the maximum range of $R = 1000$ m, which results in a bound of $\Delta f < \pm 30$ kHz.

Now we consider the effect of jitter on the clocks driving the waveform generator and ADC. Jitter will result in random deviations in both the pulse length and the start time of each pulse (i.e. PRI timing errors). This has been shown to limit the clutter cancellation possible in MTI processing(118), as well as result in an increase of the noise floor and widening of PRF spectral peaks in the received signal, therefore degrading detection in pulse doppler processing(119). As will be shown in the analysis of local oscillator phase noise below, the effects are reduced when the jitter is correlated over the total observation period, and in general the effect is small compared to other phase noise induced degradation. The effect of jitter on the transmitted waveform itself is dependent on the exact nature of the synthesiser, and is discussed further in Section 4.5.3.

Jitter affecting the ADC performance is often delineated into 'aperture jitter' and 'clock jitter'. The ADC is a sampling device that essentially performs multiplication of the ana-

logue input with unit-pulses derived from its reference clock, which is equivalent to convolution in the frequency domain. Therefore close-in reference clock phase noise appears directly around each frequency component of the input signal, and it is desired that this noise should be small compared to the phase noise contribution from the local oscillators described below. Aperture jitter is caused both by thermal noise in the sample-and-hold and by *wideband* noise on the ADC clock, and results in the well-known frequency dependent degradation of the digitised signal-to-noise ratio(120):

$$\mathrm{SNR}_{\mathrm{jitter}} = -20\log(2\pi f\sigma) \tag{4.16}$$

where f is the input signal frequency and σ is the rms time jitter in seconds. This effect can be analysed for the prototype system. The chosen ADC has a maximum sample rate of 100 MHz, so we can assume a 'worst case' 50 MHz input signal. For the effect of the jitter to be insignificant, we wish the resulting signal-to-noise ratio upper bound to be greater than the SNR with harmonics (SINAD) of the ADC, which is related to the ENOB and given by the manufacturer as 67 dB. In order to determine this jitter from the phase noise density of an oscillator, it is necessary to integrate over the bandwidth of interest as shown in Equation 4.13. We consider this effect over a period of contiguous signal reception corresponding to the transmission of a single pulse in the prototype system. We can assume the approximate maximum range of interest for this short range system to be 1,000 m, which (for a monostatic system) corresponds to an observation time of 10 μs. This sets the lower bound on the integral to $1/2T = 50$ kHz. The upper bound is set by the bandwidth of the ADC encoding pin (its reference clock input), which is usually considerably higher than the sampling rate. A typical value for high-speed pipelined converters is stated as $f_{\mathrm{clkbw}} = 350$ MHz in (121). However, the sampling action results in the noise above the sample rate being aliased back into the Nyquist bandwidth several times. This additional degradation of the SNR can be approximated by $3\log_2(f_{\mathrm{clkbw}}/0.5f_{\mathrm{clk}}) \approx 8.4$ dB (121).

Therefore we require an effective SNR of 75.4 dB, which results in a maximum permissible rms jitter is 0.54 ps, which is equivalent to 0.02° for the $f_{\mathrm{clk}} = 100$ MHz reference clock, and should be calculated by integration of the phase noise over the bounds shown above. It is noted that a ten-fold increase in rms jitter results in a dynamic range reduction of 20 dB, so it is desired that the jitter in the prototype system is not substantially greater than this

value.

Now, we consider the effect of local oscillator phase noise on doppler processing performance, specifically the discrimination of moving targets from clutter in the prototype system. An empirical approximation for the monostatic 'clutter spread' due to foliage motion for a ground-based radar in the L- to X-band range given in (122) demonstrates that the doppler spread is usually less than 1 m/s, or < 16 Hz for the chosen 2400 MHz carrier frequency. Therefore, doppler processing is likely to be 'clutter limited' for detection of very slow moving targets, and for targets at other doppler frequencies where the residual phase noise relating to this clutter is dominant over thermal noise and other interferences. Initially, we assume that the baseband signal produced by the waveform generator is an ideal unmodulated sinusoid, so that the phase noise profile of the RF transmitted signal is the same as that of the local oscillator used for its upconversion at the time of transmission t_1. Figure 4-5 shows the power spectrum of the corresponding signal at the receiver antenna comprising two components. The first component, shown by a dashed line, results from the reception of a clutter component, and is shown by a spread of this signal power due to phase noise away from its nominal doppler frequency (shown at DC on the graph). The second component is a smaller received signal with doppler frequency offset f_d.

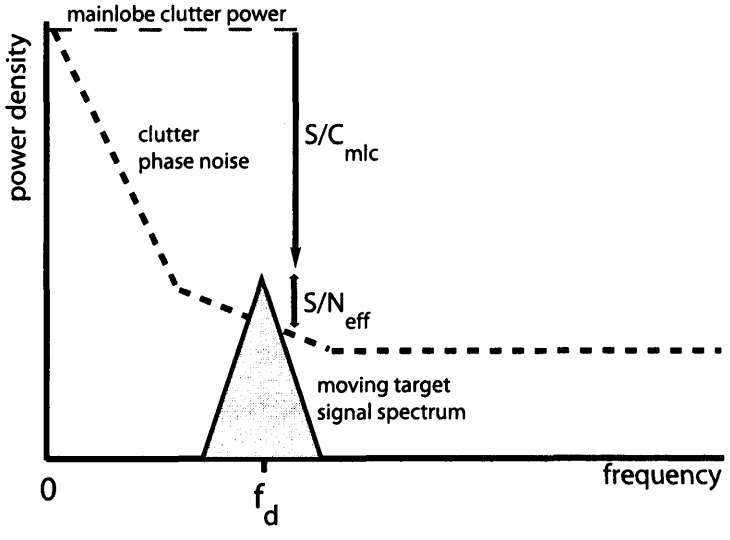

Figure 4-5: The effect of phase noise on the detection of a doppler-shifted signal

If instead the transmitted signal is comprised of a train of coherent pulses, as will often be the case for the prototype system, the baseband signal spectrum will consist of a series

of spectral lines separated by the PRF, which is then convolved with the phase noise profile of the local oscillator. Therefore the true effective clutter power at a given frequency offset is the sum of all aliased contributions of the LO phase noise, which may be significant for a low PRF system. Nevertheless, simplified calculations are appropriate for the initial performance assessment.

We firstly assume that the receiver local oscillator is 'ideal' (so performs perfect frequency translation of the received RF signal). A pulse doppler processor then attempts to discriminate this moving target from the clutter by performing a Fourier transform on the array of received digitised values corresponding to a certain range bin. An adequately low PRF is used such that there is no ambiguity in range, and clutter from several locations does not collapse into a single bin. The signal at f_d is obscured by the incoherent phase noise resulting from the clutter, reducing the effective signal-to-noise ratio and therefore degrading the probability of detection. The effective doppler filter bandwidth B_d of such a system is given by the ratio of the PRF and the number of pulses N processed in the Fourier transform. The phase noise spectrum $S_\phi(f)$ is expressed in terms of the noise power compared to the carrier in a 1 Hz bandwidth, so the power in a certain doppler bin with centre frequency f is approximately given by:

$$N_{\text{dop}} = S_\phi(f) + 10\log(\text{PRF}/N) \tag{4.17}$$

The expected doppler spread of the clutter itself is very small, so detection of the moving target with doppler shift f will be clutter-limited if the phase noise at that offset relating to clutter is greater than the thermal noise and interferences. In that case, the maximum allowable oscillator phase noise at this offset $S_{\phi\text{max}}(f)$ can be calculated (in dB) if the expected signal-to-mainlobe-clutter ratio $S/C|_{\text{mlc}}$ and the minimum allowable signal-to-noise ratio at the doppler filter $S/N|_{\text{eff}}$ for the required detection performance are both known (see Figure 4-5)(118):

$$S_{\phi\text{max}}(f) = S/C|_{\text{mlc}} - S/N|_{\text{eff}} - 10\log(\text{PRF}/N) \tag{4.18}$$

We can now apply this analysis to an expected typical scenario for the prototype system. It is assumed that we wish to detect a small target with RCS = 10 m^2 at short range (R = 500 m) using transmitted pulses of length τ = 1 μs and a low PRF of 1 kHz, with

a directional antenna of beamwidth $\Delta\theta = 5°$ mounted at a height of 50 m to give a small depression angle of $\epsilon = 6°$. Then, the clutter RCS can be estimated using the expression:

$$\sigma_c = R\Delta\theta\left(\frac{c\tau}{2\cos\epsilon}\right)\sigma^0 \tag{4.19}$$

where σ^0 is the clutter backscatter coefficient which, using the simple 'constant gamma' assumption(123) $\sigma^0 = \gamma\sin\epsilon$, we can assume to be small for low grazing angles, and assign a nominal value of -20 dB in accordance with Scheer(118). The resulting clutter RCS is 18 dB, giving a signal-to-mainlobe-clutter ratio $S/C|_{\text{mlc}} = -8$ dB. We then state that a (typical) signal-to-noise ratio of 13 dB is required for detection[7], and use Equation 4.18 to calculate the maximum allowable phase noise to avoid detection performance degradation, which on the basis of these assumptions is -31 dBc/Hz. The combination of a directional antenna and short range gives quite a favourable result due to the low illuminated clutter volume, although may be mitigated by aliasing of noise associated with adjacent spectral lines. Given the typical shape of the phase noise spectrum in Figure 4-3, it is evident that fulfilling this requirement is more demanding when slow moving targets must be detected.

Now, we assume that in fact the receiver local oscillator signal is common to that of the transmitter, which is typical for monostatic systems. Then, the incoming RF signal is multiplied with this LO by the mixer at time t_2, which is equivalent to convolution of the signal spectral density with the LO phase noise profile at that time. It is well-known that in such systems, the apparent effect of local oscillator phase noise is range dependent. This is sometimes known as the 'range correlation function', as for short propagation times τ, the LO maintains some temporal coherency between the time of transmission and time of reception, resulting in partial phase noise 'cancellation'. This situation is analysed by considering a single 1 Hz bandlimited phase noise sideband of the LO at an offset p Hz from the carrier. It was shown previously that, for a period of one second, this noise component can be represented as a sinusoidal phase modulation $\theta(t) = \theta\sin(2\pi pt + \phi)$. The baseband transmitted waveform is assumed to be an ideal sinusoidal waveform with frequency f_w without affecting generality. In this case, the transmitted RF signal can be represented as:

$$V(t) = A\exp[j(2\pi(f_0 + f_w)t + \theta(t))] \tag{4.20}$$

[7]A conservative estimate is used here, as the real 'partial' signal-to-noise ratio required in a multistatic system may be somewhat less than this figure for the same detection criteria.

Then, after a propagation time of $\tau = t_1 - t_2$, the local oscillator can be expressed as $\exp[j(2\pi f_0(t+\tau) + \theta(t+\tau))]$, and the received baseband signal (given propagation loss a) is given by:

$$v(t) = \frac{A}{a} \exp[j(2\pi f_w t + \theta(t+\tau) - \theta(t) - 2\pi f_0 \tau)] \tag{4.21}$$

where the non-deterministic phase shift involving the phase noise component $\theta(t)$ can be written as:

$$\theta(t+\tau) - \theta(t) = 2\theta \sin\left(\frac{2\pi p\tau}{2}\right) \cos\left[2\pi pt + \frac{2\pi p\tau}{2} + \phi\right] \tag{4.22}$$

Therefore, the phase noise sideband at offset p Hz from the carrier results in a sinusoidal phase modulation of the received baseband signal with peak modulation index given by $2\theta \sin(2\pi p\tau/2) = 2\theta \sin(2\pi Rp/c)$, where R is the corresponding monostatic range for propagation delay τ. We can then consider this sideband as a random process with known variance, and write the effective phase noise power attenuation (compared to the local oscillator sideband with peak modulation index θ) as a result of the range correlation effect as:

$$G_{\text{pn}} = 10 \log(4 \sin^2(2\pi Rp/c)) \quad \text{dB} \tag{4.23}$$

Hence, the apparent phase noise of the received signal resulting from the common local oscillator is greatly reduced at small doppler offsets and relating to targets at short ranges. One can envisage the same result intuitively by surmising that, for a propagation time τ, phase noise at carrier offsets much less than $1/\tau$ will remain correlated, as those components appear in the Allan variance graph over observation times greater than the propagation time. However, local oscillator phase noise at very large offsets from the carrier will not be correlated between transmission and reception as its integration time is small compared to τ. As a result, its effect is to increase the apparent noise floor of the received signal and reduce dynamic range. Using Equation 4.23, we find that, for clutter at a range of 500 m ($1/\tau$ = 300 kHz), the received phase noise power is attenuated by some 74 dB at an offset of 10 Hz; the improvement reducing to 34 dB at 1 kHz offset. This implies that, for a system where common local oscillators can be used, the constraint of maximum phase noise power at small offsets from the carrier may be significantly reduced compared to the model described previously. A comparable result is found using somewhat different analysis by Budge(124), who also shows that at low doppler frequencies, amplitude modulation of

the LO may become the dominant noise contributor from clutter as it is not significantly attenuated by this effect.

It is noted that, in each case for the analysis so far, it is the *temporal* coherency of the local oscillator over each propagation time τ that is of concern. Phase noise present in the region of doppler shifts of interest (i.e. corresponding to random deviations over several pulse repetition intervals), as well as longer term frequency deviations, are rendered largely irrelevant by the range correlation function. In other words, it is the differential phase shift over τ that is of importance, not the absolute values.

4.4.4 Coherency in Multistatic Systems

Here, an original analysis is presented of the effect of phase noise in a multistatic system, based on the previous discussion. Unlike the monostatic case, it is no longer possible to assume that the local oscillator signal driving the transmitter and receiver mixers is completely identical. Equation 4.21 shows that in the monostatic case, the phase of a given received signal has a deterministic component $2\pi f_o \tau$ plus random components related to the LO phase noise modulation at the receiver $\theta(t+\tau)$ and at the transmitter $\theta(t)$. We can now re-write this equation for a single transmitter and receiver of a multistatic system, and take into account that $\theta(t)$ is not necessarily a correlated process at each node by inserting separate phase functions θ_T and θ_R for the transmitter and receiver:

$$r(t)_{\text{multi}} = \frac{A}{a} \exp[j(2\pi f_w t + \theta_R(t+\tau) - \theta_T(t) - 2\pi f_0 \tau)] \tag{4.24}$$

If there is complete *spatial* correlation of phase noise power at a given offset so that:

$$\theta_R(t) = \theta_T(t) + \varphi \tag{4.25}$$

for all t given some constant phase value φ, then it follows that Equation 4.22 holds and the range correlation function applies. If however the two processes are mutually independent, then no such effect will occur, and the spectrum of the local oscillator at the receiver will convolve with that of the received signal, the powers summing[8] in each case. It is quite common for bistatic radars to be positioned such that the receiver can obtain a direct RF or

[8]Assuming both are independent Gaussian processes

LO signal from the transmitter by line-of-sight (for example by using an antenna sidelobe), the phase noise of which is clearly correlated with the transmitter, and so can be used as a reference to avoid problems of independent oscillator stability(43).

A similar analysis determines the requirements for coherent integration of multiple pulses transmitted by one node and received by another in a multistatic system, which depends on the phase of each received pulse being approximately constant. Here, unlike the pulse doppler processor, there is no filtering of frequency bands, so the upper limit over which the phase noise must be measured is the maximum IF frequency of the receiver, which is assumed to be 50 MHz. The lower limit is then given by $1/2T$ where T is the total observation (integration) time. Any phase noise components that are spatially correlated will be subject to attenuation from the range correlation effect described above, so will largely cancel. However, uncorrelated phase noise powers will sum in the receiver mixer convolution as before. It was found using a simple Matlab simulation that, as expected, small random changes in the initial phase of each pulse (less than 20° rms) result in negligible loss of integration gain. Therefore in general, modest amounts of phase noise have negligible effect on coherent integration processing. However, it is noted that for long integration times (which may be of the order of seconds), the lower bound of the phase noise calculation becomes very small (a fraction of a Hz), and so large *uncorrelated noise* close to the local oscillator carriers may cause the system to decohere.

Now we consider the effect of phase noise where the signals from *multiple* transmitters and/or receivers are combined coherently, such as the detection algorithms described in Chapter 2. For a single transmitter-receiver pair, the *absolute* phase of the separated local oscillators is usually irrelevant as long as the relative phase (e.g. φ in Equation 4.25) is deterministic over the period of interest (and hence the oscillators are coherent). However, Equation 2.75 demonstrates that the initial phase φ_{ik1} of each signal relative to a nominal 'reference' transmitter-receiver pair must be known. For a pair of real oscillators, this phase offset will not be constant, but will in fact be a random variable $\varphi(t)$ that is related to phase noise extremely close to the carrier resulting from phase or frequency deviations much longer than the integration time. Calculation of the required oscillator stability therefore requires

'integration'[9] of phase noise down to offsets commensurate with the *calibration interval* of the oscillators (i.e. how often the phase offset between oscillators is measured). Depending on the frequency of calibration, this noise may be most appropriately considered as short-term or long-term frequency stability. It is noted that a momentary relative frequency deviation of 1 Hz for local oscillators with a nominal frequency of 2400 MHz will result in a $\pi/2$ phase drift in only 250 ms. Therefore, adequate coherence in a multistatic radar can only be obtained using either exceptionally stable oscillators, a very frequent or continual method of system calibration, or mutual discipline of all oscillators. The final method is otherwise known as 'time transfer'.

The analysis is concluded by summarising the requirements for the oscillator system in the prototype multistatic system. Firstly, the integrated wideband phase noise of the clock driving the ADC in each receiver should be adequately small to not reduce dynamic range as per Equation 4.16. This result is unchanged in the multistatic case as the phase noise at large offsets is invariably uncorrelated. Secondly, the close-in phase noise of this clock should be small compared to the influence of the local oscillators (which will usually be the case). Then, the phase noise at local oscillator offsets of interest for doppler measurement should be less than -31 dBc/Hz based on Equation 4.18. We define this range as being from 10 Hz to 1000 Hz, which is equivalent to monostatic radial velocities from approximately 2 km/h to 200 km/h and is likely to include all targets of interest. Within these constraints, we require the maximum possible correlation of phase noise between oscillators such that the advantages of the range correlation function are enjoyed. Uncorrelated noise, particularly that very close to the carrier, must be very small in order to not decohere the relative phase of each oscillator between calibrations.

4.5 System Oscillator Design

In this section, the design of the clock, oscillator and waveform synthesis systems in the prototype radar is developed. It is clear from Figure 4-1 and the analysis in the previous section that two signals must be provided to each node in the multistatic system - a clock for driving the ADC and waveform generator with a frequency of 100 MHz, and a local

[9] In practice, phase noise extremely close to the carrier will not fulfil the small-signal model for linear integration of phase noise power, so specifications should be stated in terms of the frequency stability of each oscillator.

oscillator driving the frequency translators at 2400 MHz. The phase noise of each local oscillator should be mutually correlated close to the carrier. Further, each clock should be mutually coherent so that signal phase is preserved throughout the transmitter and receiver chains. Firstly, methods of generating these oscillators in all nodes are considered and a design strategy finalised. Then, consideration is given to the generation of baseband waveforms in each transmitter that are coherent to the reference clock.

4.5.1 Oscillator Generation and Synthesis

There are two distinct methods of implementing the requirement for coherent oscillators across the system. The first method involves the generation of a single 'reference' signal, which is distributed to each node, where the local oscillator and clock are locally synthesised. The second method involves synthesis based on some coherent third-party reference such as GPS. Here, the former case is considered and analysed in more detail due to its potentially lower complexity for implementation in the prototype system. The alternative GPS-based system is considered in Appendix E.

Firstly, a reference signal of arbitrary frequency must be generated using a free-running oscillator. For simplicity this signal should be chosen to be either 100 MHz or 2400 MHz so that the synthesis of only one oscillator (by some method of integer frequency multiplication or division) is required in each node. The choice of reference oscillator should take into account the cost and requirements for noise performance determined in the previous section, and to a lesser extent issues of size, weight, 'startup time' and power consumption. Further, in some situations the effects of acceleration, magnetic field and radiation effects are also important, although they are not considered here. Three major categories of signal generators are considered here - quartz, surface acoustic wave (SAW), and atomic.

Quartz oscillators are fundamentally equivalent to the generic model in Figure 4-2, where the LC tank is replaced by a resonating crystal. They are available at frequencies of typically a few MHz using overtone resonators, with a maximum of about 100 MHz. Such designs may have excellent phase noise properties, but are sensitive to frequency fluctuations due to changes in temperature. A typical crystal oscillator has a frequency stability of ± 20 ppm (i.e. ± 2 kHz for a 100 MHz nominal frequency). Other 'flavours' of crystal oscillator designed to improve this stability include the temperature controlled crystal oscillator (TCXO) where a thermistor is used to generate a correction voltage that is applied

to a varactor in the crystal network (typical stability ± 1 ppm), and the oven-controlled crystal oscillator (OCXO) where the crystal and other temperature sensitive components are maintained at constant temperature in a small oven, and the crystal is manufactured to have a zero-slope frequency-against-time characteristic at the oven temperature(125). The typical stability for a good quality OCXO is often better than $\pm 5 \times 10^{-9}$, or ± 0.5 Hz deviation for a 100 MHz nominal frequency. The cost of such a device may be several thousand dollars in small quantities for the best performance, compared to tens of dollars for a good quality uncompensated crystal oscillator. The phase noise power at larger offsets from the carrier may be similar between the two devices (≈ -150 dBc/Hz at 1 kHz), however that closer to the carrier is significantly improved in the OCXO (≈ -120 dBc/Hz compared to ≈ -80 dBc/Hz at 10 Hz offset[10]).

Surface acoustic wave (SAW) oscillators exist at considerably higher frequencies than crystal oscillators - they are 'natively' available up to approximately 3 GHz, although are more common at approximately 500 MHz. Fundamentally they consist of two 'interdigital transducers' (IDTs) mounted on a piezoelectric substrate such as quartz. The IDTs consist of interleaved metal electrodes that launch and receive acoustic waves along the substrate to create a resonator which is used in place of the crystal in the circuits outlined above. SAW oscillators are tolerant to vibration, and are often smaller, cheaper and more ruggedised than equivalent crystal oscillators. However, their frequency stability is quite poor, and the available tuning range may be too narrow to perform adequate temperature compensation.

SAW oscillators are frequently 'multiplied up' in radar applications from the typical native frequency of 500 MHz to the necessary LO frequency. Within a commercial oscillator unit, this is usually done by applying the signal to a non-linear circuit (e.g. a mixer using common inputs) and filtering the appropriate harmonic. The multiplied output signal has the same phase noise profile as the reference input (on a new carrier), but the noise power for all offsets increases by $10\log(N^2)$ dB due to the corresponding increase in modulation index, where N is the multiplication factor. Further, phase noise is also increased due to the multiplication of superposed thermal noise by a factor of $10\log(N^2/4)$ dB (113). An X-band generator based on a SAW oscillator has been documented with phase noise levels of -180 dBc/Hz at 1 MHz offset for its native 500 MHz frequency, which after multiplication to 8 GHz becomes -55 dBm/Hz at 10 Hz offset and -150 dBm/Hz at 1 MHz offset(126).

[10]Sources: www.vectron.com, www.crystek.com

Crystal oscillators can also be multiplied in a similar way. Multiplication of a 100 MHz crystal oscillator to 2400 MHz increases phase noise by 27.6 dB and the thermal noise contribution (which is usually dominant at large offsets) is increased by 21.6 dB. When a SAW device is compared to a 'multiplied-up' OCXO at the same frequency, the SAW oscillator usually provides lower phase noise at large offsets from the carrier at the expense of poorer noise at small offsets and poor stability.

Atomic oscillators are created by locking an electronic oscillator in a servo feedback loop to the frequency of an atomic transition, and are commonly based on caesium and rubidium. Caesium clocks are large and expensive ($30,000 - 60,000) devices that are generally confined to time standards laboratories, however small rubidium oscillators are available ($1,000 - 3,000) and are fairly widely used in bistatic radar systems. The commercially available Temex RMO is such a device, which produces a 10 MHz output signal with phase noise of -80 dBc/Hz at 10 Hz offset, and -135 dBc/Hz at 1 kHz offset. It can therefore be seen that for a similar output frequency, the OCXO offers considerably superior phase noise compared to the atomic oscillator. However, the Temex RMO has an averaged short term stability of 3×10^{-11} over one second, and 3×10^{-12} over 100 seconds, which is between two and three orders of magnitude better than a typical OCXO. In situations where both very high frequency stability and very low phase noise are required, one solution is the use of an atomic oscillator to discipline an OCXO in a suitable feedback loop. The PTF 4220a is such a device, and has stability of 2×10^{-12} over 100 seconds combined with phase noise of -128 dBc/Hz at 10 Hz and -170 dBc/Hz at 1 kHz[11].

There are several other oscillator types that are common in radar, including the Dielectric Resonator Oscillator (DRO), Gunn oscillator and reflex klystron, although for the sake of brevity and difficulties of implementation in the prototype system they are not discussed here. It is clear that the use of dedicated atomic clocks is not within the budget of this system, and that low-cost SAW devices will provide poorer close-in phase noise in the critical region for doppler detection. Further, the synthesis of the 100 MHz clock from a 2400 MHz SAW oscillator reference by frequency *division* inherently results in phase ambiguity, which would require additional synchronisation techniques to resolve. Therefore a moderately low-cost ($30) crystal oscillator is proposed, the Crystek CCHD-950, which has a nominal frequency of 100 MHz and has the phase noise spectrum shown in Figure 4-6.

[11]Source: www.ptfinc.com

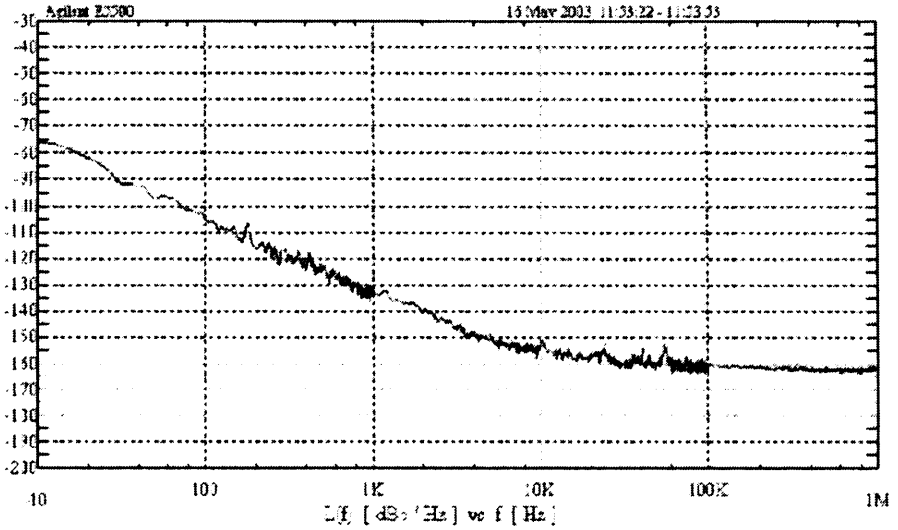

Figure 4-6: Phase noise spectrum of CCHD-950 crystal oscillator

This reference signal must be distributed to each node and used to synthesise the local oscillator before the final phase noise and coherency can be evaluated. It was shown above that the use of a simple analogue multiplier for this synthesis with $N = 24$ would result in a phase noise increase of 27.6 dB (plus the contribution of multiplied thermal noise and a non-zero 'noise figure' for the multiplier itself). If there is no degradation of the reference during the distribution process, this would result in a phase noise of -48.4 dB at a 10 Hz offset. Whilst this is still within the derived doppler processing bounds, a similar increase throughout the spectrum would result in large increases in wideband integrated noise. Further, such a multiplier would be bulky, lossy and expensive. Therefore the phase locked loop (PLL) is considered as an alternative method of synthesising the LO source.

A PLL uses a digital divider as the feedback element in a closed loop system to phase lock the output of a discrete voltage controlled oscillator (VCO) to a reference signal, as shown in Figure 4-7. The $1/R$ divider at the reference clock input reduces the input frequency to a value that is suitable for the phase detector. The second input to the phase detector is the divided $(1/N)$ output signal from the VCO. In 'fractional-N' PLLs, this division ratio is modulated to provide improved frequency resolution, at the expense of additional phase noise. The phase detector generates some response at its output (typically 'charge pump' current pulses) that is proportional to the phase difference between the two input signals. This response is filtered, and the resulting signal applied to the DC tuning input to the

VCO. Once transients have settled, the loop will lock such that the output of the VCO has a frequency that is N times larger than the reference frequency, and locked in phase.

A typical COTS integer-N PLL, the National Semiconductor LMX2326, is considered. This chip integrates a digitally programmable R-counter, phase detector, charge pump, prescaler and N-counter into a single integrated circuit. The VCO output will track changes in the reference input (including frequency and phase deviations) within the constraints of the bandwidth of the loop filter (and the tuning range of the VCO). Therefore a wide bandwidth loop filter allows short 'lock times' (the time taken for the VCO output frequency to change in response to a change in the reference input frequency), although in this situation the lock time is of no consequence as a constant frequency local oscillator signal is desired. The phase noise of the reference signal is multiplied within the loop bandwidth (similarly to the analogue multiplier described above), however importantly it is attenuated by the filter out-of-band. Therefore the phase noise of the VCO signal is largely correlated with that of the reference within the loop bandwidth and, if this is commensurate with the doppler range of interest, it will be possible for the phase noise within that band for all local oscillators in the system to be correlated, and the range correlation function may be (at least partially) apparent.

On the other hand, the loop attenuates VCO phase noise within its bandwidth, but noise that is out-of-band is unaffected. Therefore in reality, the chosen bandwidth is also a compromise between attenuation of in-band VCO noise, attenuation of out-of-band reference oscillator noise (which together largely determine the total integrated phase noise), and the realisability of the filter from practical components. Other sources of noise include those generated internally by the loop, especially that from the phase detector, and also thermal and flicker noise. A commercial VCO, the Universal Microwave Corporation UMV-2450-R16 was selected for relatively low phase noise, low cost, and compatibility with the chosen

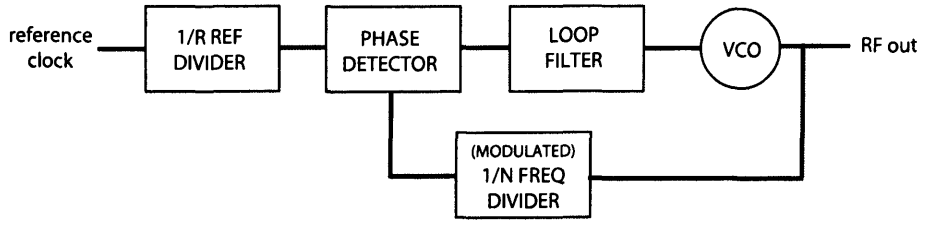

Figure 4-7: Generic phase lock loop

PLL. The NatSemi 'Webench EasyPLL' software was then used to analyse the device and design the loop filter. The optimal filter bandwidth for minimisation of integrated noise can be estimated by finding the frequency offset at which the unattenuated VCO phase noise and 'multiplied-up' reference oscillator noise intersect. This was found by simulation to be approximately 2 kHz, which conveniently coincides with the minimum filter bandwidth that is practically realisable using a simple third-order passive filter, and is also just outside the doppler band of interest. It is known that a large N division factor raises the loop gain of the reference signal and phase detector noises, which results in a further increase in the in-band phase noise(127). Therefore it is advantageous to reduce the feedback ratio, and so raise the sampling frequency at the phase detector inputs as high as possible. It was found that the maximum input frequency to the phase detector at which the loop was stable was 6.25 MHz, so the R-counter was set to 16 and the feedback N-counter to $2400/6.25 = 384$. The resulting RF output phase noise profile is shown in Figure 4-8.

The light blue line represents the reference oscillator contribution, and the dark blue line the 'native' VCO contribution. The black line shows the total VCO output phase noise. The remaining lines refer to contributions from resistors in the loop filter and the PLL itself. It is evident that at offsets below 500 Hz, the dominant contributor is the multiplied reference phase noise, and so is largely correlated with the input. In this region, the VCO noise is well attenuated by the feedback from the loop filter. At offsets above 2 kHz, the noise is dominated by the VCO and so is uncorrelated, whilst the wideband reference oscillator phase noise is strongly attenuated. It is noted that the (multiplied) reference oscillator contribution does not quite match that of Figure 4-6 due to limited parameters in the software. In particular the expected noise is too high at small offsets and so slightly miscalculates the close in total phase noise. Nevertheless, it is clear that the phase noise in the doppler region of interest is within the bounds derived in the previous section. It is also evident that the close-in phase noise contribution from the reference oscillator at the ADC will always be small compared to that of the local oscillator.

4.5.2 Distribution and Synchronisation

Here, consideration is given to methods of distributing the 100 MHz reference oscillator to each node. Indeed, one might suppose that such a reference could be employed in *every* node (in which case no distribution would be required), if the oscillator were adequately

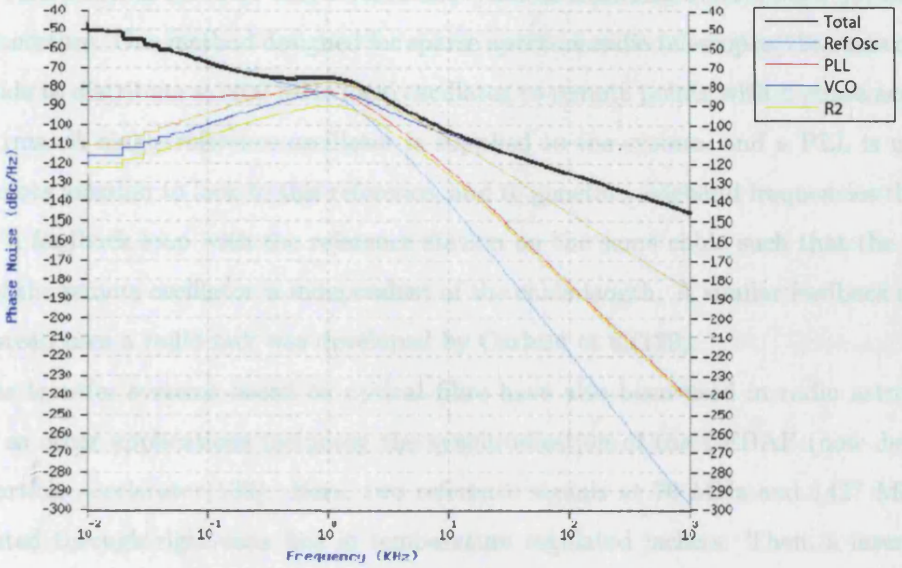

Figure 4-8: Phase noise spectrum of PLL output

stable. This approach is common in bistatic radar, where rubidium oscillators are often used because they offer the lowest long-term oscillator drift out of all of the 'portable' oscillators, so regular frequency recalibration is unnecessary. A bistatic radar may perform coherent processing even if the oscillators in the transmitter and receiver are 'undisciplined' (i.e. their phase noise is mutually uncorrelated), provided the systematic frequency drift between calibrations and the phase noise integrated over a single coherent integration period are both small. Random changes in the relative phase of the oscillators between integration periods (caused by noise close to the carrier) is of no consequence. Such a design extrapolated to the multistatic case has 'short term coherence', as defined in Section 1.3.3. However, it was shown in Section 4.4.3 that fully coherent multistatic processing (such as detection algorithm L_2 in Chapter 2) is only possible if the relative phase between *all* oscillators is known, which implies regular system-wide phase calibration between integration intervals. One such method proposed for the TechSat 21 satellites requires each node to broadcast a series of microwave synchronisation pulses across the system prior to each data collection. Then, provided the location of each satellite is known very accurately, the phase offsets of each oscillator can be estimated(23).

Such a scheme of synchronisation is likely to be too complex to implement in the low-cost prototype system designed here. Therefore a direct form of 'time transfer' is required.

Several such schemes based on either wired and wireless technologies have been documented in the literature. One method designed for sparse aperture radio telescopes(128) uses coaxial waveguide to distribute a 1400 MHz local oscillator to remote points with a phase accuracy of 1.1° rms. A single reference oscillator is supplied to the system, and a PLL is used at each remote location to lock to this reference, and to generate sideband frequencies that are used in a feedback loop with the reference station on the same cable such that the locked phase of the remote oscillator is independent of the cable length. A similar feedback system that instead uses a radio link was developed by Carlson et al(129).

Time transfer systems based on optical fibre have also been used in radio astronomy, as well as other applications including the synchronisation of the CEBAF (now Jefferson Lab) particle accelerator(130). Here, two reference signals at 70 MHz and 1427 MHz are distributed through rigid coax line in temperature regulated jackets. Then, a laser diode distributes a further 1427 MHz reference signal by optical fibre, which is mixed with the coax signal at the beginning and end points in order to estimate and adjust for phase differences caused by temperature fluctuations. A scheme based on a combination of these fibre optic and wireless methods was proposed for bistatic and multistatic radar by Kesheng(131). A further method for radio telescope control is proposed by Grover(132), based on use of an optical source that is intensity modulated at the LO frequency, used to illuminate the entire aperture from a vantage point. A single reference detector at the array centre provides feedback control to the source to compensate for path instabilities.

Clearly wireless methods are preferable due to the potential for much greater distances between nodes and complete portability. Completely passive systems such as GPS-based time transfer (described in Appendix E) are optimal because they do not hinder covertness of operation. However, due to the complexity of implementation and cost of these schemes, a simpler scheme is proposed here for the prototype system. As the coverage range of each node in the system is expected to be in the order of 20 m - 1,000 m, it will be possible to perform both 'short' and 'long' baseline experiments with node separation of the order of only 50 m, and so a wired approach is feasible. A low-cost COTS chip-set manufactured by National Semiconductor is considered, consisting of the CLC005 cable driver and CLC012 cable equaliser and receiver, designed as a transceiver set for Synchronous Digital Hierarchy (SDH) telecommunications systems with a data rate of 155 Mbps. The CLC005 will differentially drive up to 300 m of 75Ω co-axial or twisted-pair cable, and so has a

higher output voltage than most comparable line drivers. Further, due to the synchronisation requirements of SDH, it is designed for low residual jitter. The CLC012 performs line equalisation by measuring the high frequency energy received from the cable, which is used as an estimate for the cable length.

In this application, the chip-set is not used for transmitting data, but instead for distribution of the carrier oscillator at 100 MHz. The receiver effectively performs bandpass filtering of noise resulting from signal degradation on the cable, followed by digital thresholding. Therefore the effect of the distribution process is to add wideband thermal noise to the reference signal, of which half will be amplitude noise, and half phase noise. The result will be an increase in integrated jitter, but the close-in phase noise of the reference will dominate and be mutually correlated at each node in the regions important for frequency stability and doppler coherence, as shown in Figure 4-9. The disadvantages of this low-cost approach are that the wideband phase noise may affect ADC dynamic range, and further that as no control loop is provided, the phase stability of the reference at each node may be susceptible to thermal effects and movement of the cables.

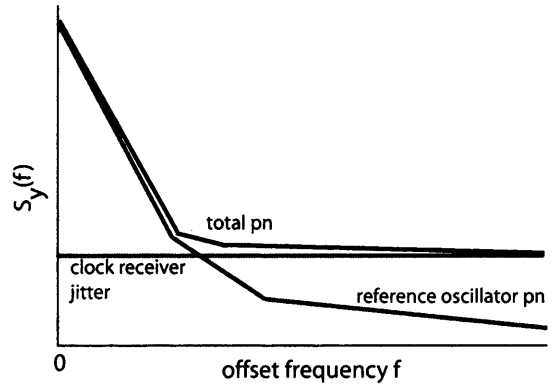

Figure 4-9: The effect of a wired time transfer system on reference oscillator phase noise

4.5.3 Waveform Synthesis

Finally in this section, technologies for implementation of the waveform generator in Figure 4-1 are considered. A system is required that will produce signals that are coherent to the 100 MHz reference clock, and therefore some traditional analogue radar signal generators such as magnetrons and analogue banks of phase shifters fed by tapped delay lines are discounted. The baseband bandwidth is specified as 50 MHz in order to match that of the

ADC and the requirement for approximately 3 m monostatic range resolution. Further, the synthesiser must have the necessary frequency and phase agility to create the required waveforms described in Appendix C, which include linear frequency modulation (chirp) over the entire bandwidth, frequency and phase modulated codes. The half-power bandwidth of a polyphase code is given by $1/t_b$ where t_b is the bit length, and so a waveform with similar range resolution capability requires a bit length of 20 ns.

The potential solutions can be divided into brute force and non brute force techniques(133). Brute force approaches are based on banks of switchable open-loop analogue or digital frequency dividers, which are expensive, bulky, may suffer from aging and thermal changes and are very limited in their versatility. There then remain two 'non-brute-force' synthesiser techniques - the PLL and the Direct Digital Synthesiser (DDS). Much recent work has studied *fractional-N* PLLs, which modulate the frequency divider to create a pseudo-fractional ratio that provides good frequency resolution even with a high phase detector frequency. *Sigma delta* noise shaping algorithms are typically used for divider modulation to minimise the spurious products produced(134). However, PLL lock times are usually measured in tens of microseconds or even several milliseconds, so the synthesis of radar waveforms by manipulating PLL division ratios is not feasible given the degree of frequency agility required. Some alternative designs make use of coarse tuning ports on the VCO in order to slew the output frequency to a selected harmonic of the reference input (e.g. created by a comb generator) for faster lock time over wide bandwidths, although the total lock time is rarely better than that stated above(135).

The DDS is an architecture that has become increasingly popular over the last few years due to an increase in the quality of its components. The modern DDS was invented by Tierney et al in 1971(136), and is unique as a *direct* coherent method of frequency synthesis. Its structure, shown in Figure 4-10, is based on a digital phase accumulator (or register), which is clocked by a reference signal. On each clock cycle, the accumulator is incremented by a digitally programmable value. This increment may be changed arbitrarily on each cycle, or determined by a second programmable accumulator to produce controlled changes in frequency. The digital accumulator output is mapped non-linearly to a sinusoidal amplitude representation, and then converted to an analogue signal with a digital-to-analogue converter (DAC). Frequency and phase update rates are fundamentally identical to the reference clock frequency, frequency changes are phase continuous, and the effective 'lock time' is zero.

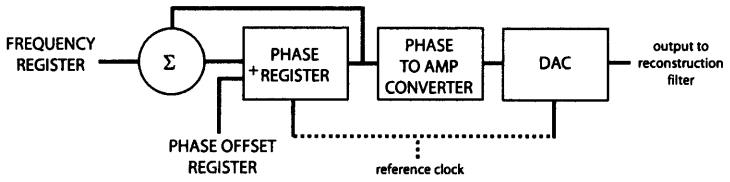

Figure 4-10: Generic structure of a direct digital synthesiser

The noise characteristics of a DDS are related both to its accumulators and its DAC. The greatest challenge in the design of a DDS is related to the look-up table. The phase accumulator can be made arbitrarily large in modern logic (typical devices have a width of 48 bits), however a look-up table based on this size word would require $2^{48} \approx 2.8 \times 10^{14}$ entries, which is infeasible in silicon ROM. Certain techniques may be used to reduce this problem, firstly exploiting the quarter-wave symmetry of a sine wave, and then using Taylor approximations with separate 'coarse' and 'fine' look-up tables. Nevertheless, in practical designs the phase accumulator value is truncated, and only a certain number of the most significant bits (typically 12 to 16 bits) are used at the input of the look-up table. This results in a slowly and periodically increasing error between the accumulator phase and the truncated phase value used, unless the programmed frequency results in phase changes that are 'magic' integer multiples of the truncated least significant bit (LSB). Clearly the error is bounded by this LSB, so the result of this periodicity is the well-known 'phase-truncation spurs'(137), the frequency of which are predictable from the size of the look-up table and the programmed frequency. The maximum spur level can be estimated by $-6.02P$ dBc where P is the number of bits of the truncated word, equal to -96 dBc for a 16-bit look-up table. In some designs these spurs can be reduced with the use of dither, at the expense of greater wideband noise. The finite DAC input word length also results in quantisation noise which is manifested as discrete spurs, where the signal-to-quantisation-noise (SQR) power is given by $1.76 + 6.02B$ where B is the number of bits of DAC resolution. A typical high-performance DDS has a 12-bit DAC, resulting in an SQR of 74 dB. The SQR is degraded if the digital amplitude is below full-scale, as the quantisation spurs remain constant. However, the effect of the SQR can be reduced if a higher clock frequency is used, as the noise power is spread over the entire bandwidth from DC to the Nyquist frequency.

The phase noise of the DAC output signal has some contribution from the jitter inherent in its own electronics, but is generally dominated by that of the reference clock. However, as

the DDS effectively performs frequency *division* of the clock, its narrow-band phase noise is also attenuated by $20\log(f_{out}/f_{clk})$ dB, which amounts to some -40 dB for a 1 MHz output signal, and -6 dBc at the worst case of a 50 MHz output for a 100 MHz reference. Therefore in general, reference clock phase noise will have a negligible effect compared to that of the local oscillators and ADC.

The DDS architecture may be implemented in a single integrated circuit, or as two components where a logic device such as an FPGA contains the necessary accumulators and control logic, and a discrete DAC generates the analogue output signal. This is sometimes known as a Numerically Controlled Oscillator (NCO), and here the look-up table may be substituted by a technique based on the CORDIC algorithm, which numerically generates trigonometric values from complex phase rotations, and despite its complexity of implementation is well suited for use in FPGAs as it requires no multiplies. However, despite the compactness of such an approach, the required development time dictated that an integrated COTS device should be chosen. The Analog Devices AD9854 is proposed, which accepts a reference clock input in excess of 200 MHz. However, whilst this capability to 'oversample' will reduce effective quantisation noise and reference phase noise, the complexity of multiplying-up the 100 MHz reference and the inherent increase in noise in doing so means there is negligible performance benefit. The device contains programmable frequency and phase registers, amplitude control and dual 12-bit DACs with in-phase and quadrature outputs in a single chip. The mode registers can be set to produce chirp and single tone outputs, and real-time programming of the frequency and phase registers across a parallel interface at up to 100 MHz can be used to synthesise arbitrary frequency and phase coded waveforms. Therefore it is theoretically possible to meet the requirements for frequency and phase agility as well as total bandwidth with a single device, programmed in real-time by external logic that can be implemented in the FPGA.

4.5.4 Coherent Subsystem Design Summary

In this section, several methods have been considered for the implementation of the coherent subsystems in the prototype radar based on analysis of the performance requirements. An outline design has been finalised and is shown in Figure 4-11. A simple wired architecture for the distribution of the 100 MHz reference clock is proposed, to which the DDS waveform generator, ADC and synchronous control logic in the FPGA are all referenced. A PLL in

each node, also referenced to this clock, synthesises a local oscillator that is common to both the transmitter and receiver. A narrow loop bandwidth is used to minimise the total integrated phase noise whilst ensuring mutual correlation (and thus coherency) of close-in noise across the system. The design has maximised the use of COTS and digital components in order to simplify the analogue signal chain and minimise cost.

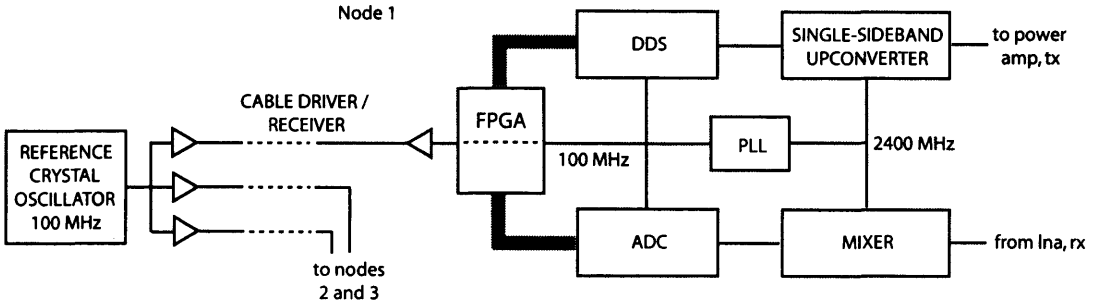

Figure 4-11: Outline design of prototype system

4.6 A Computer Simulation of a Coherent Multistatic Radar

In this section, the development of a computer simulation is described for modelling the prototype multistatic radar based on the outline specification and coherency analysis in this chapter. In particular, this simulation is designed to demonstrate the effects of incoherency and synchronisation errors on the instrument function and performance of the system when using the detection algorithms described in Chapter 2.

The model is developed in Agilent Advanced Design System (ADS)[12] using a time-domain component-based approach. It is the successor to, and is based on, a Matlab simulation designed by the author and outlined in Derham et al(138). Time-domain simulations have many disadvantages compared to approximated analytic simulations, in particular long simulation times and considerable processing and memory requirements. However, the advantage of such an approach is that the simulation may be designed to output simulated data in the same format as the real radar receivers, which may then be used with the actual signal processing algorithms developed for the system.

The layout of the model is shown in Figure 4-12. There is a danger of 'over-design' in the development of such simulations, to the extent that there are too many variable parameters

[12]This software is still commonly known by its former name, 'HP ADS'.

to be able to make meaningful conclusions. Therefore, only the critical sections of the radar for examining the effect of coherency are modelled in detail. Given the constraints of processing time, and the focus in this thesis on location estimation and ranging rather than doppler processing (although the prototype system has been specified for both cases), the simulation models the transmission and reception by multiple receivers of a single pulse only. Firstly, the model comprises an 'ideal' transmitter module, which transmits a chirp pulse of length 1 μs and bandwidth 50 MHz on an ideal 2400 MHz carrier. These figures are chosen as being indicative of those for the prototype system. The 'channel' or propagation path is then simply modelled by an RF delay line and attenuator that are dependent on the simulated target range, and a Gaussian noise source to represent atmospheric noise.

This signal is fed to the inputs of three receivers, which are shown as 'black boxes' in Figure 4-12. The internal model for each receiver is shown in Figure 4-13. The receiver model takes as its input a 100 MHz clock and a 2400 MHz local oscillator. The focus of the simulation is on the manipulation of the relative nature of these signals. The total simulation time for the model is only 3 μs (corresponding to the transmission and reception of a single pulse at short range), therefore phase noise at offsets less than approximately 300 kHz cannot be modelled. Instead, noise at these offsets manifests itself as some fixed phase (or possibly frequency) offset over the period of the simulation. As a result, the clock and oscillator are modelled in two ways. Firstly, the phase noise at offsets greater than 300 kHz is estimated from the profiles for the reference oscillator and PLL output in the previous section. The size of these offsets (much greater than the loop bandwidth) means that they should be simulated as *independent* (uncorrelated) processes at each receiver - hence three separate local oscillator models are shown in the figure.

Secondly, the close-in phase noise is simulated by setting fixed (but random) offset parameters in the oscillator models. The local oscillator at 2400 MHz is phase locked to the 100 MHz reference clock in each receiver, so the effect can be modelled in the most illustrative way by applying relative time *delays* to each reference clock (equal to a fraction of a period). Such a delay $t_{\Delta\text{del}}$ will cause a corresponding relative phase shift in the local oscillator given by:

$$\phi_{\Delta i} = 2\pi t_{\Delta\text{del}} f_{\text{LO}} + \phi_{\text{pn}}(t) \quad \text{rads} \tag{4.26}$$

where $\phi_{\text{pn}}(t)$ is a function describing the phase noise at offsets less than 300 kHz. These

time delays may be caused by uncompensated differences in clock distribution cable lengths, or, in the general case, uncorrelated close-in phase noise or frequency drifts on the reference clock. Then, the perturbation of the local oscillator phase over the simulation period is given by the sum of $\phi_{\Delta i}$ and the random phase noise modelled separately at large offsets.

Within the receiver in Figure 4-13, the signal is amplified both at RF and baseband (and can be modelled using specific noise figures if desired), and downconverted using a mixer driven by the local oscillator signal described above. The resulting baseband signal is then digitised using an ADC model based on 12-bit resolution, and clocked by the incoming reference signal. Therefore, unknown delays on this clock result both in phase shifts of the local oscillator and synchronisation errors in the digitisation of the received signal.

The output data from the ADC in each receiver can be plotted, and also saved to a file (having been decimated from the very high temporal resolution of the simulation to that of the ADC sample rate). These files can then be imported into Matlab, where a simplified form of the processing algorithms described in Chapter 5 (and based on the detection algorithms in Chapter 2) is used to process the simulated data. Here, some simplifications are made with reference to Equations 2.75 and 2.46. Firstly, each transmitter and receiver is modelled to be equidistant from a single isotropic target, such that the actual time-of-arrival for all bistatic pairs is identical. Secondly, each receiver has identical characteristics, and therefore the mean noise power associated with each signal is equal. Thirdly, the *assumed* relative phase between stations is zero (the offsets in the simulation are assumed random and unknown to the radar processor). As a result, variables A_{ik1} and $\Delta\varphi_{ik1}$ in Equation 2.75 and N_i in Equation 2.46 cancel.

Therefore, the signal processing proceeds by firstly performing matched filtering on each of the received signals as per Equation 2.46. Then, the detection algorithm hypothesises possible target location vectors on a grid over the two-dimensional plane of interest and calculates the corresponding expected time-of-arrival for each bistatic pair. The value of the matched filter output at each of these times is found, phase shifted according to Equation 2.46, and then coherently summed (no weighting is required due to the equal signal and noise powers). This process is described in detail in the context of the prototype system signal processing system in Section 5.10.

Now, some illustrative results are presented from the simulation. Figure 4-14 shows the topology used in this case, where each node is positioned 150 m away from the target at

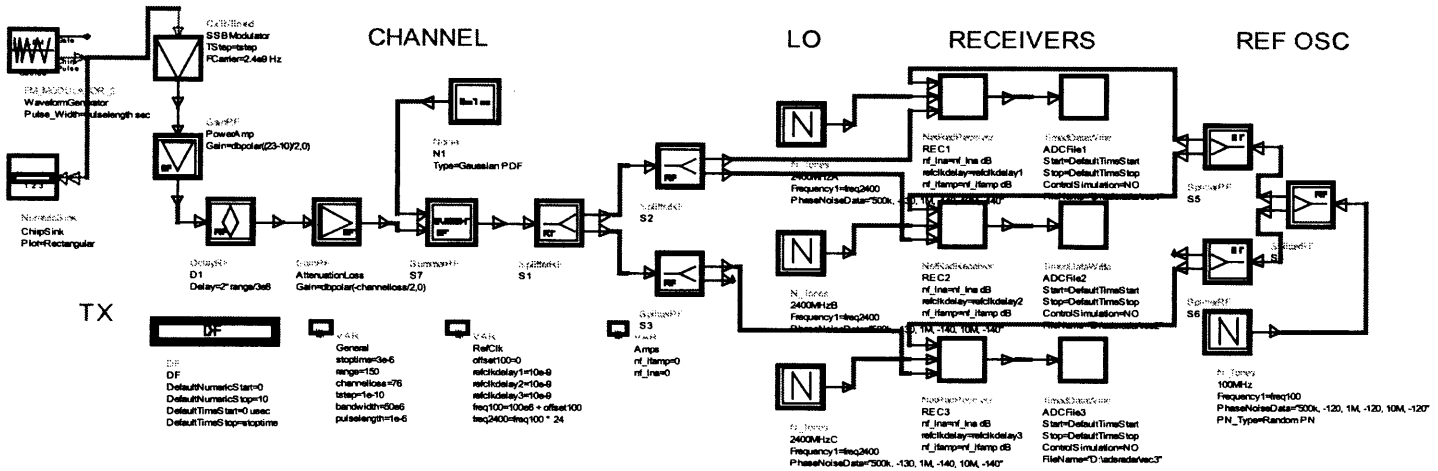
CHANNEL
LO
RECEIVERS
REF OSC
TX
SSBModulator
TStep=tstep
FCarrier=2.4e9 Hz
WaveformGenerator
Pulse_Width=pulselength sec
PowerAmp
Gain=dbpolar(23-10)/2,0)
ChipSink
Plot=Rectangular
D1
Delay=2* range/3e8
AttenuationLoss
Gain=dbpolar(-channelloss/2,0)
N1
Type=Gaussian PDF
S1
S2
S3
Amps
nf_ltamp=0
nf_lna=0
S5
S6
DF
DF
DefaultNumericStart=0
DefaultNumericStop=10
DefaultTimeStart=0 usec
DefaultTimeStop=stoptime
General
stoptime=3e-6
range=150
channelloss=76
tstep=1e-10
bandwidth=50e6
pulselength=1e-6
RefClk
offset100=0
refclkdelay1=10e-9
refclkdelay2=10e-9
refclkdelay3=10e-9
freq100=100e6 + offset100
freq2400=freq100 * 24
2400MHzA
Frequency1=freq2400
PhaseNoiseData="500k, -130, 1M, -140, 10M, -140"
REC1
nf_lna=nf_lna dB
refclkdelay=refclkdelay1
nf_ltamp=nf_ltamp dB
ADCFile1
Start=DefaultTimeStart
Stop=DefaultTimeStop
ControlSimulation=NO
2400MHzB
Frequency1=freq2400
REC2
refclkdelay=refclkdelay2
ADCFile2
2400MHzC
Frequency1=freq2400
REC3
refclkdelay=refclkdelay3
ADCFile3
FileName="D:\adsradar\rec3"
100MHz
Frequency1=freq100
PhaseNoiseData="500k, -120, 1M, -120, 10M, -120"
PN_Type=Random PN

Figure 4-13: Receiver simulation design

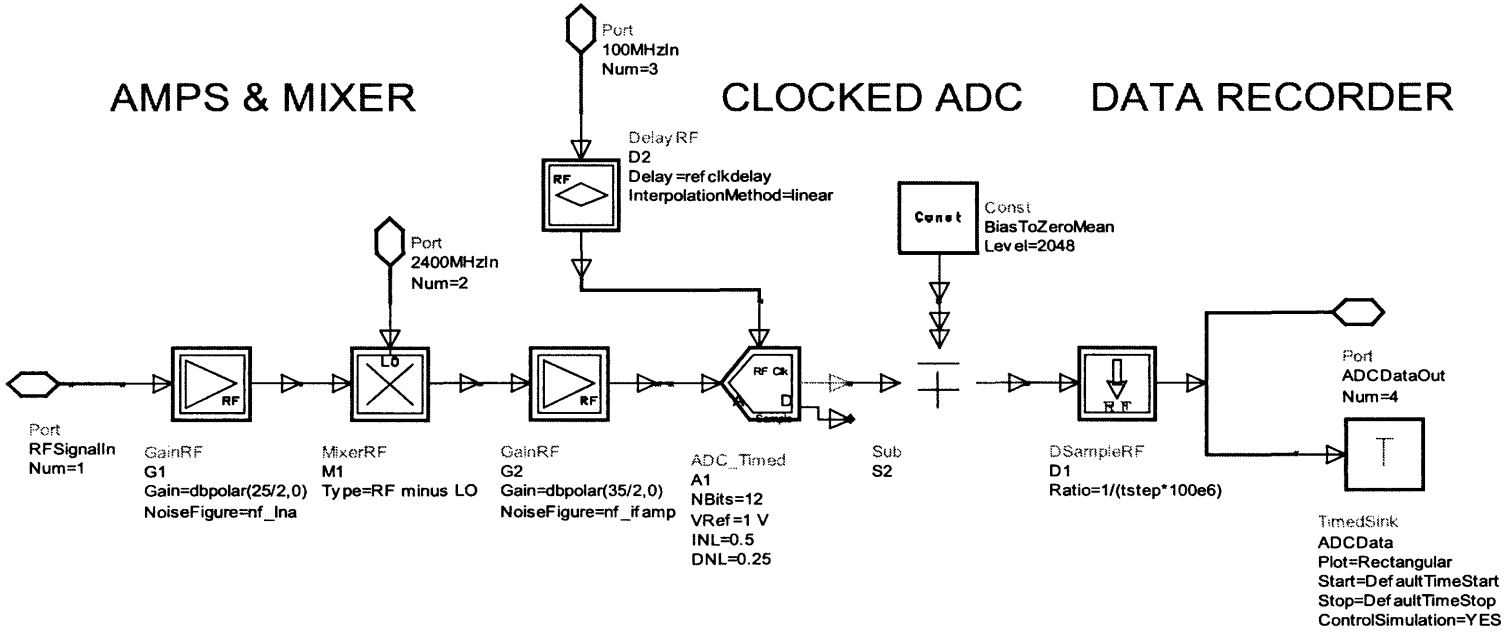

location $\{0, 150\}$.

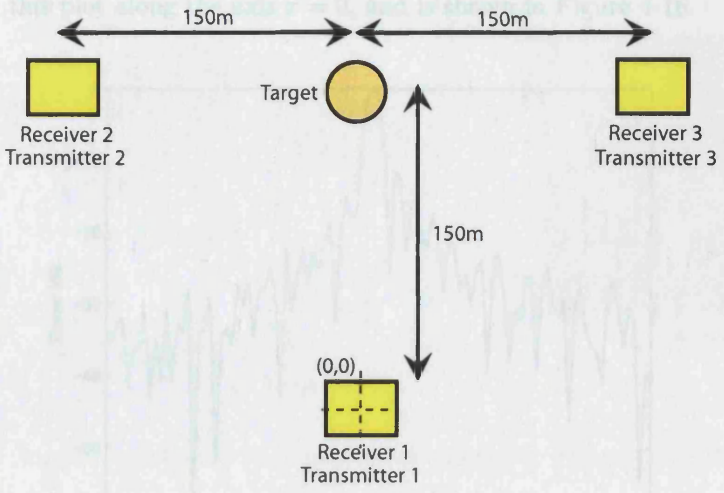

Figure 4-14: Multistatic topology for system simulation

The target RCS and transmitted power are chosen arbitrarily such that there is a very high signal-to-noise ratio at each receiver. Whilst this may be unrealistic in practice, it avoids the problem of informative features from the simulation response being buried in thermal noise. Firstly, only node 1 is used to demonstrate the baseline performance in a monostatic configuration. A two-dimensional grid is defined spanning 50 m in each direction from the actual target location, and the resulting output of the processor is shown in Figure 4-15.

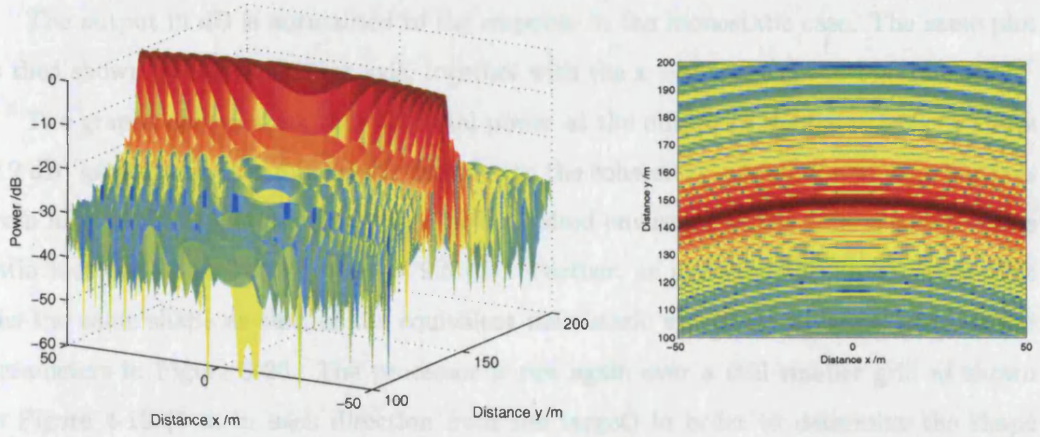

Figure 4-15: Surface and intensity plots for the simulator output in monostatic mode

As expected, there is a ring of equal-intensity response at all iso-range points on the

grid from the monostatic radar. The equivalent range-response graph is formed by taking a cut through this plot along the axis $x = 0$, and is shown in Figure 4-16.

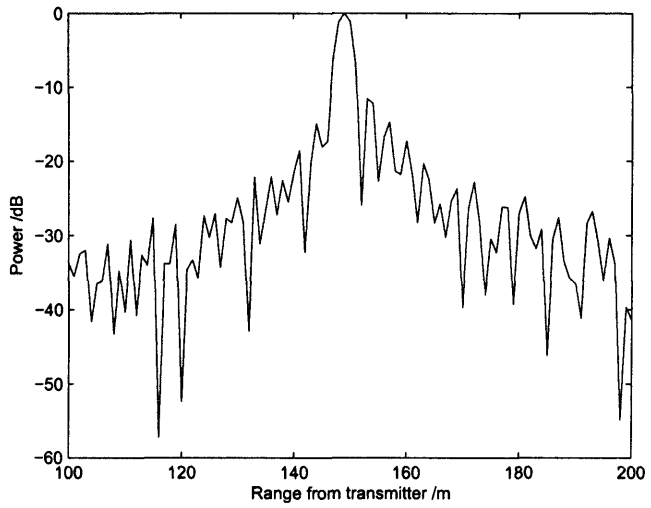

Figure 4-16: Range-response graph for simulator output in monostatic mode

Here the matched filter response with the characteristic sidelobes of an unweighted chirp can be seen[13]. Now, the simulation is repeated where all transmitters and receivers are operating as shown in Figure 4-14, such that the system now comprises three monostatic and six bistatic pairs. Firstly, no synchronisation offsets are modelled beyond small amounts of phase noise at large offsets and low levels of thermal noise. The results (for a reduced grid spanning 20 m either side of the target) are shown in Figure 4-17.

The output in dB is normalised to the response in the monostatic case. The same plot is then shown on a linear power axis, together with the $x = 0$ range cut in Figure 4-18.

The graphs demonstrate that the total power at the output of the detector is 81 times (19 dB) greater than the monostatic case due to the coherently summation of contributions from nine identical bistatic pairs. In a noise limited environment the total signal-to-noise ratio increase would be $N^2 = 9$ (= 9.5 dB). Further, as expected the linear power plot has the same shape as that of the equivalent multistatic ambiguity diagram with similar parameters in Figure 3-26. The processor is run again over a still smaller grid as shown in Figure 4-19 (5 m in each direction from the target) in order to determine the shape

[13]The response has slight asymmetry that is caused by a minor artifact related to the complex processing of the baseband chirp close to DC.

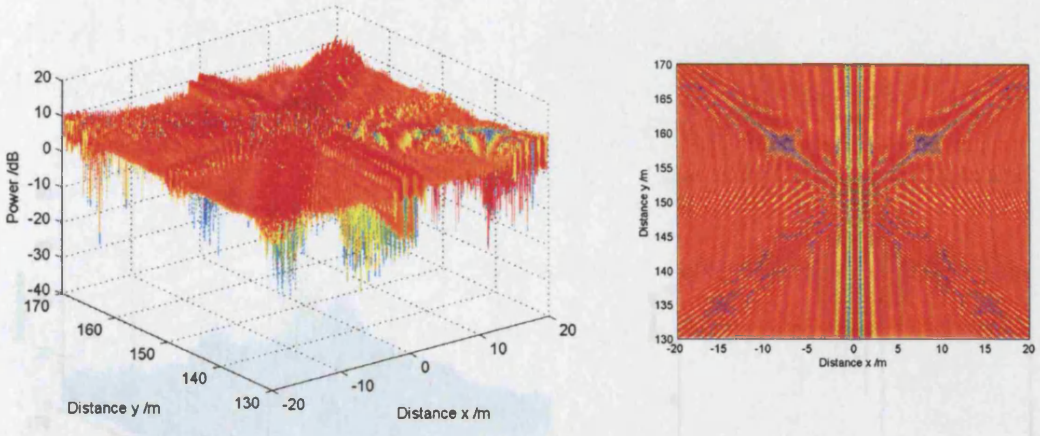

Figure 4-17: Surface and intensity plots for the simulator output in multistatic mode

of the mainlobe response. The chosen topology provides considerable reduction in range ambiguity on the iso-range contour shown in Figure 4-15, at the expense of significant 'sidelobe' response over the entire surface shown. The strong 'grating lobes' are also visible resulting from the coherent processing and the regularity of the topology.

Now, the simulation is repeated where reference clock time delays of 1 ns and 2 ns are applied to receivers 2 and 3 respectively compared to receiver 1. These figures represent minor synchronisation errors (small fractions of the 10 ns reference clock period), as might occur due to uncompensated differences in the clock distribution cable length. Equivalently, they also represent instantaneous phase offsets of 36° and 72° respectively, as might occur in the general case when noisy, inadequately disciplined reference oscillators are used. The direct output of the simulator is shown in Figure 4-20, where the phase offsets in the baseband signal due to the synchronisation errors in the reference can be clearly seen. The output of the coherent detector is again plotted on a small grid (5 m in each direction from the target) in order to clearly show the mainlobe, and is presented in Figure 4-21. A comparison with Figure 4-19 shows immediately that these uncompensated synchronisation errors have a devastating impact - the peak output power is reduced by some 9 dB, the mainlobe has become very broad, and in fact the response at the exact target location is almost zero. Application of Equation 4.26 to the time delays chosen reveals that the local oscillators in each receiver had phase offsets of 144° and 288° respectively, which amounts to complete incoherence, so it is not surprising that the coherent detector performs so poorly.

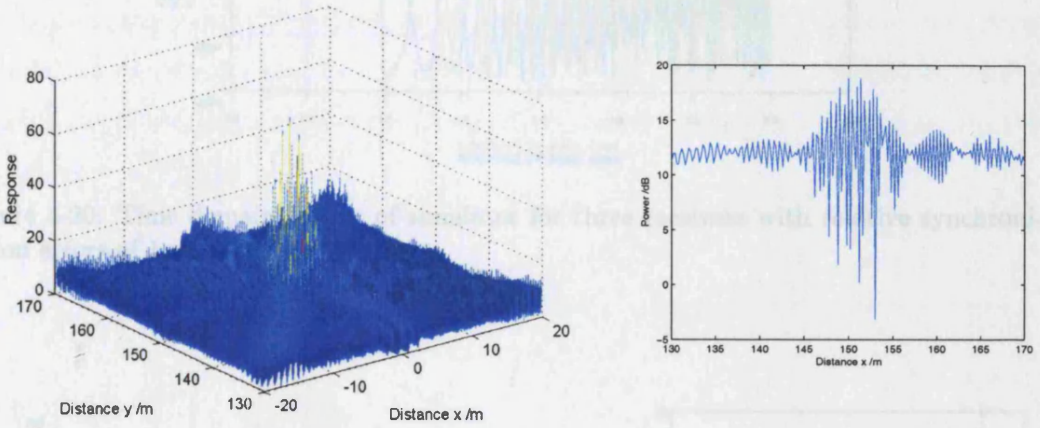

Figure 4-18: Surface plot (linear scale) and range-response graph (dB) for the simulator output in multistatic mode

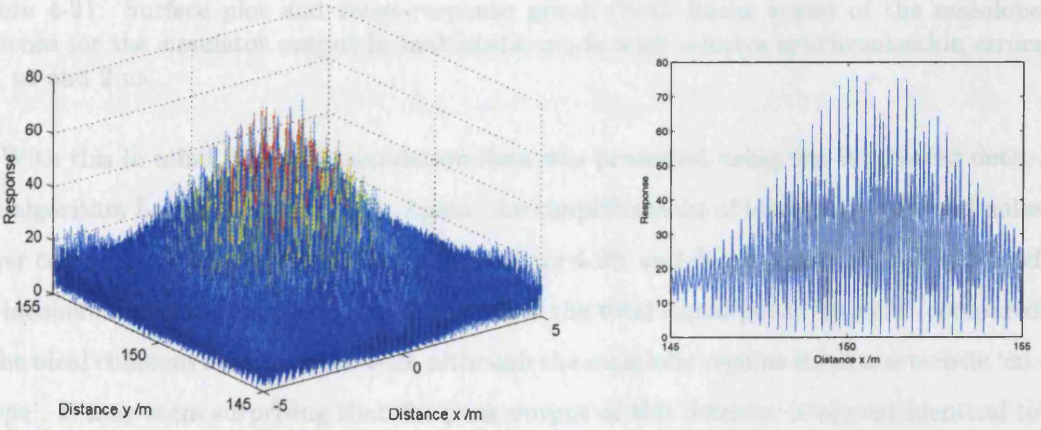

Figure 4-19: Surface plot and range-response graph (both linear scale) of the mainlobe response for the simulator output in multistatic mode

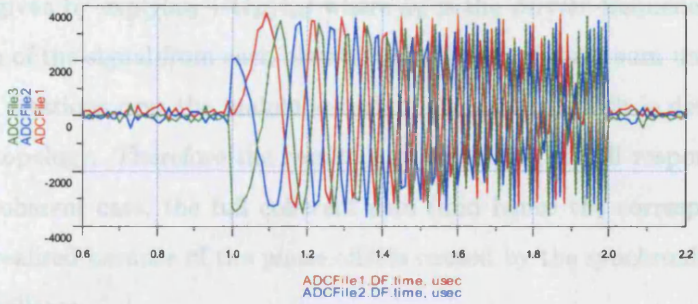

Figure 4-20: Time domain output of simulator for three receivers with relative synchronisation errors of 1 ns and 2 ns

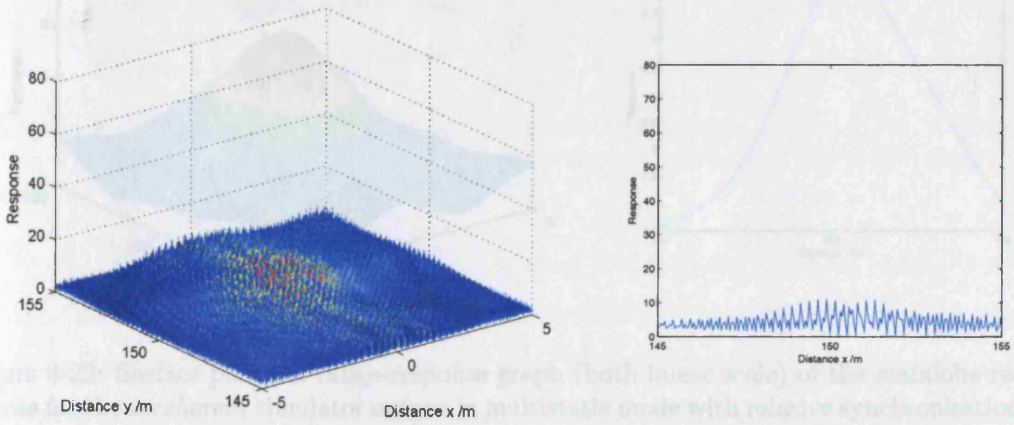

Figure 4-21: Surface plot and range-response graph (both linear scale) of the mainlobe response for the simulator output in multistatic mode with relative synchronisation errors of 1 ns and 2 ns

With this in mind, the same simulation data was processed using the incoherent detection algorithm L_{3m} in Equation 2.77. Again, the simplifications of identical signal and noise power can be used. The results are shown in Figure 4-22, and demonstrate that as expected the incoherent processing results in a reduction of the total signal power by $1/N^2$ compared to the ideal coherent case in figure 4-19, although the mainlobe regains its characteristic 'envelope'. It may seem surprising that the peak output of this detector is almost identical to that of the coherent detector in this case - after all, we might expect that such large phase errors would result in almost complete coherent cancellation across the entire mainlobe. However, it should be noted that the detection algorithm performs a phase shift on each

received signal given by $\exp[j(\omega_0 + \Omega_{si})t_{si}]$ where ω_0 is the *carrier* frequency[14]. Therefore, the contribution of the signal from each bistatic pair to the coherent sum undergoes several complete phase rotations over the mainlobe region, the rate of which is determined by t_{si} and hence the topology. Therefore the result is an 'averaging' of all responses that tends towards the incoherent case, the full coherent sum (and hence the corresponding grating lobes) is never realised because of the phase offsets caused by the synchronisation errors in the reference oscillator.

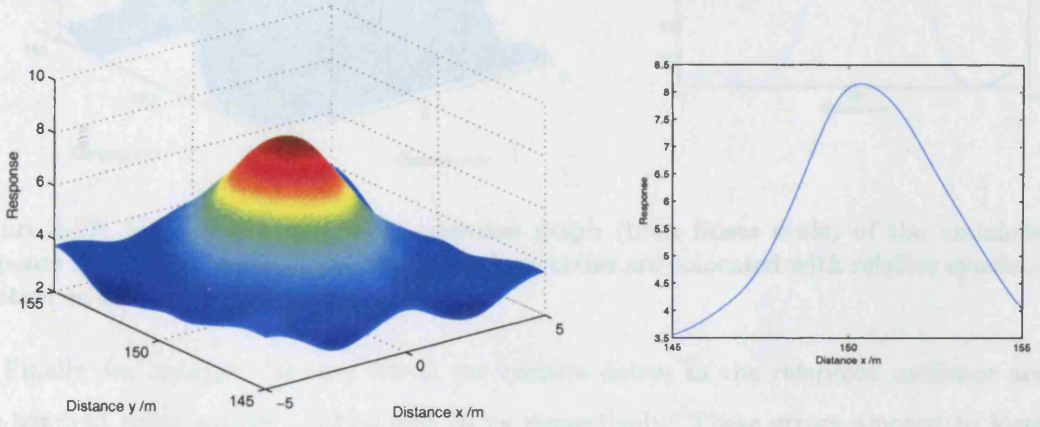

Figure 4-22: Surface plot and range-response graph (both linear scale) of the mainlobe response for the *incoherent* simulator output in multistatic mode with relative synchronisation errors of 1 ns and 2 ns

The response in Figure 4-21 demonstrates the performance loss in coherent processing for synchronisation errors when the multistatic topology is spatially diverse. However, it was shown in Section 3.3 that when nodes are closely spaced (the 'short baseline' topology), the instrument function shape approximates the monostatic case. Therefore, we now examine the effect of these same synchronisation errors for the extreme case - when all nodes are colocated. The results are shown in Figure 4-23. Despite the appearance, these graphs are indeed the result of coherent processing. However, having essentially resolved to the monostatic case, the output is equivalent in form to that expected from the coherent integration of a train of three *incoherent* pulses in a monostatic radar. Hence the instrument function is the same as for a monostatic system, and the peak response is somewhat *less* than that expected for a single pulse due to the partial phase cancellation. It can be concluded that

[14]This process is conveniently illustrated in the time domain in Equation 2.27.

not only does multistatic topology have a large influence on the ambiguity function of a system, it also influences its response in the case of coherency errors.

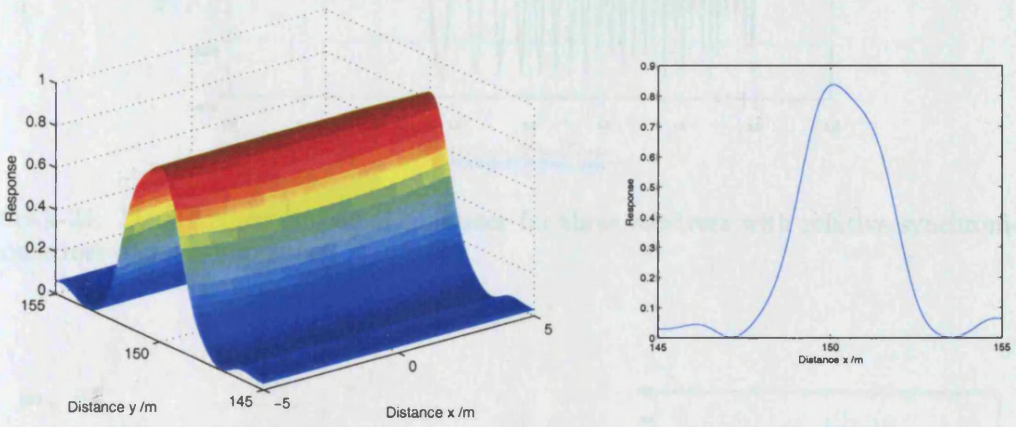

Figure 4-23: Surface plot and range-response graph (both linear scale) of the mainlobe response for the simulator output where all three nodes are colocated with relative synchronisation errors of 1 ns and 2 ns

Finally, we consider the case where the relative delays in the reference oscillator are one-hundred times smaller - 10 ps and 20 ps respectively. These errors amount to local oscillator phase shifts of 8.6° and 17.2°, which are of the order that may be considered within acceptable calibration tolerances. The simulation was run using the coherent processor and based on the original topology shown in Figure 4-14. The direct output of the simulator is shown in Figure 4-24, and the results of the processing are shown in Figure 4-25. A comparison with Figure 4-19 shows that the response is virtually identical to the ideal case. Further simulations (not plotted here for brevity) demonstrate that phase errors of the order of $< 30°$ can be tolerated without significant degradation, although the apparent effect is topology dependent.

In summary, a computer simulation has been developed that allows the effects of coherency errors in the prototype multistatic system to be estimated. It was shown that, when a spatially diverse topology was modelled, errors that resulted in large instantaneous phase differences between the local oscillators in each receiver degraded the coherent detector output to a broad interference pattern around the mainlobe region with a mean power degradation of the order of $1/N^2$ where N is the number of nodes. It was demonstrated that, for this case, LO phase errors less than 30° could be tolerated without substantial

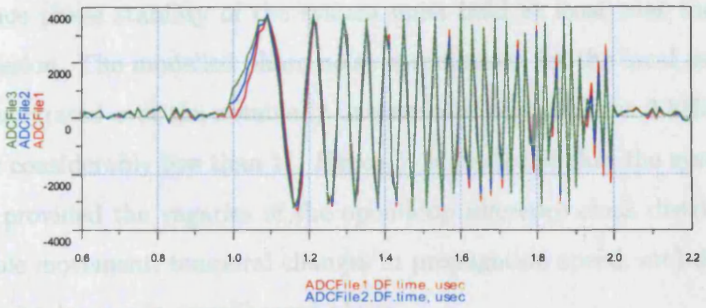

Figure 4-24: Time domain output of simulator for three receivers with relative synchronisation errors of 10 ps and 20 ps

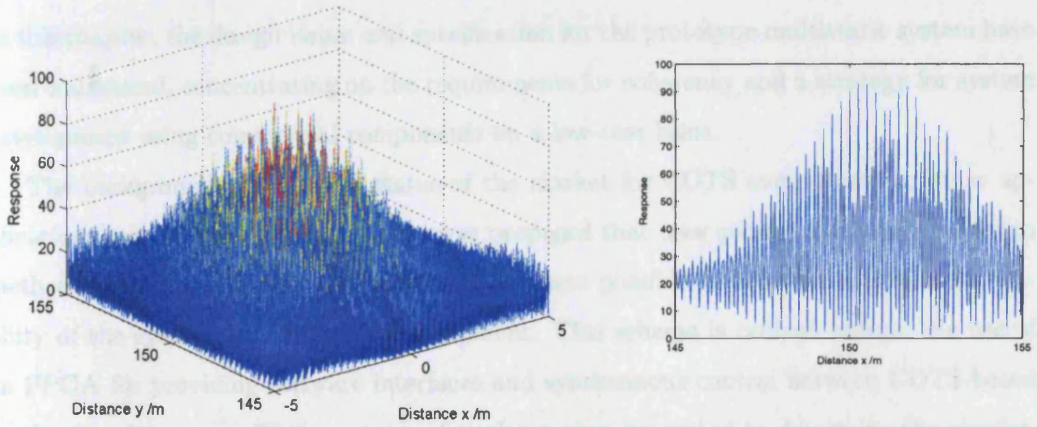

Figure 4-25: Surface plot and range-response graph (both linear scale) of the mainlobe response for the simulator output in multistatic mode with relative synchronisation errors of 10 ps and 20 ps

performance degradation. Evidently, such gross relative errors may be caused by uncorrelated close-in phase noise, or variations in the clock distribution (time transfer) channel itself. The period for which all oscillators can maintain phase stability within these bounds dictates the frequency at which system calibration is required.

Over short periods of time (such as the integration period for a train of pulses), this constraint may not present a problem even for quite unstable oscillators - the relative rms phase error over this period can be determined by integration of the uncorrelated phase noise in each case at offsets greater than the inverse of the pulse integration period. However, it is clear that significantly tighter specifications would be required for doppler processing, as was shown in the previous section.

The prototype system specification has no explicit in-built capability for autonomous

calibration, hence phase stability of the system must hold at least over the course of an experimental session. The modelled phase noise specification for the local oscillator shown in Figure 4-8, integrated over the nominally uncorrelated region above 2 kHz, results in an rms phase error considerably less than 1°. Hence, it is predicted that the system will maintain coherency provided the vagaries of the open-loop reference clock distribution system (e.g. due to cable movement, temporal changes in propagation speed, etc) do not result in significant discrete changes in uncalibrated phase.

4.7 Conclusions

In this chapter, the design issues and specification for the prototype multistatic system have been considered, concentrating on the requirements for coherency and a strategy for system development using commercial components on a low-cost basis.

The background and current status of the market for COTS components in radar applications was reviewed, and a scheme was proposed that uses generic and modular design methodologies based on an open architecture where possible in order to maintain the viability of the system for long-term development. This scheme is centred around the use of an FPGA for providing software interfaces and synchronous control between COTS-based hardware subsystems. Then, a series of analyses were presented to determine the requirements in terms of phase noise and coherency for the oscillators driving the system. From this specification, a range of designs were considered for both the coherent components in each node and ensuring adequate coherency between them. A solution was chosen that, whilst not providing optimal performance, will be adequate for the intended applications of the system, and is in keeping with the budgetary requirements. Finally, a time-domain simulation was described that demonstrates the effects of coherency and synchronisation errors on the instrument function of the radar when using the detection algorithms developed in Chapter 2. It was shown that the coherent detector is highly sensitive to large changes in local oscillator relative phase, but that the time transfer system designed for the prototype system is expected to meet the requirements for phase and synchronisation stability.

Chapter 5

Development and Construction of the Multistatic Radar

5.1 Introduction

In this chapter, the development and construction of the prototype multistatic radar is described based on the outline design in Figure 4-11. The system comprises three nodes, each identical and capable of both transmission and reception. Each contains an FPGA and digital signal processor (DSP), which jointly perform local timing, control and signal processing. The DSP chip also performs traditional 'CPU' functions such as system configuration, memory management, and interaction with the user interface (in which context it will be referred to as 'the processor'). Each node is supplied with a mutually coherent clock at 100 MHz that is distributed by cable from a reference oscillator module. Further, each node has a network interface that allows communication with all other nodes so that raw or semi-processed data can be transferred for centralised processing, and the system can be jointly configured (the so-called 'cooperative mode').

The prime objectives of the development are stated, based on the intended experimental applications for the system, and taking into account the budgetary constraints. Firstly, the construction of the single reference oscillator and distribution system is documented. Then, the development of the major subsystems within each node is described, beginning with the transmitter and receiver chains, and proceeding to the design of the cores within the FPGA and the network controller. Lastly, the design and coding of the signal processing system in each digital signal processor is documented, including the implementation of the detection algorithms described in Chapter 2. In each case, the use of distinguishing and novel engineering techniques is emphasised, both in order to meet the low-cost requirements, and to ensure the unique performance requirements for the system.

5.2 Overall System Objectives

In this section, the design-time objectives and system specification are stated, based on the proposed applications for the prototype system. The primary aim is to enable novel experimental research in order to determine the relative performance and characteristic features of coherent and incoherent multistatic radar compared to traditional monostatic systems. A few examples of such applications are outlined below, based on the potential advantages cited in Section 1.4:

- Testing the performance of the multistatic detection algorithms described in Chapter 2 and the resulting instrument functions → *effect on sensitivity and ambiguity*;
- Determination of location and velocity vectors in two- and three-dimensions for a range of multistatic topologies→ *effect on parameter estimation capability*;
- Analysing the multistatic RCS for different topologies given a range of real and test targets → *effect on detectability and classification capability*;
- Determining the ability to operate in an environment of strong noise, interferences, jamming or clutter → *effect on tolerance.*

Evidently, the headline requirement is for a system that can make simultaneous location and velocity measurements corresponding to short times-of-arrival and small doppler shifts, and that is capable of operating in monostatic, bistatic and versatile multistatic topologies. The data capture and signal processing requirements are considerably greater for continuous wave radar compared to pulsed systems, and there is no inherent advantage in CW capability for the proposed applications, so it is decided to design a system for pulsed mode data capture only in order to reduce the total cost.

The design specification is expressed in terms of the requirements for each node of the system operating in monostatic mode. Such an approach ensures the system is adequately specified to determine the 'baseline' monostatic performance from which multistatic experimental results can be compared. However, clearly the *underlying* design must also take into account the unique requirements for coherent multistatic operation.

An outline of this specification is given in Table 5.1. The minimum pulse length of 0.1 μs is chosen so that 'eclipsing' of received signals by the transmitted pulse can be avoided outside the nominal minimum range of interest (20 m) when the node is operating in monostatic mode. The peak transmitted power should be constrained by the regulations for operation in the licence-exempt ISM band, defined in ERC Recommendation 70-03 (139) and the related technical guidelines in ETSI EN 300 440 (140). Military use of this band is limited to aircraft and missile telemetry in the range 2310 - 2450 MHz, so radars are not specified explicitly in the standard. Therefore, the most appropriate classification is 'non-specific short-range devices in the band 2400 - 2483.5 MHz', which covers the nominal frequency range of the transmitter, and specifies a maximum transmitted output power

of 10 mW (+10 dBm) eirp. The duty cycle is stated over a one hour period, however the likely sporadic usage pattern of the system is rather dissimilar to typical devices used in this band. We make the assumption of a maximum of thirty one-second integration (operational) periods per hour, during which time a duty cycle of 1/50 is used (equal to the maximum 10 μs pulse length with a PRF of 2 kHz). Then, allowing for the use of a directional transmit antenna with up to 24 dBi gain, the maximum peak power of the transmitter should be 200 mW (23 dBm). Similar parameters were used in Section 3.2, where it was shown that transmission of a single pulse results in an SNR of 13 dB at $\approx$ 400 m range, so the desired maximum range of 1,000 m will be possible using the realisable pulse compression and coherent integration.

The requirement for maximum range resolution is clearly for the minimum ambiguity possible, and further that, when operating in multistatic mode, a demonstrable and accurately measurable effect on location vector estimation can be realised. In reality, it is constrained by the bandwidth of the digitiser used in the low-cost receiver, and the stated value of 3 m demonstrates an acceptable compromise between cost and performance.

The maximum PRF of 2 kHz was defined in the previous chapter in order to allow pulse doppler detection of targets with moderate radial velocities less than 200 km/h. The minimum PRF of 50 Hz is defined to provide doppler resolution over the expected clutter region, for very slow moving or oscillating targets, and for testing the system doppler performance in the region where it may be limited by local oscillator phase noise.

The system should be developed as a low-cost open test-bed that may be expanded further for additional applications in the future. Therefore, the design and construction should be modular so that components can be replaced or augmented in a piecemeal fashion.

Parameter	Value
Pulse length	0.1 - 10 μs
Baseband bandwidth	50 MHz
Range resolution (nominal)	3 m (max)
Waveforms	Arbitrary linear FM and polyphase
Peak transmitted power	200 mW
Maximum unambiguous range	1,000 m
PRF	50 Hz - 2 kHz
Maximum unambiguous velocity	200 km/h
Carrier frequency	2400 MHz

Table 5.1: Outline design-time specification

In the main, analogue RF components (such as mixers and amplifiers) may be purchased from commercial manufacturers as plug-in modules with SMA connectors. In the case of digital and mixed-signal subsystems, the purchase of 'evaluation boards' developed by the manufacturer is preferred in order to decrease development time, but only where costs are not prohibitive and the physical external interfaces are well-defined. In other cases, due to non-availability or unsuitability of these boards, or the desire to use custom design techniques in the implementation of COTS components, circuits, schematics and printed circuit board (PCB) layout are designed in-house.

Finally, the system must be adequately portable so that it can be used outside the laboratory in experimental test locations. Therefore the entire system should be controllable from a single notebook personal computer. A software user interface on this computer should allow control of all system parameters, off-line data storage and visualisation of results. For convenience, the computer will be directly interfaced to a 'master' node, which will be responsible for programming the 'slave' nodes through the network interface. As a result, these slave nodes will be completely embedded systems, and should be self-booting with minimal interaction required by the user.

An overview of the final design of a single node is shown in Figure 5-1. In the next sections, the development and construction of each of the major subsystems in this figure is described in turn.

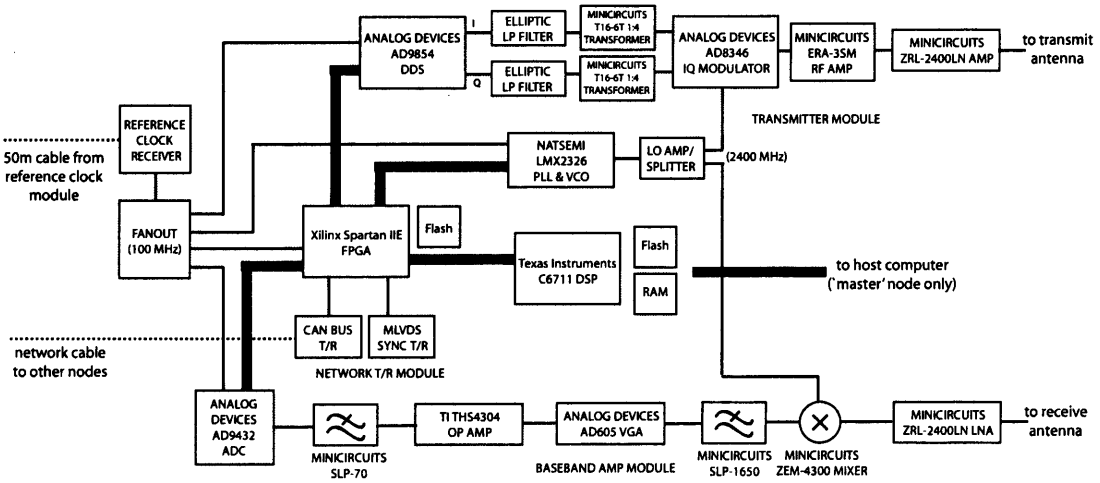

Figure 5-1: Overview of the design of a single node in the prototype system

5.3 Oscillator Subsystems

In this section, the reference clock generation and distribution subsystem is presented, based on the strategy outlined in Section 4.5. Then, the construction of the local oscillator synthesiser in each node is described, which is phase referenced to this distributed clock.

An outline of the system reference oscillator subsystem is shown in Figure 5-2. The primary aim is that the oscillator noise profile should be degraded as little as possible during the fan-out and distribution process. It is common to use differential emitter-coupled logic (ECL) for board level clock distribution due to the superior jitter performance resulting from cancellation of common-mode noise, so the first step is conversion of the TTL output of the oscillator to low-voltage positive ECL (LVPECL) using COTS logic components from a very low jitter family of devices manufactured by On Semiconductor. This standard is chosen to minimise the number of power supply voltages required and the size of voltage transitions that may result in electromagnetic interference in nearby sensitive radar components. This signal is then fanned-out three ways, and interfaced to the NatSemi CLC005 cable drivers. A schematic and PCB layout for this circuit were designed in Orcad CAD software, and are shown in Appendix F. The PCB uses a four-layer design with dedicated power and ground planes, and careful attention was paid to the differential track layout, impedance matching and decoupling in order to minimise the effect of nearby EMI and supply noise.

Whilst 75Ω coaxial cable such as Belden 8281 is usually preferred for long-distance distribution because of its low attenuation (8.3 dB per 100 m at 100 MHz), due to the high cost (£510 per 150 m reel) it was decided to use a high-quality unshielded twisted-pair (UTP) cable (Belden 1872A Category 6) instead, which is typically used for 'gigabit Ethernet' network cabling and is only one-eighth of the cost, although has significantly

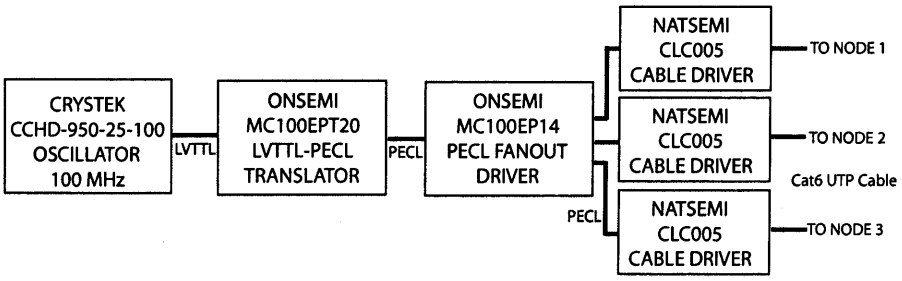

Figure 5-2: Reference clock module

higher attenuation at 19.8 dB per 100 m. Construction of the subsystem demonstrated that the received signal was within the bounds of the clock receiver equalisation capability, although clearly some wideband phase noise performance was sacrificed to meet the budget. The clock receiver in each node is shown in Figure 5-3, where the NatSemi CLC012 performs adaptive line equalisation and thresholding, regenerating the clock output in PECL format, which is then further fanned-out by OnSemi logic in order to generate clocks at appropriate levels for each of the coherent components - the FPGA, ADC, PLL and DDS. Again, the schematic and PCB layout for this module were designed in Orcad, and are shown in Appendix F.

The local oscillator is then synthesised in each node from this reference clock. Here, an evaluation board was used from National Semiconductor that integrates the LMX2326 PLL, VCO and a monolithic RF amplifier on a single PCB with nominal output power of -3 dBm. The loop filter designed in Section 4.5 was assembled onto this board[1]. Then, a small RF power splitter circuit was designed based on a Minicircuits surface-mount device, together with a Minicircuits monolithic ERA-series RF amplifier mounted on one of the outputs[2]. The schematic is shown in Appendix F, and the resulting LO signals, at -8 dBm and +7 dBm, are used to drive the single-sideband upconverter in the transmitter and mixer in the receiver respectively.

[1]Care was taken to use NP0 capacitors where possible in the loop filter as they are temperature compensating and not piezoelectric. However, the large capacitances required for the narrow loop filter meant certain components were only available with X7R/X5R dielectrics, which could cause the filter to exhibit minor transient behaviour in an environment with strong vibrations.

[2]The AC coupling capacitors were chosen carefully for parasitic inductance and equivalent series resistance (ESR) at the local oscillator frequency in order to minimise insertion loss.

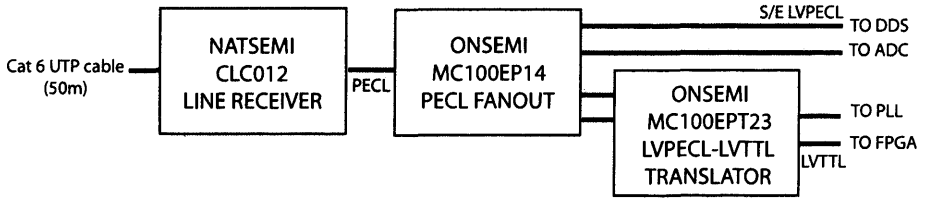

Figure 5-3: Clock receiver and fan-out module

5.4 Transmitter Design

In this section, the design and construction of the transmitter chain in each node is described. The design is based around the Analog Devices AD9854 direct digital synthesiser (DDS), which synthesises a programmed waveform at baseband that is phase coherent to the supplied reference clock. The internal structure of the AD9854 is shown in Figure 5-4. The device registers are programmed using a (proprietary) parallel interface, and include a frequency tuning word (FTW), a delta-frequency word (DFW), phase adjust register (PAR), amplitude control and flags to reset/hold the phase accumulator (CLRACC) and set the operation mode (MODE). Programming is arbitrated asynchronously using the write strobe (WRB), however a separate I/O update strobe (IOUDCLK) is used to 'activate' each new program, which is then synchronised to the next reference clock edge. Therefore, it is possible to ensure that the baseband signals are coherent as there is a known latency between the clock edge following assertion of IOUDCLK and the effect on the analogue output signal.

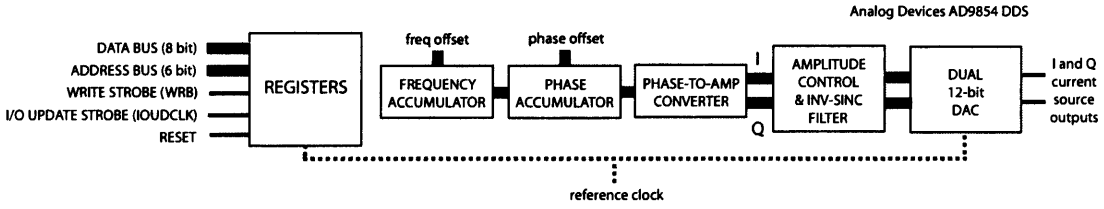

Figure 5-4: Structure of the Analog Devices AD9854 DDS

A integral digital filter compensates for the 'sinc' shaped roll-off resulting from the action of the output DACs as the frequency approaches Nyquist. These dual DACs approximate current sources that are proportional to the in-phase and quadrature baseband waveform. The sampling action of the DAC also generates images at all integer multiples of the sampling frequency, so it is necessary to implement reconstruction filters at each output to minimise power wastage and out-of-band spurs. An analogue 11th order elliptic (Cauer) low-pass filter was designed to have a narrow transition region at the edge of this pass-band (shown in Figure 5-5), and the S21 parameter response in Figures 5-6 (passband) and 5-7 (wideband) was simulated using Agilent ADS. Amplitude ripple in the passband is less than 0.5 dB, although the group delay rises slightly toward the Nyquist frequency as expected. The wideband response shows better than 50 dB attenuation beyond 80 MHz. Therefore, a 10 MHz signal generated by the DDS will result in the most significant image at

$f_{clk} - f_{out} = 90$ MHz being attenuated by some 50 dB, plus an additional 15 dB attenuation resulting from the sinc roll-off response from the DAC. However, a 40 MHz signal will result in an image at 60 MHz that is only ≈ 3 dB below the carrier. Clearly this problem could be circumvented by designing a filter with lower cut-off frequency (at the expense of greater group delay distortion in the passband) or by clocking the DDS at a higher frequency (at the expense of additional analogue complexity), although it was decided within the context of this design where transmitter power and out-of-band emissions are not critical that a suitable compromise had been found.

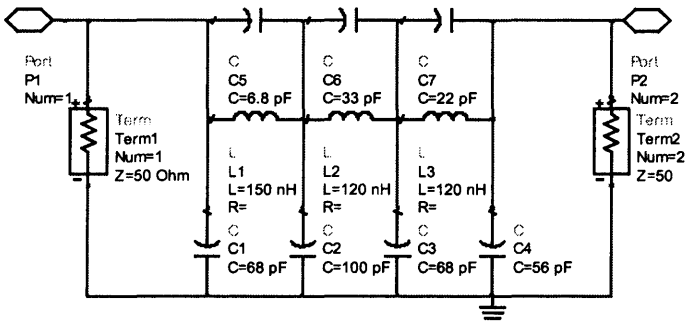

Figure 5-5: DDS output reconstruction filter design

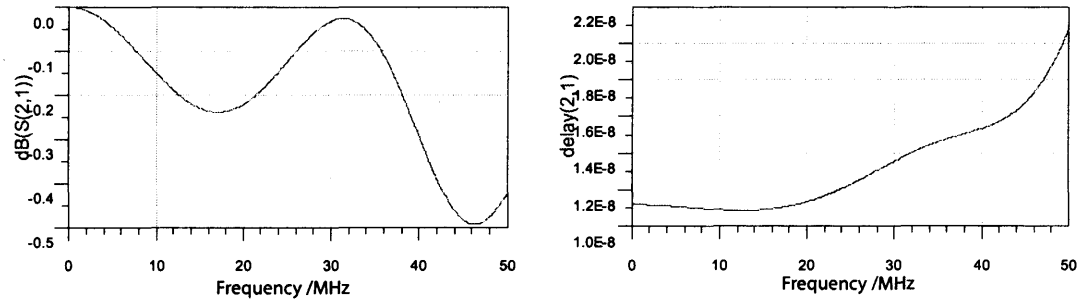

Figure 5-6: DDS output reconstruction filter passband S21 simulation

The dual I and Q outputs from these filters enable the convenient implementation of a quadrature modulator with the structure shown in Figure 5-8 for direct single-sideband upconversion. The synthesised 2400 MHz local oscillator is applied to a polyphase network phase splitter that generates quadrature channels and applies them to the LO inputs of two Gilbert-cell double balanced mixers. The Q and I channels (respectively) from the DDS

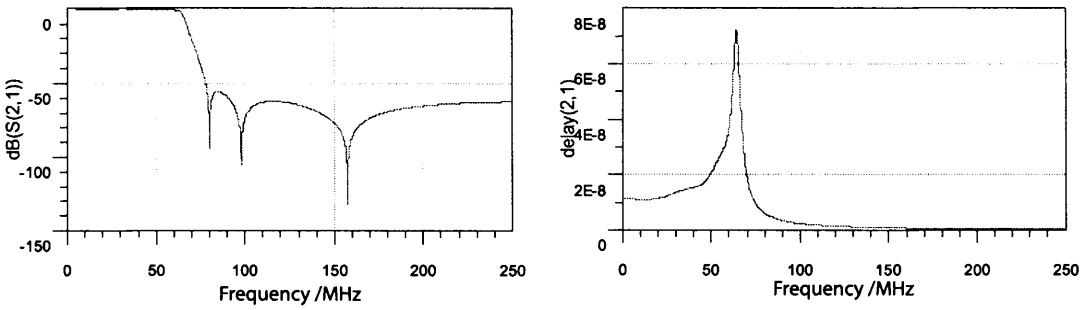

Figure 5-7: DDS output reconstruction filter wideband S21 simulation

reconstruction filter are used as baseband inputs, where transformers are used to provide impedance matching, voltage step-up, and create the required differential signals. Finally the outputs of both mixers are summed. The result is the cancellation of the (unwanted) lower sideband, resulting in an SSB RF output at $f_{LO} + f_{DDS}$. Therefore, baseband signals arbitrarily close to DC can be used without the concern of filtering unwanted images. This design effectively implements a homodyne system as there is no explicit intermediate frequency stage, although an effective IF for unmodulated or phase coded pulses can be programmed by setting the FTW register in the DDS to any frequency within its bandwidth[3].

Here, the Analog Devices AD8346 IC is used, which implements the entire modulation circuit in a single IC. Its nominal LO input frequency range is 800 - 2500 MHz, and accepts baseband signals from DC to 70 MHz. The LO frequency range is restricted to that where the outputs of the integrated phase splitter are approximately in quadrature. However in practice, small errors over the passband are also present that result in imperfect suppression

[3]This is in fact necessary as the DDS output is AC-coupled and therefore cannot generate DC baseband signals.

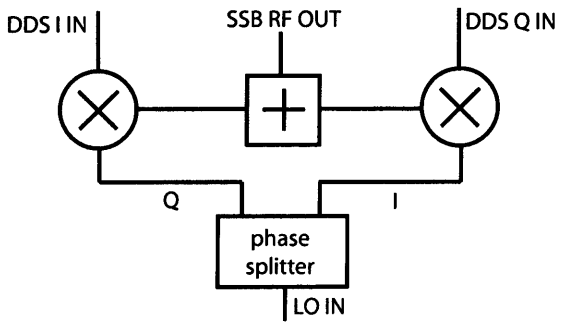

Figure 5-8: A quadrature modulator used by single sideband upconversion

of the image, which has a typical value of -35 dBc. Local oscillator 'feed-through' is specified as -45 dBm. The resulting simulated RF spectrum[4] is shown in Figure 5-9. Therefore, it is preferable to arrange the effective IF for phase modulated waveforms to be in the centre of the DDS bandwidth, as this gives maximum isolation from phase noise related to these images.

The combination of a DDS waveform synthesiser and quadrature modulator, designed completely from COTS components, forms a very low-cost transmitter subsystem that meets in principle the requirements for freqency/phase agility and bandwidth required by the radar. A block diagram of the transmitter module is shown in Figure 5-10. A Minicircuits ERA-series monolithic RF amplifier is placed after the modulator to provide a nominal output power of -2 dBm. The complete subsystem was designed and manufactured on a single circuit board using Orcad - the schematic and PCB layout for which is shown in Appendix F. As the design is mixed-signal, particular care was taken with digital and analogue separation and layout, grounding, decoupling, and the provision of controlled impedance microstrip signal paths. Further, good quality, small tolerance components were used in the reconstruction filters to minimise differences in group delay that would affect quadrature and degrade image attenuation. The reference clock input to the AD9854 is comprised of two differential pins with low-voltage ECL logic levels, so a translator was implemented on the board so that the reference could be single ended, to avoid the practical inconvenience of running differential signals between modules.

The transmitter chain is completed by the addition of a modular, SMA-connectorised Minicircuits linear RF amplifier (model ZRL-2400LN) providing a further 25 dB gain, giving a total output power of +23 dBm as per the specification. The 50Ω output from this amplifier may be connected directly to the transmitter antenna.

[4]Based on figure from Analog Devices AD8346 datasheet

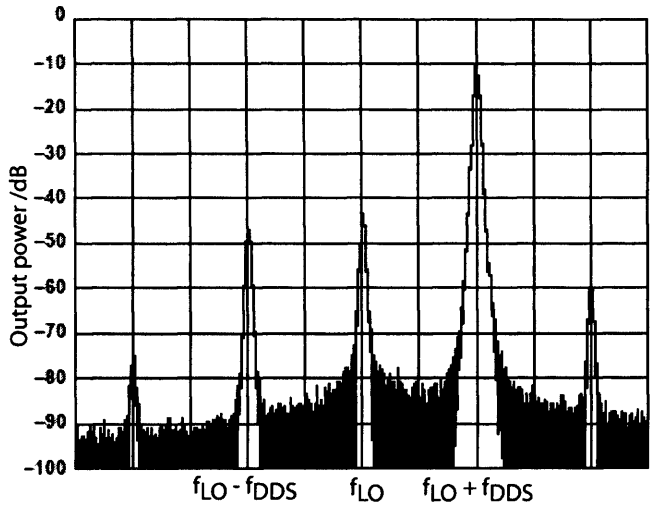

Figure 5-9: Illustrative SSB RF transmitter output

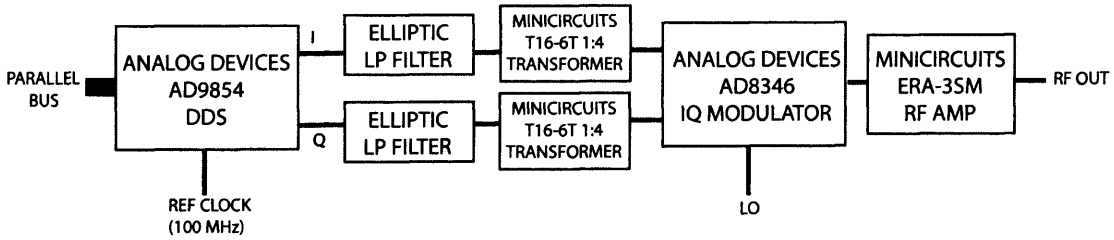

Figure 5-10: Block diagram of transmitter PCB

5.5 Receiver Design

In this section, the design and construction of the receiver chain in each node is described. The receiver should take the RF signal at its input, amplify it whilst adding as little additional self-noise as possible, downconvert the signal to baseband using the synthesised local oscillator, and digitise it with adequate bandwidth for faithful digital reproduction.

Firstly, a power budget is calculated in order to determine the gain required in the receiver chain. We start by considering the sensitivity of the analogue-to-digital converter. The full-scale amplitude of the ADC is 2 V pk-to-pk, equal to a +10 dBm sinusoidal signal into 50Ω, so the maximum receiver gain possible before saturation is given by $10 - P_r$ dBm. The quantisation step size for the ADC with ENOB = 11 is given by $v_q = 2/2^{11} = 9.766 \times 10^{-4}$ V. Therefore, the receiver noise level at the ADC input should be at least $10\log(v_q^2/50) = -56.2$ dBm in order to cause toggling of the effective LSB so that integration gain can be realised. This value also designates the minimum detectable signal at the ADC, so its dynamic range is 66.2 dB. Assuming that the receiver is dominated by thermal self-noise generated at its input and that the baseband signal is band-limited to 50 MHz, the noise power prior to amplification is $kTB = -97$ dBm, and the minimum receiver gain on this basis (disregarding the receiver chain 'noise figure') is $-56.2 + 97 = 40.8$ dB.

Now, the specification is completed by analysing the monostatic radar equation, which can be expressed as:

$$P_r = \frac{P_t G_t G_r \sigma \lambda^2}{(4\pi)^3 R^4} \tag{5.1}$$

where P_r is the signal power at the input to the receiver chain. For a transmitted power $P_t = 0.2$ W, and assuming directional antennas with gain $G_t = G_r = 250$ (24 dBi), we can write $P_r(\text{dBm}) = 20 + \sigma(\text{dB}) - R^4(\text{dB})$. Firstly assuming a small target with unity RCS at the maximum range 1,000 m, $P_r = -100$ dBm, and a gain of $-56.2 + 100 = 43.8$ dB is required for the received signal to be detected by the ADC. Now assuming a very large calibration target with RCS 150 m^2 (21.8 dB) at the minimum range of 20 m, $P_r = -10.2$ dBm, and a gain of only 20.2 dB would saturate the ADC. Clearly there is inadequate dynamic range to meet both requirements, so some compromise is required. It is trivial to attenuate the transmitted signal by DDS amplitude control or bypassing the power amplifier gain when large targets must be observed at close range, and high signal power at the ADC minimises the effect of quantisation distortion. Therefore, taking into account insertion

losses of ≈ 8 dB for the mixer and 2 dB for general cabling and filter losses, it is decided to implement receiver *amplifier* gain totalling approximately 60 dB.

An outline of the receiver chain design is shown in Figure 5-11. COTS amplifiers with low noise and distortion are relatively expensive, so the total gain is split between RF and baseband stages. The RF stage uses a high quality SMA-connectorised Minicircuits low-noise amplifier (model ZRL-2400LN) with nominal gain of 25 dB and a typical noise figure of 1.2 dB, as this first gain stage has the largest influence on the total receiver noise figure. Then, a single frequency mixer (Minicircuits ZEM-4300) specified for high IP3[5] together with a modular low-pass filter perform signal downconversion using the synthesised local oscillator. A high-gain baseband amplifier was then designed in Orcad and constructed, the schematic for which is shown in Appendix F. This amplifier comprises a low-noise COTS monolithic device[6] (Analog Devices AD605) followed by a wideband voltage-feedback op-amp (Texas Instruments THS4304) with adequate slew rate to drive the ADC input at full scale without distortion. The combined power gain of this amplifier is nominally 35 dB over the 50 MHz baseband bandwidth, giving a total gain between the amplifier stages of 60 dB as required. The amplified baseband signal is then low-pass filtered to minimise aliasing of high frequency noise into the passband. An evaluation board from Analog Devices was used for the ADC itself, which provides a back-to-back transformed-coupled input path converting the single-ended signal to differential form for the ADC chip, which is then clocked directly by the system reference oscillator at 100 MHz.

[5]The minimisation of mixer spurs is desired to prevent their aliasing into the doppler bandwidth.

[6]The AD605 is in fact a variable-gain amplifier, and although it is currently operated in fixed-gain mode, provision is made in the circuit design for an analogue control voltage signal to be used.

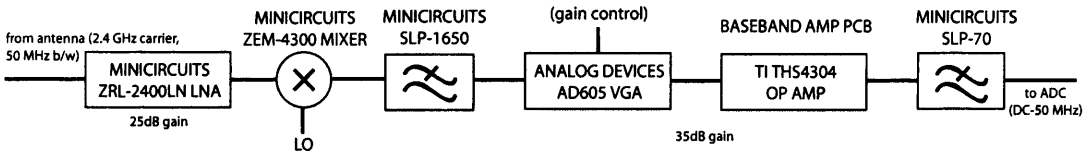

Figure 5-11: Block diagram of receiver chain

5.6 FPGA Design

In this section, the design and implementation of the functionality contained within the FPGA in each node is described. The FPGA is the hub of the digital systems within each node, providing an interface between the mixed-signal COTS components (DDS, ADC, PLL and the network transceiver) as well as performing synchronous control of the coherent transmission of signals and reception of data, and buffering of the digitised signals from the receiver and programming commands for the DDS. Further, it contains a soft-core implementation of a network controller, and also provides an interface with the digital signal processor (DSP), and ultimately the user interface. An overview of this functionality is given in Figure 5-12.

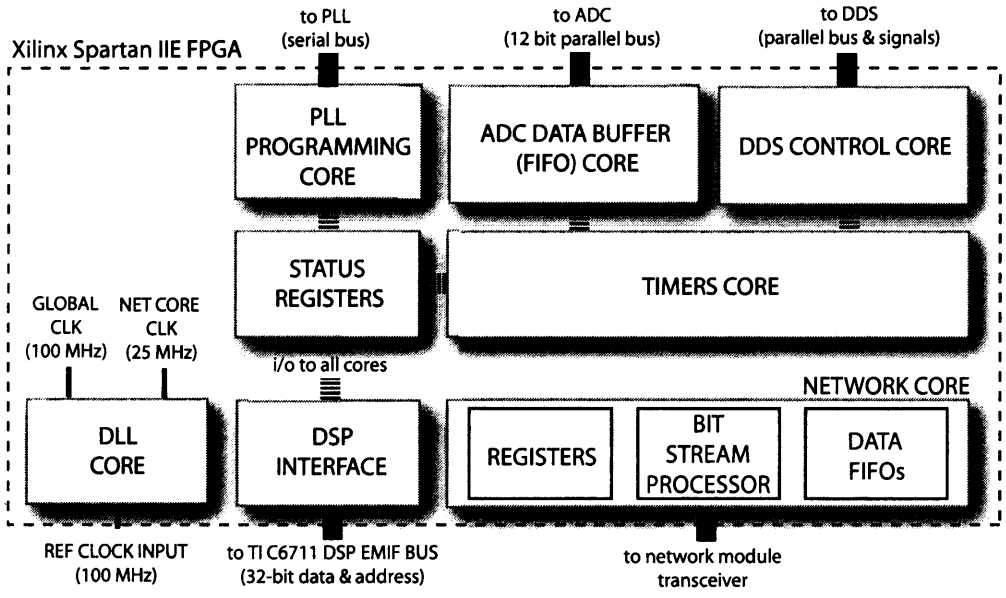

Figure 5-12: Block diagram of FPGA functionality

This complete set of cores is run synchronously at a high speed (clocked by the reference oscillator at 100 MHz). However, it necessary to use a fairly modest FPGA in terms of cost (the Xilinx Spartan IIE) in order to meet the budgetary requirements, so careful coding techniques were used in order to optimise the logic to meet the timing requirements. The FPGA in each node was purchased on a development board[7], and a daughtercard designed and constructed to enable each interfacing subsystem to connect directly to the FPGA pins.

[7]Memec Design Spartan IIE LC Development Kit, www.memec.com

Careful attention was paid to maintaining constant impedance digital signal paths and the control of FPGA output drive currents in order to minimise the effect of 'ground bounce'. The FPGA software design was implemented almost exclusively in VHDL, and amounts to some 2,500 lines of code, excluding the third-party network controller core. The compiled 'bitstream' can be uploaded to flash memory on the development board so that the FPGA automatically boots and configures itself each time it is powered up. Below, each of the cores is described in the context of their relationship with the radar system. Each core was tested by simulation using VHDL testbenches prior to implementation in the real device.

5.6.1 DLL Core

The delay locked loop (DLL) core is designed to ensure that the input reference clock is fanned-out over the FPGA chip itself with minimal skew, which could result in timing offsets between critical coherent modules. Its general structure is shown in Figure 5-13.

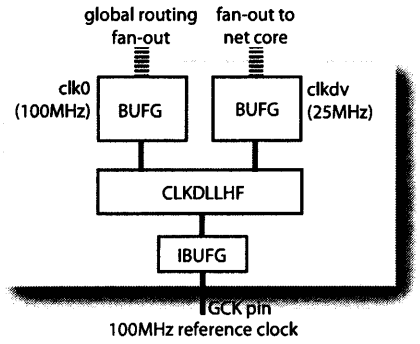

Figure 5-13: DLL Core

Whilst such timing offsets would be deterministic for a particular implementation, they require physical testing to determine, are difficult to compensate for outside the digital domain, and are likely to alter whenever changes are made to the FPGA design or the code is ported to a different device. Therefore, this core implements a Xilinx primitive[8] Delay Locked Loop structure, for which the input is the 100 MHz reference oscillator applied to a dedicated input pin. The core instantiates so-called 'primary global routing resources' across the FPGA, which form a feedback loop with variable delay control so that clock

[8]'Primitives' are physical entities within an FPGA, typically including large numbers of unassigned logic blocks as well as fixed resources such as the DLL structure that may be vendor specific (although usually common amongst a 'family' of devices). Primitives may be utilised by 'inferring' them in generic VHDL code, or by 'instantiating' them using specific libraries.

edges appear to arrive at every logic element in phase. After lock is achieved, the feedback loop can be deactivated so that there is no additional jitter contribution resulting from its use. The maximum skew for this design was shown by simulation to be less than 7 ps. The DLL core has a further function that is to divide this reference clock by a factor of four to create a skew-compensated 25 MHz clock, which is used as a reference for the network controller core.

5.6.2 PLL Programming Buffer Core

The PLL programming buffer core, shown in Figure 5-14, provides an interface between the processor (which ultimately determines the programming parameters) and the PLL used to synthesise the local oscillator. The core is activated by an internal flag during system configuration, and converts three parallel programming words (describing the load values of the R and N counters determining the oscillator multiplication ratio) held in the FPGA registers into a serial bitstream with appropriate handshaking that is compatible with the PLL device's (proprietary) programming interface.

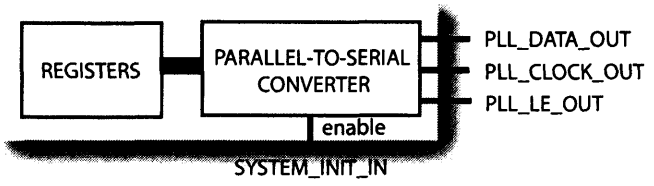

Figure 5-14: PLL programming core

5.6.3 ADC FIFO Core

This core is a virtual implementation of a dual-port first-in-first-out (FIFO) buffer for providing temporary storage of the received data from the ADC. Its general structure is shown in Figure 5-15. The FIFO is based around Xilinx primitive 'blockram' (fast static RAM) units integral to the FPGA. Six such blocks, each configured as 2 bit × 2048 word static RAM units, are used in parallel to implement a 12-bit wide FIFO that can operate at 100 MHz and so store a total of 2,048 samples from the ADC in real-time, equivalent to 20.48 μs of contiguous data capture. Therefore, if the FIFO commences data collection at the time of transmission, data can be captured corresponding to a monostatic range of

up to 3,072 m. The secondary port of the FIFO is routed internally to the DSP interface core so that data can be transferred to secondary storage during the remainder of the pulse repetition interval.

Synchronisation of the core with the digital output from the ADC board is guaranteed when the ADC manufacturer's timing parameters are factored into the FPGA timing constraints for its input pins. In order to achieve this speed, read and write address pointers for the two ports are generated efficiently using linear feedback shift register (LFSR) counters, as linear contiguity is not required in memory as long as data is written and read in the same order. 'Empty' and 'full' flags are derived to determine when valid data can be written or read to the memory.

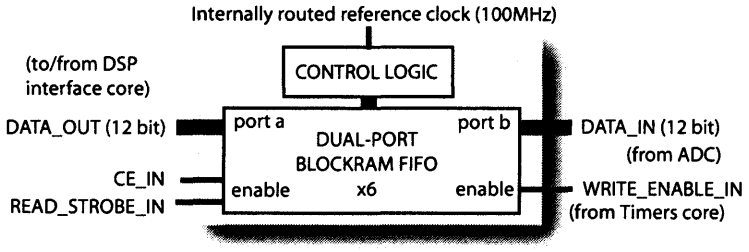

Figure 5-15: ADC FIFO core

5.6.4 Timer Core

The timer core comprises a series of synchronous counters operating from the 100 MHz reference clock with programmable load values. They are concerned with timing the pulse repetition interval for the transmitter, and the 'window' over which data is captured in the receiver. Their interrelationship is shown in Figure 5-16.

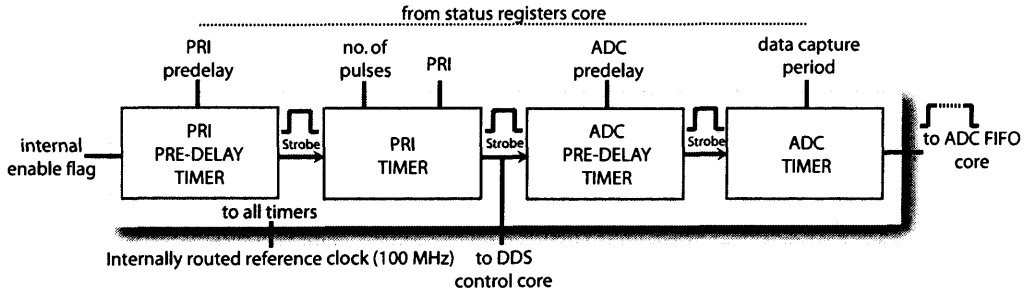

Figure 5-16: FPGA timer module

Each of the timers is programmed by values held in FPGA registers, and the core is

enabled by an internal flag. The 'PRI pre-delay timer' enables deterministic timing offsets between nodes to be synchronised at the start of an integration period. The 'PRI timer' is then used to generate single-cycle strobes at intervals determined by the pulse repetition interval, repeated for the programmed number of pulses. These strobes are used to enable the DDS control core and the ADC timers. Usually, the system starts collecting data from the ADC at the same time each pulse is transmitted, however the 'ADC pre-delay' timer can be programmed to delay the start of this capture so that the range 'swath' is user-definable. Finally, the 'ADC timer' generates an enable strobe for the ADC FIFO core to determine the period for which data is collected corresponding to each transmitted pulse.

The timers run at the full speed of the reference clock (100 MHz), so the resolution of the PRI and synchronisation offsets is 10 ns. In order to achieve this speed in the FPGA, each timer is implemented as a down-counter using a binary word that is one bit larger than the load value. Then, one cycle after the counter reaches zero, the counter 'rolls over' such that this MSB forms the strobe output directly. This method allows considerably faster timers to be constructed compared to traditional methods where each bit of the current value must be compared to a 'terminal' value using a long carry chain on every cycle.

5.6.5 DDS Control Core

The DDS control core implements an interface between the processor (which ultimately determines the programming parameters) and the AD9854 DDS chip in the transmitter module. This core includes a buffer to store commands for programming the DDS waveforms in real-time, a synchronous interface that implements the necessary timing and control signals for compatibility with the DDS's proprietary parallel programming port, and the related control logic. The general structure of the core is shown in Figure 5-17.

DDS waveform programming commands are written to the FIFO by the processor. This FIFO is implemented using Xilinx primitive 'distributed RAM' configured as a 24 bit $\times$ 128 word structure, which has zero clock latency on read cycles. This 24-bit programming word is divided into three sections: an eight-bit data word, a five-bit address word, and a six-bit 'delay' word. The data and address words are used to program the DDS across its parallel interface. The delay word is fed internally to an enable counter in order to control when the next word in the buffer should be read out.

During system configuration, the transmitter module should be setup by programming

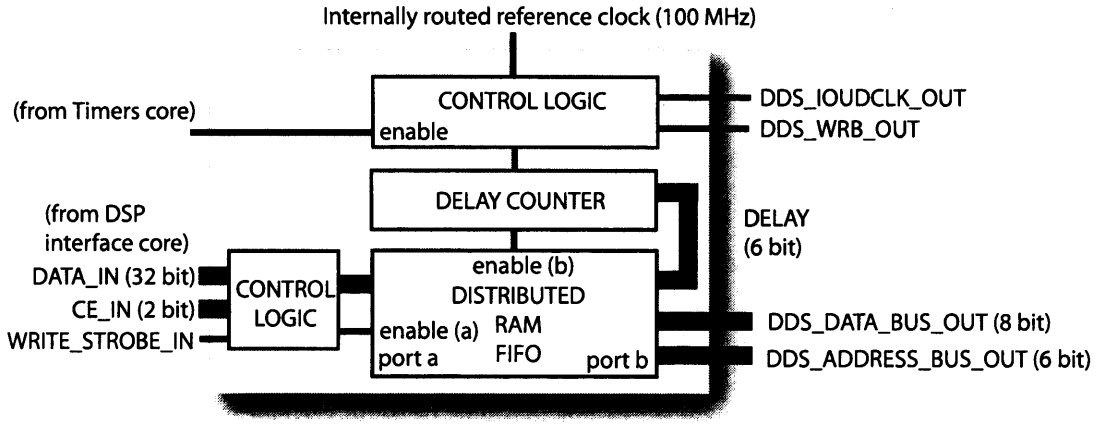

Figure 5-17: DDS control module

the DDS internal registers with the appropriate MODE[9] ('single tone' or 'linear FM') and the DFW, which sets the 'ramp rate' of a chirp pulse. Then, a single pulse can be defined by up to 128 discrete 'real time' programming commands, which should be loaded into the FIFO from the DSP. These will consist of the release of the phase accumulator (CLRACC), followed by a delay for the pulse length duration, after which CLRACC is reset. During the transmission of the pulse, the required phase changes for each bit of a phase modulated code should be programmed in real-time by modifying the phase adjust register (PAR). For example, a chirp waveform would be programmed using the following pseudo-commands:

MODE and DFW preset

[1]	Start pulse	Release CLRACC	delay = pulse length
[2]	Stop pulse	Set CLRACC	

An arbitrary phase-coded waveform can be programmed similarly:

MODE preset

[1]	Start pulse	Release CLRACC	delay = bit length
[2]	Change phase	Write phase ϕ_2 to PAR	delay = bit length
[3]	Change phase	Write phase ϕ_3 to PAR	delay = bit length
$\vdots$	$\vdots$	$\vdots$	$\vdots$
$[n+1]$	Stop pulse	Set CLRACC	

[9]Full definitions for the DDS internal registers can be found in the Analog Devices AD9854 datasheet, www.analog.com

As 'distributed RAM' is used to instantiate the FIFO, the value of the delay word can be read on the same cycle that the command is programmed into the DDS, which in turn loads the delay counter. Therefore, these commands can be programmed in real-time at a rate of up to 50 MHz (where delay = 0), which results in a minimum bit length of 20 ns for phase coded pulses, and a maximum effective bandwidth of 50 MHz. Chirp waveforms may also be programmed using DFW to span the entire DDS bandwidth (DC - 50 MHz). Further, unlike a discrete FIFO buffer, the programmed words remain in constant positions in the distributed RAM, such that only the address pointers move. As a result, these pointers may be reset between every pulse so that efficient use is made of the FPGA resources when a train of identical pulses is to be transmitted.

During each programming cycle, control logic is used to toggle the handshaking lines DDS_WRB and DDS_IOUDCLK (see Figure 5-4) in order to latch each word into the DDS internal registers and 'activate' them synchronously to the reference clock, resulting in the timing and phase of each pulse being completely deterministic.

5.6.6 DSP (EMIF) Interface Core

The DSP interface core provides an asynchronous interface between the DSP (processor) external memory interface (EMIF) and the FPGA. The EMIF is a 32-bit parallel data and address bus with asynchronous handshaking signals. This core performs the necessary decoding of the address bus such that the FPGA appears as a memory-mapped device in the processor's memory space. The general architecture of the core is shown in Figure 5-18.

The interface allows the processor to write to the programming buffers (PLL and DDS) and status registers in the cores described above, as well as read from the ADC data FIFO and interact bi-directionally with the network core. All of these data transfers occur asynchronously and are controlled by the processor itself.

The most demanding facet of the implementation of this core is ensuring the stability of the high-speed data transfer between the two clock domains. The EMIF is controlled by the *processor's* internal clock, which by coincidence also runs at 100 MHz, but is not phase coherent to the FPGA reference. A two-stage method has been implemented (described in Appendix G) that firstly caches the DSP address and data bus values on the appropriate read and write strobes, and then synchronises internal strobes to the FPGA internal oscillator. This method prevents timing problems due to the asynchronous nature of the two clocks,

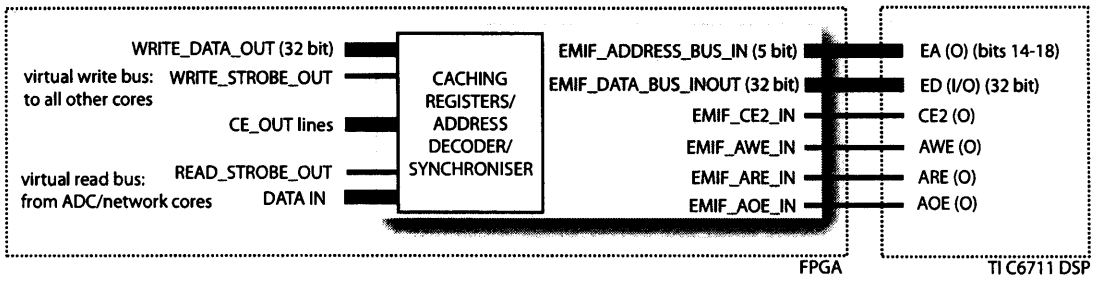

Figure 5-18: DSP (EMIF) interface core and external connections

and minimises the potential for metastability at the inputs.

5.6.7 Network Core

The network core is based on an open-source third-party implementation of a Controller Area Network (CAN bus) controller(141) written in Verilog. It uses the Wishbone open architecture virtual interface to communicate with the other cores in the FPGA. The network core contains both the CAN controller implementation itself and a 'wrapper' to interface the Wishbone interface to the DSP EMIF interface. The general architecture is shown in Figure 5-19. This core forms part of the network system between the nodes, which is described in the next section.

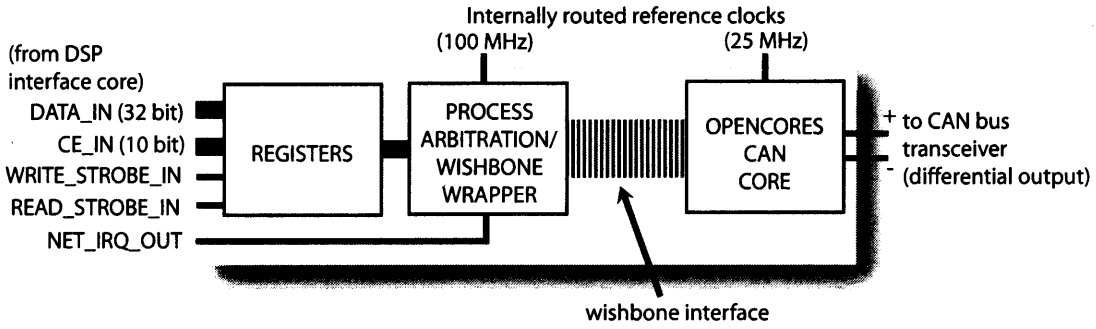

Figure 5-19: Network core

5.7 Network

In this section, the implementation and construction of the network subsystem between the three nodes is described. The network should allow each of the nodes to be configured from a central point (a notebook personal computer), and enable raw (or semi-processed) data at each receiver to be transferred to the 'master' node for joint processing, and then to the computer for off-line storage and visualisation of results.

In this prototype system, some small latency during data transfer will normally be acceptable, so whilst in general a relatively large amount of data must be transferred for coherent processing (compared to fusion of plots or tracks), a very high bandwidth real-time network is not necessary in this case. As an example, we assume that the two 'slave' nodes capture 10 μs of 12-bit data each, sampled at 100 MSPS, which must be transferred to the 'master' node for joint processing. The total data transferred is given by:

$$10 \times 10^{-6} \times 12 \times 100 \times 10^{6} \times 2 = 22.4 \quad \text{kb} \tag{5.2}$$

If multiple pulses are captured over an integration period, it was shown in Chapter 2 that temporal integration could be performed locally prior to centralised detection, in which case a very modest transfer rate of 20 kb/s is adequate[10].

Therefore the main requirements for the network are a moderate bandwidth coupled with good reliability and, in particular, minimal overhead in terms of cost, processing power and design complexity. As a result, the Controller Area Network (CAN bus) was chosen for implementation in the radar. This protocol was developed by Bosch, and is designed for and very widely used by the automotive industry for networking critical components (e.g. engine management system, by-wire brakes and so on) in vehicles. Hence reliability is paramount, and rigorous collision detection and error-correction techniques are used to prevent data loss[11]. Crucially, because it is designed for embedded systems, arbitration of the network is performed completely within hardware (or, in this case, the FPGA core) so there is virtually zero processing overhead imposed on the host processor. For example, a

[10]It is noted that there may be greater network bandwidth requirements in the future if multistatic doppler processing or spatial-temporal processing (e.g. for adaptive cancellation of interferences) is implemented in the system.

[11]Further information on this protocol is available in the CAN Specification(142).

standard implementation of IEEE 802.3 Ethernet[12] requires a physical transceiver, hardware medium access control (MAC) sublayer, as well as network and transfer layers (e.g. TCP/IP) implemented in software as well as a complex application layer interface. In contrast, the OSI model for CAN bus comprises only physical (transceiver) and datalink layers - the latter is implemented in its entirety in the FPGA. Indeed, this core is less than half the size of the equivalent for the Ethernet MAC sublayer alone in terms of the number of FPGA gates used.

The network system implemented in the radar comprises three components: the CAN bus core integrated into each FPGA, a hardware transceiver module in each node, and the physical wiring itself. The FPGA core is essentially an emulation of a hardware CAN bus controller (Philips SJA1000), including replication of its internal memory-mapped configuration registers. A single data 'frame' consists of 64 bits of data plus 40 bits for the total identifier. The local processor in a given node can broadcast a data frame simply by writing the data and identifier to memory-mapped registers in the FPGA core. The receiving nodes use a configurable filter in the core to determine whether a frame should be accepted based on the identifier, and then alert the processor using an interrupt line in the EMIF interface. Similarly, a node can request data by broadcasting a frame with an identifier only. In this case, the 64 bits of data in a frame are adequate for transmitting a single complex 32-bit sample (or a 64 bit configuration word). The identifier is used to specify the node(s) that should receive it and its context (for example, the sample index in an array of received data).

The output of the FPGA core comprises two signals (CAN_HIGH and CAN_LOW), which are connected to the hardware transceiver module. This module contains a discrete line driver/receiver IC that is compatible with the CAN bus specification. The transceiver modules in each node are connected with Category 6 UTP cable in a bus topology, as shown in Figure 5-20. The maximum speed of the bus is determined by the total cable length, which in this case (100 m) results in a maximum data rate of 128 kb/s. This is well above the required rate stated above, although due to the very small data packet size the frame overhead and 'turn-around time' at the processor will be significant.

A secondary purpose for the hardware transceiver module is to enable the *synchro-*

[12]Ethernet is chosen as the comparative example because it is the industry-standard wired networking protocol over the distances considered here.

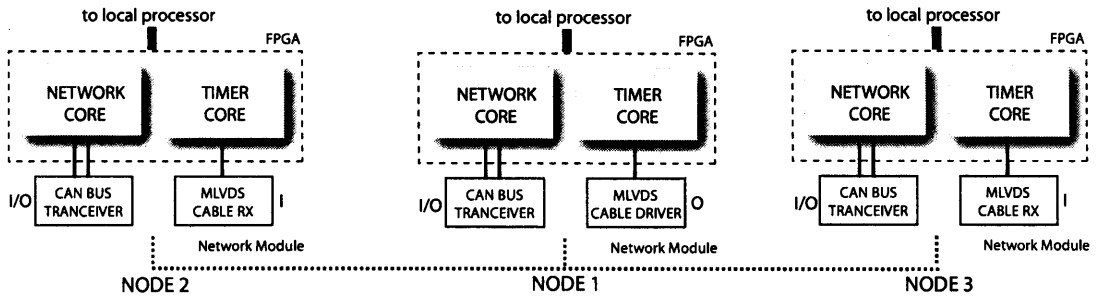

Figure 5-20: Network subsystem

nisation of the timing cores in each node. Whilst the distributed (continuous) reference oscillator maintains clock synchronisation across the network, this additional facility is required to simultaneously reset the timers in each node to a known state. In practice, this is achieved by transmitting a synchronisation pulse prior to the start of the radar activity from the FPGA of the 'reference' node to the 'slave' nodes on an second twisted pair in the UTP network cable. Therefore, a COTS Multipoint Low Voltage Differential Signalling (MLDVS) chipset by Texas Instruments is also implemented on the transceiver module. This standard is used due to the large output voltage transition designed to assist recovery of the 'smeared' pulse *after a deterministic number of clock cycles* at each slave node. The deterministic delay caused by propagation of the pulse can be determined in calibration and offset using the 'PRI pre-delay' counter in the Timers core described above.

The schematic and PCB layout for transceiver module (comprising both CAN bus and MLVDS transceivers) were designed in Orcad and are shown in Appendix F[13].

5.8 DSP Hardware

In this section, the digital signal processing hardware and related control software in the system is described. The hardware takes the form of a Texas Instruments C6711 floating point DSP in each node that was purchased on a development board[14]. These processors can communicate with each other via the network subsystem described above. The development board also includes 16 MB of SDRAM and a daughter-card header, so a small daughter-card was designed and constructed to interface the processor's EMIF interface to its local FPGA

[13]The design for node 1 (the 'master' node) is slightly different to that for the 'slave' nodes 2 and 3 as the MLVDS system is unidirectional.

[14]Texas Instruments C6711 'DSP Starter Kit' (DSK), www.ti.com

in each node. The DSP software was developed almost entirely in C, and amounts to some 2,200 lines of code. In addition, certain signal processing functions are based on C-callable assembler in order to maximise performance.

The functionality of the processor code includes determination of DDS and PLL programming commands from the user-configurable radar parameters, writing these commands and timer load values to the appropriate FPGA cores through the memory-mapped interface, transfer of digitised signals from the ADC FIFO core in the FPGA to SDRAM during the 'free time' in the pulse repetition interval, bidirectional communication with other nodes across the network, and finally signal processing of the received data. The implementation of the signal processing itself is described in Section 5.10.

The transfer of digitised signals from the ADC FIFO core to RAM is time-critical because it must be completed before the capture of data for the following pulse repetition interval commences. For example, given a 1 kHz PRF and data capture period of 20 μs starting at the time of transmission, there is a 980 μs period in which the transfer of the 2,000 samples must occur, which reduces proportionally if a higher PRF is chosen. Hence, the limiting factor on the maximum PRF in this design is the speed at which this transfer can be completed. The transfer is initiated as soon as each capture is complete by a hardware interrupt request (IRQ) that passes from the ADC FIFO core on the FPGA through the EMIF interface to the processor. This triggers the integrated direct memory access (DMA) controller on the processor with the highest possible priority, which is then responsible for streaming the data from the FPGA directly to the processor memory-mapped RAM.

The compiled code is uploaded to flash memory on the development board, such that each processor auto-boots when it is powered on. The 'master' node 1 is responsible for transferring user-programmed radar parameters to the 'slave' nodes 2 and 3 across the network[15]. An outline of the procedures performed by the processor in both the master node and the slave nodes is given in pseudo-code in Appendix G.2. It can be seen that, after booting, the master node checks the network status and then broadcasts the user-programmed radar parameters, whilst the slave nodes remain idle until they are received. After configuration, the slave nodes again remain idle until they receive the synchronisation

[15]In fact, the code base for all nodes is identical, and each node determines its own 'identification' at boot-time by reading the value of a set of hardware DIP switches on each FPGA board. This strategy was adopted to resolve the development issues resulting from the maintenance of two sets of similar code.

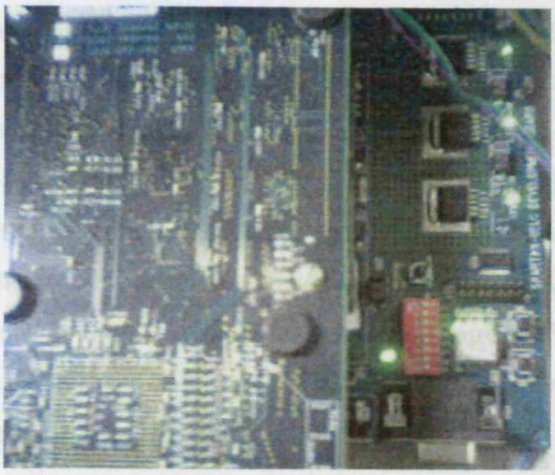

Figure 5-21: DSP and FPGA subsystem

pulse from the master node. At this stage, synchronisation is controlled completely by the FPGA, and the only role of the processor whilst the radar is active is the IRQ-initiated DMA transfer of received data to RAM. When all data collections are complete, each node performs the required local processing, at which point the master node requests all remote data across the network, and then performs the joint multistatic processing centrally.

This design realises an autonomous embedded system where synchronisation is achieved directly between the FPGAs in each node operating from coherent clocks, and the system configuration is completely mediated by the master node. The result is that slave nodes may be positioned in any location (within the constraints of the clock distribution and network cable lengths) with no user-intervention required after power-on.

5.9 System Construction

5.9.1 User Interface

The user interface takes the form of software running on a notebook computer. This computer is connected directly from to the DSP development board in the master node through the (proprietary) host port interface (HPI) connector. The software was developed for Microsoft Windows using the Visual C++ .NET programming environment, and totals some 5,000 lines of code. It makes use of a dynamic link library (DLL) supplied by Texas Instruments that allows the host computer to directly read and write into the processor's internal

memory space. As a result, the software can set flags and parameters in this memory to control the operation of the master node, which in turn controls the entire network. Radar parameters may be user-defined both at system level and for each of the three nodes as shown in Figure 5-22. Further, pre- or post-processing data held in the master node's RAM may be selected and visualised in a number of forms, including delay-response graphs for each bistatic pair in the system, and three-dimensional images for viewing the multistatic response. A full screen-shot of the software is shown in Figure 5-23. Finally, all the data stored on the nodes may be saved as a 'bundle file', or alternatively exported to a Matlab compatible file for further processing.

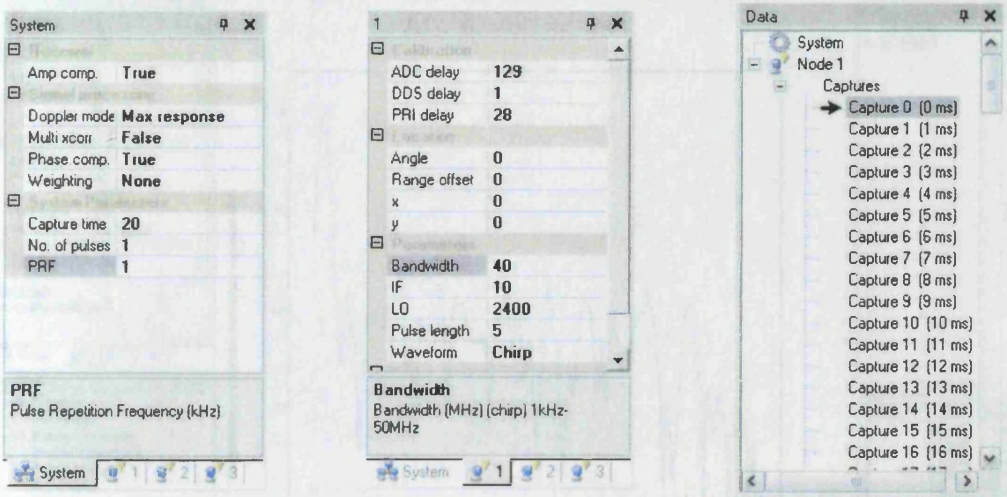

Figure 5-22: User interface control options

5.9.2 System Build

The first stage of the system build involved the design and build of a power supply module for each node. Whilst the FPGA and DSP evaluation boards are ready-supplied with 'wall-wart' DC adaptors, the remaining evaluation and custom-designed boards and amplifiers require DC supplies at 3.3 V, 5 V and 12 V. It was of considerable concern that noise resulting from the digital components (such as the reference clock receiver and ADC) may generate ground bounce and electrical noise that would cause interference in nearby sensitive analogue stages, particularly the low-noise amplifiers and PLL loop filter. Therefore, careful attention was paid to ensuring low impedance ground paths and the provision of separate regulated supplies for digital and analogue components. The design of the power supply

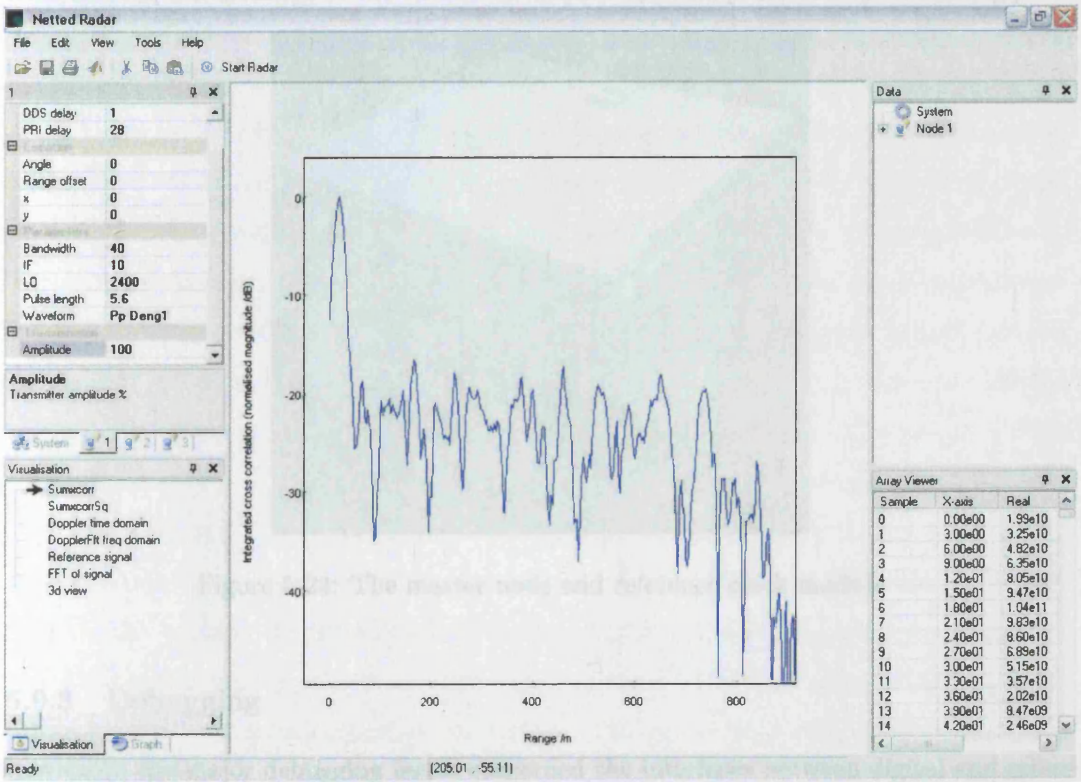

Figure 5-23: User interface screen shot

board, shown in schematic form in Appendix F is based on a bank of Burr Brown low-dropout linear regulators with very low noise characteristics, which are themselves supplied by two low-cost switched mode DC power supplies.

The 'master' node is shown in Figure 5-24. It is necessary for the system to be relatively lightweight and portable, yet adequately rugged to withstand experimental testing. Further, excellent grounding of all RF components must be provided to minimise noise. Therefore each node was constructed in a small (30 cm × 30 cm × 20 cm) steel case, and the reference clock module was mounted to the outside of the master node, protected by a blanking plate.

Figure 5-24: The master node and reference clock module

5.9.3 Debugging

Inevitably, the major debugging issues concerned the interfaces between digital and mixed signal components. The design ensured that digital connections for *all* components are routed into the FPGA, which meant that in most cases problems could be solved in software. The remaining components in the design can be divided into three categories: purely analogue (amplifiers, mixers, clock receiver, PLL), signal converters (ADC, network transceivers) and 'ASIC'-type devices (DSP and DDS). It was found that the vast majority of the development and debugging was related to this final category, mainly due to their proprietary external interfaces. In contrast, integration of the several soft-cores within the FPGA (despite the complexity of the Wishbone interface for the CAN bus controller) was a relatively trivial task, and could be debugged relatively easily in software. Whilst a single

design experience is inadequate to draw firm conclusions about optimal design strategies in the general case, it is suggested that the greatest potential for incompatibility and deviations from specification arises at the hardware *interfaces* between digital components.

A case in point is that of the control of the DDS interface for programming waveforms in real-time. In reality, the order that commands should be programmed is complicated somewhat by various (deterministic) latencies in each logical component of the DDS (see Figure 5-4). Therefore, it is necessary to offset the programming of commands related to, for example, the phase offset register (PAR) and the accumulator control register (CLRACC), by a certain number of cycles in order that the effect on the waveform will be synchronised. Unfortunately, it was found (and confirmed by the manufacturer) that in certain situations these latencies are not constant when commands are programmed close to the maximum speed of the interface. Therefore it was necessary to adopt a complex scheme to ensure that the pulses would always be transmitted at a deterministic time, and a side-effect of this is a considerable reduction in the maximum bandwidth available for phase-coded pulses (chirps are unaffected). Clearly if the DDS had instead been implemented as a digital core in the FPGA plus external DACs, such a problem could be corrected in software, and the performance of the system would not be constrained. Evidently, the paradigm of 'FPGA plus signal converters' is well worth consideration in modern radar designs.

Having completed the debugging for the master node, the construction process was repeated in order to build the two slave nodes, and finally the network interface was tested. Despite the limited debugging capability across such an embedded system, this section of the construction was relatively straightforward as the FPGA interfaces had already been debugged using software simulation testbenches. The general operation of the system was confirmed, and synchronisation of digital clocks was tested using a logic analyser and high speed digital oscilloscope, and was followed by the campaign of performance evaluation and calibration described in the next chapter.

5.9.4 Cost Considerations

The budget of £6,000 was approximately met for the design of the complete system. However, this cost inevitably includes a certain degree of prototype 'wastage' - redesign of components, failures during testing, minor explosions and so on. Therefore it is more illustrative to consider the true total parts cost for the design, as any commercial low-cost

system following a similar design strategy would invariably use greater integration of modules in order to minimise costs. The component cost breakdown is illustrated in Table 5.2, which is based on low-volume (100-unit) budgetary guidance pricing from the appropriate manufacturer or major distributor, and makes allowance for the manufacture and assembly of a compact printed circuit board. It can be seen that the total parts cost is approximately £500, and that this is dominated by assembly, RF analogue components and the high-speed ADC.

This design bridges the gap between very low-cost, dedicated radars (such as those found in motor vehicles for collision avoidance), and much higher cost proprietary commercial and military systems. It offers the potential for considerable development flexibility and modular upgrades, and therefore could be applied to many applications. It is evident that, if the transmission power is increased somewhat by the addition of a further modest power amplification stage (e.g. up to 1 Watt peak output), then ranges of 10 km should be achievable for a single monostatic node. Then, potential applications include local area surveillance, battlefield surveillance and even ground-based air defence. As a multistatic system (with appropriate modifications to a completely wireless design), potential applications include coastal monitoring[16] and airport surface surveillance.

[16]Particularly in maritime applications, the nature of the expected clutter must be considered to determine individual dynamic range requirements.

Item	Cost per item $ (100 unit pricing)
Crystek CCHD-950-25-100 100 MHz crystal oscillator	22.23
OnSemi MC100EPT20 LVTTL-PECL translator	4.00
OnSemi MC100EP14 LVPECL fan-out driver	3.14
NatSemi CLC005 line driver	10.34
NatSemi CLC012 line receiver	18.56
OnSemi MC100EP14 LVPECL fan-out driver	3.14
OnSemi MC100EPT23 LVPECL-TTL translator	4.00
National Semiconductor LMX2326 PLL	1.35
Universal Microwave UMV-2450-R16 VCO	19.45
Agilent MGA-81563 RF amplifier	2.22
Minicircuits TCP-2-25 power splitter	1.99
Minicircuits ERA-3SM amplifier	1.72
Analog Devices AD9854 DDS	19.45
Analog Devices AD8346 IQ modulator	4.62
Minicircuits ERA-3SM RF amplifier	1.72
Minicircuits ZRL-2400LN amplifier	139.95 (unit)
Minicircuits ZRL-2400LN low noise amplifier	139.95 (unit)
Minicircuits ZEM-4300 frequency mixer	79.95 (unit)
Minicircuits SLP-1650 low pass filter	36.95 (unit)
Analog Devices AD605 VGA	14.35
Texas Instruments THS4304 op amp	2.33
Minicircuits SLP-70 low pass filter	34.95 (unit)
Analog Devices AD9432 ADC	64.59
Texas Instruments SN65MLVD201D LVDS transceiver	2.46
Texas Instruments SN65HVD232D CAN bus transceiver	2.32
Xilinx Spartan IIe XC2S300E-6FG456 FPGA	56.30
Xilinx XC18V02 PROM	19.95
Texas Instruments TMS320C6711 DSP	25.95
Atmel AT29LV010A-15JC PROM	3.25
Burr Brown REG104A LDO regulator * 3	8.43
Texas Instruments TL780-12 LDO regulator	0.80
Stontronics EPA-201D-06 6V switched mode PSU	26.55 (unit)
Stontronics EPA-201D-15 15V switched mode PSU	29.31 (unit)
Passives (SMT L, C, R), discrete logic, etc	100
6-layer 3dm^2 PCB manufacture and assembly	100
Total	**1006.27 = £531.31**

Table 5.2: Cost of parts

5.10 Multistatic Signal Processing

In this section, the implementation of the signal processing algorithms used in the prototype radar is described. These algorithms include both standard monostatic or bistatic matched filtering and pulse doppler processing, and the multistatic algorithms developed in Chapter 2. This processing is performed jointly between the digital signal processors in each of the three nodes. Firstly, a brief outline is presented of the processing that is performed at every node on the signals obtained from the local receiver. Then, the implementation of the multistatic detection algorithms is described, which may be performed at the master node or 'off-line', and involve joint processing of the received data from all three nodes.

The signal processing at each node is performed by the local Texas Instruments C6711 DSP. Initially, the raw data captured by the receiver ADC is stored in memory as a set of 12-bit, two's complement arrays, each corresponding to the capture period subsequent to each transmitted pulse. If data is captured for the maximum possible length (determined by the size of the FIFO in the FPGA), each array will be 2,048 samples in length. The C6711 chip is optimised for floating point operation, so the first stage of processing is to convert each 12-bit integer value to a 32-bit floating point format.

The data arrays contain real values only, however the coherent ADC reference clock ensures that the phase relationship between the digitised signals is preserved. It is convenient to perform coherent signal processing using complex sample values, so the real signals in each array are converted to the complex 'analytic signal', defined such that the real part is identical to the input array, and the imaginary part is equal to the Hilbert transform of this array, having undergone a $\pi/2$ phase shift. This process may be considered as the digital 'generation' of a quadrature channel, and the background to the process is presented in Appendix G.3. It is shown that a good approximation to the analytic signal can be derived trivially in the frequency domain by setting the values of the negative frequency Fourier transform components to zero, and halving the amplitude of the values corresponding to DC and the Nyquist frequency. Further, it is shown that this transform enables the decimation of the array by a factor-of-two[17], which conveniently results in the each range bin (assuming a full-bandwidth waveform is used) being represented by a single complex sample. Therefore,

[17]No information is lost during this process because the conversion results in two orthogonal channels that jointly observe the Nyquist limit.

the real data arrays are processed by first zero-padding each to twice their original length, and then calculating the discrete fourier transform (DFT) using an optimised fast fourier transform (FFT) assembler library on the DSP. The analytic signal is then generated, which is represented here in the frequency domain as $\chi(\omega)$.

Matched Filter

Now, we wish to perform matched filtering of each data array, so a digital complex 'reference waveform' $s_0(t)$ is generated in software with the same sample rate as the decimated signal, that is an ideal replica of the waveform of each transmitted pulse. This reference waveform may be amplitude weighted using standard techniques (e.g. Hamming, Blackman-Harris, etc) in order to reduce pulse compression range sidelobes if a chirp signal is used. It is then also zero-padded and the DFT found, which we represent as $\Psi_0(\omega)$. Then, as shown in Appendix A.2, matched filtering can be performed in the frequency domain by the multiplication of the complex conjugate of $\Psi_0(\omega)$ with the complex data signal $\chi(\omega)$:

$$S_0(\omega) = \chi(\omega)\Psi_0^*(\omega) \tag{5.3}$$

where $S_0(\omega)$ is the fourier transform of the matched filter output, and the zero-padding of both arrays ensures the *linear* cross-correlation of the two signals is found. The inverse FFT of $S_0(\omega)$ is then calculated to realise the matched filter output $s_0(t)$ in the time domain. If each received pulse has a constant phase, then the responses may then be coherently temporally integrated. This processing system can be written in pseudo-code as follows:

```
1: for n=0; n<pulses; n++ do
2:     arr = [arr_n zeros(length(arr_n))]        ▷ process data for nth pulse, zero-pad
3:     farr = fft(arr);
4:     farrcomp = create_analytic_signal(farr)        ▷ results in decimation by 2
5:     frefwave = fft(create_waveform(type))        ▷ complex, zero-padded waveform
6:     fmatchf = farrcomp * conj(frefwave)
7:     matchf_n = ifft(fmatchf)
8:     int_matchf += matchf_n                        ▷ coherently integrate
9: end for
```

Pulse Doppler Processing

Doppler processing is then performed on these same data arrays. In the general case (for chirp signals or the polyphase codes described in Appendix C), the transmitted waveforms will be doppler tolerant over the range that can be unambiguously measured (±500 Hz for a 1 kHz PRF). Therefore, implementation of a pulse doppler processor is straightforward provided the transmitted pulse train is coherent. The outputs of the zero-doppler matched filter described above may be used where the N output samples from N pulses with the same index (i.e. corresponding to the same range bin) are processed with an FFT. By definition, the first output of the FFT is the coherent sum of the N input samples, whilst the second output is the coherent sum where the nth sample is first multiplied by the complex coefficient $\exp(j2\pi n/N)$, and so on. These complex coefficients create phase shifts $\phi_n = 2\pi n/N = 2\pi f_d nT$, which are equal to the phase shift that would have accumulated after a delay nT by a doppler shift of $f_d = 1/NT$, so each sample of the FFT effectively forms a doppler filter matched to f_d. The resulting frequency domain response is almost the same as if a doppler filter bank had been constructed with an impulse response based on the entire coherent pulse train, except that in this method there is no doppler compensation within each pulse(53). However, where pulses are short compared to the PRI, the error is very small and the resulting processing considerably more efficient. This system can be written in pseudocode as follows:

```
1: for r=0; r<length(arr); r++ do                    ▷ for each range bin
2:     for n=0; n<pulses; n++ do
3:         dop[n] = matchf_n[r]                      ▷ create array of samples for given range bin
4:     end for
5:     dopfilt_r = fft(dop)
6: end for
```

Multistatic Detection Algorithms

Now, having developed signal processing schemes for monostatic[18] range and doppler processing at each node, the implementation of the multistatic detection algorithms is considered[19].

[18] Clearly this processing is equally applicable to the bistatic case where one of the other nodes acts as the transmitter.

[19] These algorithms are also used in the processing in the computer simulation described in Section 4.6.

We begin with consideration of the coherent algorithm L_{2m} in Equation 2.75, which is repeated here for convenience:

$$L_{2m} = \left| \sum_{k=1}^{n} \sum_{i=1}^{m} A_{ik1} \exp(-j\Delta\varphi_{ik1}) G_{ik} \right| \tag{5.4}$$

where G_{ik} (Equation 2.46) can be written in the time domain as:

$$G_{ik} = \frac{1}{N_i} \int_{-T/2}^{T/2} X_i(t) s_{0k}^*(t - t_{sik}) \exp[-j(\omega_0 + \Omega_{sik})(t - t_{sik})] dt \tag{5.5}$$

where X_i is the RF signal at the input to receiver i. We can write the equivalent sampled baseband signal (after downconversion by the receiver local oscillator) as $x_i(t) = X_i(t) \exp[-j\omega_0 t]$, and substitute into Equation 5.5 to give:

$$G_{ik} = \frac{1}{N_i} \exp[j(\omega_0 + \Omega_{sik}) t_{sik}] \int_{-T/2}^{T/2} x_i(t) s_{0k}^*(t - t_{sik}) \exp[-j\Omega_{sik} t] dt \tag{5.6}$$

Therefore, G_{ik} is equal to the output of a matched filter after a delay of t_{sik} where the received baseband signal $x_i(t)$ is the input, matched to a signal with complex envelope s_{0k} with a doppler shift Ω_{sik}, which is then amplitude weighted by $1/N_i$ and phase shifted by $\phi = (\omega_0 + \Omega_{sik}) t_{sik}$. In the monostatic case, it was stated that 'doppler tolerance' of the waveforms over the frequencies of interest meant that the mismatch between the doppler frequency of the received signal and the zero-doppler matched filter could be ignored. However, in the multistatic case, doppler tolerance implies both negligible error in amplitude *and phase* of the filter output due to this mismatch, as the multistatic detection process involves coherent summation of these output signals. A simple Matlab simulation, shown in Figure 5-25, demonstrates that for a typical 1 μs, 50 MHz chirp, the phase of the filter output changes by less than 0.2° over the $\pm$500 Hz band considered here, although it varies considerably for larger offsets. Therefore in this case, the output of the standard matched filter processor described above at time t_{sik} may also be used to determine the integral in Equation 5.6. If $k > 1$, the first stage of the multistatic processing is to repeat this matched filter on the stored input signal for each transmitted waveform with complex envelope s_{0k}. If the waveform is a coherent train of N pulses and the doppler frequency is small, the result of coherent temporal integration of these N pulses may be used to achieve a higher signal-to-noise ratio.

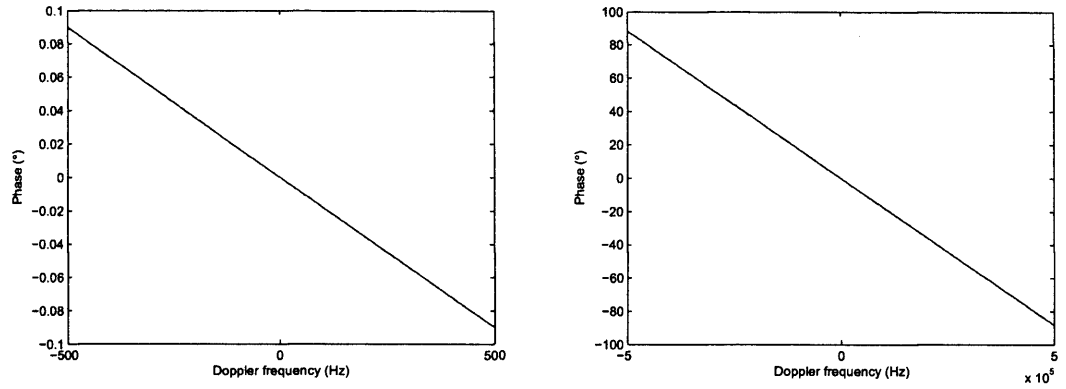

Figure 5-25: Phase of the response of a chirp matched filter with doppler frequency mismatch over (a) 1 kHz band; (b) 1 MHz band

It is necessary to determine the matched filter output at time t_{sik} from a discrete-time array where t_{sik} will not in the general case correspond to an exact sampling point. A similar problem occurs in traditional array beamforming where, in the simplest case, only a set of 'synchronous beams' are used where the required delays are integer multiples of the sampling period. Alternative methods include oversampling at the ADC and digital interpolation using multirate techniques(143), although in this application the computational requirements would be excessive. Therefore, the use of a 'fractional delay filter' is proposed, which ideally takes the form of an all-pass filter (no effect on amplitude or phase) that delays the input signal by some fraction of a sample so that the value at t_{sik} lies exactly on a sampling point. Such filters are quite commonly cited in the context of digital modems(144), and there are also infrequent accounts in the literature related to radar and sonar beamforming(145). The ideal transfer function for the filter is given by $D(\omega) = \exp(-j\beta\omega)$ where β is the desired group delay of the filter[20]. A simple FIR filter with 'sinc' impulse response given by $h(k) = \text{sinc}(k - \beta)$ is popularly implemented in such applications, despite very poor linearity of response across the frequency range DC - Nyquist. Indeed, it has been shown that there is an irreducible error bound (the 'Tarczynski bound') on any realisable fractional filter as the frequency tends towards Nyquist. Nevertheless, recent research has resulted in weighting functions for the 'sinc' filter that provide performance approaching this bound(146). Such a filter was implemented here, based on a raised-cosine window applied to a digital 80th order FIR filter ($N = 81$). The filter was analysed in Matlab for a specified

[20]A phase shift in the frequency domain corresponds to a delay in the time domain.

delay of 8 ns (4/10 of a sample at the decimated rate of 50 MHz) as shown in Figure 5-26. It can be seen that the group delay has an integer component equal to $(N-1)/2$ as expected, plus the required 0.4 sample offset at normalised frequencies up to 0.95 (45 MHz) where it starts to deviate. The amplitude response is also extremely flat over this same band. The integer group delay offset can be trivially corrected, so it is apparent this filter may be used provided received signals do not have a large response close to Nyquist.

The effect of the filter in the time domain can be seen in Figure 5-27. On the left hand side, the magnitude of the autocorrelation of an uncompressed pulse is shown together with replicas that have been (negatively) time-shifted by the filter by 1/4, 1/2 and one sample. For a half-sample delay, the peak response straddles two range bins equally as expected. On the right hand side, a similar plot is shown for the autocorrelation of a 20 MHz chirp sampled at 50 MSPS. The same effect occurs at the peak, although the *apparent* shape of the sidelobes is very different. Simulations have revealed that this effect is to be expected, and results from sample points occurring at different positions over the rapidly fluctuating sidelobes. The Nyquist limit is clearly still obeyed here for the complex response, and low-pass filter interpolation results in the restoration of the expected shape in every case.

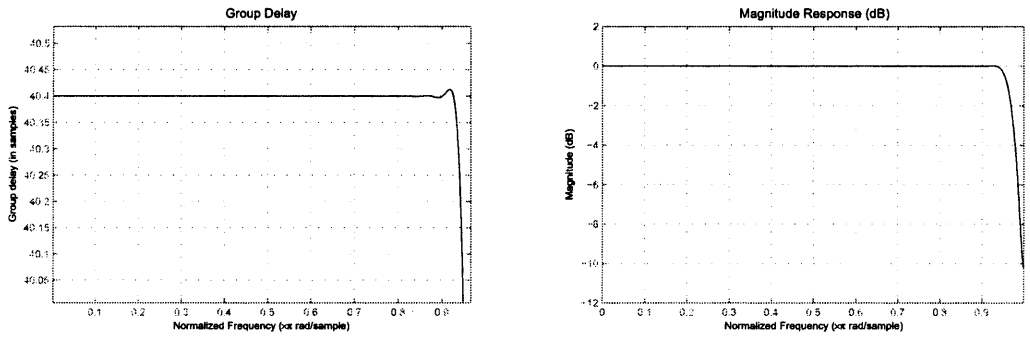

Figure 5-26: Fractional delay filter characteristics set to a delay of 4/10 of a sample

Finally, this matched filter output should be phase shifted by $\phi = (\omega_0 + \Omega_{sik})t_{sik}$ and weighted by $1/N_i$ to form G_{ik}. The phase shift is dependent on the carrier frequency, doppler frequency, and matched time of arrival. For the doppler range of interest (± 500 Hz) and short range targets ($t_{sik} < (2 * 1000)/c = 6.67$ μs), the doppler shift Ω_{sik} results in a maximum difference in ϕ of 2.4°, so disregarding this term will result in negligible loss in coherent summation. Clearly for large doppler shifts, the coherent algorithm will not be doppler tolerant, and both this factor and the doppler-compensated matched filter should

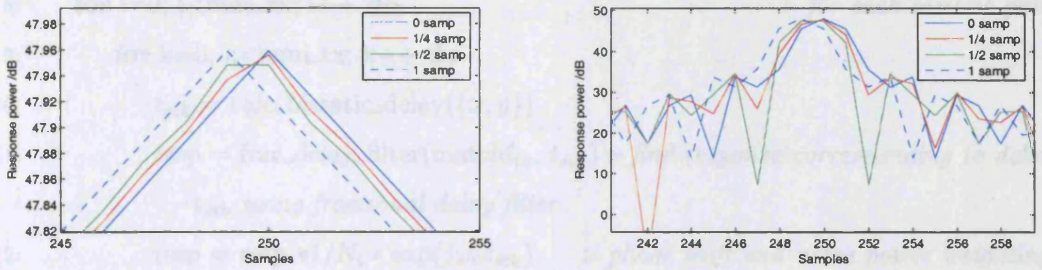

Figure 5-27: Magnitude response of the fractional delay filter to (a) the autocorrelation of a rectangular pulse; (b) the autocorrelation of a 20 MHz chirp

be calculated for each hypothesised value. The amplitude weighting term assumes the total noise and interference at the receiver has a flat spectral density N_i. For this assumption to be true, the dominant sources will be (stationary) thermal and atmospheric noise in the usual case, so N_i may be estimated with the use of a 'training run' of passive signal capture prior to transmission.

Having calculated G_{ik} for all bistatic pairs, they are coherently summed in Equation 5.4, having been phase shifted by the 'engineering' term $\Delta\varphi_{ik1}$ (which results from deterministic phase differences between oscillators in each transmitter and receiver and is determined during calibration), and weighted by A_{ik1}. The weighting term was defined in Section 2.4.7 as the square root of the ratio of the signal energy at receiver i pertaining to transmitter k compared to a 'reference' signal, and may be estimated (inevitably with some error dependent on the signal-to-noise ratio) from the relative amplitude of the matched filter response for each bistatic pair[21]. The resulting processing algorithm is given in pseudo-code as follows:

1: **for** i=0; i<num_rx; i++ **do** ▷ *Local processing at each receiver*
2: **for** k=0; k<num_tx; k++ **do**
3: matchf$_{ik}$ = matched_filter(arr) ▷ *Repeat matched filter for each of k waveforms*
4: matchf$_{ik}$ = ifft([fft(matchf$_{ik}$) zeros(length(matchf$_{ik}$))]) ▷ *Interpolate by 2 by zero-padding FFT so filter response is not aliased*
5: **end for**
6: **end for**
7: **for** $|\{x,y\}|$<bounds **do** ▷ *for each hypothesised location with coordinates* $\{x,y\}$

[21] A further potential cause of error is the inability to discriminate between the matched filter peak response and the sidelobes when estimating the received signal power using this method.

```
    for i=0; i<num_rx; i++ do                          ▷ for each bistatic pair
        for k=0; k<num_tx; k++ do
            t_sik = calc_bistatic_delay({x, y})
            resp = frac_delay_filter(matchf_ik, t_sik) ▷ find response corresponding to delay
                t_sik using fractional delay filter
            resp = resp *1/N_i * exp(jω_0 t_sik)       ▷ phase shift and noise power weighting
            if i=k=1 then
                a_s11 = abs(resp)                      ▷ store 'reference' bistatic pair amplitude
            end if
            L2m(x,y) + = resp * (abs(resp)/a_s11) * exp(−jΔφ_ik1)   ▷ weight and
                coherently sum
        end for
    end for
    L2m = abs(L2m)
end for
```

Now, we consider the simplified incoherent multistatic detector L_4, which can be written in a form suitable for multiple transmitters as:

$$L_{4m} = \sum_{k=1}^{n} \sum_{i=1}^{m} |G_i|^2 N_i \tag{5.7}$$

It can be shown that in most practical situations the performance of this detector is almost identical to the more complicated detector L_{3m}, which requires explicit estimation of the partial signal-to-noise ratio for each bistatic pair. Here, the squared modulus of G_i is taken, hence the phase shifts associated with the coherent detector above are unnecessary. Further, the $1/N_i$ weighting term in G_i and that in Equation 5.7 cancel, so the result is the simple incoherent square-law summation of each G_{ik} found from the matched filter outputs using the fractional delay filter, and can be written in pseudo-code as:

```
    ▷ local matched filter processing for each transmitter signal as per detector L_2m
for |{x, y}|<bounds do          ▷ for each hypothesised location with coordinates {x, y}
    for i=0; i<num_rx; i++ do                          ▷ for each bistatic pair
        for k=0; k<num_tx; k++ do
            t_sik = calc_bistatic_delay({x, y})
```

```
            resp = frac_delay_filter(matchf_ik, t_sik)
            L4m(x,y) += abs(resp)^2                    ▷ square-law detect and sum
        end for
    end for
end for
```

5.11 Conclusions

In this chapter, the development and construction of a novel multistatic radar design was presented. An initial specification was produced based on the expected applications for the system, and the construction commenced with the implementation of the reference clock distribution system. Then, the development of each subsystem within the nodes was described, including custom-designed mixed-signal transmitter and receiver chains, a complete FPGA design for synchronous control and the implementation of a network controller using an open architectures soft-core interface, and the construction of several modular circuit boards based on COTS components. The result is an embedded system with autonomous nodes, controlled by custom control and visualisation software on a notebook computer. Finally, the digital signal processing hardware was described, together with the implementation of both standard monostatic signal processing and multistatic detection processors based on the algorithms described in Chapter 2.

Chapter 6

Calibration and Initial Performance Evaluation

6.1 Introduction

This chapter is concerned with the calibration of the prototype multistatic system and some initial experiments to verify its temporal and spatial coherency and test its performance. Firstly, the results of the 'acceptance testing' and laboratory calibration are presented and compared to the design-time specification. In particular, issues regarding the synchronisation and mutual spatial coherency of the system are analysed. Then, a test target is used to calibrate the radar at short range, firstly for each node operating as a monostatic radar, and then for the entire multistatic system using the detection algorithms developed in Section 5.10. The results are compared between these two cases and with respect to the theory in order to give an initial indication of the multistatic instrument function for the system.

6.2 Acceptance Tests

In this section, a summary of the results of the laboratory calibration and performance testing procedures is presented. It is not the purpose here to define a *formal* acceptance test specification, but a similar approach is used to analyse the results obtained against the design-time specification and the coherency requirements defined in Section 4.4. One reason for the lack of formal specification is that the premise of the design was partially to determine the performance that can be achieved within a limited budget, rather than being performance-led. Nevertheless, the tests are presented in some detail so that the limiting factors resulting from this low-cost design can be determined. The test procedure is loosely based on the structure outlined in Scheer(118) and Barton(147), and extended to apply to the coherent multistatic case.

The first set of tests is conducted on the individual subsystems in the system using laboratory test equipment. These are concerned with oscillator stability and phase noise, transmitter power and spectrum, and receiver sensitivity and noise. The equipment was used for testing purposes is shown in Table 6.1. Then, tests are conducted on the complete system using a closed-loop configuration between pairs of transmitters and receivers in order to determine the instrument function under controlled, high signal-to-noise ratio conditions.

Instrument	Usage
Hewlett Packard 8450E spectrum analyser	Signal power and phase noise
Rohde & Schwartz SMP04 signal generator	Receiver signal injection
Hewlett Packard 8510B network analyser	RF amplifier linearity
Hewlett Packard 4195A network analyser	Baseband amplifier linearity
Hewlett Packard 8496B step attenuator	Closed-loop tests
Tektronix TDS5052 digital phosphor oscilloscope	Synchronisation tests

Table 6.1: Laboratory test equipment

6.2.1 Reference Oscillator

The phase noise and frequency stability of the 100 MHz reference oscillator was measured at each node, subsequent to the clock distribution and inter-node fan-out process. The phase noise, measured with a spectrum analyser, is shown in Figure 6-1. The manufacturer's phase noise specification for the crystal oscillator itself (derived from Figure 4-6) is shown with a dashed line. As anticipated in Section 4.5, the phase noise close to the carrier is only slightly increased ($\approx$ 2.5 dB), whereas that at larger offsets is dominated by thermal noise jitter resulting from the distribution and reception process.

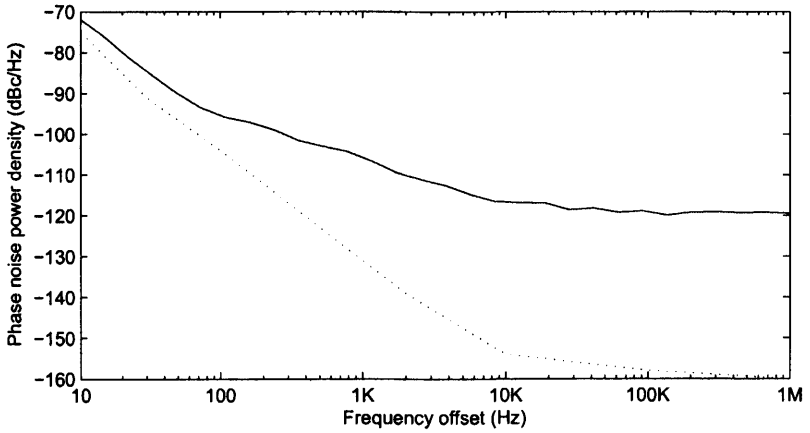

Figure 6-1: Reference oscillator phase noise at a node after distribution and fan-out

The effect of this noise on the analogue-to-digital converter signal-to-noise ratio can then be calculated using Equation 4.16. The integrated phase noise in Figure 6-1 over the bandwidth 100 kHz to 350 MHz was found to be 0.09°, which results in an SNR upper bound at the ADC of 62.1 dB, which is 13.3 dB worse than the 'effective SNR' specification stated in Section 4.4.3. It is possible that this figure is slightly overestimated due to the real phase noise being below the noise floor of the spectrum analyser at very large offsets.

In addition, the noise is Gaussian with a flat power spectrum, and may be mitigated by pulse integration in the same manner as thermal receiver self-noise. Still, high bandwidth ADCs will inevitably be particularly sensitive to wideband jitter, and the result here is a consequence of the direct, low-cost method of time transfer used.

Long-term frequency stability was estimated by simple observation of the peak frequency on the spectrum analyser after a 15 minute 'warm-up' period to allow the oscillator to stabilise. The maximum deviation was found to be ±2500 Hz, with a mean frequency very close to 100 MHz, which is within the manufacturer's specification for the oscillator (±25 ppm) and much better than the bound of ±30 kHz stated in Chapter 4 in order to prevent gross ranging errors due to an incorrect sample rate. The equivalent effect on PRF timing is an error of $\pm 25 \times 10^{-3}$ Hz, which is clearly negligible. As fluctuations are completely correlated between nodes (except for wideband jitter), no inherent degradation of phase coherency is expected. Evidently considerably improved frequency stability could be realised using oven-controlled or atomic reference clocks.

6.2.2 Local Oscillator

The phase noise of the synthesised local oscillator at each node was determined at the input to the frequency mixer (i.e. subsequent to the power splitter and amplifier), and is shown in Figure 6-2.

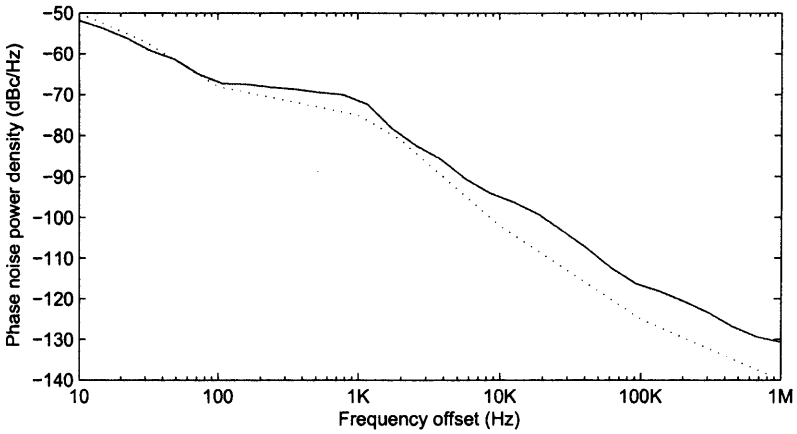

Figure 6-2: Synthesised local oscillator phase noise

Here, the measured spectrum quite closely follows the (approximate) PLL simulation shown in Figure 4-8, which is duplicated with a dashed line, and therefore is well below the

maximum bound of -31 dBc/Hz that was determined in the requirements for the system. The integrated phase noise over the bandwidth 10 Hz to 50 MHz[1] was found to be 1.2°, which is often considered as a figure-of-merit for the local oscillator, and describes the total phase noise contribution of each oscillator in the signal path. The actual phase noise close to the carrier is increased by 26 dB at 100 Hz offset compared to the reference in Figure 6-1, which is in approximate agreement with the theoretical increase due to multiplication of the modulation index, given by $10\log(N^2) = 27.6$ dB. At a 1 kHz offset (still within the PLL loop bandwidth), the increase is some 33 dB as the additional multiplied thermal noise becomes more dominant. However, at larger offsets the phase noise is dominated by the VCO itself, and indeed falls below that of the reference oscillator at 100 kHz offset as the wideband reference clock noise resulting from its distribution is well attenuated by the loop, and so plays no part in signal degradation.

Frequency stability of the local oscillator is determined by that of the reference clock, and was found by visual inspection to be ±60 kHz. As these fluctuations are completely correlated between nodes, and the maximum target range is short ($t_{si\max} < 7$ μs), the effect on pulse doppler measurement is expected to be very small.

6.2.3 Synchronisation

Given that constant phase offsets between local oscillators in each node may be measured and 'calibrated out', the issue of synchronisation relates to offsets between rising edges of the reference clock. It was found using a high-speed digital oscilloscope that the distribution cables could be constructed with sufficient accuracy to result in a clock offset tolerance of ±1.5 ns, equivalent to a maximum ranging error of ±22.5 cm, which is a small fraction of the native range resolution. Further, it was found that the timing of the 'event synchronisation' pulse from the master node to the slave nodes consistently arrived after a deterministic number of cycles, which was calibrated out in software so that each node begins transmission and reception at the same time.

[1]The lower bound corresponds to an expected total doppler integration time of 100 ms, and the upper bound corresponds to the receiver bandwidth.

6.2.4 Transmitter

The transmitter was tested by programming the DDS to operate in a *continuous* single tone mode at 10 MHz. Then, the single-sideband output of the transmitter power amplifier (at a nominal power level of +23 dBm and frequency 2410 MHz) was analysed using a spectrum analyser with a suitable attenuating pad. The phase noise spectrum is shown in Figure 6-3.

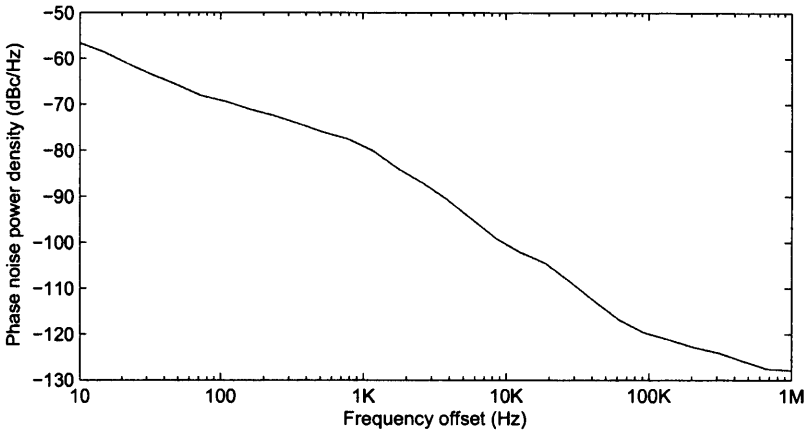

Figure 6-3: Transmitter output phase noise

It is perhaps surprising that the apparent phase noise of the transmitted signal is typically 5 to 10 dB *lower* than that of the local oscillator that drives its upconverter, and results in an integrated phase noise of 0.8° over the same 10 Hz to 50 MHz bandwidth. This can be explained by the fact that the 'Gilbert cell' balanced mixers in the single-sideband upconverter cause considerable suppression of amplitude noise (to the order of 30 dB) derived from the local oscillator(113). True phase noise is unsuppressed, however as the spectrum analyser cannot discriminate phase and amplitude noise, the apparent effect is a moderate decrease in the total noise. In particular, the large reduction at an offset around 1 kHz implies there is considerable amplitude noise on the LO at that point, which is confirmed in Figure 4-8, which shows that the dominant noise contributor in that region (the orange line) is thermal noise generated by resistor R3 in the loop filter. This effect is beneficial because the dominant contributors to uncorrelated noise within the doppler band of interest are in fact partially suppressed in the signal path.

The results for wideband spectral analysis of the transmitter output are shown in Table 6.2 for the same 10 MHz baseband tone. The values for suppression of feedthrough, im-

ages and harmonics are within the manufacture's specifications for the upconverter, which demonstrates that the transmitter module design was correct and quadrature between the channels was maintained within the required tolerances. Importantly, no significant spurs were present at offsets over the doppler band of interest.

Frequency	Power
SSB output power ($f_{LO} + f_{DDS}$)	+23.7 dBm
LO feedthrough (f_{LO})	-30.2 dBc
Image suppression ($f_{LO} - f_{DDS}$)	-33.6 dBc
Second harmonic ($f_{LO} + 2f_{DDS}$)	-35.7 dBc

Table 6.2: Transmitter output spectrum

For the chosen baseband frequency of $f_{DDS} = 10$ MHz, the image at $f_{LO}+f_{DDSCLK}-f_{DDS}$ resulting from the 'sampling' action of the DDS was not visible above the noise floor. However, the test was repeated for a DDS tone at 45 MHz tone, where it was shown that the image at 2455 MHz was only 2.6 dB below the SSB signal. The SSB output power as a function of frequency is shown in Figure 6-4, and shows a corresponding roll-off of 1.9 dB over the useful bandwidth of 45 MHz. Whilst the DDS inverse-sinc filter maintains good linearity of the baseband output, images within the passband of the reconstruction filter result in substantial out-of-band spurs that reduce the effective gain of the SSB signal in the power amplifier. In situations where spurs in the frequency region slightly out-of-band are a concern, it is necessary to either increase f_{DDSCLK}, decrease the maximum f_{DDS} (and hence the bandwidth), or design steeper attenuating filters at baseband or RF.

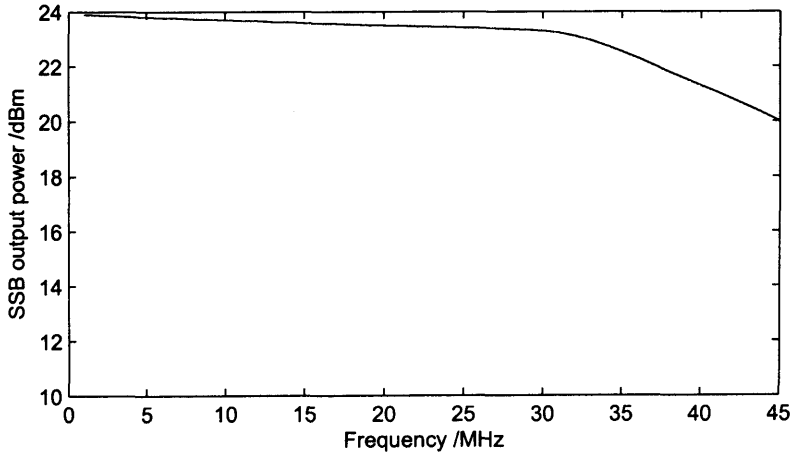

Figure 6-4: Transmitter output power against DDS baseband frequency

6.2.5 Receiver

The receiver module was tested by injecting a continuous low-power RF signal into the receiver input from a calibrated laboratory reference oscillator. The radar receiver was programmed to capture a single burst of data for a period of 20 μs. Firstly, the receiver gain was measured for an input tone at 2410 MHz over a range of input powers. Then, the receiver linearity over its nominal frequency range 2400 - 2445 MHz was measured. The results are shown in Figures 6-5 and 6-6. The receiver gain for the 2410 MHz input (resulting in a 10 MHz baseband tone) is 57 dB, which is flat to within $\pm$0.2 dB over the input range -90 to -55 dBm. Above -55 dBm (corresponding to an ADC input power of -8 dBFS), it was found that output harmonics rise sharply as the baseband amplifier begins to saturate.

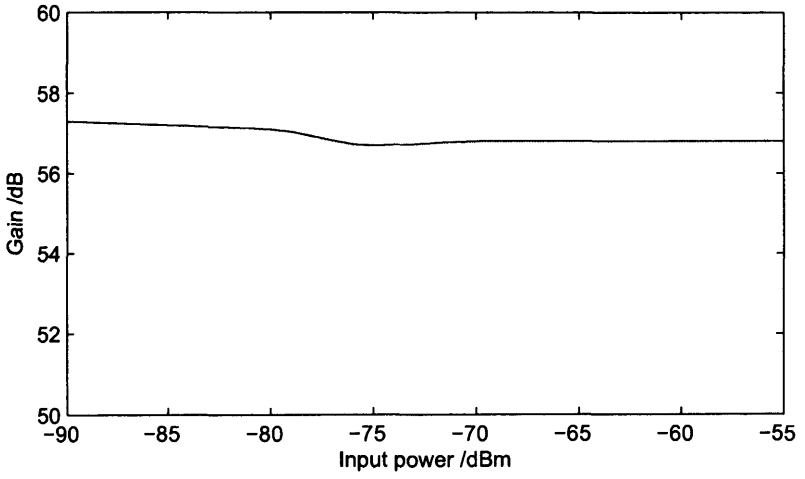

Figure 6-5: Receiver gain for an input signal at 2410 MHz

The minimum detectable signal power was measured in two ways - firstly by observation by eye of the raw digitised signal in a background of thermal noise generated by the receiver (which was found to be -88 dBm), and secondly by a 1024-point FFT of the received signal, which was then found to be -108 dBm. The latter result is lower because of the bandpass filtering action of the FFT, and allows us to state the approximate dynamic range of the receiver to be $-55 + 108 = 53$ dB. This minimum detectable signal is equivalent to -61 dBFS at the ADC input, which is comparable to the ADC SNR maximum bound of 62.1 dB calculated above when limited by the maximum bound for the wideband jitter on its reference clock. Then, using Equation 5.1, we find that for the nominal transmitter power

$P_t = +23$ dBm and antenna gains $G_t = G_r = 24$ dBi, the receiver can theoretically detect the reflected *signal* from a unity RCS target at a maximum range of 1585 m, which meets the specification outlined in the previous chapter. Clearly at ranges of this order, integration of multiple pulses will be required in order to achieve acceptable detection characteristics.

Figure 6-6 shows that the receiver has a 3 dB bandwidth of 25 MHz, above which there is a steady roll-off totalling 7.5 dB at 2445 MHz. It was found that this was mostly related to the baseband amplifier, so a digital linear-phase filter was designed to compensate for this roll-off and is implemented in the frequency domain at the first stage of signal processing. The disadvantage of this filter is a slight rise in high frequency noise, however because most losses occur in the final stage of amplification, the effect is not severe.

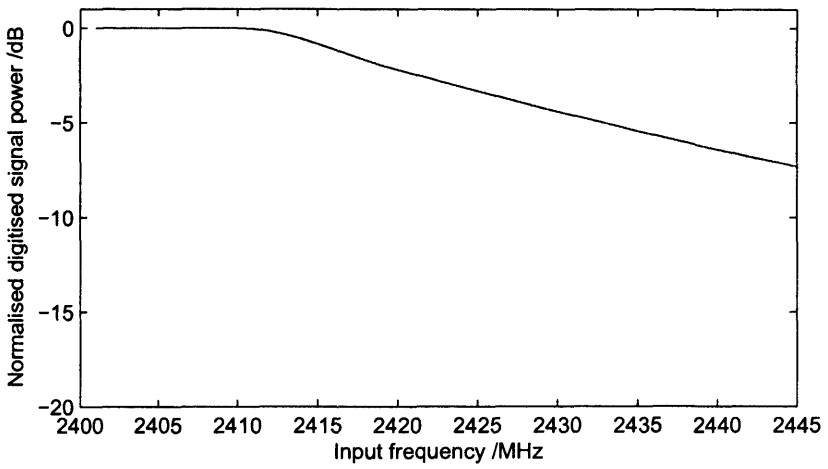

Figure 6-6: Receiver linearity over RF bandwidth

The noise figure of the receiver (defined as the ratio of the SNR at the input to the SNR at the output) was estimated using the 'Y-factor method'(148) and a noise source applied to the receiver input with a known 'excess noise ratio' (ENR). The result was found to be 5.2 dB, which is quite favourable considering the amount of gain and component cost. It is known that 1.2 dB of this figure is derived from the low-noise amplifier, leaving a contribution of 4 dB from the mixer and baseband amplifier.

Then, the nature of the receiver self-noise only was analysed by placing a 50 Ω terminating load at the receiver input and capturing the digitised noise. It is expected that the self-noise will be dominated by Gaussian thermal noise, however 'breakthrough' and coupling of oscillator signals and digital noise from other subsystems of the radar into the

sensitive receiver may cause significant correlated harmonic content that reduces coherent integration gain and may cause unwanted aliased spurs in doppler measurements. Firstly the FFT of the noise signal was found, and showed no significant spurs. Then, a standard Gaussianity test was applied by calculating the first four normalised moments, shown in Table 6.3.

The significance of these results can be defined using the 'standard error of skewness' (SES) and 'standard error of kurtosis' (SEK), which can be approximately defined as(149):

$$\begin{aligned} \text{SES} &= \sqrt{6/N} \\ \text{SEK} &= \sqrt{24/N} \end{aligned} \tag{6.1}$$

where N is the number of samples. Then, for Gaussian noise we expect both the skewness and kurtosis excess to be zero, and can state that there is no statistically significant deviation if the actual values are less than $\pm 2\times$SES or $\pm 2\times$SEK. In this case, $N = 1000$ (for 20 μs captured signal at the decimated rate of 50 MHz), so $2\times\text{SES} = 0.15$ and $2\times\text{SEK} = 0.31$, and as expected the self noise is well within the bounds of Gaussianity.

6.2.6 Closed Loop Range Response Tests

The next set of tests were performed on each node in a closed loop configuration, by inserting a suitable RF attenuator at the output of the transmitter and feeding this attenuated signal directly into the input of the receiver as shown in Figure 6-7, resulting in a total path length of approximately 3 m. The purpose of these tests was to determine the instrument function of the node as a monostatic radar in range and doppler in a controlled environment with high signal-to-noise ratio.

The monostatic instrument function is first analysed by determining the range response profile. The radar is programmed to transmit 40 MHz bandwidth chirp pulses of 5 μs length. The attenuator is set to 83 dB in order to realise a signal power at the receiver

Central Moment	Value
1st (Mean - normalised to ADC full-scale)	1.82×10^{-4}
2nd (Variance σ^2 - normalised to ADC full-scale power)	9.92×10^{-5}
3rd (Skewness - normalised by σ^3	0.05
4th (Kurtosis excess - normalised by σ^4)	0.06

Table 6.3: Receiver self-noise statistics

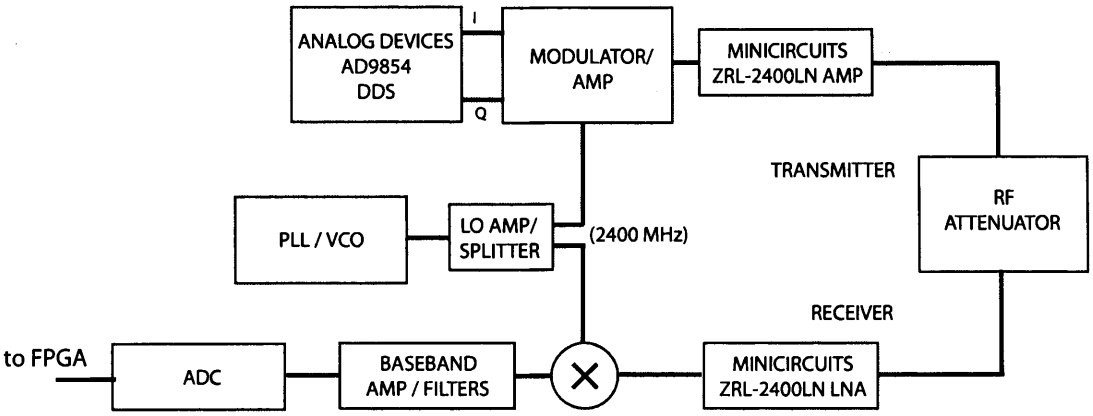

Figure 6-7: Closed loop test configuration for a single node

input of -60 dBm, which is 5 dB below the maximum input signal so presents a high signal-to-noise ratio at the receiver. The digitised signals are then processed with the standard matched filter algorithm described in Section 5.10. The 'ideal' response simulated from an autocorrelation function in Matlab is shown with a dashed line. The results for an unweighted chirp are shown in Figure 6-8. It can be seen that the 3 dB range resolution is approximately 3 m as expected[2], with high sidelobes typical of the chirp point-spread function[3].

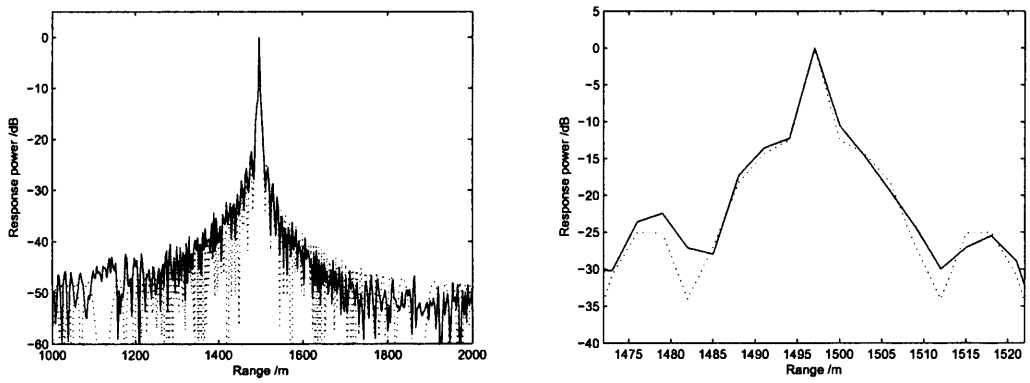

Figure 6-8: Range response profile for 40 MHz unweighted chirp

There is a slight asymmetry in the cross correlation caused by a small mismatch between

[2]The apparent range offset of 1497 m results from an artificial change in the start time of data collection by the ADC so that the sidelobes on both sides of the mainlobe peak can be seen.

[3]The -13 dB sidelobes cannot be clearly seen because there is inadequate oversampling on the graph (i.e. linear interpolation between samples is used rather than low-pass reconstruction).

the transmitted and reference signals. It is thought this is partly derived from group delay error in the signal path, for example that simulated in the design of the DDS reconstruction filters in Section 5.4. However, attempts to correct this error using a digital all-pass filter in signal processing have proved only partially successful. Further analysis in Matlab revealed that the error in approximation of the analytic signal using the simple FFT method described in Section G.3 results in a similar effect. This is confirmed in Reilly et al(150), where an alternative (but more computationally costly) method is presented if this asymmetry should prove unacceptable. It is possible a further contribution is derived from the response of the AC components in the DDS output path (e.g. the step-up transformers) when the baseband chirp is close to DC, although difficulties with the practicality of programming chirps with non-zero start frequencies across the DDS interface have prevented this being proven.

The test was then repeated where the Blackman weighting function is used *on receive only* (i.e. by weighting the amplitude of the reference signal used for the matched filter), as shown in Figure 6-9.

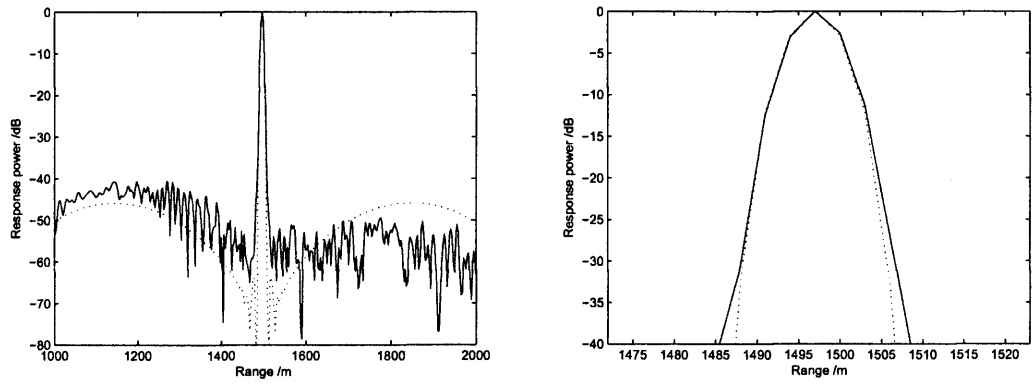

Figure 6-9: Range response profile for 40 MHz Blackman weighted-on-receive chirp

Again, the 'ideal' autocorrelation is shown in a dashed line. It can be seen that the mainlobe has widened to 6.4 m, but the near-in sidelobes fall to a null at -67 dB, before rising at either side. This shape is a result of using receiver weighting only, compared to the common 'textbook' form where the square-root of the weighting function is applied on both the transmitted signal and at the matched filter. It is evident that these experimental results show a good correlation with the ideal response, and demonstrates satisfactory monostatic operation of the system in terms of range resolution.

Now, coherency of the node is confirmed by examining the effect of the integration of a train of $N = 128$ coherent chirp pulses in loop back configuration. Firstly, Figure 6-10(a) shows an example of a chirp pulse captured by the receiver with a high signal-to-noise ratio[4]. Then, Figure 6-10(b) shows a close-in range profile of the output of the matched filter for the coherent sum of 128 such pulses compared to that of a single pulse. The expected signal integration gain of $10\log(N^2) = 42$ dB for ideal coherency is observed.

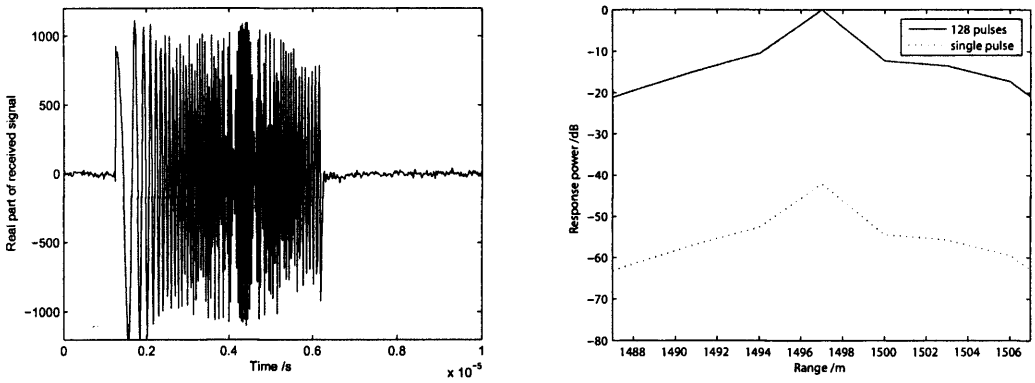

Figure 6-10: (a) A raw chirp pulse captured by the receiver; (b) matched filter output range profile for the coherent integration of 128 pulses compared to a single pulse

6.2.7 Closed Loop Doppler Response Tests

Here, the instrument function response is determined for pulse doppler processing of a train of 128 coherent pulses. Firstly, a baseline experiment (with no doppler offset) was performed in the loop-back configuration using the same chirp waveform as described above, and standard pulse doppler processing based on the algorithm described in Section 5.10. Firstly a PRF of 1 kHz was programmed, and the phase of the matched filter output corresponding to the nominal loop-back range bin (3 m) was plotted in the time domain together with its unweighted FFT in Figure 6-11.

The time domain array is in this context a useful, if somewhat unconventional measure of the effective phase noise of the system, where the effective lower bound is set by the total integration time (1/128 ms $\approx$ 8 Hz) and the upper bound is curtailed by the averaging effect of the matched filter over the pulse length, which can then be approximated as 1/5 μs = 200 kHz. The result here shows an rms phase error of 0.04°, which is the result of local

[4]The apparent aliasing is because only the real part of the decimated analytic signal is shown.

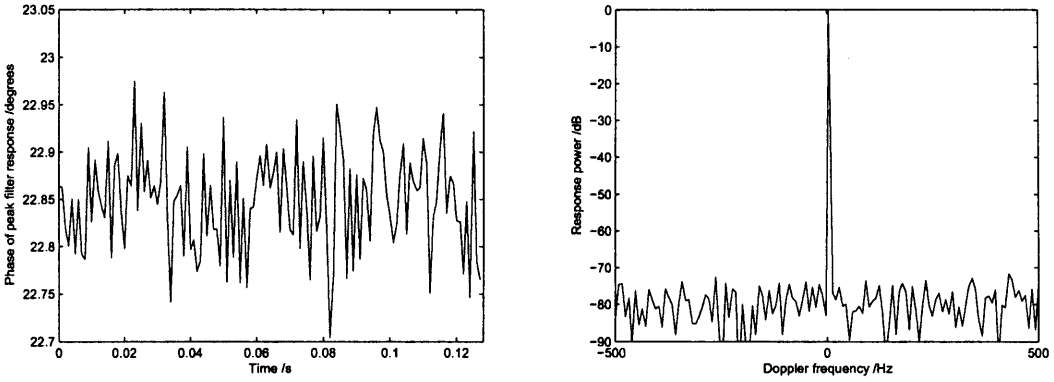

Figure 6-11: (a) Phase of peak matched filter response for each of 128 chirp pulses with PRF of 1 kHz; (b) unweighted FFT

oscillator phase noise suppression by the range correlation function described in Equation 4.23 due to the common local oscillator signal in transmitter and receiver. This equation reveals an expected suppression of some 32 dB at 200 kHz offset for this effective range $R =$ 1.5 m, so it is expected that the small phase error shown is dominated by the contribution of uncorrelated thermal noise in the signal path and jitter on the reference clock. The resulting doppler spectrum shows no significant spurs and a noise floor at -80 dBc.

Now it is desired to test the capability to detect a doppler shifted signal, whilst maintaining the controlled environment and high signal-to-noise ratio of a closed loop test. This may be done in a CW system by phase-locking a laboratory oscillator to the radar local oscillator and applying a small doppler offset. Here, a simple alternative method was used where the transmitter DDS was programmed to produce a continuous tone at a nominal IF (10 MHz) plus a small 10 Hz offset. The radar receiver is then programmed to capture 20 μs blocks of data at a PRF that is an integer factor of the IF. Therefore, the RF signal from the transmitter appears to the receiver as a coherent train of unmodulated 20 μs pulses with an IF of 10 MHz and a doppler shift of 10 Hz, which is then digitally downconverted, matched filtered and processed using the standard pulse doppler algorithm. Further, this method allows the contribution of both the transmitter and the receiver to doppler measurement stability to be measured simultaneously. The resulting doppler spectra measured by the radar (with Blackman weighting applied to the FFT) at PRFs of 1 kHz and 50 Hz are shown in Figure 6-12. The 10 Hz doppler peak is clearly evident, and the general noise floor is approximately -80 dBc as before. There is a small image at -10 Hz with a power of

-70 dBc, which may be caused by the small error in digital quadrature channel generation in the receiver.

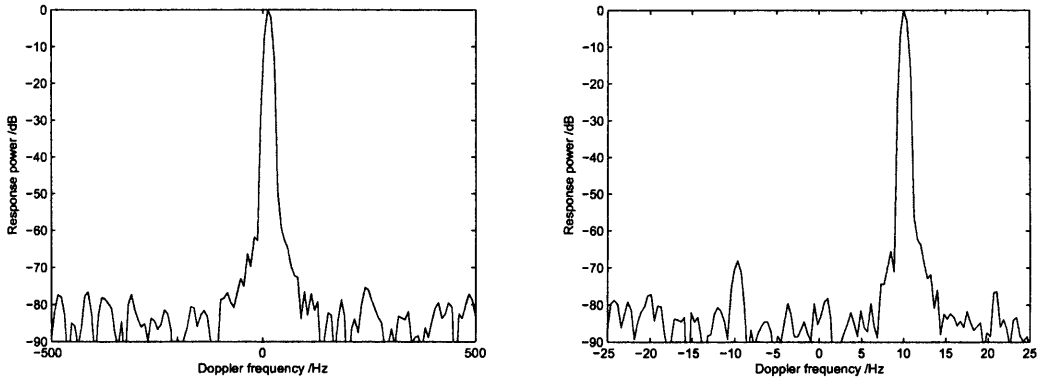

Figure 6-12: Doppler spectra measured by radar in loop back test configuration with a PRF of (a) 1 kHz and (b) 50 Hz with a simulated doppler frequency of 10 Hz

6.2.8 Inter-node Closed Loop Tests

The closed loop tests documented in the previous sections are now repeated where the transmitter and receiver used are from *different nodes*, as shown in Figure 6-13.

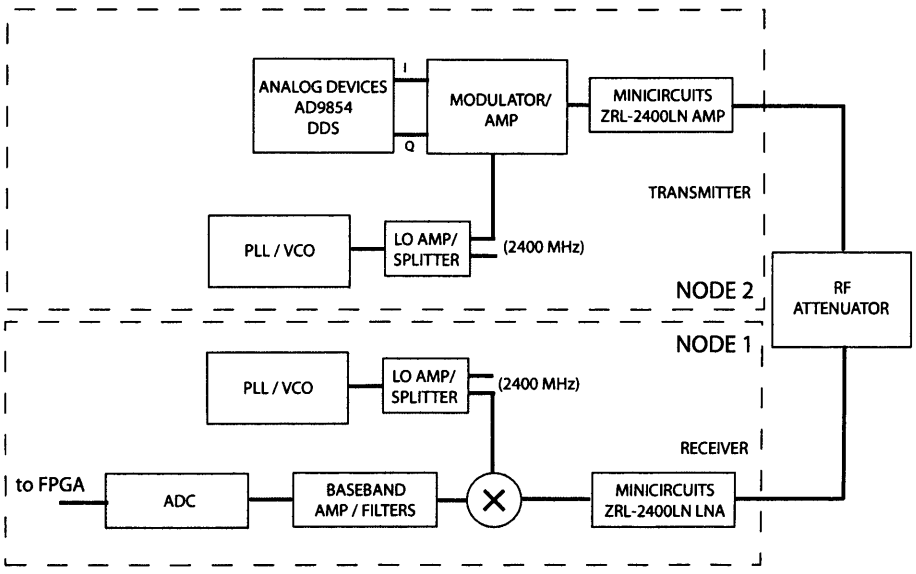

Figure 6-13: Closed loop test configuration between two nodes

The simulated doppler response from the processing of 128 'pulses' is shown in Figure 6-14, where the FFT is again Blackman weighted, for PRFs of 1 kHz and 50 Hz. The peaks

are again clearly visible, but the noise floor has increased to approximately -50 dBc, a rise of 30 dB compared to the monostatic case. This performance degradation may have two causes - firstly some wideband jitter on the ADC reference clock, DDS clock and PRI timer that maintained some correlation within a single node but is now uncorrelated, or secondly a reduction in the effect of the range correlation function due to some uncorrelated noise on each local oscillator. In the latter case, it was expected that phase noise within the doppler band would maintain strong correlation between nodes in which case the range correlation function would still apply. However, it should be remembered that phase noise at offsets up to approximately $c/2R = 100$ MHz will undergo substantial suppression in the monostatic case, whereas clearly now the majority of this wideband noise will be uncorrelated and contributory due to aliasing into the doppler bandwidth. It is noted that there is no significant increase in noise when the PRF is decreased (the 50 Hz PRF results in a total integration time of some 2.56 seconds), suggesting that the phase noise close to the carrier is indeed strongly correlated. Further, the doppler resolution using this technique is similar in both the single node and inter-node cases, and 50 dB dynamic range is expected to be adequate for short-range applications.

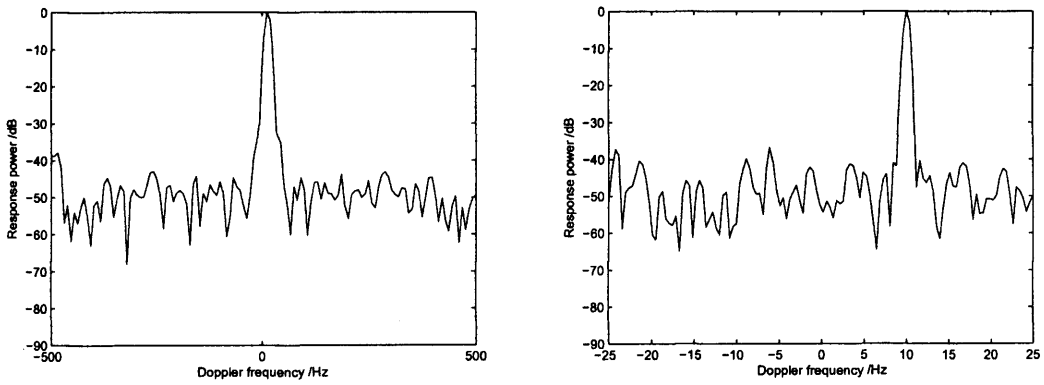

Figure 6-14: Doppler spectra measured using two radar nodes in loop back test configuration with a PRF of (a) 1 kHz and (b) 50 Hz with a simulated doppler frequency of 10 Hz

Then, the integration gain test is repeated between the two nodes, as shown in Figure 6-15. Again, the full theoretical signal power increase of 42 dB is realised, indicating that the system coherency is adequate for the purposes of implementing the coherent multistatic

detection algorithms[5].

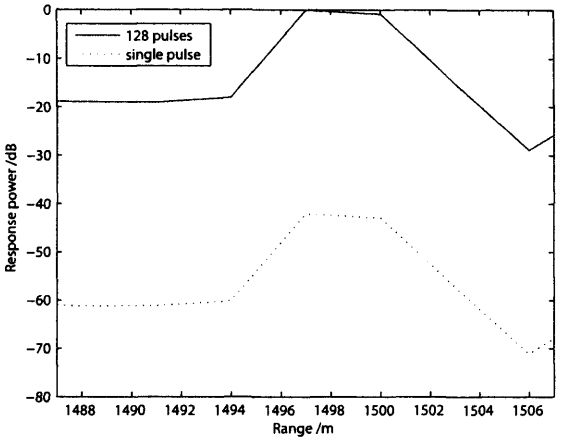

Figure 6-15: Matched filter output range profile for the coherent integration of 128 pulses compared to a single pulse using two radar nodes

Finally, the *mutual* phase stability of the local oscillators in each node is tested over long time intervals. It was stated in Section 4.4.3 that the stability period defines the interval at which the system must be phase calibrated. The test was performed indirectly by periodically programming the system to transmit a coherent train of 128 pulses between two nodes in the closed loop configuration. On each occasion, the received signals were coherently integrated and the phase of the peak response found. The integration averages the effects of wideband phase noise, so changes in this value are a good measure of longer term changes in relative phase between the oscillators. The results over a 30 minute period are shown in Figure 6-16.

It can be seen that the phase over this period is stable to within 2°, and so is well within the requirements determined in the computer simulation in Section 4.6, where it was shown that uncalibrated phase errors up to approximately 20° could be tolerated in the coherent detection algorithms. However, it was noted that movement of the cables used for reference clock distribution caused very large discrete changes in relative oscillator phase, probably due to skew resulting from dielectric deformation caused by the movement. Evidently, this is a further inherent disadvantage in the low-cost open-loop time transfer method used.

[5]The slight change of shape of the main lobe is caused by a small increase in the loop back path length for this experiment compared to the monostatic case, which results in the real time-of-arrival of the pulse being located between two range bin samples.

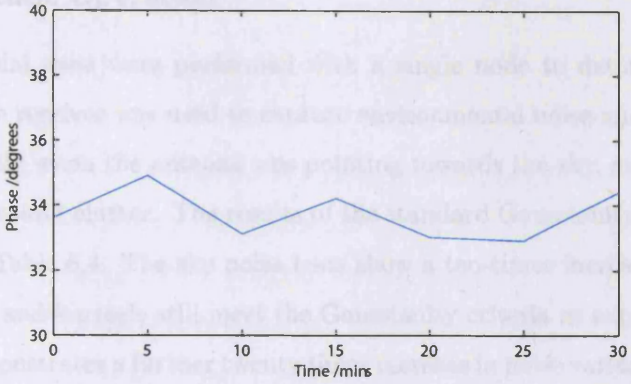

Figure 6-16: Relative phase stability of the local oscillators in two nodes

6.3 Experimental Tests

In this section, the results of a series of initial short range calibration and performance tests are described. The experiments were carried out on a rooftop at University College London, which presented quite a challenging environment for the system in terms of interference, particularly due to nearby mobile phone basestation antennas and IEEE 802.11 devices operating in the same frequency band. Low-cost parabolic mesh antennas with 24 dBi gain, 8° 3 dB beamwidth and diameter of 94 cm, designed for use in wireless LAN point-to-point links, were used for each transmitter and receiver[6] and mounted adjacently with horizontal polarisation. A trihedral corner reflector with an RCS of 150 m^2 was constructed as a test target for the experiments(151). Images of the antennas and reflector are shown in Figure 6-17.

Figure 6-17: Antennas and test target used for system calibration

[6]Stella Doradus 24 SD27, www.stella-doradus.com

6.3.1 Monostatic Operation

Firstly, some initial tests were performed with a single node to determine the operating environment. The receiver was used to capture environmental noise and interference over a 20 μs period, firstly when the antenna was pointing towards the sky, and secondly pointing towards nearby ground clutter. The results of the standard Gaussianity tests for both cases are presented in Table 6.4. The sky noise tests show a ten-times increase in noise variance, but the skewness and kurtosis still meet the Gaussianity criteria as expected. However, the ground noise demonstrates a further twenty times increase in noise variance with statistically significant skew and kurtosis. In fact, high-level interference of varying intensity is clearly visible in the time-domain raw data plots, such as that shown in Figure 6-18. This bursty noise is almost certainly due to wireless communications devices in the local area.

Central Moment	Sky	Ground
1st (Mean - normalised to ADC full-scale)	6.01×10^{-5}	1.46×10^{-4}
2nd (Variance σ^2 - normalised to ADC full-scale power)	9.6×10^{-4}	0.02
3rd (Skewness - normalised by σ^3	-0.03	-0.83
4th (Kurtosis excess - normalised by σ^4)	0.15	1.6

Table 6.4: Atmospheric noise statistics

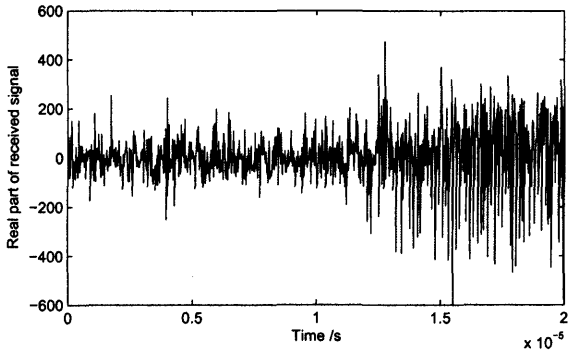

Figure 6-18: Environment interference captured by radar receiver

Then, some very short range monostatic tests were performed for verification of the instrument function and range calibration. The trihedral reflector was placed at a distance of 18 m from the (colocated) transmitter and receiver antennas. This distance was chosen to obtain a high signal-to-noise ratio for calibration, taking into account the antenna far-field

boundary given by the standard equation:

$$R_{\min} = \frac{2D^2}{\lambda} = 14.1 \quad \text{m} \tag{6.2}$$

where D is the largest dimension of the antenna. The output power of the transmitter was attenuated due to the small range and large RCS target in order to prevent saturation of the receiver. Standard matched filter detection was performed for unweighted and Blackman weighted 0.6 μs 40 MHz chirp waveforms and a 5.6 μs 7.1 MHz polyphase code[7] from the orthogonal set described in Appendix C, as shown in Figures 6-19, 6-20 and 6-21.

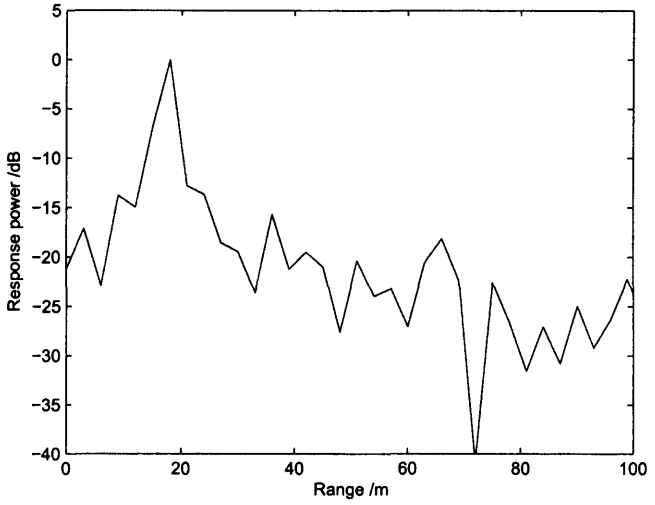

Figure 6-19: Matched filter output range response for a trihedral reflector placed 18 m from a single node for an unweighted 40 MHz chirp pulse

[7]The bandwidth and hence minimum length of the polyphase codes is limited in the current design due to the incorrect operation of the DDS when phase commands are rapidly programmed.

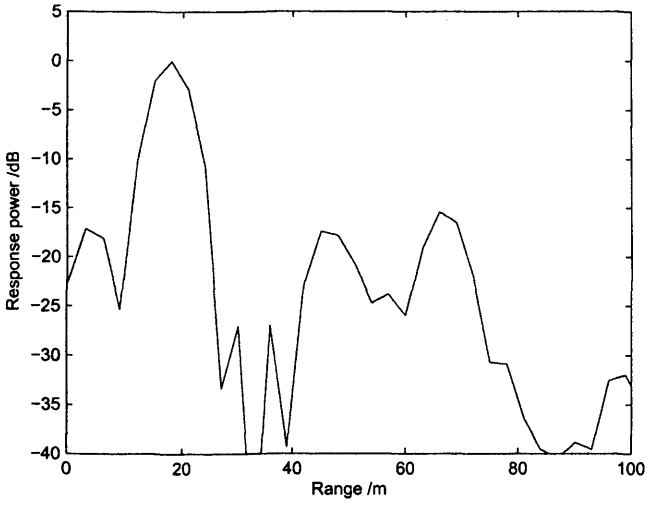

Figure 6-20: As Figure 6-19 for a Blackman weighted chirp

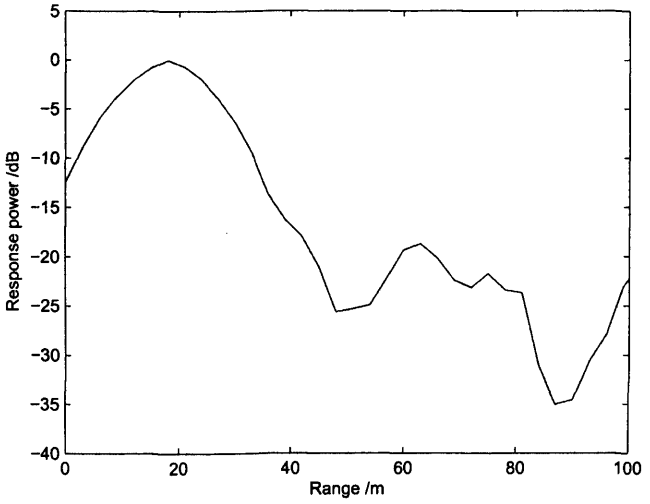

Figure 6-21: As Figure 6-19 for a 7.1 MHz polyphase code from an orthogonal set

Unfortunately, the rooftop and surrounding area contains several other metallic scatterers, although in each case the corner reflector 'point target' is clearly visible. The range resolution in all cases is similar to that obtained in the laboratory, the resolution of the polyphase code being considerably poorer both due to its lower bandwidth and the relatively high non-degrading range sidelobes.

Next, a 'clutter survey' of the surrounding area in Central London was conducted to give a qualitative indication as to the coverage of a single node operating in monostatic mode. The transmitter and receiver antennas shown in Figure 6-17 were co-mounted on the rooftop (approximately 50 m above ground level) with a depression angle of 5° such that their 8° elevation beamwidth would illuminate the range 300 - 2500 m from the radar as shown in Figure 6-22. The antennas were then rotated horizontally on their mounting over 180° in 10° increments such that a semicircular land surface area was mapped. On each occasion, a single node of the radar was used to transmit and coherently integrate a train of 128 chirp pulses with a pulse length of 5 μs and bandwidth of 40 MHz. The responses were used to create an intensity image (thresholded to achieve good contrast), shown with a map underlay in Figure 6-24.

It is evident that there is significant clutter arising from the antenna sidelobes at short range. However, there is clear detection of a number of clutter objects with large RCS, including several cranes surrounding the Kings Cross station development project (marked (a)), and the tall buildings in the Barbican complex (marked (b)). The latter case demonstrates a detection capability over a range of some 2,600 m, which is shown in the range-response matched filter output for this direction in Figure 6-23.

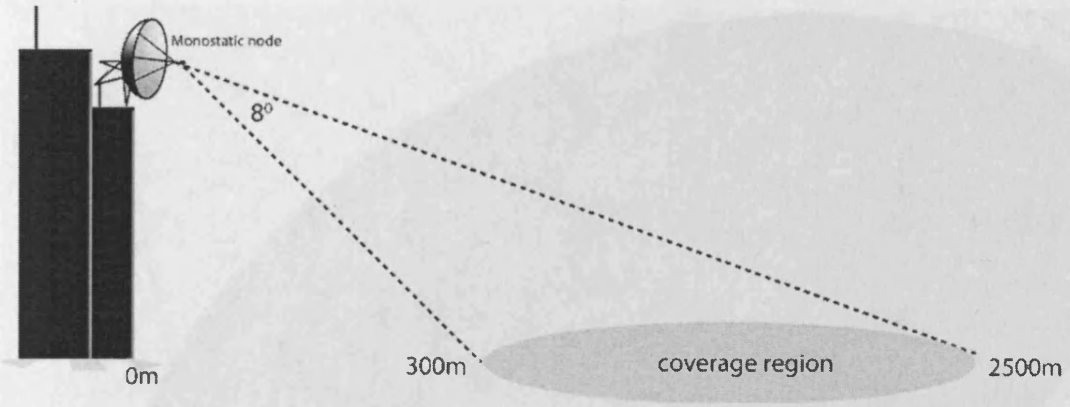

Figure 6-22: Topology for urban clutter experiment

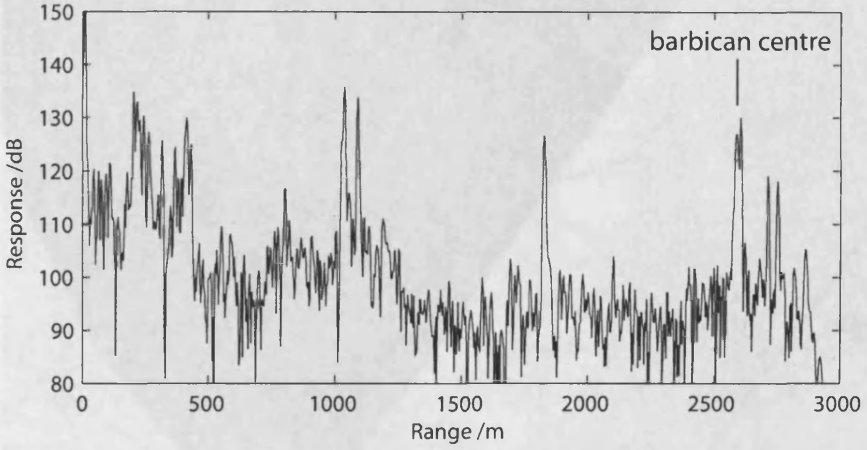

Figure 6-23: Matched filter range-response in direction towards Barbican complex (2600m)

Figure 6-24: Urban clutter in Central London

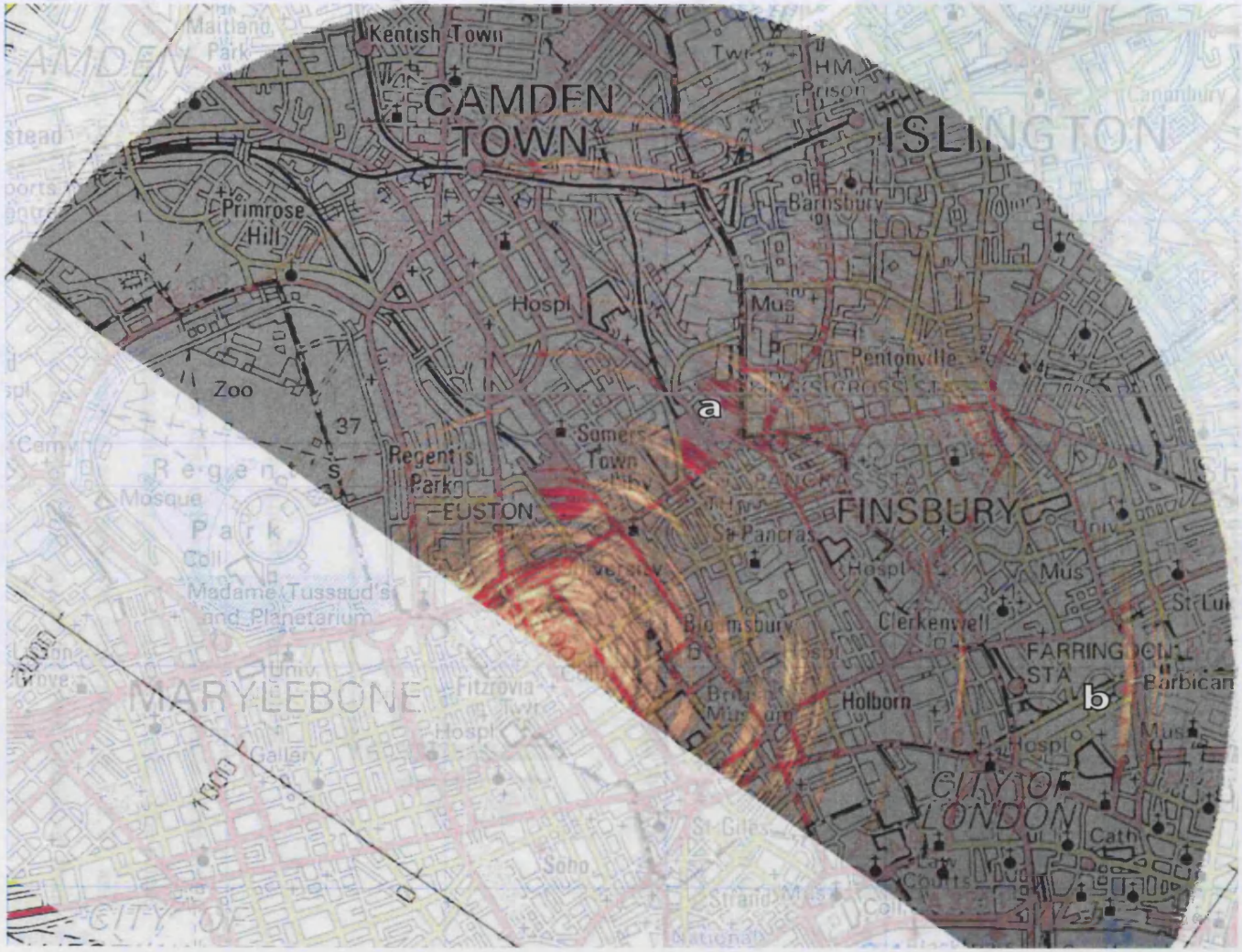

6.3.2 Multistatic Operation

Some initial experiments were then performed using all three nodes in a multistatic configuration. Images of the complete system are given in Figure 6-25.

Figure 6-25: Experimental multistatic setup on rooftop at University College London

Firstly the system was calibrated using the trihedral reflector positioned 29.8 m from the closely spaced antennas, as shown in Figure 6-26. The path length difference for receivers 2 and 3 compared to receiver 1 is only 2.4 cm, so this topology is essentially a replication of three identical monostatic radars.

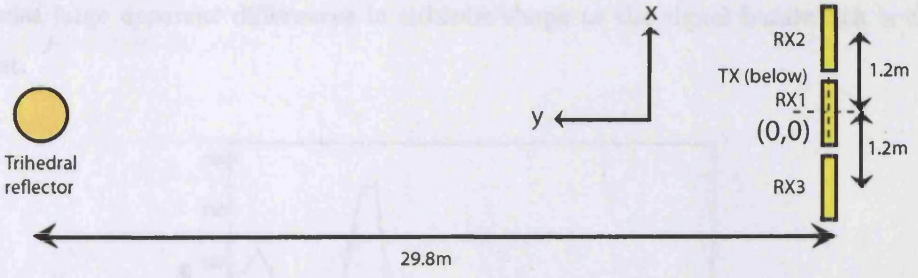

Figure 6-26: Multistatic topology for short range calibration

The local oscillators in the system were first calibrated using a simple closed-loop (waveguide and attenuator) between the transmitter and each receiver in turn. The phase of the peak integrated matched filter response ϕ_i was found in each case ($i = 1, 2, 3$), and the values $\Delta\varphi_{ik1}$ to be used in the multistatic detection Equation 5.4 were calculated from

the *relative* phase between each receiver:

$$\begin{aligned} \Delta\varphi_{11} &= 0 \\ \Delta\varphi_{21} &= \phi_2 - \phi_1 \\ \Delta\varphi_{31} &= \phi_3 - \phi_1 \end{aligned} \tag{6.3}$$

Then, the noise powers N_i (in Equation 5.5) at each receiver were estimated by passively capturing data, and found to be almost equal. The responses of the *individual* matched filters in each receiver to the transmission of a 0.6 μs 40 MHz chirp pulse are shown in Figure 6-27. It is clear that the target position is straddling two range bins in each case, although it is perhaps surprising that there are quite significant differences in the shape of the sidelobes for each receiver. This may be accounted for by the differing reflectivity of nearby clutter due to the slightly different illumination angles, or due to small differences in synchronisation between nodes. A skew of ± 1.5 ns ($\pm 7.5\%$ of a decimated sample period) on the distribution of the reference clock was considered acceptable during calibration as the equivalent ranging error is much less than a range bin, and the large resulting LO phase skew ($\pm 1296°$) can be separately 'calibrated out'. Nevertheless, it was shown in Figure 5-27 that small fractional-sample shifts in the matched filter response to a compressed pulse can cause large *apparent* differences in sidelobe shape as the signal bandwidth is close to Nyquist.

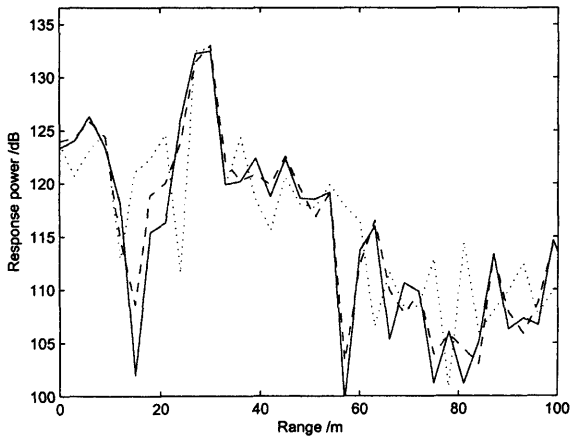

Figure 6-27: Matched filter output range response for the three receivers

Before processing this data using the multistatic detector, a simple simulation was per-

formed using the detection algorithm, based on an *ideal* matched filter response (i.e. chirp autocorrelation) that is replicated exactly for all three receivers under the assumption that they are exactly colocated. This amounts to the simple coherent summation of the same signal three times. The simulated matched filter response is shown in Figure 6-28(a), and the output of the detector is shown as a location intensity plot in Figure 6-28(b). The detection algorithm was set to calculate the response on a 100×100 point grid over the range $-20 \leq x \leq 20$ and $10 \leq y \leq 50$ (the target is at $\{0, 30\}$). A range cut through Figure 6-28(b) at $x = 0$ is shown in Figure 6-29, where the detector output when processing a single receiver only is shown with a dashed line.

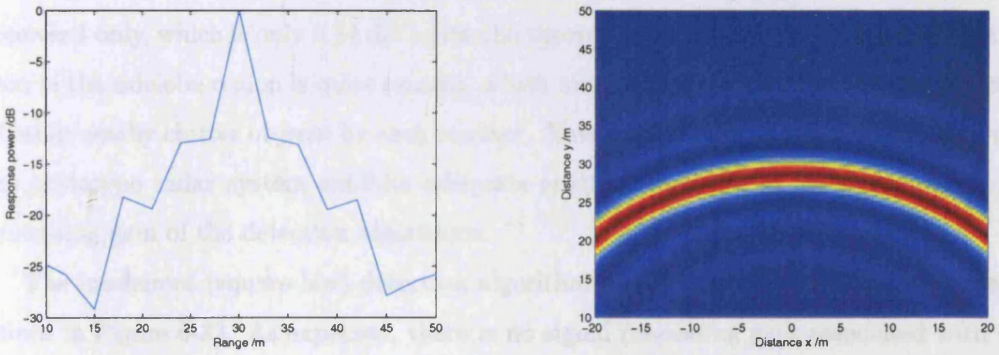

Figure 6-28: Simulation of the multistatic calibration - (a) raw data; (b) output of the coherent multistatic detector

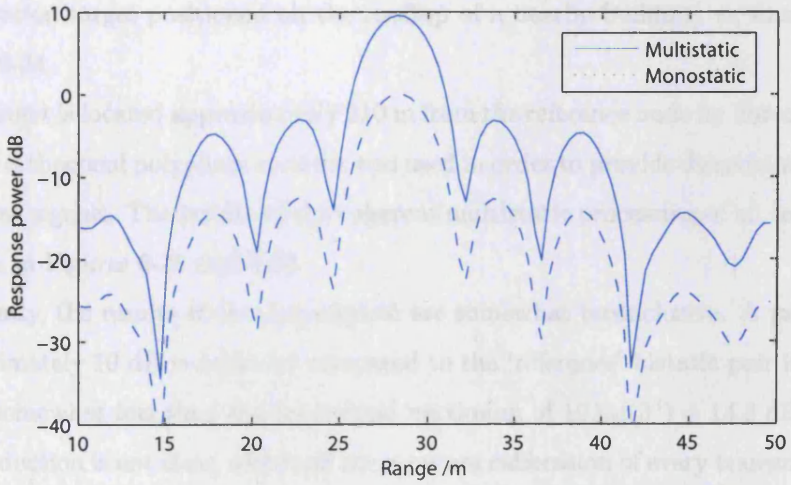

Figure 6-29: Range cut of the simulated coherent multistatic detection

Firstly, it can be seen that, as expected, the multistatic detector output is identical in

form to that in the monostatic case, and similar to that shown in the ambiguity diagrams in Section 3.3. The range cut demonstrates the expected $10\log(3^2) = 9.54$ dB increase in response for the coherent sum of the three simulated receivers compared to the monostatic radar. Further, it is noted that, because the number of points in the grid over which the detection algorithm operated is greater than the sample rate of the raw data in Figure 6-28(a), the fractional delay filter effectively performs interpolation of the received signal - the typical chirp sidelobes are well formed in Figure 6-29.

Then, the data received from the real experiment was processed in the same way, and is shown in Figures 6-30 and 6-31. The intensity plot appears identical to the simulation, and the range cut demonstrates a coherent signal gain of 9.2 dB compared to the response at receiver 1 only, which is only 0.34 dB below the theoretical improvement. It is noted that the gain in the sidelobe region is quite uneven, which may be due to differences in the detection of other nearby clutter objects by each receiver. Nevertheless, this result demonstrates that the prototype radar system exhibits adequate spatial coherency to realise the maximum processing gain of the detection algorithms.

The incoherent (square-law) detection algorithm was then used with the same data, as shown in Figure 6-32. As expected, there is no signal processing gain associated with this detector, and the sidelobe shape is the same as the coherent case due to the very small angular diversity.

Finally, an experiment was performed using all transmitters and all receivers to detect the calibration target positioned on the rooftop of a nearby building, as shown in Figures 6-33 and 6-34.

The target is located approximately 210 m from the reference node by line-of-sight. Here, the 5.6 μs orthogonal polyphase code set was used in order to provide discrimination between transmitted signals. The results of the coherent multistatic processing of all received signals are shown in Figures 6-35 and 6-36.

Evidently, the results of this experiment are somewhat inconclusive. A processing gain of approximately 10 dB is achieved compared to the 'reference' bistatic pair in the system, which is somewhat less than the theoretical maximum of $10\log(3^3) = 14.3$ dB. The reason for this reduction is not clear, although the accurate calibration of every transmitter to every receiver using the direct closed-loop method is particular tedious in this case and prone to error. A more substantive solution would clearly benefit the usability of the system. Equally

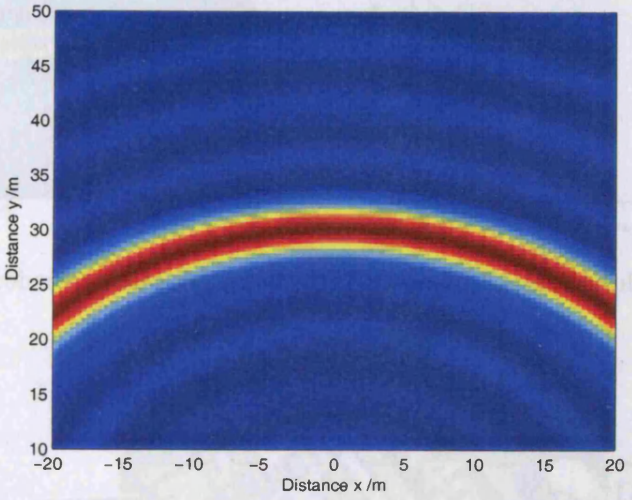

Figure 6-30: Coherent multistatic algorithm intensity plot for a calibration target at $(0, 30)$

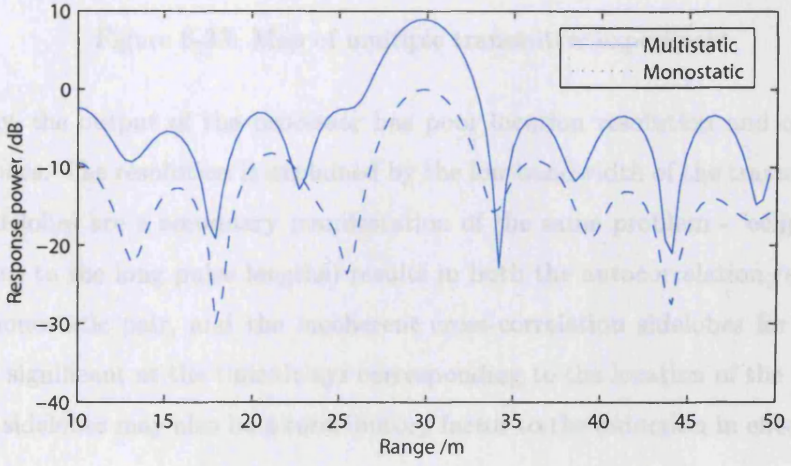

Figure 6-31: Coherent multistatic algorithm range cut for calibration target at $(0, 30)$

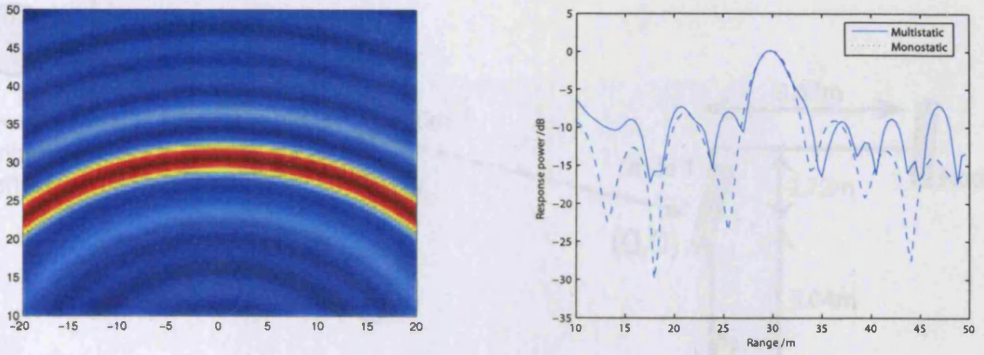

Figure 6-32: Incoherent multistatic detector output - (a) intensity plot; (b) range cut

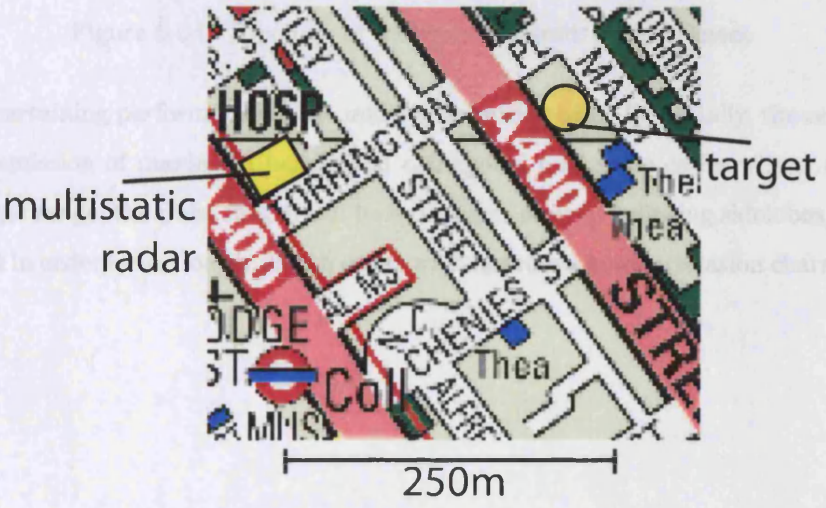

Figure 6-33: Map of multiple transmitter experiment

importantly, the output of the processor has poor location resolution and contains many large sidelobes. The resolution is explained by the low bandwidth of the transmitted pulses, and the sidelobes are a secondary manifestation of the same problem - 'eclipsing' at each receiver (due to the long pulse lengths) results in both the autocorrelation range sidelobes for each monostatic pair, and the incoherent cross-correlation sidelobes for each bistatic pair, being significant at the time delays corresponding to the location of the target. These incoherent sidelobes may also be a contributory factor to the reduction in effective coherent gain.

It is clear that, whilst the prototype system has been shown to operate close to the theoretical expectations when in a single transmitter multistatic mode (albeit for the limited experiments performed so far), some minor design changes are required for it to be a useful

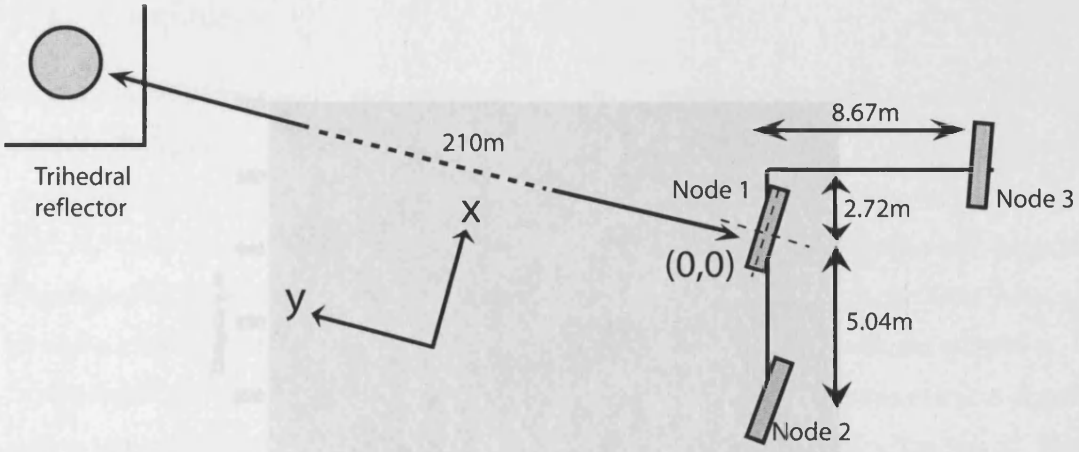

Figure 6-34: Topology of multiple transmitter experiment

tool for ascertaining performance in the multi-transmitter case. Essentially, the requirement is for transmission of maximum bandwidth orthogonal polyphase codes where, depending on the target range, the pulse length can be reduced to prevent eclipsing sidelobes, or can be lengthened in order to use longer length codes with improved autocorrelation characteristics.

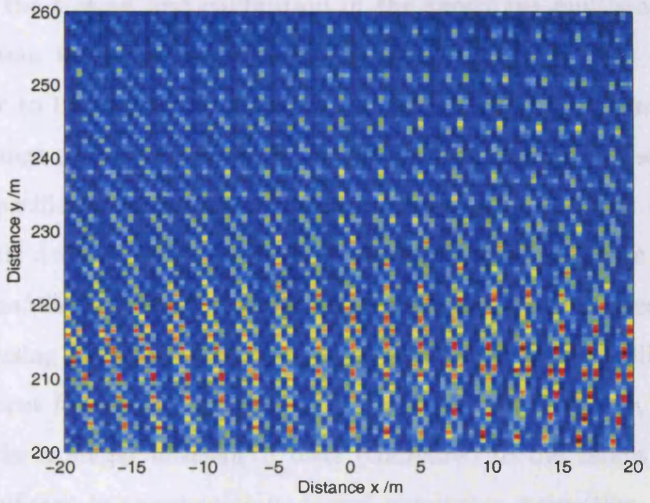

Figure 6-35: Coherent multistatic algorithm intensity plot for multi-transmitter experiment

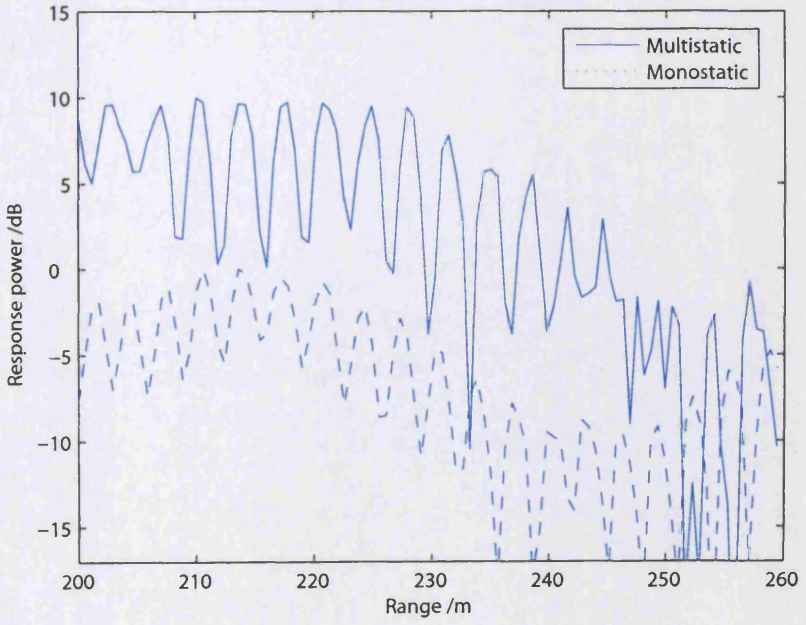

Figure 6-36: Coherent multistatic algorithm range cut for multi-transmitter experiment

6.4 Conclusions

In this chapter, the testing and calibration of the prototype multistatic system was described. Subsystem tests revealed that the measured characteristics of each component were very similar to those predicted during the design process. A combination of closed-loop and short range calibration experiments showed that the range resolution and doppler discrimination specifications can be achieved by the system. Longer range tests demonstrated monostatic detection of large urban clutter objects at ranges in excess of 2500 m.

Preliminary multistatic experiments demonstrated that the full expected coherent signal gain is achieved using multiple receivers in short range tests with a calibration target. The resulting instrument functions approximate those developed in theory, although it will be necessary to perform longer baselength tests (compared to the target range) in order to demonstrate significant improvements in target parameter estimation. Experiments with the system operating in multiple transmitter mode were hindered by the poor characteristics of the relatively low bandwidth orthogonal codes used, and further work is required to resolve this issue. Nevertheless, the design and development of the system has resulted in a versatile, low-cost platform that has been shown to be suitable for conducting novel coherent and incoherent multistatic experiments.

Chapter 7

Conclusions

7.1 Summary of Findings

The objective of this work has been the design, development and evaluation of a low-cost, short range prototype multistatic radar, that operates in the 'cooperative' mode and is capable of both spatial and temporal coherent processing of received signals. The novelty of the system meant it was necessary to analyse fundamental aspects of the related theory, develop models and simulations to determine the expected instrument function, and consider several unique implementation issues in the lead-up to the design and construction of the radar system.

This thesis begins by presenting an overview of the history and current research interests in the field of multistatic radar, and a critique of its capabilities and differentiating features compared to traditional monostatic systems.

Chapter 2 is concerned with analysis of the detection and parameter estimation theory applied to the multistatic case. Its contributions include:

- A thorough review of the relevant statistical background theory and a presentation of multistatic detection algorithms in such a form that can be implemented in the prototype system;
- An analysis of noise sources in a multistatic radar, and the resulting system requirements in order to achieve optimality of the detection algorithms;
- An original analysis and comparison of these detectors using both incoherent and coherent processing, their relative performance and dependent factors, and the effects of signal fluctuations and multi-path on the choice of detector.

Chapter 3 is concerned with theoretical aspects of the performance of both coherent and incoherent multistatic radars. Its main contributions include:

- The development of a simple model for prediction of coverage from extrapolation of the 'radar equation';
- The original derivation of an ambiguity function for multistatic radar based on the structure of the detection algorithms analysed in Chapter 2;
- Use of this function to determine the instrument function of the radar for both coherent and incoherent processing and its related measurement ambiguity, expressed both as

a traditional range-velocity plot on arbitrary vectors for a specific topology, and as a new location ambiguity diagram that allows the native localisation capability of such systems to be visualised;

- A comparison of these results with that of traditional array antennas, and the determination of the effect of functional dependencies such as system topology and target location.

In Chapter 4, an analysis of the design considerations and an outline specification for the system is presented, focussing on development of the system from a low-cost, open architectures approach. The main contributions include:

- A thorough review of the sources of noise pertaining to each oscillator in a multistatic radar and their mutual relationship;
- An original analysis of the effects of this noise and the development of a specification to meet the requirements;
- A review of low-cost technologies for oscillator generation, synthesis and distribution (including a comparison of wired and wireless techniques), leading to an outline design strategy;
- The design and development of a time-domain computer simulation of the multistatic system that demonstrates the effects of coherency and synchronisation errors on the radar instrument function.

Chapter 5 describes the development and construction of the prototype system. Its contributions include:

- A description of several hardware design and software programming techniques applied in a novel way to ensure coherency of the system and meet the performance requirements using low-cost components;
- Methods of implementing the multistatic detection algorithms described in Chapter 2 in discrete-time signal processing, including the novel application of a fractional-delay filter to enable accurate temporal and phase alignment of received signals;

- The completed construction of the three-node prototype system, user interface and control system, that may be used to enable a range of novel multistatic experiments to be performed.

Finally, Chapter 6 documents the calibration and initial experiments with the prototype system. Its contributions include:

- A demonstration that the design almost completely meets the system requirements in laboratory testing, and therefore that the low-cost design approach formulated is viable and may be applicable to a wide range of other radar applications;
- Monostatic testing of individual nodes showed that the expected range instrument functions are revealed in short-range calibration, and that the radar is capable of detecting large clutter objects at ranges in excess of 2,000 m;
- Multistatic calibration using a short baseline topology demonstrated that the instrument function and increase in detected signal energy are in agreement with the predicted theory, and that (with some qualification) the system exhibits further sensitivity gains when multiple transmitters are used.

The theoretical aspects of this work have demonstrated that in the general case a multistatic radar capable of coherent detection affords considerable advantages in terms of detection capability and measurement accuracy. The strong dependency of the system performance on the topology, target location and signal fluctuations means that versatility of operating mode and signal processing is a distinct advantage in order to optimise performance.

The key achievement in this work has been the design, development, construction and testing of a novel, low cost coherent multistatic radar. This system represents a unique instrument that opens up new possibilities for research, and will enable a wide range of experiments to be performed in order to increase our understanding of these types of radars.

7.2 Further Work

Firstly, the possibilities for further hardware development of the prototype system are considered. It is evident from the system testing that the limiting factor to its versatility is

the wired clock distribution system, both because of the limited baselines possible, and more importantly because of the sensitivity of the open-loop system to physical movement. Ultimately, the optimal design should use a completely wireless distribution system (such as GPS), although a low-cost closed-loop wired system may be feasible, incorporating a reference PLL at each node, disciplined by the incoming clock and using feedback on the same cable to compensate for its movement.

This may be complemented with, or replaced by, a more robust method for regular phase calibration of the system in place of the direct closed-loop method used in testing so far with its inherent limits on maximum baselength. This method may take the form of point-to-point calibration broadcasts between nodes, or possibly the use of a calibration point target in an accurately known position, from which high signal-to-noise ratio coherent detection can be used to determine phase offsets between nodes. The ability to perform experiments with longer baselengths will enable experimental determination of the effects of angular diversity on the instrument function and measurement capability, as was demonstrated theoretically in Chapter 3, as well as analysis of the multistatic RCS for complex targets. However, methods are required for the accurate determination of the location of each node in order to gain the full benefit from coherent processing, which may include the use of GPS and a calibration process for jointly solving unknown variables relating to synchronisation, RF phase and precise antenna location.

The replacement of the COTS direct digital synthesiser in the transmitter of each node with equivalent functionality in an FPGA core would provide greater versatility and overcome the restrictions found in transmitting high bandwidth polyphase codes. Finally, the analogue subsystems may be developed to use multiple carrier frequencies or stepped frequency to increase the effective resolution and allow experiments using frequency diversity, although it should be noted that the practical implications for achieving coherency using small wavelengths are more onerous.

The second main area of future research is in the general field of coherent multistatic radar, including detection, tracking and target identification. Studies in these fields could utilise this system in a range of configurations and with a range of targets to obtain novel and unique multistatic radar data.

Further, the development and testing of detection algorithms that are capable of the

estimation and cancellation of spatially correlated interferences may be considered, using similar techniques to those available in the Space-Time Adaptive Processing (STAP) that is quite widely used for conventional antenna arrays(152). In addition, the performance of such systems operating both coherently and incoherently should be considered for a low signal-to-noise environment or where there is strong time-variant signal fading. In the case of multipath fading in short baseline topologies, consideration may be given to mitigating the resulting null patterns using frequency diversity across all transmitters. Experiments may be designed to determine the realisable performance improvement when performing multistatic data fusion at the 'raw data' or 'signal' level rather than at a plot/track level, in particular when the partial signal-to-noise ratios at each receiver are very diverse.

It is noted that the best potential signal-to-noise ratio can be achieved if multiple multistatic transmitters coherently focus their energy at the target location, although evidently this is not feasible if the target position is unknown a-priori. Therefore a three-stage multimode scheme of operation might be considered. In the first stage, a wide search mode might be employed using incoherent processing and a large baselength topology, such that preliminary detection decisions may be made quickly over a large coverage area without the requirement for spatial coherent calibration. This may be followed by spatially coherent surveillance in specific regions of interest. It may be necessary to only utilise certain nodes in the system with short mutual baselengths in order that fluctuations in received RF phases are mutually correlated. Finally, classification and tracking of detected targets may be performed at the highest possible signal-to-noise ratio using coherency on both transmit and receive, once the target location is approximately known.

It is clear that, as technologies improve such that the bandwidth utilisable by radars increases further, so the disparity between range and angle resolution, and the limitations arising from a single look-angle in a traditional monostatic radar become greater. Then, the advantages of spatial diversity available from multistatic radars becomes increasingly important to enable overall improvements in performance.

Appendix A

Detection Theory Derivations

A.1 Neyman-Pearson Criterion

The classic solution to the detection problem is based on the testing of hypothesis likelihoods. Two such hypotheses or situations are considered - H_0 that no target is present, and H_1 than a target is present. The output of the detection receiver is a decision - either D_0 that the target is absent, or D_1 that the target exists.

The probability of detection P_d is the conditional probability of the decision D_1 occurring given the situation H_1:

$$P_d = P(D_1|H_1) = 1 - P(D_0|H_1) \tag{A.1}$$

where $P(D_0|H_1)$ is the probability of missed detection. The probability of false alarm is therefore given by $P_f = P(D_1|H_0)$.

The most general criterion for decision thresholding is *Bayes' Rule*, which assigns 'costs' to the various responses (e.g. correct detection, false alarm, etc) and chooses a decision rule to minimise the total cost. To do so, it is necessary to determine *a priori* the values of these costs, and those of the underlying probabilities for the hypotheses.

However, the *Neyman-Pearson* criterion(153) is more suitable for radar, as here the maximum allowable false alarm rate is chosen a-priori, and within that constraint, the probability of missed detection is minimised (or, equivalently, the probability of detection is maximised).

Formally, the aim is to calculate:

$$\min\{P(D_0|H_1)\}, \text{ given } P(D_1|H_0) \leq P_f \tag{A.2}$$

For a received value y, R_1 is defined as the region of *y-space* (or values of y) for which the receiver will make decision D_1. Further, $p_0(y)$ is defined as the probability density function for y given the hypothesis H_0 is true, and similarly $p_1(y)$ for the situation when H_1 occurs. Then the detection criteria can be expressed as:

$$\max\left\{\int_{R_1} p_1(y)dy\right\}, \text{ given } \int_{R_1} p_0(y)dy \leq P_f \tag{A.3}$$

Therefore points in y should be included in the region R_1 where they contribute proportionally more to increasing the first integral compared to the second integral. From this statement, the Neyman-Pearson criterion forms a *likelihood ratio test* for a given false alarm probability:

$$\lambda(y) = \frac{p_1(y)}{p_0(y)} > \lambda_0 \tag{A.4}$$

where λ_0 is some variable to be found. Conveniently, the Neyman-Pearson test requires no assumptions to be made about the forms of $p_0(y)$ and $p_1(y)$, nor about the a-priori probabilities of H_0 and H_1.

In fact, it can be shown that the likelihood ratio is identical regardless of the criterion chosen - only the threshold λ_0 changes if a Bayes or alternative model is used instead.

A.2 The Matched Filter

In early works such as the classic text by North(154), the criterion for designing a radar receiver was based on the maximisation of the *signal-to-noise ratio*, defined as the ratio of the squared magnitude of the peak response to the signal and the mean noise power at the output of the receiver.

Here it is shown that the optimal receiver on this basis is the *matched filter* (or *correlation filter*). When the input to such a filter is a combination of a particular signal $s(t)$ and white Gaussian noise with two-sided spectral density $N_0/2$, its frequency response function is chosen to maximise the ratio:

$$\text{SNR} = \frac{|s_0(t)|^2}{\overline{n_0^2(t)}} \tag{A.5}$$

where $s_o(t)$ is the output of the filter, defined as the inverse Fourier transform of the product of the filter transfer function $H(\omega)$ and $S(\omega)$, the Fourier transform of $s(t)$, i.e.:

$$s_0(t) = \frac{1}{2\pi}\int_{-\infty}^{\infty} S(\omega)H(\omega)\exp(j\omega t)d\omega \tag{A.6}$$

Similarly the mean square noise power can be written as:

$$\overline{n_0^2(t)} = \frac{N_0}{4\pi}\int_{-\infty}^{\infty} |H(\omega)|^2 d\omega \tag{A.7}$$

so the signal-to-noise ratio is given by:

$$\text{SNR} = \frac{|\int_{-\infty}^{\infty} S(\omega)H(\omega)\exp(j\omega t)d\omega|^2}{\pi N_0 \int_{-\infty}^{\infty}|H(\omega)|^2 d\omega} \tag{A.8}$$

The Schwarz Inequality(53) states that for any two complex signals $A(\omega)$ and $B(\omega)$:

$$\frac{\left|\int_{-\infty}^{\infty} A(\omega)B(\omega)d\omega\right|^2}{\int_{-\infty}^{\infty}|B(\omega)|^2 d\omega} \leq \int_{-\infty}^{\infty}|A(\omega)|^2 d\omega \tag{A.9}$$

Applying this to the SNR gives:

$$\text{SNR} \leq \frac{1}{\pi N_0}\int_{-\infty}^{\infty}|S(\omega)|^2 d\omega \tag{A.10}$$

Given that the average energy E in signal $s(t)$ is given by:

$$E = \int_{-\infty}^{\infty} |s(t)|^2 dt = \frac{1}{2\pi} \int_{-\infty}^{\infty} S(\omega)^2 d\omega \tag{A.11}$$

then the SNR can be expressed as:

$$\text{SNR} \leq \frac{2E}{N_0} \tag{A.12}$$

The equality in Equation A.9 is true if $A(\omega) = KB^*(\omega)$ for some constant K. Therefore, the filter is matched when its frequency response function $H(\omega)$ equals the complex conjugate of $S(\omega)$. In other words, the filter impulse response *matches* that of the signal being sought. It has therefore been proved that this matched filter maximises the output signal-to-noise ratio in the case of a known signal in additive zero-mean white noise.

Various forms of the matched filter have been almost universally adopted in radar receivers since, although theoretically it was accepted that signal-to-noise ratio is not the natural criterion for the detection problem(48). Woodward(155) states that the ideal receiver is one that optimises the extraction of useful *information* from a signal embedded in noise, and there is no general theorem to show that maximum SNR ensures maximum gain of information.

The connection of the detection problem to statistical hypothesis testing (such as the Neyman-Pearson test in Appendix A.1) was made almost simultaneously from several routes. Notably Woodward described a method of 'inverse probabilities' in order to calculate the probability distribution $p_y(x)$ which maximises the information about a message x from a knowledge of the received signal y, and it was shown that this *likelihood function* results in a minimum variance delay (range) estimator. It can be easily shown that the optimal detector defined by the likelihood ratio test is in fact the matched filter, given the signal is in a background of additive zero-mean Gaussian noise.

A.3 The Likelihood Ratio Test

Here, the likelihood ratio for signal detection is determined given a background of coloured noise and a finite observation period. This is performed by expressing the process $x(t)$ of signal and coloured noise using the Karhunen-Loève expansion(52) given by:

$$x(t) = \sum_{i=1}^{\infty} x_i \phi_i(t) \quad -T/2 \leq t \leq T/2 \tag{A.13}$$

where coefficients x_i are random variables, and $\phi_i(t)$ is a set of orthonormal functions in the interval $\{-T/2, T/2\}$, such that:

$$\int_{-T/2}^{T/2} R(t_1, t_2)\phi_i(t_2)dt_2 = \lambda_i \phi_i(t) \quad -T/2 \leq t \leq T/2 \tag{A.14}$$

where $R(t_1, t_2)$ is the covariance function of $x(t)$. The functions $\phi_i(t)$ are eigenfunctions of the kernel $R(t_1, t_2)$ and λ_i are the corresponding eigenvalues. By definition, the noise component $n(t)$ is Gaussian and therefore so are the coefficients x_i, which can be defined by mean and variance only. The covariance of x_i can be expressed as:

$$\begin{aligned} E[x_i x_j^*] &= \int_{-T/2}^{T/2} \int_{-T/2}^{T/2} \phi_i^*(t_1) R(t_1, t_2) \phi_j(t_2) dt_1 dt_2 \\ &= \lambda_j \int_{-T/2}^{T/2} \phi_i^*(t_1)\phi_j(t_1)dt_1 = \lambda_j \delta_{ij} \end{aligned} \tag{A.15}$$

Therefore, it can be seen that the coefficients x_i are uncorrelated with variances λ_j. These coefficients form the new process, and can be defined as:

$$x_i = \int_{-T/2}^{T/2} \phi_i^*(t) x(t) dt \tag{A.16}$$

As the noise component of $x(t)$ is zero-mean and the signal component is deterministic, the mean s_i of x_i for the two hypotheses h_1 and h_0 is given by:

$$h_{[1/0]} : \mathrm{E}[x_i]_{[1/0]} = s_{i[1/0]} = \int_{-T/2}^{T/2} \phi_i^*(t) s_{[1/0]}(t) dt \tag{A.17}$$

where $s_1(t)$ is the wanted signal component when a target is present (H_1), and $s_0(t) = 0$ for the null hypothesis.

Therefore, from Equations A.15 and A.17 the multidimensional Gaussian probability density function (PDF) for N coefficients of x_i is given by:

$$p_{1/0}(\mathbf{x}) = \prod_{i=1}^{N} (2\pi\lambda_i)^{-1/2} \exp\left[\frac{-(x_i - s_{1/0i})^2}{2\lambda_i}\right] \tag{A.18}$$

It is possible to express $p_{1/0}$ as a simple product of individual PDFs only because all coefficients x_i are independent. The covariance kernel $R(t_1, t_2)$ from Equation A.15 is known to be symmetric and positive definite, and has an inverse defined by:

$$\int_{-T/2}^{T/2} R^{-1}(t_1, t_2) R(t_2, \tau) dt_2 = \delta(t - \tau) \tag{A.19}$$

which can be expanded using Mercer's theorem as:

$$R^{-1}(t_1, t_2) = \sum_{i=1}^{\infty} \left(\frac{1}{\lambda_i}\right) \phi_i(t_1) \phi_i^*(t_2) \tag{A.20}$$

Then, we can transform back to the original variable $x(t)$ by taking the limit of Equation A.18 to $N \Rightarrow \infty$, and using Equations A.14, A.16 and A.20 (see (49)) to give:

$$p[x(t)] = C \exp\left[-\frac{1}{2} \int_{-T/2}^{T/2} \int_{-T/2}^{T/2} [x(t_1) - s_{1/0}(t_1)] R^{-1}(t_1, t_2) [x(t_2) - s_{1/0}(t_2)] dt_1 dt_2\right] \tag{A.21}$$

for some normalising constant C. Setting $s_0(t) = 0$ for the null hypothesis (target absent), the likelihood ratio λ can be expressed as:

$$\begin{aligned} \lambda = \frac{p_1[x(t)]}{p_0[x(t)]} = \exp\Big\{ \mathrm{Re} \int_{-T/2}^{T/2} \int_{-T/2}^{T/2} s_1^*(t_1) R^{-1}(t_1, t_2) x(t_2) dt_1 dt_2 \\ - \frac{1}{2} \int_{-T/2}^{T/2} \int_{-T/2}^{T/2} s_1^*(t_1) R^{-1}(t_1, t_2) s_1(t_2) dt_1 dt_2 \Big\} \end{aligned} \tag{A.22}$$

A.4 Performance of the TOA Location Estimator

Here, a technique is described that is based on Chernyak(73) for determining the performance of the location estimator described in Section 2.6.

The total parameter vector $\boldsymbol{\Theta}$ is divided into useful parameters α and stray parameters β. Estimates of the useful parameters α are generally dependent on β, obtained from the joint solution of likelihood equations for both. To obtain the likelihood ratio as a function of useful parameters only, likelihood equations for β should be averaged over the received signals. The general frequency domain likelihood function of Equation 2.21 can be used to express elements of the Fisher information matrix from Equation 2.91 as:

$$\tilde{J}_{np}^{(\alpha)} = \mathrm{Re} \sum_{i=1}^{m} \sum_{k=1}^{m} \frac{1}{2\pi} \int_{-\infty}^{\infty} \frac{\partial \Psi_i^*[\omega, \alpha_0, \mathbf{u}_1(\alpha_0)]}{\partial \alpha_n} \frac{\partial \Psi_k[\omega, \alpha_0, \mathbf{u}_1(\alpha_0)]}{\partial \alpha_p} f_{ik}(\omega) d\omega \tag{A.23}$$

where $\mathbf{u}_1(\alpha)$ is the vector of solutions to the likelihood equations for the stray parameters β averaged over the received signals, $\boldsymbol{\Psi}(\omega)$ and $\mathbf{f}(\omega)$ are the Fourier transforms of the wanted signal vector and inverse of the covariance matrix respectively (see Equation 2.21).

In this case, the wanted parameters α_n are the times of arrival t_{sn}. The partial derivatives above can be solved using Equation 2.24 to give:

$$\frac{\partial \Psi(\omega)}{\partial t_{sn}} = -j a_{s1}^0 \Psi_0(\omega - \omega_0) \exp[-j(\omega t_{si}^0 + \varphi_{si})] \left(\frac{\partial \varphi_{si}}{\partial t_{sn}} + \omega \frac{\partial t_{si}}{\partial t_{sn}} \right) \tag{A.24}$$

where the partial derivatives of φ_{si} and t_{sn} are taken at the true time-of-arrival t_{si}^0. Clearly, the values of $\partial t_{si}/\partial t_{sn}$ are given by δ_{in} for $i \leq 2$, and $\partial h_i(t_{s1}, t_{s2})/\partial t_{sn}$ for $i > 2$. Solutions to $\partial \varphi_{si}/\partial t_{sn}$ can be found from the generation of likelihood functions for φ_{si} and averaging over the received signal vector $\chi(\omega)$. It can be shown that substitution of these into Equation 2.91, assuming no external interferences such that $f_{ii}(\omega) = 1/N_i$, yields:

$$\tilde{J}_{np}^{(t_s)} = 2E_i \delta_{np} \overline{\Delta\omega_n^2}/N_i + \sum_{i=3}^{m} \frac{2E_i \overline{\Delta\omega_n^2}}{N_i} \frac{\partial h_i(t_{s1}, t_{s2})}{\partial t_{sn}} \frac{\partial h_i(t_{s1}, t_{s2})}{\partial t_{sp}} \tag{A.25}$$

where $\overline{\Delta\omega_n^2}$ is the mean-square (effective) bandwidth of the general spectrum.

Appendix B

The Radar Cross-Section and Correlation of Scattered Signals

It was shown in Section 2.4 that the optimal detection algorithm is dependent on the correlation of signal fluctuations at each receiver, and that the target is often a major contributor to these fluctuations. Here, an outline of the main classes of targets and general models for the nature of their scattering is presented. The models can be used to determine appropriate test targets and detection algorithms used in experiments with the prototype multistatic system.

When energy is intercepted by a target, the measure of the proportion of incident power reflected back towards the radar is given by the *radar cross section* (RCS) σ. It is well known from bistatic experiments (see Willis(75)) that the 'bistatic RCS' σ_{bistatic} is dependent on the bistatic angle (see Figure 1-2) as well as the aspect angle in three dimensions. Therefore in a multistatic radar, the apparent RCS σ_{ik} is a function of the relative location of the target and the bistatic transmitter-receiver pair k-i considered, as well as the target orientation.

The RCS of a target is defined as being equal to the surface area of a symbolic isotropically scattering object that creates the same flux density at the (distant) receiver as the target. Analytic solutions are available only for a few simple objects, hence experimental measurements have traditionally been used for calculations involving complex targets.

In situations where the target dimensions are considerably smaller than the transmitted wavelength λ, scattering is in the *Rayleigh region* where the RCS is given by the relationship $\sigma \propto \lambda^{-4}$. When scatterers are similar in size to the wavelength (the *Mie region* or *resonance*

region), the RCS exhibits a complex oscillatory behaviour with small changes in size. If the target is large, but approximates a convex perfectly conducting object, physical optics methods can be used.

In general however, targets are large compared to λ, and in addition comprise many points (or *flare spots*) at which scattering occurs. Then, the total signal reflection towards a receiver is a complex sum of the contribution from each of these points. Hence the RCS is heavily dependent on the relative location of each of these scattering centres with respect to the transmitter and receiver. Even small target vibrations, rotations or movements can cause changes in the location of these flare spots which are large compared to $\lambda = c/\omega_0$, resulting in large phase shifts of the individual scattering contributions. The resultant scattered signal towards a receiver will have complex amplitude fluctuations (i.e. real amplitude and phase fluctuations). When the number of flare spots is fairly large and each scatters signal with approximately equal intensity, these complex fluctuations have a zero-mean Gaussian distribution (an 'exponential' power distribution) and are described *temporally* by the Swerling cases 1 and 2.

In a multistatic system, complete characterisation of the temporal *and spatial* complex fluctuations apparent at the receivers can be defined by the space-time correlation matrix. This method has been used in Chernyak(50) to analyse the case of a moving target with large dimensions compared to λ that is perceived by all receivers as a set of N flare spots fixed rigidly relative to the target's centre of mass. It is assumed that the initial aspect of the target is random, and is the result of a preceding rotation from its mean position through a small angle $\delta\theta$. This angle can be expressed by the sum of Cartesian components $\theta_{x,y,z}$ relative to axes originating at the target centre of mass. Each of these components is assumed to be a mutually independent random variable distributed uniformly within known limits $\pm\Delta\theta_{x,y,z}/2$. Approximations have been derived for situations of 'high' and 'low' spatial and temporal correlation of the complex Gaussian fluctuations between two arbitrary receivers. The boundaries for each of these two situations for spatial correlation are simply stated here, such that they may be used in determining the topology of the prototype system:

$$\begin{aligned} (L_{12\text{eff}}/R_1) &\leq (0.14 - 0.24)\lambda/l_{12} \quad \text{high correlation} \\ (L_{12\text{eff}}/R_1) &\geq \min[0.8\lambda/l_{12}; 3\lambda/\Delta\theta_y l_z; 3\lambda/\Delta\theta_z l_y] \quad \text{low correlation} \end{aligned} \tag{B.1}$$

where L_{12} is the *effective baseline* (the length of the bistatic baseline projection onto the plane orthogonal to the bistatic bisector between the two receivers), l_{12} is the projection of the target dimension onto that same plane, l_y and l_z are the projections of the target dimension onto respective Cartesian axes, and R_1 is the distance from the first receiver to the target. High correlation is defined as the modulus of the complex correlation co-efficient being at least 0.95; low correlation is defined where the co-efficient is less than 0.5. Therefore the region between the two stated boundaries will exhibit some intermediate degree of correlation. These bounds apply to the mutual correlation between the signals at two receivers with a common transmitter. Similar bounds are stated for the case of two monostatic radars, obtained by halving the coefficients in the above equation.

Let us take the case where the two receivers are equidistant from the target. Then the effective baseline equals the distance between the receivers. Evidently, given an appropriate target for this model, high spatial correlation of echo fluctuations between receivers will only occur if the ratio of the distance between the receivers to the distance to the target is a small fraction of the ratio of the wavelength to the target dimension along the baseline direction. Alternatively, it suggests that the optimal conditions for incoherent detection are met if this ratio approaches unity or the other conditions are met in Equation B.1 for *all* bistatic pairs in the system.

The boundaries for temporal correlation are given as:

$$\begin{aligned} \Omega \sin \varepsilon_{kb} T_0 &\leq (0.07 - 0.12)\lambda / l_k \cos(\beta_{0k}/2) \quad \text{high correlation} \\ \Omega \sin \varepsilon_{kb} T_0 &\geq \min[0.4\lambda / l_k \cos(\beta_{0k}/2); 1.5\lambda / \Delta\theta_y l_z \cos(\beta_{0k}/2); \\ &\qquad 1.5\lambda / \Delta\theta_z l_y \cos(\beta_{0k}/2)] \quad \text{low correlation} \end{aligned} \tag{B.2}$$

for receivers $k = 1, 2$ where Ω is the angle velocity of the target rotation about its centre of mass, ε_{kb} is the angle between the vector of rotation and the bistatic bisector vector between the transmitter and receiver k, T_0 is the observation time interval, β_{0k} is the bistatic angle for receiver k and l_k is the projection of the target dimension onto the distance vector from the target to receiver k.

Temporal correlation is considered for the signal received at each receiver individually. Equation B.2 shows that high correlation will only occur if the angle of target rotation about the axis perpendicular to the bistatic plane over time T_0 is a small fraction of the ratio of

the wavelength to the projection of the target dimension along the direction perpendicular to the rotation axis and bistatic bisector. This situation is not unique to multistatic radar, and indeed provides an analytic basis for the adoption of cases 1 or 2 of the Swerling models, as well as determining the appropriate form of temporal integrator. However, it is reliant on knowledge of the rate of target 'rotation' used as the basis for the model, which in the general case will not be available a-priori.

Some targets (for example, stealth aircraft) have scattering characteristics that are very different from the models referenced so far. For the purposes of detection, a general knowledge of the type of target to be expected may be adequate to guide the choice of detection algorithm. However, precise models for scatter from particular targets for bistatic systems may be useful for target identification. Further discussion of the theory for modelling target scatter with application to bistatic and multistatic radar can be found in Kostylev(156). In addition, a recent study(157) has attempted to model the expected multistatic RCS of certain targets by a combination of measurement and CAD modelling.

In summary, this approximation for the conditions of spatial correlation may be a useful method of determining the optimal detector algorithm, or alternatively for guiding the placement of receiver antennas. It provides a more rigorous alternative to the delineation between 'small' and 'large' baselength systems described in Section 1.3.3. In particular, it has been shown that such definitions are conditional on the nature of the target itself and the topology. If target fluctuations mutually decorrelate the signals at each receiver, then attempts at coherent detection will perform very poorly and detector L_3 becomes optimal. The calculation relies only on the geometry and the target dimensions, which will often be known or can be estimated. Finally, it should be noted that this condition applies to targets that are large and can be modelled as a collection of similar flare spots. Simple or 'test' targets may display strong spatial scattering coherency well beyond the bounds described here.

Appendix C

Waveform Schemes for Multiple Transmitter Systems

Here, consideration is given to the waveforms used by each transmitter in a multistatic radar. It was shown in Section 2.5 that the addition of transmitters to a system will normally result in improved detection performance. Two general schemes were outlined in Section 2.4.7 - firstly where the waveforms are diversified so that each can be discriminated in a receiver, and secondly where each transmitter sends identical waveforms that are appropriately timed so as to be coherently focussed at some point in space. It was also shown in Section 3.3 that the ambiguity function is dependent on the waveform(s) used, and so affects both resolution capability and parameter estimation accuracy. Here, these waveform schemes are analysed for their appropriateness to particular detection situations, ambiguity characteristics, and their implementation in the prototype multistatic system.

Firstly we consider the signal diversity method such that each of the signals from n transmitters can be discriminated at each of m receivers. Then, the radar can be considered to consist of $m \times n$ bistatic components. In Section 3.3, the method of discriminating between the signals from each transmitter in the ambiguity diagram models was not considered (it was implicitly assumed that temporal discrimination was used). Temporal methods are generally not optimal when targets are moving, as it is necessary to extrapolate measured time-of-arrival and doppler shifts back to a common time reference in order to jointly calculate target parameters from all received signals. Therefore, we consider discrimination based on frequency diversity, and on diversity using sets of non-identical waveforms.

The detection algorithms L_{2m} and L_{3m} were described in Section 2.4.7 for use in the case where signal discrimination is available. However, a criterion for their optimality is that the noise associated with each received signal in every receiver should be mutually uncorrelated. For this to be true, the integral in Equation 2.81 should equal zero.

It was shown that if frequency diversity is used and the separation is such that the frequency response functions of the matched filters for each signal do not overlap, then this criterion is met. Then, any waveforms can be transmitted on each separated sub-carrier without risk of interference, so a suitable scheme may be devised to provide overall favourable ambiguity characteristics.

Frequency diversity may have a further advantage in the case that received signals are fluctuating. It was shown in Section 2.5 that, in this case, improved detection performance is usually attained if the fluctuations of signals pertaining to each bistatic pair are mutually independent in order to maximise 'smoothing gain' and the incoherent detection algorithm L_{3m} is used. It was shown in Appendix B that the fluctuations resulting from a large target comprised of many scattering centres are frequency dependent. Therefore, frequency diversity may have the additional benefit in this context of causing the decorrelation of the fluctuations of each transmitted signal.

However, frequency diversity has some major disadvantages. Firstly, when fluctuations at a given frequency are very small and it might otherwise be possible to use coherent detection optimally, such diversity may cause unwanted decorrelations. Secondly, the required receiver bandwidth may be very high, as it must be capable of capturing signals on all frequencies simultaneously.

Therefore it may be advantageous if signals occupying the same frequency spectrum (or that have partially overlapping frequency response functions) can be used. However, it is still necessary for the integral in Equation 2.81 to be zero to ensure optimality of the detection algorithms. We start by defining the frequency response function $H(\omega)$ of an arbitrary matched filter (matched to a delay of τ) as(46):

$$H(\omega) = S^*(\omega)\exp(-j\omega\tau) \tag{C.1}$$

where $S(\omega)$ is the Fourier transform of the expected input signal $s(t)$ to which the filter is

matched. Then, for two such filters in the bank we can write:

$$H_1^*(\omega)H_2(\omega) = S_1(\omega)S_2^*(\omega) \tag{C.2}$$

Then, substituting Equation C.2 into Equation 2.81 gives:

$$\int_{-\infty}^{\infty} S_1(\omega)S_2^*(\omega)\exp(j\omega\tau)d\omega = 0 \tag{C.3}$$

where the resulting integral is equal to the cross correlation of the 'matched' expected signals $s_1(t)$ and $s_2(t)$ at zero lag ($\tau = 0$). This is the requirement for *orthogonality*, which we can write as:

$$\int_t s_1(t)s_2^*(t)dt = 0 \tag{C.4}$$

Hence we have shown that if orthogonal signals are used at each transmitter, and a bank of matched filters is used at each receiver, the noise at the output of each filter will be uncorrelated, and so detectors L_{2m} and L_{3m} are optimal.

In addition, it is required that each matched filter in the bank completely rejects components of the input signal from other transmitters, which will otherwise add to the total noise. Hence, we require the cross correlation of all such signals to be zero *for all possible lags* - this is a stronger requirement that orthogonality. Further, the scheme should provide the desired ambiguity characteristics. In particular, in order to achieve good close-in range ambiguity properties, the autocorrelation of each signal should approximate a delta response at zero lag.

The use of diverse waveforms in radar originated from the so-called 'complementary sets' studied by Golay(158). A code may be simply defined as a finite series of (usually phase or frequency) values that expresses the baseband modulation of a signal. If the signal is a pulse, then the pulse length may be divided by the length of the code, and the resulting sub-pulses of constant modulation are called 'bits' or 'chips'. The codes are usually chosen to have some particular correlation characteristics. A binary complementary set is a set of such binary codes where the sum of their individual autocorrelations is zero for all non-zero shifts. These waveforms are quite widely used for *temporal* diversity in order to reduce recurrent range sidelobes by phase coding each pulse in a train with a member of the set. The resulting autocorrelation of the entire train exhibits a zero correlation zone

around $|\tau| \geq t_b$ where t_b is the bit length, and low recurrent multiple-time-around sidelobes. However, such pulse trains suffer from large doppler sidelobes in the resulting ambiguity function.

A similar scheme was proposed by Mozeson and Levanon(159), but here the scheme is based on overlaying orthogonal coding (which is a stronger demand than that for a complementary set) onto a standard signal such as a chirp that has the desired ambiguity properties. The ambiguity function of the resulting pulse train shows improved sidelobe characteristics compared to the standard complementary sets.

Evidently it is possible to use similar sets of codes in systems with multiple transmitters. Instead of wishing to reduce recurrent range sidelobes in a train of pulses, we wish to allow discrimination between several pulses that may be received simultaneously at the receiver. Several code sets are in widespread use in the field of mobile telecommunications where the basestation and each handset must be able to distinguish between the signals from multiple users. The so-called 'near-orthogonal' codes are binary pseudo-noise (PN) sequences, including maximal length and Gold codes. Completely orthogonal codes include Walsh and 'orthogonal Gold' codes. Whilst these codes have zero cross-correlation at zero lag, they have larger cross-correlations at other offsets compared to the near-orthogonal codes. Therefore they are normally used when systems are synchronised so that each signal arrives at the same time. In addition, the autocorrelation response of the orthogonal codes less approximates a delta function compared to the near-orthogonal PN sequences(160). Therefore, despite the non-optimality of the near-orthogonal codes (there will inevitably be some small correlation between the noise associated with the filtered component of each received signal), they are more likely candidates for use in such radar applications. The PN codes are specified for several 'optimal' bit lengths N, and it is known that the expected autocorrelation peak sidelobes are at a level of $20\log(1/N)$ dBc. The range sidelobes roll-off very slowly compared to frequency modulated pulses (such as chirps), so the use of long bit length codes is preferable. In addition, the number of members in a set is related to the bit length, so long codes must also be used if the number of transmitters is large. However, the use of long codes in short pulses (in order to minimise 'eclipsing') implies a large total bandwidth, which can be approximated by $1/t_b$ where t_b is the bit period (i.e. the pulse length is equal to Nt_b).

A set of 33 Gold codes with length of 31 bits was investigated by Hale(161) for the

purpose of temporal pulse train diversity, and improvements were shown in the ambiguity sidelobes of the complete train autocorrelation function compared to sets of multi-slope chirp waveforms. The Gold codes have also been implemented in the Norwegian continuous-wave multistatic system(162) (see Section 1.5.3), which comprises two transmitters and a single receiver. Here, members from the set were used by each continuous wave transmitter. CW operation enabled long code lengths can be used (1,023 in this case), which resulted in an average range peak response to maximum sidelobe ratio of approximately 16 dB.

For the purposes of the pulse-based prototype radar described in Chapter 5, a set of short codes is required that still offer adequate discrimination and ambiguity characteristics. Therefore a set of (near) orthogonal polyphase codes is considered, which were optimised for desired correlation properties using simulated annealing, and published by Deng in (163). This particular set has only four members, but each has a length of 40 bits. The resulting auto-correlation and cross-correlation of two arbitrary members of this set are shown on linear and log scales in Figure C-1.

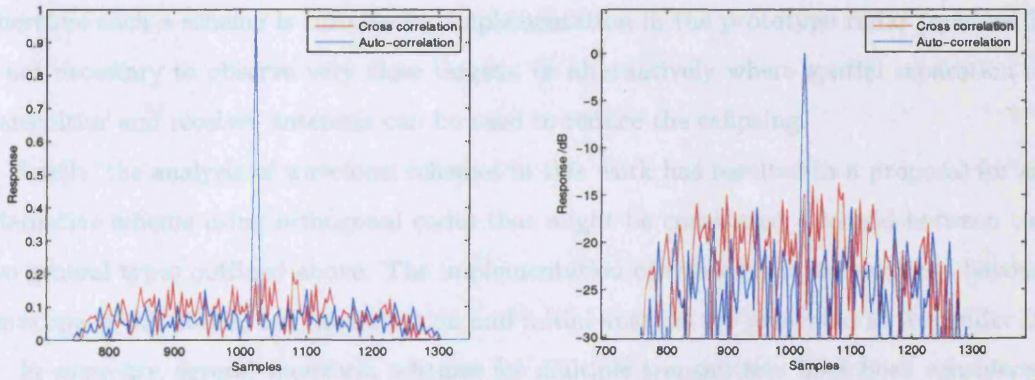

Figure C-1: Auto- and cross-correlation functions of two codes from an optimised polyphase orthogonal set

The maximum cross-correlation response is approximately 15 dB below the peak auto-correlation response, which sets the bound for the maximum discrimination possible. A Matlab simulation was run to model the mutual correlation of noise for a matched filter bank based on these codes. A complex Gaussian noise source was modelled in the time domain, and this common input signal was passed through two matched filters for members of this set. The cross correlation of the output signals was calculated, and normalised with reference to the autocorrelation peak of one of the codes. The resulting correlation

was 0.21, which is normally considered to be 'low correlation', and hence the detection algorithms L_{2m} and L_{3m} would be expected to approach optimality using this waveform set. It is noted however that the autocorrelation sidelobes have a similar level to the cross-correlation response, which limits the resolution ability of the system for closely spaced targets. Therefore, pulse lengths should be kept as short as possible (which implies a high bandwidth) in order to minimise resolution ambiguity of adjacent weak targets. Deng also shows that longer length codes exhibit lower auto-correlation sidelobes and cross-correlation peak responses, albeit at the expense of a wider ambiguity range for fixed bandwidth. It was also shown that, again typically of pseudo-noise codes, sensitivity to doppler is quite high, and the response falls to the sidelobe noise floor for doppler shifts in excess of $1/T$ where T is the pulse length.

For an arbitrary radar transmitter with bandwidth of 50 MHz, the minimum pulse length of the length-40 polyphase codes is 0.8 μs, which makes the pulse 'doppler tolerant' up to approximately 1.25 MHz. If 'eclipsing' of the received echoes by the transmitted signal is to the totally prevented, this results in a monostatic 'minimum range' of 120 m. Therefore such a scheme is suitable for implementation in the prototype radar provided it is not necessary to observe very close targets, or alternatively where spatial separation of transmitter and receiver antennas can be used to reduce the eclipsing.

Lastly, the analysis of waveform schemes in this work has resulted in a proposal for an alternative scheme using orthogonal codes that might be considered a hybrid between the two general types outlined above. The implementation of this scheme is somewhat beyond the scope of this thesis, but its derivation and initial analysis are presented in Appendix D.

In summary, several waveform schemes for multiple transmitters have been considered for use in the prototype multistatic radar. Frequency diversity provides complete freedom of waveform choice, and may aid the decorrelation of fluctuations where incoherent processing is desired, but the large bandwidth requirement at the receiver is prohibitive for the prototype system. Various orthogonal waveform schemes were then considered that would allow the same bandwidth can be used by multiple transmitters, and it was shown that a small optimised code set could provide reasonable ambiguity and discrimination characteristics, and could be implemented in the prototype system.

Appendix D

An OFDM-based Multi-transmitter Waveform Scheme

Here, a proposal for a waveform scheme based on orthogonal codes is presented that might be considered a hybrid between the 'discrimination' and 'coherent' methods described in Appendix C. An outline of the scheme and initial analysis is included here for possible future implementation into the prototype system, and to demonstrate the potential advantage of concurrent waveform diversity.

A *multi-carrier* waveform based on OFDM (Orthogonal Frequency Division Multiplexing) was first proposed by Levanon(164) for use in monostatic radar, where he demonstrates highly superior ambiguity properties compared to similar single-carrier phase codes. Here, the waveform is formed from the sum of signals modulated onto several different carriers. OFDM is currently a very popular method in communications of increasing channel capacity and reducing interference caused by inter-symbol interference due to multipath. In communications, the data stream to be transmitted is parallelised to several streams with correspondingly longer bit duration t_n. Each stream is then modulated with a complex carrier of frequency n/t_n.

In OFDM, each of the simultaneously transmitted waveforms $u_n(t)$ is selected to have

a carrier separated by the inverse of the bit duration t_n such that:

$$u_n(t) = \exp\left(j2\pi n\frac{t}{t_n}\right) \quad 0 \leq t < t_n \tag{D.1}$$

Then, using Equation C.4, it can be shown that any two of these (non-identical) waveforms are orthogonal:

$$\frac{1}{t_n}\int_0^{t_n} u_n(t)u_m^*(t)dt = \frac{1}{t_n}\int_0^{t_n} \exp\left[j2\pi(n-m)\frac{t}{t_n}\right]dt = 0 \quad m \neq n \tag{D.2}$$

The normalised integral equates to 1 on the condition $n = m$. Each carrier can be modulated independently with any complex modulation symbol without affecting the orthogonality, despite the spectra of each subcarrier overlapping. For such a signal comprising N separate carriers and M bits per carrier, the total bandwidth occupied is MN/T where $T = Mt_n$ is the pulse length. The resulting large time-bandwidth product MN (compared to M for a single carrier signal), combined with lack of regularities in the pulse structure means that the ambiguity function is closer to the ideal thumbtack response. The disadvantage of this method, apart from additional transmitter complexity, is that multiple carriers create varying amplitude of the total signal, which is undesired due to the inefficiency of linear power amplifiers.

It is therefore proposed here that a similar system could be used in a multistatic radar based on OFDMA (Orthogonal Frequency Division Multiple Access), otherwise known as multiuser OFDM. In this case, each transmitter of the system sends only one of the orthogonal carriers. In a communications context, each user (e.g. a mobile base station) is assigned one of the orthogonal carriers according to optimal capacity usage calculated from channel estimates(165).

Consider a multistatic radar system comprises n transmitters and a single receiver. The system is operating in the co-operative mode, and has accurate estimates of the location of each station. The purpose is to probe the existence of a target at some point in space. Each transmitter calculates the range to the proposed target position, and transmits a pulse on a modulated OFDM orthogonal carrier such that they arrive at the target at the same point in time. Then, at a given receiver, each carrier of the OFDM waveform will also arrive at the same time, and can be processed by a single matched filter. As each transmitter need only operate on a single carrier, 'saturated' power amplifiers with greater efficiency may be

used.

For the purpose of this analysis, we use a pulse comprising 25 bits, and simply code each bit of each carrier with a random phase. The resulting ambiguity function and zero-doppler cut are shown in Figure D-1 for a single carrier only, and in Figure D-1 where five carriers are used, corresponding to five transmitters in a multistatic radar.

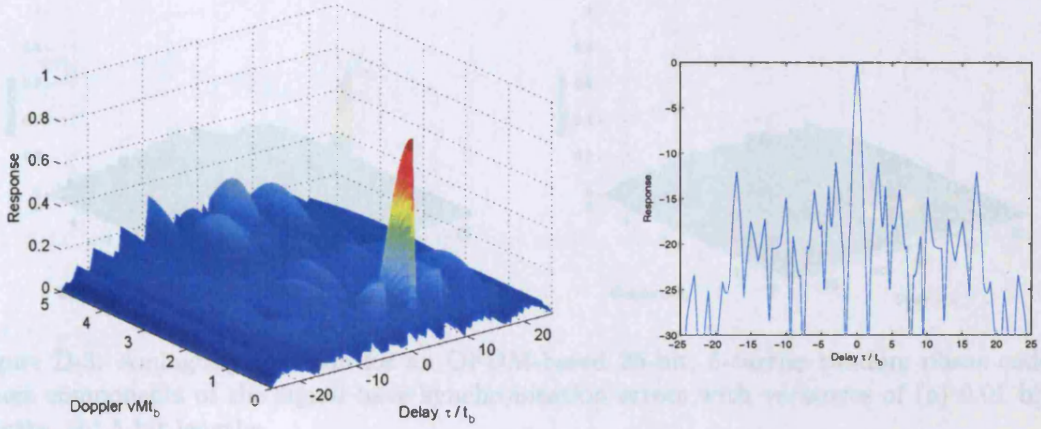

Figure D-1: Ambiguity function for a 25-bit random phase code on a single carrier

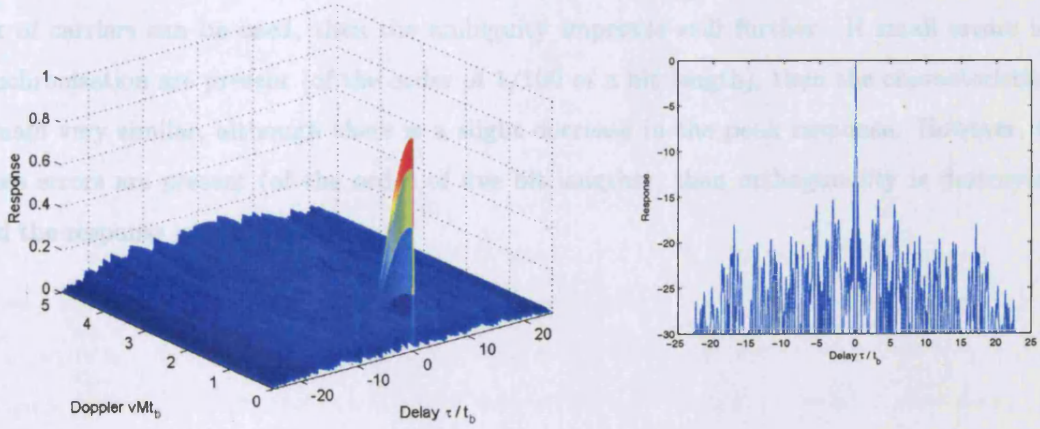

Figure D-2: Ambiguity function for an OFDM-based 25-bit, 5-carrier random phase code

Now the ambiguity function is modelled for the case that there is not perfect synchronisation between transmitters or there are errors in the transmitter location information. Then, the components of the OFDM signal arrive at the receiver with random Gaussian offsets. Firstly, the error variance is set to be equal to one-hundredth of a bit length which,

for a typical pulse length of 1 μs, corresponds to a synchronisation error variance of 0.4 ns or a range error of 0.12 m. Then, a much larger error variance of five bit lengths is modelled (synchronisation variance of 200 ns). The results, normalised to the maximum response of the perfectly synchronised case, are shown in Figure D-3.

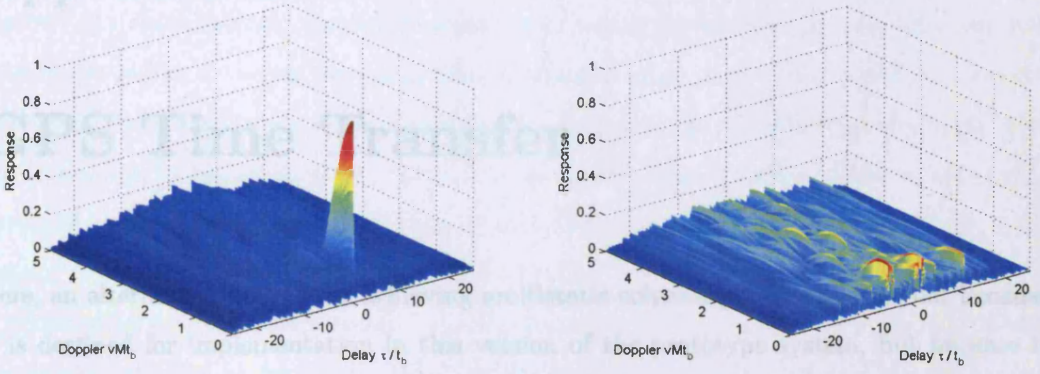

Figure D-3: Ambiguity function for an OFDM-based 25-bit, 5-carrier random phase code where components of the signal have synchronisation errors with variances of (a) 0.01 bit lengths, (b) 5 bit lengths

Evidently, given perfect synchronisation, this method provides considerably improved ambiguity characteristics compared to the single carrier pseudo-noise code. If larger number of carriers can be used, then the ambiguity improves still further. If small errors in synchronisation are present (of the order of 1/100 of a bit length), then the characteristics remain very similar, although there is a slight decrease in the peak response. However, if gross errors are present (of the order of five bit lengths), then orthogonality is destroyed and the response is very small.

Appendix E

GPS Time Transfer

Here, an alternative method for achieving multistatic coherency is considered, not because it is destined for implementation in this version of the prototype system, but because it offers a highly attractive method of time transfer when the distances between stations or their required mobility mean that wired connections are infeasible. The Global Positioning System (GPS) comprises a network of 24 satellites circling the earth twice per sidereal day in six orbits, together providing global coverage. A GPS receiver can measure the distance between itself and the satellite by referencing the timestamped signals from each satellite to its internal clock to calculate a range delay. This internal clock will have an unknown bias compared to the satellite's reference, therefore at least four satellite signals must be detected in order to determine the receiver location in three-dimensions.

The GPS signal currently comprises two types of code - *course-acquisition* C/A and *precision* P(Y). The P(Y) code is encrypted and classified for military use only. The satellites currently transmit both codes on *L1* frequency (1575.42 MHz) and P code only on *L2* frequency 1227.6 MHz, although a new satellite will shortly begin civil transmissions on the *L2* frequency. Both frequencies are phase coherent integer multiples of an atomic frequency standard at 10.23 MHz, and are adjusted to account for relativistic effects. Access to both codes simultaneously allows estimation of the ionospheric delay of signals, allowing for more accurate position and timing measurement. The codes are used to modulate the carrier at each satellite using a CDMA direct sequence BPSK scheme, and incorporate ephemeris data giving an estimate of the current location of the satellite and the difference between its internal clock and GPS 'system' time (although is only updated daily), which is ultimately

referenced to the UTC(USNO) coordinated atomic time scale.

Using this information during the signal acquisition and tracking process, a GPS receiver effectively locks its internal oscillator to the caesium atomic reference and therefore provides a method of time transfer as well as location estimation. In fact, GPS receivers can be implemented almost completely in software(166), which at first glance offers a perfect method of extremely accurate time transfer to arbitrarily positioned stations of a low-cost multistatic radar. However, uncompensated errors in ionospheric delay, satellite location, reference clocks, temperature variations and so on mean that the stability of the GPS receiver internal oscillator is quite poor in the short term. Nevertheless, if the signal can be averaged over long periods of time, then its mean frequency tends towards that of the UTC 'world' time clock, which provides ultimate stability.

Several commercial products are available that allow this synchronisation to be exploited for estimating time or frequency. Most commercial receivers provide a 1PPS (Pulse Per Second) output which is referenced to the receiver's internal oscillator, although the cycle-to-cycle jitter of this signal is very poor due to the granularity of the microprocessor used to control it. Several manufacturers market so-called GPSDOs (GPS Disciplined Oscillators), which combine a multi-channel GPS receiver with a good quality voltage-controlled OCXO or rubidium oscillator, which is locked to the GPS receiver internal oscillator. As this internal oscillator is considerably more noisy in the short term than the good quality VCO, the signal is averaged for a long period, ranging from a few minutes to many hours. The result is an oscillator signal that has a long term frequency stability approaching that of UTC, and a short-term stability and phase noise profile that is the same as that of the disciplined oscillator. The averaging process is effectively creating a PLL where the GPS receiver internal clock is the reference input, but where the loop filter bandwidth is extremely small. The better quality the disciplined oscillator, the longer the averaging period (because correction of short term deviations is not required), and the more accurate the long-term stability.

A comparison of commercially available GPSDOs in the context of use in multistatic radar was presented by Johnsen(167). The study was performed by measuring the error in the 1 PPS output from each unit, which was (apparently) derived from an internal rubidium oscillator. The peak-to-peak error over a 13 hour observation period between two closely spaced identical receivers was found to be in the order of ± 100 ns, although it would appear

that this error is related more to the method of synthesising the low frequency output than to any inherent instability in the rubidium oscillator. Further techniques such as 'GPS carrier phase' (where the phase of the GPS signal as well as the codes are used to reduce bias error) and 'GPS common-view' (where two very spaced receivers observe the same target at the same time to remove GPS satellite clock error) can be used to increase accuracy in GPS receivers. Such calibrated systems can result in frequency stability of the order of 2×10^{-15} over 24 hours(168).

Hence, it is indeed possible to achieve outstanding frequency stability, even using low-cost GPS receivers, but the caveat is that long-term averaging is required. Hence, a very good quality oscillator is necessary due to the weak disciplining of the control system. In general, it will be the expense of this component that precludes the use of such a system in low cost coherent radar. Further, the phase noise at all offsets of interest will be completely uncorrelated between receivers, so the benefits of the range correlation function will not be available. Therefore, GPS provides a solution for control of long-term frequency stability, but it does not remove the requirement for oscillators with low phase noise and high short-term stability in each receiver. It is noted however that a joint project between DARPA and NIST has produced a prototype of a miniature chip-scale atomic clock that is designed for very low cost applications (mobile phones, wrist watches, etc)(169)[1]. The current design has a short-term frequency stability of 10×10^{-9} over one second, although is some 300,000 times worse than caesium atomic clocks for very long-term stability. However, the combination of such a device with a GPS receiver and relatively inexpensive OCXO could provide a complete solution. The miniature atomic clock and the GPS receiver would be jointly used to discipline the crystal oscillator, the first providing short term stability, and the latter a long term frequency reference that is common to all stations. The OCXO itself has the lowest phase noise profile of all oscillators over typical small doppler frequencies, so can be used as the reference for the local oscillators and clocks in each radar station.

[1]Further information is available at tf.nist.gov/ofm/smallclock

Appendix F

Custom Circuit Schematics and PCB Designs

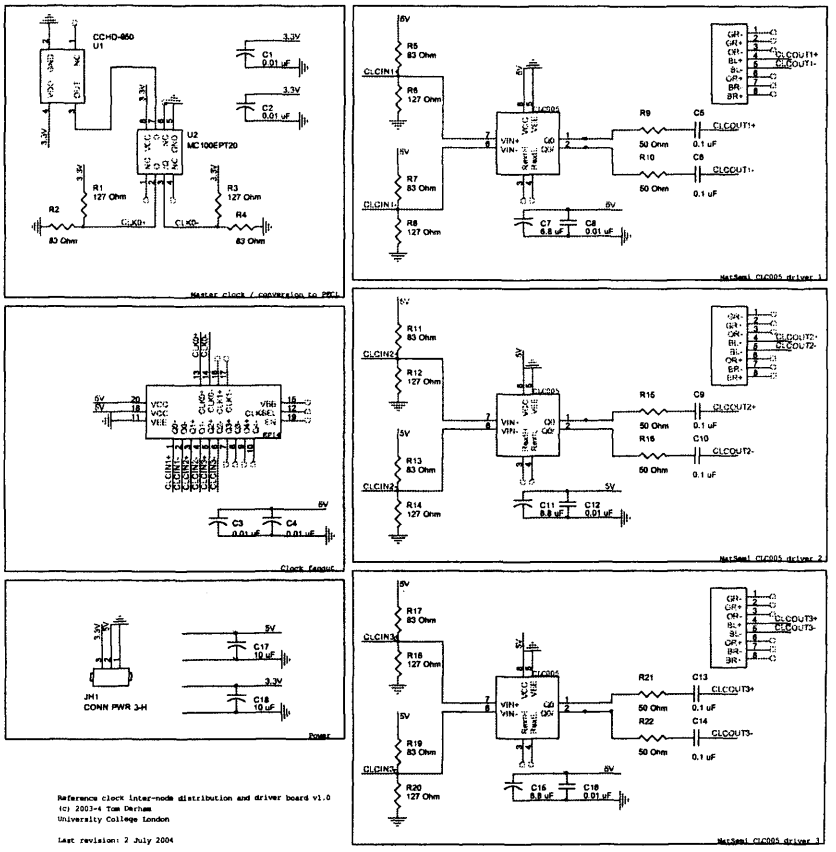

Figure F-1: Reference clock module schematic

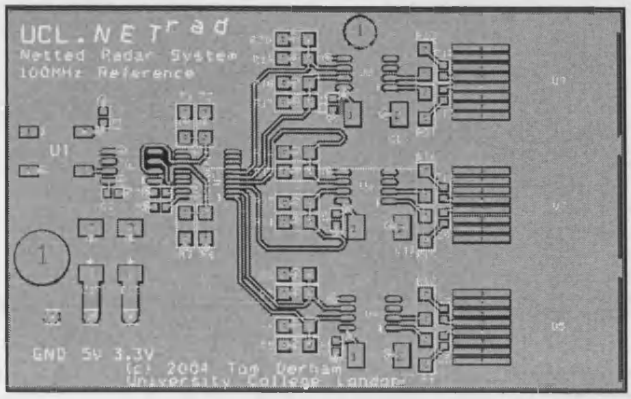

Figure F-2: Reference clock module PCB

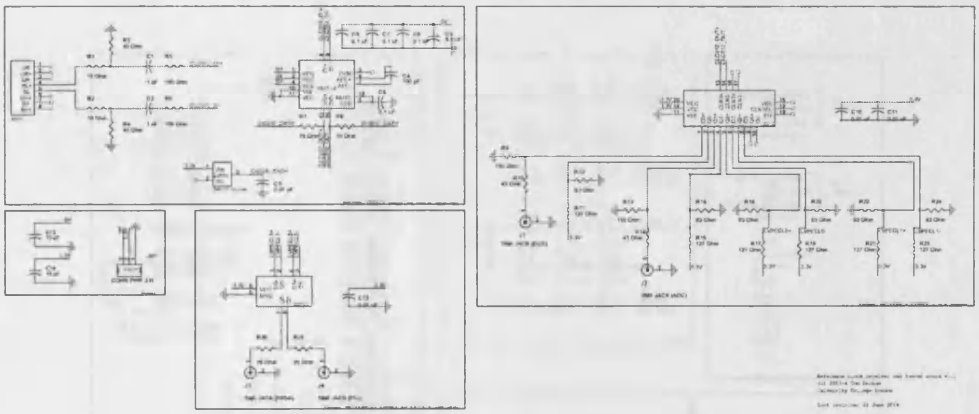

Figure F-3: Reference clock receiver schematic

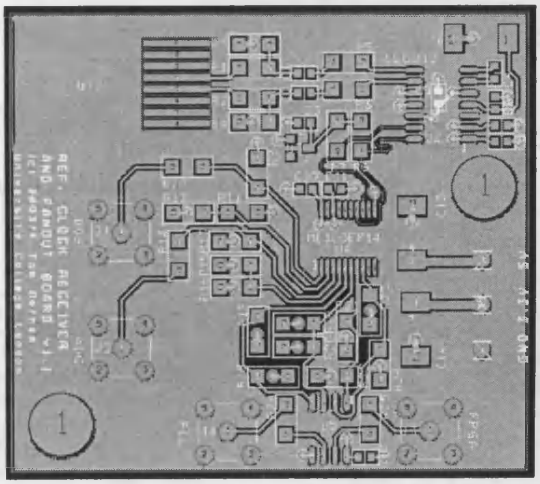

Figure F-4: Reference clock receiver module PCB

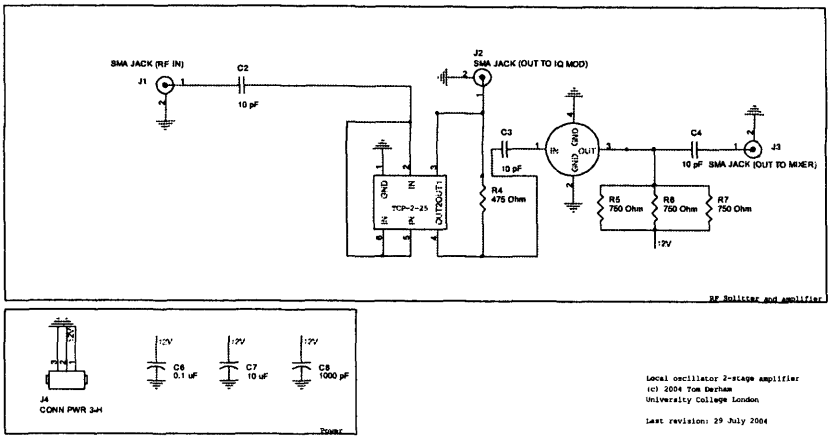

Figure F-5: Local oscillator amplifier schematic

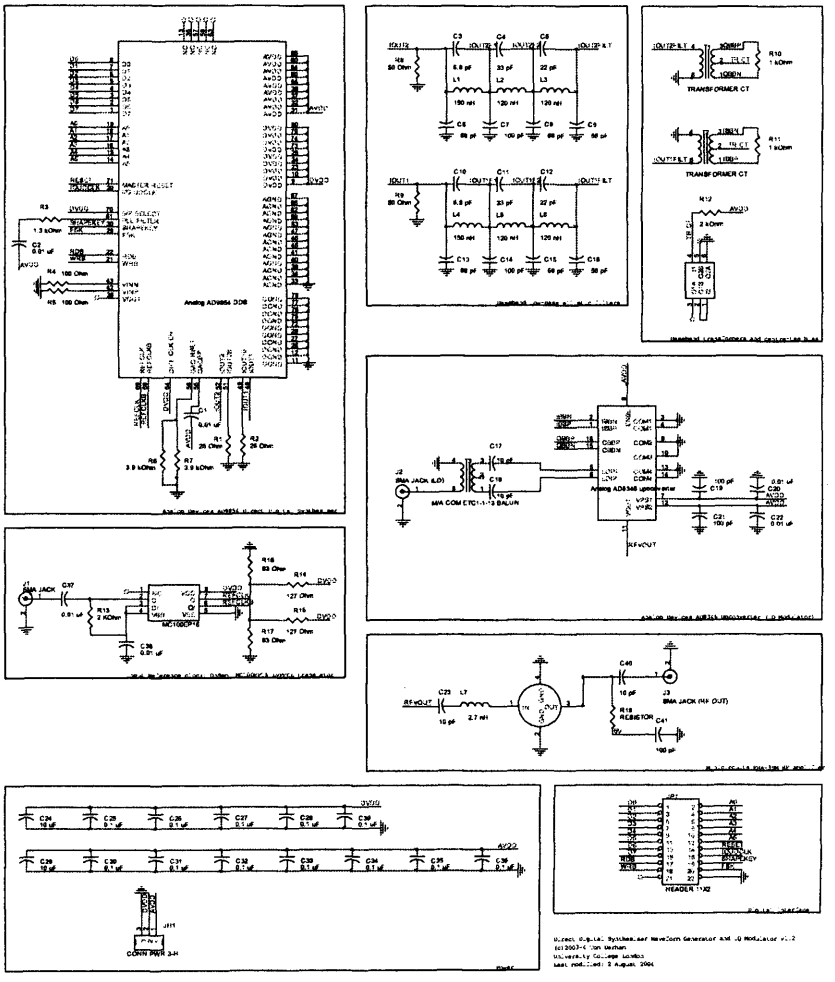

Figure F-6: Transmitter module schematic

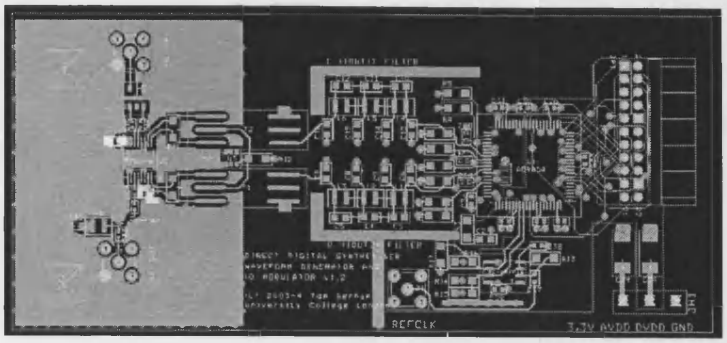

Figure F-7: Transmitter module PCB

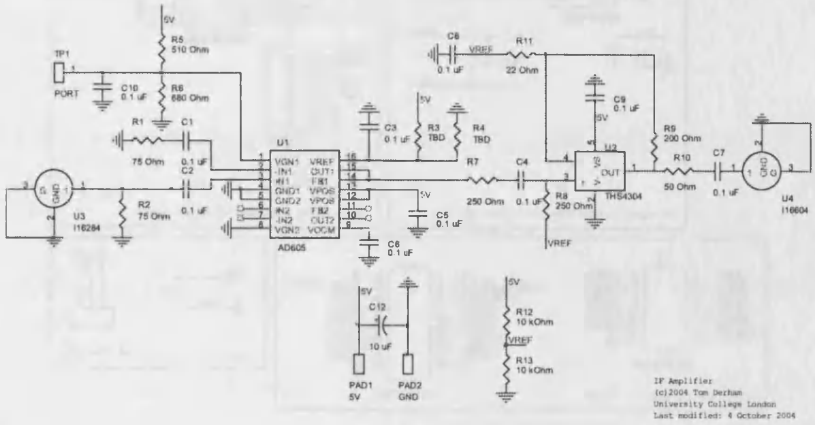

Figure F-8: Baseband receiver amplifier schematic

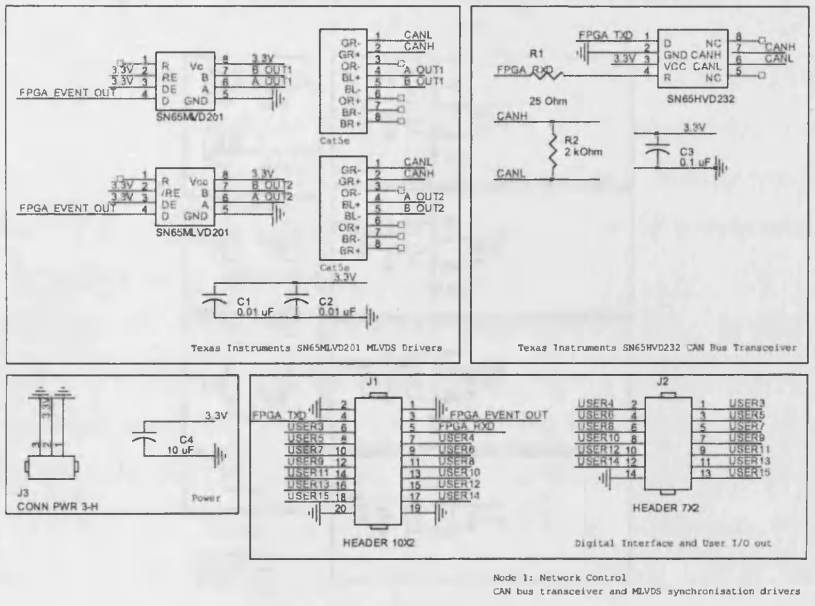

Figure F-9: Node 1 network transceiver schematic

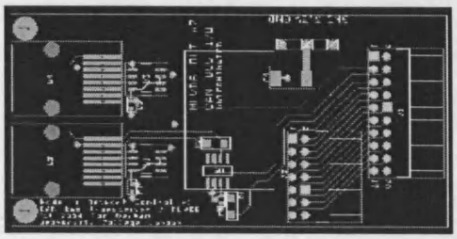

Figure F-10: Node 1 network transceiver PCB

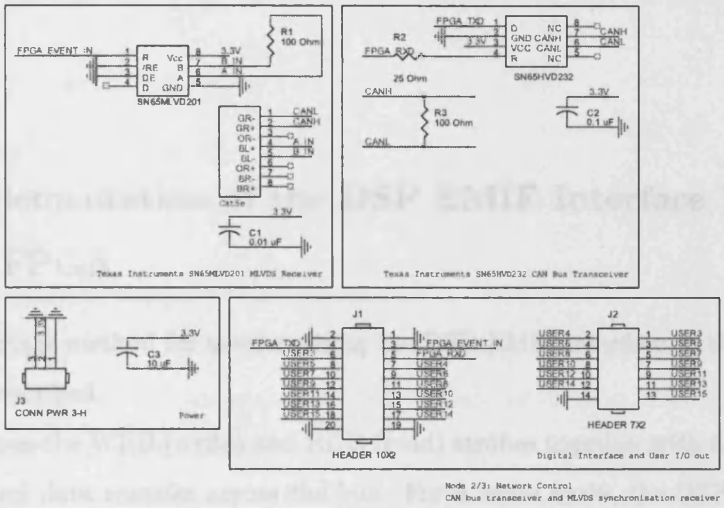

Figure F-11: Node 2/3 network transceiver schematic

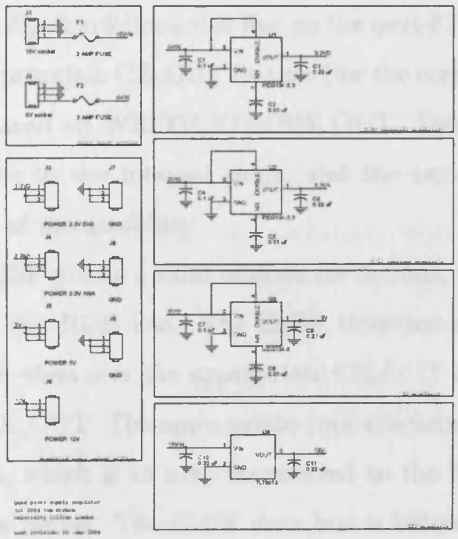

Figure F-12: Power supply module schematic

Appendix G

DSP

G.1 Implementation of the DSP EMIF Interface Timing on the FPGA

Here, the two-stage method for synchronising the DSP EMIF interface to the FPGA reference clock is described.

The DSP uses the WRB (write) and RDB (read) strobes together with a chip select line (CE2) to control data transfer across the bus. For a write cycle, the DSP places a valid address and data onto the bus, then sets CE2 (active low) and asserts (falling edge) the WRB line. The interface core on the FPGA caches the address and data on this falling edge, and toggles an internal flag. A flip-flop follows this flag on the next FPGA clock cycle. Then, the address is decoded, the appropriate CE_OUT line set (for the corresponding FPGA module) and a one-cycle strobe placed on WRITE_STROBE_OUT. This method synchronises the asynchronous WRB strobe to the internal clock, and the two-level synchronisation also minimises the probability of metastability.

For a read cycle, the DSP places a valid address on the bus, then sets CE2 (active low) and asserts (falling edge) the RDB line. The EMIF interface module caches the address and synchronises as above, then sets the appropriate CE_OUT line and places a one-cycle strobe on READ_STROBE_OUT. The appropriate core synchronously places valid data on the DATA_IN virtual bus, which is in turn transferred to the EMIF data bus within the required number of strobe cycles. The EMIF data bus is bidirectional, so virtual tristate drivers are used on the FPGA pins of EMIF_DATA_BUS_INOUT, controlled by the state

of EMIF_AOE_IN (asynchronous output enable).

Using this method, it is possible for data to be reliably transferred between the two asynchronous clock domains with full arbitration and deterministic latencies, which can be programmed on the DSP to control its timing of the bus.

G.2 System Control

Here, pseudocode is presented for the control of the master and slave nodes by the processor.

Pseudo-code: Master node 1

```
1: NET_get_slave_nodes_status()
2: NET_send_radar_parameters(waveform, pulse_length, PRF, ...)
3: program_pll(R, N)
4: program_dds_setup(MODE, FTW, DFW)
5: strobe_config_mode()        ▷ FPGA flag set to program PLL and DDS setup commands
6: program_timer_core(PRI_predelay, PRI, ADC_predelay, data_capture_period)
7: program_dds_commands(CLRACC ↓, φ1, ..., φn, CLRACC ↑) ▷ stored in FPGA buffer
8: start_system() ▷ FPGA flag set, counters start, FGPA sends sync strobe to other nodes
9: while dma_counter < pulses do
10:     if IRQ ↑ then
11:         dma_transfer()                    ▷ from ADC FIFO buffer to RAM
12:         dma_counter ++
13:     end if
14: end while
15: local_DSP()                    ▷ data cleansing, matched filter, pulse doppler
16: NET_get_slave_nodes_data()
17: joint_DSP()                                          ▷ multistatic fusion
```

Pseudo-code: Slave nodes 2/3

```
1: while radar_parameters == null do   ▷ Wait for radar parameters to be received from
       master node across network
2: end while
3: program_pll(R, N)
4: program_dds_setup(MODE, FTW, DFW)
5: strobe_config_mode()        ▷ FPGA flag set to program PLL and DDS setup commands
6: program_timer_core(PRI_predelay, PRI, ADC_predelay, data_capture_period)
7: program_dds_commands(CLRACC ↓, φ1, ..., φn, CLRACC ↑) ▷ stored in FPGA buffer
                        ▷ FPGA waits for sync strobe from master node then starts counters
8: while dma_counter < pulses do
9:     if IRQ ↑ then
10:        dma_transfer()                          ▷ from ADC FIFO buffer to RAM
11:        dma_counter ++
12:    end if
13: end while
14: local_DSP()                          ▷ data cleansing, matched filter, pulse doppler
15: while 1 do
16:    if NET_data_request then
17:        NET_send_data()
18:    end if
19: end while
```

G.3 Generating the Analytic Signal

Here, the theory of generating the so-called 'analytic signal' from a coherently timed array of sampled data is described.

Let $x(t)$ be the real, finite-energy signal at the *input* to the analogue-to-digital converter of a radar receiver, defined by its continuous-time fourier transform (CTFT):

$$X(f) = \int_{-\infty}^{\infty} x(t) \exp(-j2\pi ft)dt \tag{G.1}$$

The signal is low-pass filtered by the receiver with a cut-off frequency of 50 MHz, as shown in Figure G-1. As $x(t)$ is real, its CTFT is a complex conjugate symmetric function such that $X(-f) = X^*(f)$. Therefore the negative half of the spectrum contains redundant data. Removal of the negative frequencies creates a signal $z(t)$ with a single-sided spectrum that is known as the *analytic signal* (170). It has two properties - firstly that the real part of the analytic signal is exactly equal to the values of the original real sequence so that $\mathrm{Re}[z(t)] = x(t)$, and that the imaginary part is equal to the Hilbert transform of the original signal (phase shifted by 90 degrees) with frequency response defined in Equation G.2. Its real and imaginary components are therefore orthogonal over the period of the signal:

$$H_{ideal}(\exp(j\Omega)) = \begin{cases} +j & \text{for } -\pi \leq \Omega < 0, \\ -j & \text{for } 0 \leq \Omega < \pi. \end{cases} \tag{G.2}$$

The sampling process at the ADC yields a discrete-time signal with a spectrum described by the discrete-time fourier transform (DTFT):

$$X(f) = T \sum_{n=0}^{N-1} x[n] \exp(-j2\pi fnT) \tag{G.3}$$

where N is the sample length. The spectrum of $X(f)$ has a periodic structure shown in Figure G-2.

Strictly, a discrete-time signal can never be an analytic function because the periodic nature of the DTFT prevents the spectrum vanishing for all negative frequencies, but the term is commonly employed in discrete-time analysis to represent the signal with correspondingly similar properties (171). Generation of the discrete 'analytic' signal in the

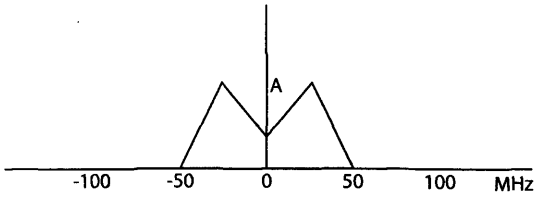

Figure G-1: Spectrum of real input signal

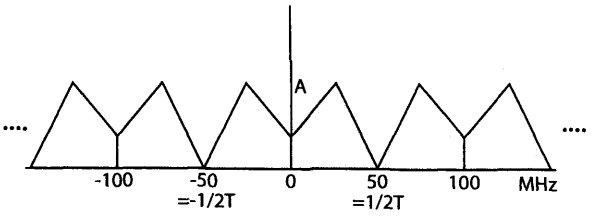

Figure G-2: DTFT of sampled signal

time domain can be approximated using two quadrature FIR filters to create the real and imaginary parts(172), or a single filter approximating the Hilbert transform to derive the imaginary part from the real signal. A true Hilbert transformer is not realisable as the number of taps required to create a 90 degree phase shift tends to infinity as the frequency tends to DC. Therefore the former method may preserve orthogonality but not the original data values, whereas the latter will preserve the original data but not create exact orthogonality between real and imaginary parts.

An approximation to the analytic signal may be generated simply in the frequency domain provided the energy close to DC and Nyquist is negligible. The finite length data stream is processed using the Fast Fourier Transform to create the DFT, a discretised version of the DTFT such that $X[m] = X(m/NT)$ ranging from $-f_{nyq}$ to $+f_{nyq}$, where the Nyquist frequency is $f_{nyq} = f_s/2$ given a sampling frequency f_s. To form the analytic signal, all complex values for negative frequencies are set to zero, and values for positive frequencies are doubled in order to maintain constant energy. However, values of the DFT corresponding to DC $X[0]$ and Nyquist $X[N/2]$ are unchanged, as they represent the average of the values either side of the discontinuity. The resulting (shifted) spectrum is shown in Figure G-3. As this rectangular 'cutting off' of the reference spectrum is equivalent to an infinite length complex time domain sequence, a wrap-around error may be introduced as a result of the finite input sequence, although this may often be small enough to be disregarded(173).

It is now clear that the sampling rate can be reduced by a factor-of-two without removing any information from the signal. This can be done simply by performing an inverse FFT of just the remaining single-sided spectrum, and scaling by 1/2 to maintain constant total energy, to create an $N/2$ point decimated-by-2 analytic signal consistent with the original data. The resulting DTFT in Figure G-4 shows the analytic spectrum intact (free from aliasing), positioned with a baseband centre of $N/4$.

This process has yielded two advantages: firstly, the data rate for all subsequent process-

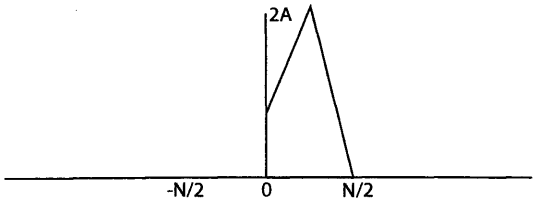

Figure G-3: DFT of analytic signal

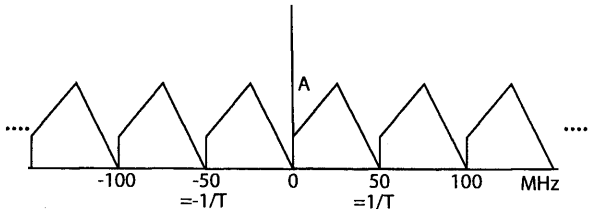

Figure G-4: DTFT of decimated analytic signal

ing has reduced by a factor-of-two; secondly, providing the entire bandwidth is utilised by the radar, a range or doppler bin is now conveniently represented by a single complex sample.

Bibliography

[1] E. Knott, J. Shaeffer, M. Tuley: *'Radar Cross Section'*, Artech House, 1993

[2] D. Dranidis: *'Airborne Stealth in a Nutshell Part II - Countering Stealth'*, Harpoon Waypoint No 6, December 2003

[3] P. Lacomme et al: *'Air and Spaceborne Radar Systems - An Introduction'*, Scitech, 2001

[4] V. Chernyak: *'Fundamentals of Multisite Radar Systems, Chapter 13'*, Gordon and Breach Scientific Publishers, 1998

[5] A. Farina (Ed): *'Optimised Radar Processors'*, IEE, 1987

[6] G. Galati: *'Advanced Radar Techniques and Systems'*, IEE, 1993

[7] A. Farina: *'Survey of Data Processing Systems in Netted Radar'*, Electro-Technology, Vol 28, No 2, June 1984

[8] J. Baniak et al: *'Silent Sentry Passive Surveillance'*, Aviation Week and Space Technology, June 1999

[9] V. Chernyak: *'Fundamentals of Multisite Radar Systems, Chapter 1'*, Gordon and Breach Scientific Publishers, 1998

[10] J. Ormsby et al: *'Analytic Coherent Radar Techniques for Target Mapping'*, IEEE Transactions on Aerospace and Electronic Systems Vol 6, 1970

[11] V. Chernyak: *'Fundamentals of Multisite Radar Systems, Chapter 8'*, Gordon and Breach Scientific Publishers, 1998

[12] B. Flanagan, K. Bell: *'Array Self-Calibration with Large Sensor Position Errors'*, Proceedings of IEEE Asilomar Conference on Signals, Systems and Computers, 1999

[13] C. Latham, A. Stobbs: *'Radar: A Wartime Miracle'*, Sutton Publishing, 1997

[14] H. Griffiths: *'Bistatic and Multistatic Radar'*, Military Radar Conference, Shrivenham, UK, 2004

[15] M. Mirkin, C. Schwartz, S. Spoerry: *'Automated Tracking with Netted Ground Surveillance Radars'*, Proceedings of the IEEE International Radar Conference, 1980

[16] J. Salah, J. Moriello: *'Development of a Multistatic Measurement System'*, Proceedings of the IEEE International Radar Conference, 1980

[17] A. Cameron: *'The Jindalee Operational Radar Network - Its Architecture and Surveillance Capability'*, Proceedings of the 1995 International Radar Conference

[18] G. Galati, M. Naldi, M. Ferri: *'Airport Surface Surveillance with a Network of Miniradars'*, IEEE Transactions on Aerospace and Electronic Systems, Vol 35, 1999

[19] H. Rohling et al: *'Multistatic Radar Principles for Automotive RadarNet Applications'*, German Radar Symposium 2002, Bonn, Germany

[20] Applied Physics Laboratory: *'The Cooperative Engagement Capability'*, John Hopkins APL Technical Digest Vol 16, 1995

[21] *'Network Enabled Capability JSP777'*, Ministry of Defence UK, 2005

[22] D. Lambert: *'Ubiquitous Command and Control'*, Proceedings of IEEE Information, Decision and Control Symposium 1999

[23] M. Martin: *'Techsat 21 and Revolutionizing Space Missions Using Microsatellites'*, Proceedings of the 15th AIAA/USU Conference on Small Satellites, Logan, UT, 2001

[24] J. Garnham et al: *'Enabling Research and Development for Flight Development of Sparse Aperture Sensing'*, AIAA Space 2001 Conference and Exposition

[25] G. Inalhan: *'Precise Formation Flying Control of Multiple Spacecraft using Carrier-Phase Differential GPS'*, American Astronautical Society Space Flight Mechanics Meeting, 2000

[26] D. Massonnet: *'Capabilities and Limitations of the Interferometric Cartwheel'*, CEOS SAR Workshop, Toulouse, 1999

[27] R. Schilizzi: *'The Square Kilometre Array'*, www.skatelescope.com, 2004

[28] E. Waltz: *'Multisensor Data Fusion'*, Artech House, 1990

[29] W. Bath: *'Association of Multisite Radar Data in Presence of Large Navigation and Sensor Alignment Errors'*, Proceedings of the Internation Radar Conference, London, 1982

[30] Q. Weiyan, P. Yingning, L. Dajin: *'An Approach to Small Targets Tracking for Netted Radar Surveillance Scenario'*, Chinese Journal of Electronics, Vol 7, 1998

[31] S. Thomopoulis, N. Okello: *'Design of a Robust Multi-Radar Distributed Data Fusion System'*, IEEE Regional Conference on Aerospace Control Systems, 1993

[32] J. López et al: *'Cooperative Management of Netted Surveillance Sensors'*, IEEE International Conference on Systems, Man and Cybernetics 1997, Florida

[33] D. Martinez, M. Gruber: *'Next Generation Technologies to Enable Sensor Networks'*, Proceedings of IEEE Sensors Conference, Vol 2, 2002

[34] V. Chernyak: *'Fundamentals of Multisite Radar Systems, Chapter 5'*, Gordon and Breach Scientific Publishers, 1998

[35] D. Baumgarten: *'Optimum Detection and Receiver Performance for Multistatic Radar Configurations'*, IEEE International Conference on Acoustics, Speech and Signal Processing, 1982

[36] E. Fishler et al: *'Statistical MIMO Radar'*, 12th Conference on Adaptive Sensors Array Processing, 2004

[37] T. Johnsen, E. Olsen, R. Gunderson: *'Hovering Helicopter Measured by Bi/Multistatic CW Radar'*, Proceedings of IEEE Radar Conference 2003, Alabama

[38] S. Coutts et al: *'Distributed Coherent Aperture Measurements for Next Generation Radar (Presentation)'*, Tri-Service Waveform Diversity Workshop, 2005

[39] H. Nyquist: *'Thermal Agitation of Electric Charge in Conductors'*, Physics Review 32, p 110, 1928

[40] F. Hooge: *'1/f noise sources'*, IEEE Transactions on Electronic Devices Vol 41, 1994

[41] R. Klemm: *'Space-Time Adaptive Processing - Principles and Applications'*, IEE, 1998

[42] J. Marcum: *'A Statistical Theory of Target Detection by Pulsed Radar'*, IRE Transactions on Information Theory IT-6, 1960

[43] M. Skolnik: *'Introduction to Radar Systems'*, McGraw Hill, 1962

[44] H. Van Trees: *'Optimum Array Processing. Part IV of Detection, Estimation and Modulation Theory'*, Wiley, 1992

[45] J. Thomas, J. Wolf: *'On the Statistical Detection Problem for Multiple Signals'*, IRE Transactions on Information Theory, 1962

[46] M. Skolnik: *'Radar Handbook'*, McGraw Hill, 1990

[47] H. Van Trees: *'Detection, Estimation and Modulation Theory, Part III'*, Wiley, 1992

[48] T. Kailath, H. Poor: *'Detection of Stochastic Processes'*, IEEE Transactions on Information Theory Vol 44, 1998

[49] R. McDonough, A.Whalen: *'Detection of Signals in Noise'*, Academic Press, 1995

[50] V. Chernyak: *'Fundamentals of Multisite Radar Systems, Chapter 4'*, Gordon and Breach Scientific Publishers, 1998

[51] J. Cui et al: *'Performance Evaluation of Optimum Combining and Maximal Ratio Combining in the Presence of Co-channel Interference and Channel Correlation for Wireless Communication Systems'*, Mobile Networks and Applicatins, January 1998

[52] A. Papoulis: *'Probability, Random Variables and Stochastic Processes'*, McGraw Hill, 2002

[53] N. Levanon: *'Radar Principles'*, John Wiley & Sons, 1988

[54] P. Swerling: *'Probability of Detection for Fluctuating Targets'*, IRE Transactions on Information Theory IT-6, 1960.

[55] S. Kingsley, S. Quegan: *'Understanding Radar Systems'*, McGraw Hill

[56] J. Teti: *'Wide-band Airborne Radar Operating Considerations for Low-Altitude Surveillance in the Presence of Specular Multipath'*, IEEE Transactions on Antennas and Propagation, Vol 48, 2000

[57] D. Shiu et al: *'Fading Correlation and Its Effect on the Capacity of Multielement Antenna Systems'*, IEEE Transactions on Communications, Vol 48, 2000

[58] T. Kailath: *'A General Likelihood Ratio Formula for Random Signals in Gaussian Noise'*, IEEE Transactions on Information Theory Vol IT-15, 1969

[59] U. Grenander: *'Stochastic Processes and Statistical Inference'*, Arkiv fur Mat., Vol 1, 1950

[60] L. Blake: *'Radar Range-Performance Analysis'*, Lexington Books, 1980

[61] A. Manikas et al: *'Evaluation of Superresolution Array-Techniques Applied to Coherent Sources'*, International Journal of Electronics, January 1997

[62] R. Schmidt: *'Multiple Emitter Location and Signal Parameter Estimation'*, Proceedings of the RADC Spectrum Estimation Workshop, 1979

[63] R. Hansen: *'Phased Array Antennas'*, Wiley, 1998

[64] R. Leahy, B. Jeffs: *'On the Design of Maximally Sparse Beamforming Arrays'*, IEEE Transactions on Antennas and Propagation, Vol 39, 1991

[65] A. Austeng et al: *'1D and 2D Algorithmically Optimized Sparse Arrays'*, Proceedings of the IEEE Ultrasonic Symposium, 1997

[66] F. Anderson: *'Ultra-Wideband Beamforming in Sparse Arrays'*, IEE Proceedings, Vol 138, 1991

[67] A. Flaig, G. Arce: *'Nearfield Spot-Beamforming with Distributed Arrays'*, Proceedings of the IEEE Sensor Array and Multichannel Signal Processing Workshop, 2000

[68] B. Kennett: *'Signal Parameter Estimation for Sparse Arrays'*, Bulletin of the Seismological Society of America, Vol 93, 2003

[69] C. Chambers et al: *'Temporal and Spatial Sampling Influence on the Estimates of Superimposed Narrowband Signals: When Less Can Mean More'*, IEEE Transactions on Signal Processing, Vol SP-44, 1996

[70] Y. Huang, M. Barkat: *'Near-field Multiple Source Localization by Passive Sensor Array'*, IEEE Transactions on Antennas and Propagation, 1991

[71] Y. Chengyou, X. Shanjia, W. Dongjin: *'Location Accuracy of Multistatic Radars Based on Ranging Information'*, Proceedings of the CIE International Conference on Radar,1996

[72] S. Axelsson: *'Estimation of Target Position and Velocity Using Data from Multiple Radar Stations'*, IEEE International Geoscience and Remote Sensing Symposium, 2003

[73] V. Chernyak: *'Fundamentals of Multisite Radar Systems, Chapter 11'*, Gordon and Breach Scientific Publishers, 1998

[74] H. Poor: *'An Introduction to Signal Detection and Estimation'*, Springer-Verlag, 1994

[75] N. Willis: *'Bistatic Radar'*, Artech House, 1991

[76] A. Hume, C. Baker: *'Netted Radar Sensing'*, IEEE Aerospace and Electronics Systems Magazine, 2003

[77] T. Tsao et al: *'Ambiguity Function for a Bistatic Radar'*, IEEE Transactions on Aerospace and Electronic Systems, July 1997

[78] H. Van Trees: *'Optimum Array Processing. Part IV of Detection, Estimation and Modulation Theory'*, Wiley, 1992

[79] *'New Radar Technology 8,500 - 10,500 MHz Band'*, International Telecommunication Union Seminar on Technical Innovation

[80] L. Corey: *'Special Project Office Briefing'*, DARPATech Symposium 2002

[81] C. Cerny: *'Analog-to-Digital Converters - the Key to Digital Receivers'*, Air Force Research Laboratory Brief, March 2001, www.afrl.af.mil

[82] R. Dressler, D. Barnum, M. Loiz: *'COTS SAR Processing Software'* Proceedings of the National Radar Conference, Michigan, 1996

[83] *'Relocatable Over-the-Horizon Radar for Homeland Security'*, Raytheon Company, www.raytheon.com

[84] http://www.fas.org/man/dod-101/sys/ship/weaps/an-spy-1.htm

[85] *'Solano Communications IC: A High-Throughput Solution for 3G Wireless and Broadband Base Stations'*, Spectrum Signal Processing Inc,

www.spectrumsignal.com

[86] *'Enhanced Plastics Overview'*, National Semiconductor, www.natsemi.com

[87] G. Fitzhugh, R. Comfort: *'Validated Modernization'*, CPU Technology, Inc

[88] *'General Requirements for Integrated Circuits'*, STACK International Specification 0001, 1993

[89] L. Condra: *'Combating Electronic Component Obsolescence by Using Common Processes for Defense and Commercial Aerospace Electronics'*, National Defense Industrial Association Conference, 1999

[90] J. Roulston, BAE Systems *'Seeking a New Way Forward'*, Proceedings of The Application of Obsolescence Strategies Conference 2003 The Component Obsolescence Group

[91] D. Leiss: *'Military Radars and WLANs Wrestle with Interference Issues'*, COTS Journal, 2005, www.cotsjournalonline.com

[92] A. Duzdar, G. Kompa: *'A Low Cost W-Band Multi-Beam Doppler Radar for Automotive Applications'*, IEEE MTT-S Digest, 1997.

[93] E. Adler et al: *'Low-cost Enabling Technology for Multimode Radar Requirements'*, Proceedings of the IEEE Radar Conference, Texas, 1998.

[94] A. Duzdar, G. Kompa: *'Applications using a Low-cost Baseband Pulsed Microwave Sensor'*, Proceedings of the IEEE Instrumentation and Measurement Conference, Budapest, 2001.

[95] M. Radford: *'Development of BLightER, a cost sensitive, high performance FMCW Radar'*, Proceedings of the European Microwave Conference, 2004

[96] J. Tirpak: *'The Problem of Outdated Avionics'*, Journal of the Air Force Association Magazine, 2000, www.afa.org

[97] S. Shank et al: *'An Open Architecture for an Embedded Signal Processing Subsystem'*, IEEE Radar Conference, Philadelphia, USA, 2004.

[98] S. Rejto: *'Radar Open Systems Architecture and Applications'*, IEEE International Radar Conference , 2000.

[99] *'Wishbone System-on-Chip Interconnection Architecture for Portable IP Cores'*, OpenCores, www.opencores.org

[100] *'INL/DNL Measurements for High-Speed Analog-to-Digital Converters'*, Maxim Semiconductor Application Note, 2000, www.maxim.com

[101] *'Interleaving ADCs for Higher Sample Rates'*, National Semiconductor Application Note, 2005

[102] *'Using Digital Clock Managers (DCM) in Spartan-3 FPGAs'*, Xilinx Application Note, 2003, www.xilinx.com

[103] *'Agilent 20 GSa/s 8b Analog-to-Digital Converter Fact Sheet'*, Agilent Technologies, 2003, www.agilent.com

[104] D. Dubbert, G. Sloan, A. Doerry: *'FPGA's Role in the Development of Small Synthetic Aperture Radars'*, Wireless Design & Development, 2004, www.wirelessdesignmag.com

[105] J. Keller: *'Radar Processing Shifts to FPGAs and Altivec'*, Military & Aerospace Electronics, 2003, mae.pennnet.com

[106] http://www.gedae.com

[107] http://www.celoxica.com

[108] R. Andraka: *'FPGAs Make Radar Signal Processor on a Chip a Reality'*, Proceedings of the Asilomar Conference on Signals, Systems and Computers, Monterey, 1999

[109] *'Evaluating DSP Processor Performance'*, Berkeley Design Technology Brief, 2002

[110] R. Stapleton et al: *'The Use of Field Programmable Gate Arrays in High Performance Radar Signal Processing Applications'*, IEEE International Radar Conference, 2000

[111] T. Lee, A. Hajimiri: *'Oscillator Phase Noise: A Tutorial'*, IEEE Journal of Solid State Circuits, Vol 33, 2000

[112] A. Dearn: *'How to Design RF Circuits - Oscillators'*, Plextek Ltd, www.plextek.co.uk

[113] W. Robins: *'Phase Noise in Signal Sources'*, Peter Peregrinus Ltd (IEE), 1982

[114] D. Leeson: *'A Simple Model of Feedback Oscillator Noise Spectrum'*, Proceedings of the IEEE, pp 329-330, 1966

[115] A. Demir, A. Mehrotra, J. Roychowdhury: *'Phase Noise in Oscillators: A Unifying Theory and Numerical Methods for Characterisation'*, IEEE Transactions on Circuits and Systems: Fundamental Theory and Applications, 2000

[116] D. Howe, D. Allan, J. Barnes: *'Properties of Signal Sources and Measurement Methods'*, Proceedings of the 35th Annual Symposium on Frequency Control, 1981

[117] D. Allan: *'Statistics of Atomic Frequency Standards'* Proceedings of the IEEE Vol 54, 1966

[118] J. Scheer, J. Kurtz (Ed.): *'Coherent Radar Performance Estimation'*, Artech House, 1993

[119] M. Budge: *'Timing Jitter Characterisation for Pulsed and Pulsed Doppler Radars'*, IEEE Southeastcon Proceedings, 1992

[120] *'Aperture Uncertainty and ADC System Performance'*, Analog Devices Application Note AN-501, 2000, www.analog.com

[121] B. Brannon: *'Understanding the Effects of Clock Jitter and Phase Noise on Sampled Systems'*, EDN, 2004, www.edn.com

[122] J. Billingsley, J. Larrabee: *'Measured Spectral Extent of L- and X-band Radar Reflections from Wind-Blown Trees'*, Lincoln Laboratory MIT, ESD-TR-86-153, 1987

[123] M. Long: *'Radar Reflectivity of Land and Sea'*, Artech House, 2001

[124] M. Budge: *'Range Correlation Effects on Phase and Amplitude Noise'*, IEEE Southeastcon Proceedings, 1993

[125] J. Vig: *'Introduction to Quartz Frequency Standards'*, Army Research Laboratory, 1992, www.ieee-uffc.org

[126] G. Montress et al: *'Extremely Low Phase Noise SAW Resonator Oscillators: Design and Performance'*, IEEE Transactions on Ultrasonics, Ferroelectrics and Frequency Control, Vol 35, 1988

[127] I. Thompson: *'Strategies for the Analysis and Design of a Low Noise, Frequency Agile Synthesiser'*, PhD thesis, University College London, May 2003.

[128] T. Landecker, J. Vaneldik: *'A Phase-Stabilised Local-Oscillator System for a Synthesis Radio Telescope'*, IEEE Transactions on Instrumentation and Measurement, Vol IM-31, 1982

[129] B. Carlson et al: *'The Large Adaptive Reflector: A 200-m diameter, wideband, cm-m Wave Radio Telescope'*, SPIE International Symposium on Astronomical Telescopes and Instrumentation, 2000

[130] K. Crawford et al: *'The CEBAF Fiber Optic Phase Reference System'*, Particle Accelerator (PAC) Proceedings, 1995

[131] L. Kesheng: *'An Analysis of Some Problems of Bistatic and Multistatic Radars'*, Proceedings of the International Radar Conference 2003, Adelaide

[132] W. Grover: *'Free-Space Optical Distribution of Local Oscillator Signals in Aperture Synthesis Radio Telescope Arrays'*, Electronics Letters, Vol 31, 1995

[133] C. Drentea: *'Designing Frequency Synthesisers'*, RF Technology Expo-88, pp. 37-58.

[134] P. Brennan: *'Frequency Synthesiser'*, Patent WO 01/61858, February 2000.

[135] Z. Galani: *'An Overview of Frequency Synthesizers for Radars'*, IEEE Transactions on Microwave Theory and Techniques, Vol 39, 1991

[136] J. Tierney, C. Rader, B. Gold: *'A Digital Frequency Synthesiser'*, IEEE Transactions on Audio and Electroacoustics March 1971.

[137] *'A Technical Tutorial on Direct Digital Synthesis'*, Analog Devices, www.analog.com

[138] T. Derham, K. Woodbridge, C. Baker, H. Griffiths: *'The Design and Development of an Experimental Netted Radar System'*, Proceedings of the International Radar Conference 2003, Adelaide

[139] *'Relating to the Use of Short Range Devices'*, ERC Recommendation 70-03, 2005

[140] *'Electromagnetic Capability and Radio Spectrum Matters; Short Range Devices'*, European Standard ETSI EN 300 440, 2001

[141] I. Mohor: *'CAN Protocol Controller'*, www.opencores.org

[142] *'CAN Specification'*, www.can.bosch.com

[143] D. Dudgeon, R. Mersereau: *'Multidimensional Digital Signal Processing'*, Prentice Hall, 1984

[144] F. Gardner, L. Erup: *'Interpolation for Timing Adjustment in Digital Modems'*, Proceedings of the 2nd International Workshop on DSP Techniques Applied to Space Communications, 1990

[145] M. Fowler: *'Pulse Extraction for Radar Emitter Location'*, 2001 Conference on Information Sciences and Systems, The John Hopkins University

[146] A. Yardim, G. Cain, A. Lavergne: *'Performance of Fractional Delay Filters Using Optimal Offset Windows'*, Proceedings of the International Conference on Acoustics, Speech and Signal Processing, Germany, 1997

[147] D. Barton, C. Cook: *'Radar Evaluation Handbook'*, Artech House, 1991

[148] *'Noise Figure Measurement Accuracy - the Y-Factor Method'*, Agilent Technologies Application Note 57-2, www.agilent.com

[149] R. D'Agostino, A. Belanger, R. D'Agostino Jr: *'A Suggestion for Using Powerful and Informative Tests of Normality'*, American Statistician, 1990

[150] A. Reilly, G. Frazer, B. Boashash: *'Analytic Signal Generation - Tips and traps'*, IEEE Transactions on Signal Processing, Vol 42, 1994

[151] K. Sarabandi: *'Optimum Corner Reflectors for Calibration of Imaging Radars'*, IEEE Transactions on Antennas and Propagation, Vol 44, 1996

[152] A. Farina, L. Timmoneri: *'Cancellation of Clutter and EM Interference with STAP Algorithms'*, IEEE Radar Conference, Pennsylvania 2004

[153] J. Neyman, E. Pearson: *'On the problem of the most efficient tests of statistical hypotheses'*, Philosophical Transactions of the Royal Society, Vol A 231 No. 9, 1933

[154] D. North: *'An analysis of the factors which determine signal/noise discrimination in pulsed-carrier systems'*, Proceedings of the IEEE, Vol 51, 1963 (reprint of RCA Lab Report PTR-6C, 1943)

[155] P. Woodward: *'Probability and Information Theory, with Applications to Radar'*, Pergamon Press, 1953

[156] V. Kostylev: *'Microwave Scattering with Application to Bistatic Radars'*, Vestnik of Voronezh State University - Physics and Mathematics, Vol 2, 2004

[157] D. Beale, A. Hume: *'Bistatic RCS Tools for the Assessment of Multi-static Radar'*, Proceedings of Radar 2002, UK

[158] M. Golay: *'Complementary Series'*, IRE Transactions on Information Theory, Vol IT-7, 1961

[159] E. Mozeson, N. Levanon: *'Removing Autocorrelation Sidelobes by Overlaying Orthogonal Coding onto any Train of Identical Pulses'*, IEEE Transactions on Aerospace and Electronic Systems, Vol 39, 2003

[160] J. Proakis, M. Salehi: *'Communication Systems Engineering'*, Prentice Hall, 2002

[161] T. Hale, M. Temple, B. Crossley: *'Ambiguity Analysis for Pulse Compression Radar using Gold Code Sequences'*, Proceedings of the IEEE Radar Conference, 2001

[162] T. Johnsen et al: *'Simultaneous Use of Multiple Pseudo-Random Noise Codes in Multistatic CW Radar'*, Proceedings of IEEE Radar Conference 2004, Pennsylvania

[163] H. Deng: *'Polyphase Code Design for Orthogonal Netted Radar Systems'*, IEEE Transactions on Signal Processing, Vol 52, 2004

[164] N. Levanon: *'Multifrequency Complementary Phase-Coded Radar Signal'*, IEE Proceedings, Radar, Sonar and Navigation Vol 147, 2000

[165] E. Lawrey: *'Multiuser OFDM'*, Proceedings of the International Symposium on Signal Processing Applications, 1999

[166] J. Bao-Yen Tsui: *'Fundamentals of Global Positioning System Receivers'*, John Wiley, 2000

[167] T. Johnsen: *'Time and Frequency Synchronisation in Multistatic Radar'*, IEEE Radar Conference, California, USA, 2002.

[168] T. Parker, D. Matsakis: *'Time and Frequency Dissemination: Advances in GPS Transfer Techniques'*, GPS World Magazine, 2004, www.gpsworld.com

[169] S. Knappe et al: *'A Microfabricated Atomic Clock'*, Applied Physics Letters, Vol 85, 2004

[170] D. Gabor: *'Theory of Communications'*, Journal of the Institute of Electrical Engineering, Pt III, Vol 93, 1946

[171] S. Lawrence Marple, Jr: *'Computing the Discrete-Time 'Analytic' Signal via FFT'*, IEEE Transactions on Signal Processing, Vol 7, September 1999

[172] A. Oppenheim and R. Schafer: *'Discrete-Time Signal Processing'*, Prentice Hall, 1989

[173] M. Otten: *'Alternative Solutions for Hilbert Filtering in a Pulse Compression Radar'*, IEEE International Radar Conference, Arlington, USA, 1990